

Ultralong-range Diatomic Molecules
in External Electric and Magnetic
Fields

Dissertation

zur Erlangung des Doktorgrades

des Department Physik

der Universität Hamburg

vorgelegt von

Markus Kurz

aus Nürnberg

Hamburg

2014

Gutachter der Dissertation:

Prof. Dr. Peter Schmelcher
Prof. Dr. Hossein Sadeghpour

Gutachter der Disputation:

Prof. Dr. Peter Schmelcher
Prof. Dr. Henning Moritz

Datum der Disputation:

19.01.2015

Vorsitzender der Prüfungskommission:

Prof. Dr. Ludwig Mathey

Vorsitzender des Promotionsausschusses:

Prof. Dr. Jan Louis

Dekan der Fakultät für Mathematik, Informatik
und Naturwissenschaften:

Prof. Dr. Heinrich Graener



Universität Hamburg

DER FORSCHUNG | DER LEHRE | DER BILDUNG



“Per aspera ad astra.”
-Seneca¹

¹Lucius Annaeus Seneca (c. 4BC-AD65): Roman statesman, philosopher and dramatist [1].

Zusammenfassung

Ultralangreichweitige diatomare Moleküle in externen Feldern – Gegenstand dieser Arbeit ist die theoretische Untersuchung der Quanteneigenschaften von ultralangreichweitigen diatomaren Molekülen in Anwesenheit externer elektrischer und magnetischer Felder. Im Rahmen dieser Dissertation werden sowohl die elektronischen Born-Oppenheimer Potentialflächen als auch die durch diese induzierte Dynamik der Rotations- und Vibrationsfreiheitsgrade analysiert. Neben analytischen Näherungen wird hierzu auf etablierte numerischen Diagonalisierungsverfahren zurückgegriffen. Im ersten Teil dieser Arbeit untersuchen wir ultralangreichweitige Rydbergmoleküle. In Abhängigkeit vom adressierten elektronischen Zustand erhält man Moleküle mit einer spezifischen Ausrichtung und Orientierung bezüglich der angelegten Felder. Reine elektrische Felder stabilisieren die untersuchten Moleküle, welche dann antiparallel zum Feld orientiert sind. Aufgrund der starken elektrischen Polarisierbarkeit genügen bereits kleine Feldstärken, um verschiedene molekulare Parameter wie den internuklearen Abstand als auch das elektrische Dipolmoment zu variieren. Für reine Magnetfelder erhält man Moleküle unterschiedlicher Ausrichtungen. Die berechneten Bindungsenergien verschiedener molekularer Zustände werden mit experimentellen Werten verglichen. Hierbei wird eine gute Übereinstimmung festgestellt. Im Falle parallel oder auch senkrecht zueinander angeordneter Feldkonfigurationen ergeben sich eine Fülle von Möglichkeiten, molekulare Eigenschaften wie das elektrische Dipolmoment sowie die spezifische Ausrichtung und Orientierung als zweiparametrische Größen der angelegten Feldstärken zu steuern. Abschließend präsentieren wir den neuartigen Bindungszustand eines Grundzustandsatoms mit einem sogenannten „giant dipole atom“. Diese Spezies ist von ultralangreichweitigem Charakter und gehört mit zu den größten bisher bekannten diatomaren Molekülen.

Abstract

Ultralong-range diatomic molecules in external fields – In this thesis, the quantum mechanical properties of ultralong-range diatomic molecules in external electric and magnetic fields are studied theoretically. Both the electronic Born-Oppenheimer potential surfaces and the rovibrational dynamics are analyzed. Besides analytic approximations, we apply standard numerical diagonalization routines. In the first part of the thesis, we study the properties of ultralong-range Rydberg molecules. Depending on the considered electronic state, one obtains molecular states possessing a specific degree of alignment and orientation with respect to the applied field. In the case of pure electric fields, the considered molecules are stabilized and oriented antiparallel to the field. Because of the high electronic polarizability, already very weak electric field strengths are sufficient to control molecular properties such as the internuclear separation and the electric dipole moment. For a pure magnetic field configuration, the molecular states are either aligned or antialigned. The molecular binding energies are calculated and confirmed to agree well with experimental data. In the case of parallel and perpendicular electric and magnetic field configurations different molecular properties such as the electric dipole moment and the molecular alignment and orientation can be tuned by varying both the electric and magnetic field strengths. Finally, we discuss the properties of a novel diatomic species where a ground state atom is bound to a giant dipole atom. These molecular species are of ultralong-range character and belong to the largest diatomic molecules known so far.

Publications

In the framework of this thesis, the following articles have been published:

- [2] M. Kurz, M. Mayle, P. Schmelcher: *Ultra-long-range giant dipole molecules in crossed electric and magnetic fields* , EPL **97**, 77, 43001 (2012) (Editor's choice)
- [3] M. Kurz, P. Schmelcher: *Electrically dressed ultra-long-range polar Rydberg molecules*, Phys. Rev. A **88**, 022501 (2013)
- [4] A. T. Krupp, A. Gaj, J. B. Balewski, P. Ilzhöfer, S. Hofferberth, R. Löw, M. Kurz, P. Schmelcher, T. Pfau: *Alignment of D-State Rydberg Molecules*, Phys. Rev. Letters **112**, 143008 (2014)
- [5] M. Kurz, P. Schmelcher: *Ultralong-range Rydberg molecules in combined electric and magnetic fields*, J. Phys. B **47**, 165101 (2014) (featured by J. Phys. B in their LabTalk)

Contents

Introduction	i
I Theoretical foundations	1
1 Rydberg atoms	3
1.1 Historical remarks	3
1.2 Rydberg states in basic atomic models	4
1.3 Rydberg states of alkali atoms	7
1.3.1 The quantum defect	7
1.3.2 Electronic Rydberg wave functions	8
1.3.3 Radiative lifetimes of Rydberg atoms	12
1.4 Rydberg atoms in external fields	13
1.4.1 Rydberg atoms in electric fields	13
1.4.2 Rydberg atoms in magnetic fields	14
2 Interaction of Rydberg atoms and ground state atoms	17
2.1 Electron-atom interaction	17
2.1.1 Fermi-pseudopotential	18
2.1.2 Higher order contributions	20
2.2 Energy dependence of the scattering phase shifts	22
3 Basic concepts of molecular physics	25
3.1 The generic Hamiltonian of molecular physics	25
3.2 Adiabatic and Born-Oppenheimer approximations	27
3.3 Diabatic potential surfaces	28
3.4 Diatomic molecules	29
3.4.1 Diatomic potential curves	29
3.4.2 Labeling of diatomic electronic states	29
II Ultralong-range molecules in external fields	31
4 The molecular system	33
4.1 The working Hamiltonian	33
4.2 The field-free system	35
4.2.1 Trilobite states	35
4.2.2 Two-state analysis	40
4.2.3 The Borodin-Kazansky model	41
4.2.4 Inclusion of additional basis states	43
5 Electrically dressed ultralong-range Rydberg molecules	47
5.1 Introduction	47
5.2 The setup	47
5.3 Methodology and symmetries	48

5.4	Potential energy surfaces	49
5.4.1	Two-state analysis	49
5.4.2	Perturbation theory and exact diagonalization	52
5.5	Electric dipole moment	55
5.6	Rovibrational states	57
5.7	Conclusion	60
6	Ultralong-range Rydberg molecules in combined electric and magnetic fields	63
6.1	Introduction	63
6.2	The setup	63
6.3	Methodology	65
6.4	The pure magnetic field configuration	65
6.4.1	P -wave interaction effects	66
6.4.2	Three-state analysis	67
6.4.3	Two-dimensional potential energy surfaces	69
6.5	Potential energy surfaces for combined field configurations	70
6.5.1	Parallel field configuration	70
6.5.2	Perpendicular field configuration	71
6.6	Rovibrational states	73
6.6.1	Parallel field configuration	73
6.6.2	Perpendicular field configuration	74
6.7	Molecular alignment and orientation	77
6.8	Electric dipole moment	78
6.9	conclusion	80
7	Alignment of ultracold $D_{5/2}$-state Rydberg molecules	81
7.1	Introduction	81
7.2	Experimental setup	81
7.2.1	Preparation of samples of ultracold rubidium atoms	81
7.2.2	Rydberg excitation	83
7.2.3	Ion detection method	83
7.3	The molecular Hamiltonian in a magnetic field	84
7.4	Potential energy surfaces	86
7.5	Rovibrational states and binding energies	89
7.6	Experimental spectra	93
7.7	Alignment of $D_{5/2}$ -state Rydberg molecules	95
7.8	Conclusion	98
8	Polarizability and susceptibility of ultralong-range Rydberg molecules	99
8.1	Molecular response properties in the adiabatic approximation	99
8.2	Magnetically dressed Rydberg molecules	100
8.3	Electrically dressed Rydberg molecules	101
9	Giant dipole states	103
9.1	Introduction	103
9.2	The model Hamiltonian	103
9.3	Methodology	105
9.4	Convergence studies	105
9.5	Molecular ground state potential surfaces	107
9.6	Potential surfaces of excited states	109
9.7	Avoided crossings of potential surfaces	111
9.8	Conclusion	112

10 Summary and conclusions	115
III Appendix	119
A Numerical concepts	121
A.1 Construction of the interaction matrix	121
A.1.1 S-wave matrix construction	121
A.1.2 P-wave matrix construction	123
A.2 Numerov integration method	124
A.2.1 General integration scheme	124
A.2.2 Application to Rydberg wave functions	124
A.3 Finite difference method	125
A.3.1 One-dimensional problems	125
A.3.2 Multi-dimensional problems	127
B Auxiliary calculations	129
B.1 Atomic units	129
B.2 Derivation of the working Hamiltonian	130
B.2.1 Coordinate and momentum transformation	130
B.2.2 Hamiltonian algebra	130
B.3 Hydrogenic giant dipole states	133
B.4 Finite difference representation	134
B.5 Field-free Hamiltonian	135
B.5.1 Rotational symmetry properties	135
B.5.2 P-wave function symmetry properties	136
B.6 Separable matrices	137
B.6.1 General properties	137
B.6.2 Rank of separable matrices	138
B.7 Nonadiabatic coupling terms	138
B.8 Matrix elements of hydrogen states	140
B.8.1 Angular matrix elements	140
B.8.2 Radial matrix elements	141
B.9 Additional notes	142
B.9.1 Elimination of single derivative terms	142
B.9.2 The radial shifted harmonic oscillator in two and three dimensions	144
B.9.3 Three-state model eigenvalues	145
Bibliography	147
Acknowledgements / Danksagung	163
Declaration / Erklärung	167

Introduction

Ultracold physics

In today's physics the variety and diversity of experiments involving ultracold atomic and molecular gases is huge. Novel cooling techniques such as laser and evaporative cooling allow to routinely produce ultracold atomic samples in the temperature regime of several nano-Kelvin [6] nowadays.

In the field of ultracold atoms certainly one of the most impressive milestones of this development was achieved in the year 1995: with the creation of a Bose-Einstein condensate (BEC) in an ultracold gas of rubidium atoms [7]. In this exotic state, a degenerate quantum gas of bosons occupies a single macroscopic state if it is cooled under a critical temperature. This effect had been predicted theoretically already 90 years before in the early years of the twentieth century by Bose and Einstein [8–10]. Independently, a BEC of sodium gas was obtained within the same year [11]. Finally, the first degenerate quantum gas of ultracold fermions was created only four years later [12]. These breakthroughs have initiated a lot of theoretical as well as experimental studies while more than a hundred labs with cold atom apparatus exist nowadays around the world. Famous examples for the rich variety of possible applications are the BEC-BCS crossover in a gas of fermionic ^6Li [13], or the Kosterlitz-Thouless phase transition studied within a two-dimensional BEC [14]. Other experiments have focused on the wave-particle duality by interference experiments [15] and the creation of an atom laser [16]. In the meanwhile, quantum gases with different species are common [17] and even BECs of molecules have been achieved [18]. From the theoretical point of view, the so-called Gross-Pitaevski equation has proven to provide an excellent description of degenerate quantum gases of ultracold bosonic alkali atoms [19]. A second milestone in the experimental study of ultracold systems has been the realization of optical lattices [20]. In these setups a huge variety of many-body models, mostly inspired from solid state physics, can be realized and studied with a large degree of controllability over the physical parameters and measurement accuracy with access to several observables. For instance, the exploration of quantum phase transitions and other important physical phenomena is nowadays performed in an artificial system much larger, cleaner and more transparent than the solid state equivalent. One of the most famous examples is the demonstration of the Mott-Insulator to super-fluid phase-transitions of ultracold atoms in an optical lattice [21] and the study of Pinning transitions of strongly interacting bosons in quasi one-dimensional gases [22]. One intriguing property of ultracold atomic gases is the possibility to tailor interatomic interactions, e.g. by using Feshbach resonances [23]. In one dimension and in the limit of infinitively strong interparticle interaction a so-called Tonks-Gireadeau gas emerges; in this case the bosons behave like spin-less non-interacting fermions pile up in the single particle eigenstates of the one-dimensional potential. Such a gas has been realized in a ^{87}Rb ultracold Bose gas of very low density [24]. Optical, electric and magnetic fields can be used to generate virtually any external potential. For instance, magnetic fields are used to manipulate atoms possessing a large magnetic dipole moment, e.g. chromium [25]. Besides the studies and applications in the field of fundamental physical phenomena, potential technical applications range from highly sensitive magnetic field detectors [26] to quantum computation and quantum information technologies [27].

Similar to ultracold atoms the field of ultracold molecules is quite young [28–31]. In molecular physics, molecules with translational temperatures between 10^{-3} -1 K are designated as cold, species with temperatures below 1 mK are called ultracold molecules. In the past years, several technical approaches have been developed in order to create samples of ultracold molecules. However, cooling molecules is more difficult than cooling atoms. A first attempt is the direct cooling of molecules. As molecules have a more complex level structure than atoms, a simple extension of laser cooling

techniques is for most molecular species precluded [32–34]. An alternative approach is to produce cold molecules from a supersonic beam source or to use a buffer gas cooled molecular sample, where molecules are cooled by collisions with a cryogenic buffer gas [35–38]. Temperatures reached with these techniques are in the range of a few mK up to several Kelvin. A more elegant way of producing samples of ultracold molecules is to form them directly by associating trapped atoms, which can be cooled down using well established laser and evaporative cooling techniques. Subsequently, molecules are either formed via photoassociation [39–42] or magnetic Feshbach resonances [43, 44]. In case of the photoassociation technique, two colliding atoms absorb a photon and form an electronically excited molecule. This approach has been successfully applied to create several both homo and hetero alkali dimers [45–48]. The second indirect procedure to create ultracold molecules is to use a Feshbach resonance, which occurs in the low energy scattering processes between the atomic constituents [49–51]. By tuning through the resonance, i.e. via changing an external magnetic field in case of paramagnetic scattering particles, the atom pair can be driven into a bound molecular state [52–55]. These Feshbach molecules are in a highly excited state and thus they are only weakly bound. However, they can be transferred into their ground state using a STIRAP technique [56].

Similar to ultracold atoms, the relevance of ultracold molecules could probably be condensed into two aspects: precision and control. At low temperatures the precision of molecular spectroscopy is increased in a twofold manner: The spectroscopic resolution is enhanced by the vanishing Doppler broadening and the interaction times are lengthened in ultracold molecular samples. High-resolution spectroscopy [57, 58] of molecules is of major importance as it provides access to several unsolved problems of today’s fundamental physics. For instance, it provides an excellent tool for the search for the permanent dipole moment of the electron [35], to study the possible time dependence of fundamental constants [59], or for the search of parity symmetry violation [60]. In the case of ultracold molecules the possibility of control applies to both the internal and external degrees of freedom. For instance, by preparing the molecules in a single internal quantum state, scattering processes providing transitions into a many different target states could be analyzed with a high accuracy in collision experiments [61, 62]. Furthermore, by preparing molecular translational degrees of freedom in the ultracold regime, one expects to access fundamental insights into how chemical reaction processes may be precisely ruled by the law of quantum mechanics. In addition, special molecular species like ultracold polar molecules provide the possibility to research novel physical regimes which are hardly accessible in degenerate atomic gases. Polar molecules exhibit an anisotropic, long range dipole-dipole interaction in contrast to atomic samples where isotropic, short-range interactions are mostly dominant. In addition, the dipole-dipole interaction among polar molecules can be modified by external fields [63–65]. For all these reasons, polar molecules are of special interest as they open the door to a plethora of various experiments, including quantum computation, precision measurements, controlled ultracold chemistry and quantum simulations of condensed matter systems.

Rydberg atoms

In modern atomic and molecular physics Rydberg atoms belong to the most intriguing systems. The defining property of Rydberg atoms is a highly excited single electron state of high principal quantum number n . Their size can easily exceed that of ground state atoms by several orders of magnitude. More precisely, a state with principal quantum number n can be associated with an electron orbit of n^2 Bohr radii around the single positively charged ionic core. Due to this, atomic states with $n \sim 40$ possess electronic orbits that measure ~ 200 nm in diameter and thus are more than thousand times larger than the corresponding ground state atoms. Recently, preparation schemes for Rydberg excitations up to principal quantum numbers of $n \sim 200$ have been achieved [66] and in astrophysical measurements spectra of Rydberg atoms with $n \approx 1000$ Rydberg states have been confirmed [67]. Prepared in such exotic atomic states, the size of the Rydberg

electron's orbit easily exceeds into the micrometer and millimeter regime which is the dimension of macroscopic objects such as viruses, Bose-Einstein condensates and fabricated optics and atom chips [68, 69]. Apart from hydrogen Rydberg states, the energy spectrum of Rydberg atoms depends on the electronic angular momentum. As for high- l states the spectrum is hydrogenic, for low angular momenta the situation changes due to the finite size of the ionic core. In this case core-penetration and scattering effects of the Rydberg electron split the low- l states energetically apart from the hydrogenic manifold by means of the so-called quantum defect [70]. The huge displacement of the atomic charges leads to large atomic dipole moments scaling as n^2 . These dipole moments are the origin of strong mutual dipole-dipole interaction. The most prominent effect of this interaction is the so-called Rydberg blockade mechanism of excitation [71, 72]. This effect arises from the competition between laser excitation and strong dipole-dipole interaction among two excited Rydberg atoms. Within a specific length scale, the so-called blockade radius, all additional Rydberg excitations are strongly suppressed.

Owed to their large size, Rydberg atoms do not only interact much stronger than their ground state counterparts but behave quite differently when placed in electric and magnetic field configurations. In fact, the Rydberg atom polarizability scales with the principal quantum number as n^7 , so the effect of an electric field strongly depends on the considered Rydberg state. As stray electric fields are hard to eliminate, electric fields are present in most experiments and perturbations due to these stray fields are often significant and cannot be ignored. However, electric fields are not always a burden for cold and ultracold Rydberg atom experiments. Electric fields can be useful, since, for example, they can be used to manipulate the interactions between Rydberg atoms [73]. One approach is to use states with large electric dipole moments which are found, for instance, in linear Stark states. Furthermore, in the presence of an external electric field, a low- l state of an alkali Rydberg atom with large quantum defects may mix with nearby manifolds of Rydberg states, inducing avoided crossings [74]. For instance, recently the state transfer from cesium nS to Stark states induced by weak electric field pulse has been investigated [75]. Rydberg atoms are of particular interest in case of homogeneous magnetic fields: in such systems the external field cannot be treated perturbatively since both the electrostatic and the magnetic interaction become comparable in strength. In other words, Rydberg atoms provide the possibility to address regimes where the competition of the Coulomb and diamagnetic interaction leads to unusual and complex properties and phenomena. Thus, they serve as a paradigm of a non-separable and non-integrable system and have major impact on the development of several fields such as nonlinear dynamics and semi-classics of non-integrable systems [76–78]. Furthermore, highly excited Rydberg states exposed to crossed electric and magnetic fields constitute a rather exotic atomic species known as giant dipole states [79]. These states emerge from the finite mass of the ionic Rydberg core and the non-separability of the center of mass and electronic motion in the presence of the external fields. Opposite to the usual Rydberg states, giant dipole states show a large electron-core separation and thus possess huge electric dipole moments in the order of 10^5 Debye. Inhomogeneous fields find their application in ultracold atomic physics for the purpose of trapping and confinement. For instance, Lesanovsky and Schmelcher analyzed the quantum properties of a Rydberg atom placed in a three-dimensional magnetic quadrupole field, exploiting a one-body approach and assuming an infinite nuclear mass [80, 81]. Furthermore, Mayle *et al.* have demonstrated that Rydberg atoms trapped in an Ioffe-Pritchard trap superimposed by a homogeneous electric field can be created in long-lived circular states exhibiting a permanent electric dipole moment of several hundred Debye [82, 83].

Rydberg molecules

Besides the enormous and fascinating physics provided by single Rydberg atoms the study of ultracold Rydberg gases has resulted in the discovery of two novel species of molecules. The first one consists of two bound Rydberg molecules, referred to as a macrodimer. These macrodimers are

bound by multipolar Coulombic interactions and can have bond lengths in the micrometer regime due to the long-range nature of Rydberg atom interaction. This is the size of a human blood cell ($\sim 5\ \mu\text{m}$), an object easily resolved using an optical microscope. It has been proposed that macrodimers could serve as an excellent tool to study vacuum fluctuations, correlations in quantum gases, quenches in ultracold collisions and Rydberg atom interactions including their controllability with applied electric fields. In particular, Rydberg macrodimer possess controllable nonadiabatic interactions between adiabatic potential energy surfaces. The latter makes them promising candidates for wave packet dynamics. This subject is relevant to recent works on generating systems that can be described by artificial gauge field potentials, because Rydberg macrodimers could serve as a test bed for such experiments. However, most of the applications have not been realized yet, except to some extent of their controllability with applied electric fields.

The second type of molecular species that has been observed is composed of a Rydberg atom bound to a ground state atom, found within the Rydberg atom itself. These novel kind of molecular species have been predicted in 2000 by C.H. Greene *et al.* where a ground state atom is bound within the electron cloud of a Rydberg electron. In case the ground state atom perturbs the high- l hydrogenic manifold, the Rydberg electron's wave function is a superposition of hydrogenic states and the corresponding electronic probability density possesses a strongly oscillating structure. As this oscillation pattern evokes similarities to a trilobite fossil [84], these molecular species have become known as "trilobite molecules" in the community of ultracold molecules. In Fig. 1(a)² the strongly oscillating electronic density distribution of a trilobite is depicted. One of the most interesting features of the second molecular species is the fact that their binding mechanism can be described by the properties of the Rydberg electron-ground state atom scattering process. Within this so-called Fermi-pseudopotential approach the electron-perturber interaction is expanded in a partial wave series according to the different angular momentum states. In this expansion the terms are labeled according to their quantum number l , i.e. s -wave term ($l = 0$), p -wave term ($l = 1$), etc. So far this concept has been unknown in the theoretical framework of conventional molecular bonding. For this reason the trilobite molecules can provide an important window into a regime where continuum properties of the constituent particle meet those of discrete bound states. The limit where the continuum electron-atom scattering and diatomic bound states are simultaneously relevant provides a testing ground for the conceptual framework of quantum defect theory and low-energy scattering of highly excited states. The trilobite states have been predicted for pure s -wave electron-perturber interaction. Later, these studies were extended including the p -wave scattering potential leading to similar "butterfly" like electronic structures [86] and molecules bound by internal quantum reflection [87]. Fig. 1(b) shows the electron density of a butterfly state. Both molecular species are typically formed at internuclear separations from several hundreds to thousands Bohr radii. Experimentally, the existence of these molecules was verified nine years later in an gas of ultracold rubidium gas. Until today most experimental works have been performed in heavy alkali systems, that is, rubidium and cesium [87, 89–93]. The reason to use these particular atomic species is that heavy alkali atoms yield deeper potentials with more bound states. This is important because the low- l states with localized vibrational states are most easily observed. The primary method to observe trilobite molecules is spectroscopy. However, there are several difficulties in trying to create and measure these molecular species. Firstly, Rydberg states in the region of $n \sim 30$ – 45 the binding energies for the rovibrational states in the range of MHz-GHz, which corresponds to ultracold temperatures. Secondly, the rovibrational states are localized at internuclear distances that lie outside the bond lengths of typical ground state molecules, and therefore it would be challenging to use bound-bound transitions to excite high- n molecules trilobite molecules. Thirdly, the potentially large permanent dipole moment can complicate the measurement because of the broadening of the rovibrational spectra, which is due to electric stray fields. The observations of trilobites around $n \sim 30$ for rubidium and cesium have been carried out in cold atom traps where the density has exceeded $10^{12}\ \text{cm}^{-3}$ for $\text{Rb}(nS) + \text{Rb}(5S)$ or $\text{Cs}(nS) + \text{Cs}(6S)$ molecular states,

²Reprinted with permission from [85], Copyright (2000) by the American Physical Society.

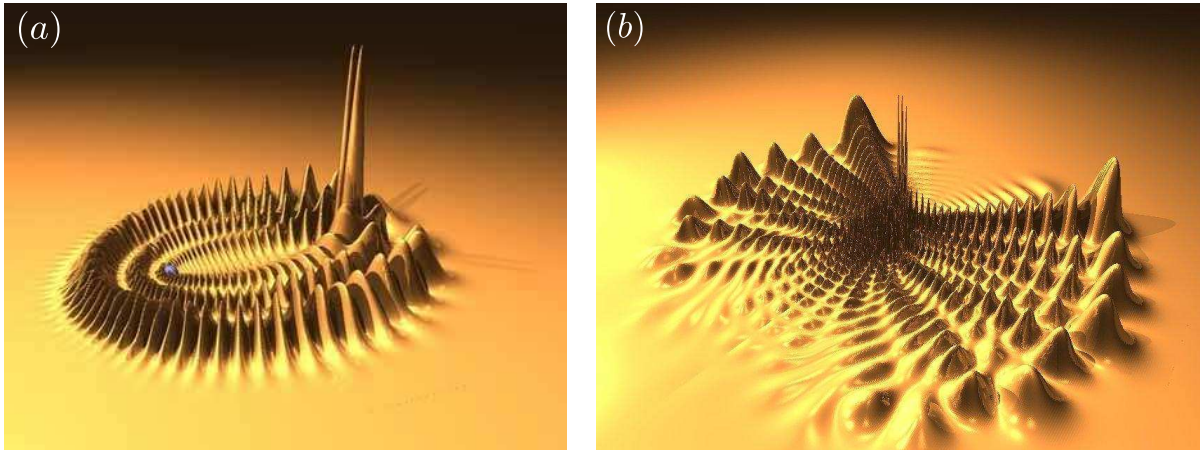


Figure 1: Probability densities of high- l perturbed electronic Rydberg states for (a) $n = 30$, ${}^3\Sigma$ trilobite state [85] and (b) $n = 30$, ${}^3\Sigma$ butterfly state [88].

respectively. Rydberg states of lower $n \sim 7 - 12$ rubidium Rydberg states have been observed in magneto-optical traps [93]. Finally, rubidium trilobite molecules have been measured for states related to $\text{Rb}(nD) + \text{Rb}(5S)$ for $n = 34 - 40$ [94] and $n = 41 - 49$ [4]. In the experiments using both cesium and rubidium the molecular association was performed via photoassociation. The excitation scheme starts with two free atoms and creates a molecule via absorption of two laser photons. The two-photon processes used for rubidium and cesium transitions are typically detuned from intermediated P -states, so that the intermediated state is adiabatically eliminated from the excitation process. The same process can be carried out with a single photon, but the wavelengths needed are generally difficult to generate using narrow-bandwidth continuous wave lasers. Due to their ultralong-range character homonuclear trilobite molecules possess amazing properties such as permanent electric dipole moment (~ 1 Debye) of nS molecular states. This dipole moment results from the large vibrational constant and a small amount of hybridization of the electronic wave function [95]. In cesium, line broadening that corresponds to dipole moments of around 30 Debye have been observed for states to the blue side of nS states [92]. Furthermore, polyatomic trilobite molecules have been created and observed as well [87, 96, 97]. In a recent experiment rubidium Rydberg states have been excited atomic $100S - 202S$ states extending the Rydberg electron's orbit to the same size as the trapped BEC ensemble. Here, the number of atoms interacting with the electron vary from 700 up to 30,000, where the Rydberg blockade radius is much larger than the extension of the BEC and the electron is strongly coupled to phononic BEC-modes [98].

Objective of this thesis

The objective of this thesis is to analyze the quantum properties of ultralong-range Rydberg molecules in both external electric and magnetic fields as well as in combined field configurations. As it has been outlined in the previous section, the study of ultralong-range Rydberg molecules has provided a plethora of fascinating and pioneering works in the field of ultracold molecular physics. Similar to Rydberg atoms, trilobite molecules are expected to be highly sensitive to applied external fields due to their high degree of electronic excitation. The exact understanding of the field-dressed trilobite molecules is of central importance for several reasons. For instance, trilobite molecules are considered to be highly polarizable, and therefore large electric and magnetic dipole moments are expected when they are exposed to even tiny external fields. This would provide the possibility to create and tune strong dipole-dipole interactions between the field-dressed molecules. In addition to this, as today's trapping technologies rely on optical, magnetic and electric fields, the precise knowledge of the properties of field-dressed trilobite molecules is essential for trapping applications. As the existence of electric stray fields in most of experimental setups the understanding of electric

field effects is considered to be highly relevant. The magnetic field calculations are important for determining the behavior of the trilobite molecules in magnetic traps.

However, until the beginning of this particular thesis the analysis of trilobite molecules in external fields had remained, more or less, unexplored. One exception is the study of Lesanovsky *et al.*, where trilobite molecules exposed to a homogeneous magnetic field were analyzed [99]. In particular, this work focused on the properties on trilobite molecules stemming from the Zeeman split high- l hydrogenic manifold. As results this study delivered the existence of antialigned molecules with respect to the magnetic field as well as a tunability of the electric dipole moment by varying the magnetic field strength. In this particular work the authors assumed a number of approximations. First, no quantum defect states had been considered. However, in the case of both electric and magnetic fields the Stark-/Zeeman splitting grow with increasing electric-/magnetic field strengths. For this reason the spacing to neighbored states in the energetic vicinity of the considered high- l manifold decreases. This might lead to important effects due to increasing couplings and hybridization of different Rydberg states. Since we are interested in both high- and low- l molecular species, we consider, apart from the hydrogenic Rydberg states, the quantum defect states as well. As indicated above, finite size effects of the ionic Rydberg core lead to deviation from the pure hydrogenic character of the quantum defect wave functions. In addition, the spin-orbit coupling of the Rydberg electron is much stronger for low angular momenta and must not be neglected. Secondly, in the case of the electron-perturber interaction only s -wave scattering was considered. In a previous study Hamilton *et al.* [86] already included the p -wave scattering term in an analysis of field-free trilobite states. As this interaction term possesses a shape resonance in the considered energy range, it turned out to be essential in order to obtain the appropriate molecular dynamics. However, it has remained unclear how the inclusion of the p -wave interaction terms affects the dynamics of field-dressed trilobite molecules. For this reason, in this thesis both s - and p -wave interactions are considered for the electron-perturber interaction.

In addition to the studies on ultralong-range Rydberg molecules we predict the existence and discuss the properties of a novel kind of diatomic molecules. In particular, we consider a diatomic molecule that consists of a neutral ground state atom and a giant dipole state [79]. Effectively, a giant dipole state can be described as a highly excited Rydberg electron of low kinetic energy exposed to crossed electric and magnetic fields. For this reason we predict that a ground state atom is bound to a giant dipole atom by the same electron-perturber interaction that leads to the existence of ultralong-range diatomic Rydberg molecules.

Structure of the thesis

This thesis is divided into three parts containing ten chapters in total. Each chapter of the thesis starts with an introductory passage which motivates its content and provides its main highlights. In brief, the structure and content of the chapters are as follows:

We start in **part I** by providing the theoretical foundations to this thesis. In particular, in **Chapter 1** we present the basic concepts of Rydberg atoms and their properties. We introduce the fundamental concept of quantum defect states and discuss how external electric and magnetic fields affect the energetic structure of electronic Rydberg states.

Chapter 2 is devoted to the central ingredient which is required for the bonding of an highly excited Rydberg state and a ground state atom. In this chapter we discuss the physics of low-energy electron-atom interaction which leads to an effective description known today as the Fermi-pseudopotential. In this approach the exact potential is replaced by a contact interaction potential which is determined by a single constant parameter, the so-called scattering length. Subsequent refinements extend the Fermi-pseudopotential approach providing additional partial wave interaction terms as well as energy dependent scattering lengths. In this chapter, both the work of Fermi and its subsequent refinements are reviewed in detail.

In **Chapter 3** we recapitulate some of the basic concepts of standard molecular physics. In

particular, we discuss the ab-initio Hamiltonian of non-relativistic field free atoms and molecules and show how a set of formally exact solutions for the molecular problem can be derived. Afterwards, we present the so-called adiabatic approximation, one of the most extensively used approaches in modern molecular physics. Beside this we briefly discuss an alternative approximative approach, the diabatic approximation. Finally, we turn our attention towards the basic properties and the standard labeling scheme of diatomic electronic states.

Part II starts with the introduction of the working Hamiltonian of this thesis in **Chapter 4**. In particular, we consider a ultralong-range diatomic Rydberg molecule in combined electric and magnetic fields. As the ab-initio Hamiltonian of the field-dressed molecular system possesses a non-separability of the center of mass and electronic motion the so-called pseudomomentum is a conserved quantity instead of the total linear and angular momentum. We derive an effective two-particle problem where the field-dressed Rydberg electron is coupled to the relative nuclear dynamics via the Fermi-pseudopotential. For the field-free molecular system we provide analytic solutions for the adiabatic potential curves in first order perturbation theory. In addition, an universal behavior of the avoided crossings of adiabatic potential energy curves is proven. Finally, we apply numerical diagonalization routines to study beyond perturbative regimes.

In **Chapter 5** we investigate ultralong-range diatomic Rydberg molecules in a homogeneous electric field. The electric field converts the angular degree of freedom between the electric field and the internuclear axis from a rotational to a vibrational degree of freedom, thereby rendering the field-free potential energy curve into a two-dimensional potential energy surface. By varying the electric field strength both a stabilization process of rovibrational molecular states and control of the molecular dipole moment in the range of several thousand Debye is provided. In addition, hybridization of the high- l trilobite state with energetically close quantum defect states provides the possibility of a two-photon excitation process of electric field-dressed high angular momentum states.

A study of ultralong-range Rydberg molecules in combined electric and magnetic fields is presented in **Chapter 6**. In this chapter we study both the parallel and perpendicular field configuration. However, we first analyze the pure magnetic field configuration taking into account both s - and p -wave interaction. This analysis is an extension of the work of Lesanovsky *et al.* [99] where only s -wave scattering was considered. The additional p -wave interaction causes strong level repulsion between adiabatic potential curves leading to a disappearance rovibrational free-field bound states beyond a critical field strength. In case of combined electric and magnetic field we obtain two- and three-dimensional potential energy surfaces for parallel and crossed field configurations, respectively. Both field configurations provide the possibility to control molecular orientation, alignment and, in addition, the electric molecular dipole moment.

In **Chapter 7** we outline the study of a novel type of highly excited $D_{5/2}$ -state Rydberg molecules which are created from an ultracold atomic rubidium gas that is exposed to a weak homogeneous magnetic field of strength $B \sim 10$ G. These studies were performed in collaboration with the experimental group of Prof. T. Pfau from the University of Stuttgart [4]. We present the calculation of the rovibrational binding energies which are compared to the experimental data. Over a large range of principal quantum numbers n the theoretical and measured data agree satisfactory. From calculating the rovibrational probability densities we identify two different kind of molecular species. Depending of the specific state the molecules possess a high degree of alignment or antialignment with respect to the applied magnetic field direction. A brief introduction into the theory of polarizability and susceptibility of field-dressed ultralong-range Rydberg molecules is provided in **Chapter 8**.

Chapter 9 is devoted to ultralong-range giant dipole molecules formed by a neutral alkali ground state atom that is bound to the decentered electronic wave function of a giant dipole atom. Giant dipole states are highly excited electronic states which emerge due to the non-separability of the center of mass and electronic motion in the presence of crossed electric and magnetic fields. The exotic atomic state underlying these molecules gives rise to novel properties such as a plethora of

different quantum states with complex three-dimensional energy landscapes and rich rovibrational dynamics. The resulting molecules possess very large rovibrational bound states at internuclear distances in the range of several micrometers.

Finally, in **Chapter 10** we conclude this thesis by briefly summarizing our results and by providing further perspectives in this intriguing field of research. This thesis is accompanied by two comprehensive appendices in **part III**. In particular, **Appendix A** provides additional information on the numeric concepts used in this thesis. Furthermore, the second **Appendix B** contains mathematical proofs and additional auxiliary calculations.

Unless stated differently, atomic units are used throughout this thesis, cf. Appendix B.1.

Part I

Theoretical foundations

Chapter 1

Rydberg atoms

The main subject of this thesis are ultralong-range diatomic Rydberg molecules and their properties in homogeneous external fields. To derive and understand their multiplex effects and remarkable properties it is essential to be at least familiar with their constituents, which are Rydberg atoms and their interactions with neutral ground state atoms. For this reason, we provide in this chapter an introduction to Rydberg atoms and their remarkable properties. We start in Section 1.1 with some short remarks on the history of atomic spectroscopy which has led to the interesting research field of Rydberg physics. In Section 1.2 we show how the concept of Rydberg atoms is embedded in the Bohr and Bohr-Sommerfeld atomic model, respectively. In the next Section 1.3 we outline the particular properties of rubidium Rydberg states and, finally, we present the basic concepts of Rydberg atoms in external fields in Section 1.4.

1.1 Historical remarks

The first step in the development of today's atomic physics was the understanding of the solar and atomic spectra. From the first systematic study of discrete absorption lines in the solar spectrum by Joseph von Fraunhofer in 1814 [100], it took almost a century until at least a partial explanation for the occurrence of atomic spectra was provided by Niels Bohr [101]. In 1868 Anders Jonas Ångström published systematic and precise measurements of the solar spectrum, which paved the subsequent efforts to identify patterns and the underlying fundamental principles. The spectrum of hydrogen provided the testing ground for a variety of hypotheses, since its spectrum contains relatively few lines, grouped into different series [102]. Early works are seldom cited in literature, since they turned out to be completely wrong. For instance, in 1871 George J. Stoney pointed out that the frequencies of observed lines in the hydrogen spectrum coincide exactly with higher harmonics of a single fundamental vibration frequency [103]. Although this approach turned out to be quite successful in the description of other atomic and even molecular species [102], it was proven to be bare coincidence by Arthur Schuster in 1880 [104]. Shortly after this major setback, it was the school teacher Johann Jakob Balmer who succeeded in providing a reliable description [105]. In 1885, he published a formula for the wavelengths of the visible series of the atomic hydrogen, depending only on one integer number n :

$$\lambda = \frac{bn^2}{n^2 - 4}, \quad n \in \mathbb{N}. \quad (1.1)$$

At that time the quantity $b = 3645.6 \text{Å}$ was introduced as a purely empirical constant. It can be shown that Eq. (1.1) can be rewritten in terms of the wavenumber $\nu = 1/\lambda$ of the observed lines. In this case we obtain

$$\nu = \frac{4}{b} \left(\frac{1}{4} - \frac{1}{n^2} \right). \quad (1.2)$$

The final breakthrough was achieved in 1890 by Johannes Rydberg [106], mainly based on spectroscopic data on alkali metals from George D. Liveing and Sir James Dewar [107]. He began to classify the spectral series of arbitrary atoms into series of lines and realized that the wavenumbers of series members are related to the corresponding wavenumbers of observed lines. This relation is

m	name	wavenumbers/ R_∞	spectral range (nm)	type of radiation
1	Lyman series [112]	$3/4 - 1$	91 – 122	ultraviolet (NUV)
2	Balmer series [105]	$5/36 - 1/4$	365 – 656	visible light
3	Paschen series [111]	$7/144 - 1/9$	820 – 1875	infrared (NIR)
4	Brackett series [113]	$9/400 - 1/16$	1458 – 4050	infrared (NIR/MIR)
5	Pfund series [114]	$11/900 - 1/25$	2280 – 7460	infrared (NIR/MIR)
6	Humphreys series [115]	$13/1764 - 1/36$	3280 – 12400	infrared (MIR/FIR)

Table 1.1: Spectral series and wavelengths of the atomic hydrogen spectrum.

provided by the simple but famous formula

$$\nu_l = \nu_{\infty l} - \frac{R_\infty}{(n - \delta_l^{\text{qd}})^2}, \quad n \in \mathbb{N}. \quad (1.3)$$

In the original notation the quantity l stands for the *sharp* (S), *principal* (P) and *diffuse* (D) series [106]. A fourth additional series called *fundamental* (F) was discovered in 1907 by Arno Bergmann [102]. The constants $\nu_{\infty l}$ are denoted as the series limits.

In today's understanding l is the angular momentum quantum number with $l = 0, \dots, n - 1$ and $\nu_{\infty l}$ is the ionization limit. However, the notation S, P, D, F is still used in today's notation to label atomic and molecular states [108]. In Section 1.3 we will identify δ_l^{qd} as the so-called quantum defect [109]. For hydrogen the quantum defects vanish. The constant $R_\infty \equiv 4/b$ is the so-called *Rydberg constant* which is universal and can be used to describe the transition wavenumbers, not only for different series but also for different atoms. In SI-units the Rydberg constant is given by $R_\infty = 10973731.568539(55) \text{ m}^{-1}$ [110]. By rewriting the series limit $\nu_\infty = R_\infty/4$ we obtain Eq. (1.2) which is directly related to Balmer's formula Eq. (1.1). Shortly after Balmer additional series were found in the hydrogen spectrum in the infrared (Paschen [111]) and ultraviolet (Lyman [112]) regime. It turns out that Eq. (1.2) can be generalized to

$$\nu = R_\infty \left(\frac{1}{m^2} - \frac{1}{n^2} \right), \quad n > m, \quad m = 1, 2, \dots \quad (1.4)$$

Obviously every integer number m defines its one spectral series with a series limit R_∞/m^2 . Until today the series up to $m = 6$ are named in the literature after the physicist who performed the first spectroscopic measurements (see Tab. 1.1). Series with $m > 6$ are unnamed but obey Eq. (1.4) as well.

1.2 Rydberg states in basic atomic models

A proving ground for the young field of atomic physics was provided by the spectroscopy of hydrogen and, in particular, alkali atoms. The latter feature on a single valence electron [116] are much easier to study because single atoms are easily obtained by heating alkali samples up into the gas phase. In contrast, hydrogen atoms first have to be created from molecular H_2 . One of the major breakthroughs in the field of theoretical atomic physics was then achieved by Niels Bohr in 1913 when he proposed his theory of the hydrogen atom [101]. Bohr employed the picture of a point-like electron classically orbiting the ionic core as a charged point particle but only on orbits fulfilling the specific condition $L = l\hbar$, $l \in \mathbb{N}$. The quantity L denotes the absolute value of the electron's angular momentum. Furthermore, the Bohr model gives a connection between the associated orbital radius r_n of the electron around the ionic core and the principal quantum

Property	n dependence
Binding energy	n^{-2}
Energy between adjacent n states	n^{-3}
Orbital radius	n^2
Geometric cross section	n^4
Dipole moment $\langle nd r nf \rangle$	n^2
Polarizability	n^7
Radiative lifetime	n^3
Fine-structure interval	n^{-3}

Table 1.2: Properties of Rydberg atoms and their dependence on the principal quantum number n . Adapted from [70].

number n whose physical meaning had remained unclear until then:

$$r_n = \frac{4\pi\epsilon_0\hbar^2}{e^2m_e}n^2 \equiv a_0n^2. \quad (1.5)$$

The quantity a_0 is the size of the ground state atom and it is called the *Bohr radius*. It defines the typical length scale in atomic and molecular physics (see B.1). However, the electron's binding energy decreases as $1/n^2$, in particular

$$E_n = -\frac{Ry}{n^2}. \quad (1.6)$$

The quantity $Ry = hcR_\infty \equiv 13.60569253(20)$ eV, the so-called *Rydberg energy*, defines the energy scale for electronic bound states in the hydrogen atom. In atomic units it is $Ry = 1/2$ (see Appendix B.1). We easily see that Eq. (1.4) simply reflects electronic transitions between different bound states.

While it is known today that the Bohr model is not valid entirely, it nevertheless introduced the properties of Rydberg states. In the notation of the Bohr model, we define *Rydberg states* as atomic states of high principal quantum number n . Because of the quadratic n -dependence of r_n in Rydberg states ($n \gg 1$) the valence electron is in a large, loosely bound orbit that is characterized by the principal quantum number n .

A further stage in the history of basic atomic models is the *Bohr-Sommerfeld model* [117]. Among the several enhancements to the Bohr model the most important is the suggestion that the valence electron orbits the ionic core in elliptical orbits instead of Bohr model's circular orbits. To characterize the electron's orbit (without spin), three quantum numbers n , l and m are introduced. Their meaning is as follows:

- **principal quantum number n**

As in the Bohr model this quantity characterizes the electron's total energy. It is $n \in \mathbb{N}$ and the binding energy E_n is given by Eq. (1.6).

- **angular quantum number l**

This quantity characterized the total angular momentum via

$$L = l\hbar, \quad l = 1, \dots, n.^1 \quad (1.7)$$

Furthermore it determines the radial shape of the electron's orbit. In this model the electron

¹These values are the historical ones. The correct ones which are obtained from full quantum mechanics and given by $l = 0, 1, \dots, n - 1$.

orbits the core on elliptical orbits with eccentricity

$$e = \sqrt{1 - \frac{l^2}{n^2}}. \quad (1.8)$$

The orbits with low- l possess a high eccentricity while for $l = n$ we obtain the spherically

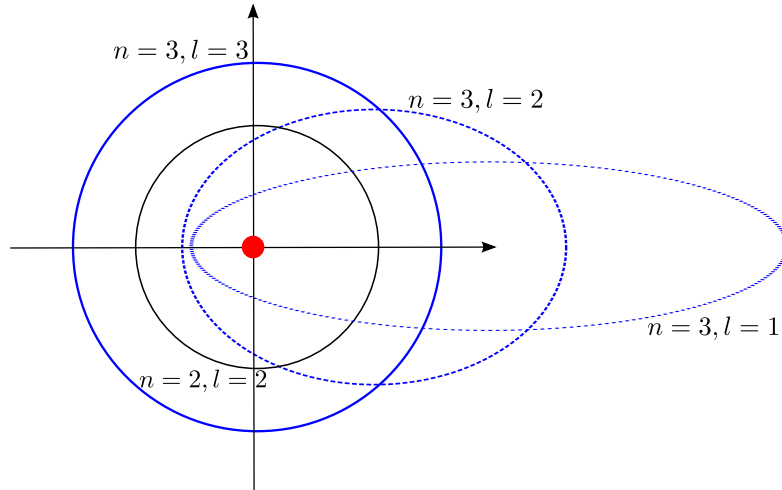


Figure 1.1: Bohr-Sommerfeld electronic orbits for principal quantum numbers $n = 2, 3$ and angular momentum states l . The orbits possess different eccentricities e which are determined by Eq. (1.8).

shaped orbit known from the Bohr model.

- **magnetic quantum number m**

This number determines the angle of inclination α between of the angular momentum \mathbf{L} and the quantization axis (see Fig. 1.2). It is

$$\cos(\alpha) = \frac{m}{l}, \quad m = -l, -(l+1), \dots, l+1, l, \quad (1.9)$$

which means we obtain $2l + 1$ possible value for m .

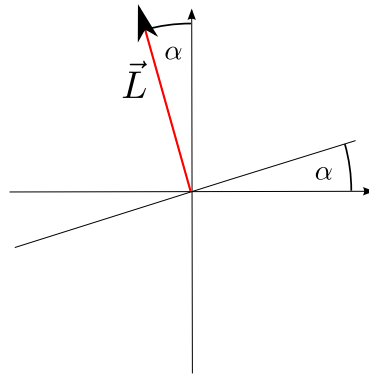


Figure 1.2: Illustration of the inclination α between the angular momentum \mathbf{L} and the quantization axis.

Within the Bohr-Sommerfeld model we can deduce the first qualitative deviations between hydrogenic and non-hydrogenic Rydberg states. For instance, alkali atoms can be transferred into Rydberg states quite easily by exciting the outermost valence electron into a high- n state. In this case the electron orbiting at small values of l approaches the nucleus, which is only partly screened

state	δ_0^{qd}	δ_2^{qd}	δ_4^{qd}	δ_6^{qd}	δ_8^{qd}
$nS_{1/2}$	3.131180	0.1784	-1.8	-	-
$nP_{1/2}$	2.6548849	0.29	-7.904	116.4373	-405.907
$nP_{3/2}$	2.6416737	0.295	-0.97495	14.6011	-44.7265
$nD_{3/2}$	1.34809171	-0.60286	-1.50517	-2.4206	19.736
$nD_{5/2}$	1.34646572	-0.59600	-1.50517	-2.4206	19.736
nF_j	0.016312	-0.064077	-0.36005	3.239	-

Table 1.3: Modified Rydberg-Ritz parameters of the rubidium atom for the calculation of the quantum defect according to Eq. (1.12). The values for $l \leq 2$ (δ_0^{qd} , δ_2^{qd} only) are taken from [119] and from [120].

by the other electrons on lower energy levels. In case the Rydberg electron penetrates the ionic core it experiences an energy shift which is accounted for by the quantum defect δ_l^{qd} (see Section 1.3.1). Within this model, the series S, P and D thus can be understood as transitions between states with different n and angular momentum l . This issue will be discussed in detail in Section 1.3.

Nowadays it is known that the Bohr-Sommerfeld model just gives an intuitive picture of a hydrogen or Rydberg atom, respectively. To get a correct description quantum mechanics has to be applied [118]. In this approach the properties of an atom are determined by its wave function ψ . The wave function itself is determined by the corresponding Schrödinger equation. For the hydrogen atom in its simplest form, i.e. neglecting all relativistic effect such as spin-orbit coupling of hyperfine structure, the Schrödinger equation reads

$$\left(-\frac{\Delta}{2} - \frac{1}{r}\right)\psi = \varepsilon\psi. \quad (1.10)$$

In this ansatz the proton is assumed to be infinitely heavy. The quantity r denotes the radial separation between the electron and the proton; ε is the electron's energy. The solutions of Eq. (1.10) can be found analytically and are well-known. From the wave functions we can infer the n scaling of many properties of Rydberg atoms. In Tab. 1.2 we present a list of the most representatives properties. Most notable is the lifetime of Rydberg atoms which scales with n^3 . A further example of the extraordinary properties is their huge polarizability. It is proportional to the sum of squares of electric dipole matrix elements divided by the energy, resulting in a n^7 scaling. As a consequence Rydberg atoms are expected to be extremely sensitive to external electric and magnetic fields.

1.3 Rydberg states of alkali atoms

1.3.1 The quantum defect

In this work we are interested in Rydberg states of alkali atoms rather than the hydrogen atom. Conceptually, electronically excited alkali atoms are very similar to the simple hydrogen Rydberg atom; both possess one valence electron orbiting around an ionic core of charge $+1$. However, for the alkali atoms the center charge is not of point particle nature as the proton in the hydrogen atom ² but is rather due to the shielding of a nucleus of charge $Z > 1$ by the remaining non-excited $Z - 1$ electrons. The latter form a closed shell ionic core such that the electronic excitations of the positively charged ion are strongly suppressed [121–123] and the single valence electron picture can be maintained. If the structure of the ionic core is not resolved - as it is the case for high angular momentum electronic states with $l \geq 3$ - alkali Rydberg atoms are well described by considering point-like charges as for the hydrogen atom. If the Rydberg atom resides in a low

²Throughout this thesis we do not consider the substructure of nucleons.

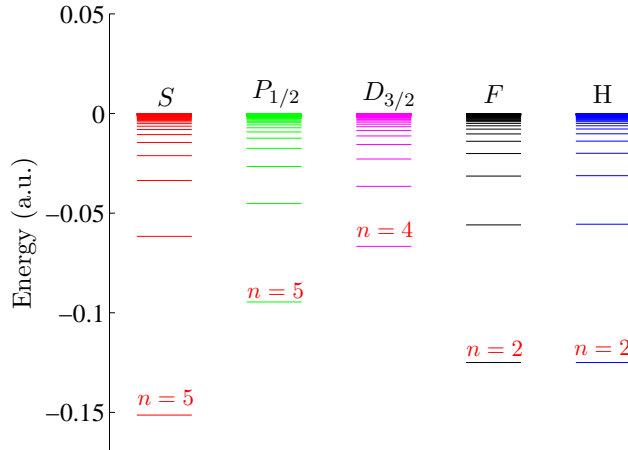


Figure 1.3: Energy levels of rubidium and hydrogen. The principal quantum number n of the lowest presented states are printed as well. The energy levels have been calculated according to Eq. (1.11) using the data from Tab. 1.3. The depression of the low angular momentum states ($l \leq 3$) is obvious.

angular momentum electronic state, on the other hand, the precise charge distribution of the alkali ionic core matters. In particular, the valence electron penetrates and polarizes the finite-size ionic core of the alkali atom, changing the wave functions and energies of the alkali Rydberg states from their hydrogenic counterparts. In Fig. 1.1, the conceptual differences between the high and low angular momentum Rydberg states of an alkali atom are illustrated. These differences can be quantified by introducing the so-called *quantum defect* δ_{njl}^{qd} that depends on the quantum numbers n, j and l of the Rydberg atom (see Section 1.3.2):

$$E_{njl} = -\frac{1}{2(n - \delta_{njl}^{\text{qd}})^2} \equiv -\frac{1}{2n^{*2}}. \quad (1.11)$$

The quantity n^* is an effective principal quantum number. The quantum defect itself can be determined via the modified Rydberg-Ritz expression [120]

$$\delta^{\text{qd}} = \delta_0^{\text{qd}} + \frac{\delta_2^{\text{qd}}}{(n - \delta_0^{\text{qd}})^2} + \frac{\delta_4^{\text{qd}}}{(n - \delta_0^{\text{qd}})^4} + \frac{\delta_6^{\text{qd}}}{(n - \delta_0^{\text{qd}})^6} + \frac{\delta_8^{\text{qd}}}{(n - \delta_0^{\text{qd}})^8} + \dots \quad (1.12)$$

The parameters $\delta_0^{\text{qd}}, \delta_2^{\text{qd}}, \dots$ are specific for each element; in Tab. 1.3 we give the corresponding values for rubidium, on which we focus throughout this thesis. We remark that for high- n states the first two terms of Eq. (1.12) are often sufficient. The figure Fig 1.3 illustrates the energy levels of rubidium for various angular momentum states l and principal quantum numbers n ; for comparison, the hydrogen level scheme is included additionally. As expected from Eq. (1.11), the low angular momentum states are lowered in energy due to the quantum defect. States with higher angular momenta are degenerate and coincide with the hydrogen manifold. For these states, the core penetration and polarization effects obviously are of minor importance, leading to a vanishing quantum defect.

1.3.2 Electronic Rydberg wave functions

From the obvious difference between the rubidium and hydrogen energy levels for low angular momentum states, it is clear that the corresponding wave functions must differ as well. Because of the penetration and polarization effects, the pure Coulomb potential $-1/r$ employed in the

	$l = 0$	$l = 1$	$l = 2$	$l \geq 3$
a_1	3.69628474	4.44088978	3.78717363	2.39848933
a_2	1.64915255	1.92828831	1.57027864	1.76810544
a_3	-9.86069196	-16.79597770	-11.65588970	-12.07106780
a_4/a_0	0.19579987	-0.81633314	0.52942835	0.77256589
r_c/a_0	1.66242117	1.50195124	4.86851938	4.79831327
α_c (a.u.)	9.01760			

Table 1.4: Parameters a_i , r_c and α_c for the l -dependent model potential V_l (1.13) as given in [124].

Schrödinger equation Eq. 1.10 is not valid for alkali atoms. Nevertheless, the one-particle picture can be sustained by replacing the Coulomb potential by a model potential of the form

$$V_l(r) = -\frac{Z_l(r)}{r} - \frac{\alpha_c}{2r^4} \left(1 - e^{-(r/r_c)^6}\right), \quad Z(r) = 1 + (z-1)e^{-a_1 r} - r(a_3 + r a_4)e^{-a_2 r}, \quad (1.13)$$

where $Z_l(r)$ is an effective charge and α_c the static dipole polarizability of the positive ionic core [125]. The quantity z is the nuclear charge of the neutral atom and r_c is the cutoff radius introduced to truncate the unphysical short-range behavior of the polarization potential near the origin. The potential (1.13) depends on the orbital angular momentum via its parameters a_i and r_c , e.g. $a_i = a_i(l)$. The actual values of a , r_c and α_c are listed in Tab. 1.4. Using this potential the Schrödinger equation for the valence electron of the Rydberg atom reads

$$\left(\frac{\mathbf{p}^2}{2} + V_l(r)\right) \psi(\mathbf{r}) = E\psi(\mathbf{r}) \Rightarrow \left(-\frac{d^2}{dr^2} + \frac{l(l+1)}{2r^2} + V_l(r)\right) u(r) = Eu(r) \quad (1.14)$$

where we have made the ansatz $\psi(\mathbf{r}) = \frac{u(r)}{r} Y_{lm}(\theta, \phi)$. For $r > r_c$ the potential $V_l(r)$ is Coulombic, but the pure hydrogenic wave function has to be replaced. We construct the solution of the radial solution $u(r)$ of the Schrödinger equation (1.14) as a linear combination of the functions $f_l(r, E)$ and $g_l(r, E)$ which possess the properties $f_l(E, r) \rightarrow r^{l+1}$, $g_l(E, r) \rightarrow r^{-l}$ for $r \rightarrow 0$.

$$u_l(r, E) = f_l(r, E) \cos(\delta_l) - g_l(r, E) \sin(\delta_l). \quad (1.15)$$

where δ_l is the radial phase shift of the Rydberg radial function $u_l(r)$ from the hydrogenic solution. The hydrogenic requirement that the wave function be finite at $r = 0$ has been replaced by the requirement that at $r \geq r_0$ the wave be shifted in phase from the hydrogenic solution by δ_l . In particular, the phase shift δ_l is given by [108]

$$\delta_l = \sqrt{2} \int_0^{r_c} dr \left(\sqrt{E - V_l(r)} - \sqrt{E + \frac{1}{r}} \right). \quad (1.16)$$

The f and g functions are commonly termed as the regular and irregular Coulomb functions [108]. In the classical allowed region these functions are real oscillatory functions with a phase shift of $\pi/2$ [70]. For $r \rightarrow \infty$ the Coulomb functions are of form

$$f_l(r, E) \rightarrow w_l(r, n^*) \sin(\pi n^*) - v_l(r, n^*) e^{i\pi n^*}, \quad (1.17)$$

$$g_l(r, E) \rightarrow -w_l(r, n^*) \cos(\pi n^*) + i v_l(r, n^*) e^{i\pi n^*}, \quad (1.18)$$

with $w_l(r, n^*) \rightarrow e^r$ and $v_l(r, n^*) \rightarrow e^{-r}$. In order to keep the function ψ square integrable we derive a condition to get rid of the w function in (1.15). For this we insert (1.17) and (1.18) into

(1.15). We get

$$\begin{aligned} \cos(\delta_l) \sin(\pi n^*) + \sin(\delta_l) \cos(\pi n^*) &= \sin(\delta_l + \pi n^*) = 0, \\ \Rightarrow \delta_l + \pi n^* &= n\pi \Leftrightarrow n^* = n - \frac{\delta_l}{\pi} \end{aligned} \quad (1.19)$$

So far the quantum defect has been introduced on an empirical basis. However, Eq. (1.19) now provides the important relation between the quantum defect and the radial phase shift:

$$\delta_l^{\text{qd}} = \frac{\delta_l}{\pi}. \quad (1.20)$$

Although Eq. (1.15) provides a solution for the outer radial wave function once the quantum defects δ_l^{qd} are known. In this thesis we determine $u_l(r)$ by solving (1.14) numerically by means of a Numerov integration technique (see Appendix A.2).

Fig. 1.4(a-d) show the probability density distribution $r^2 R(r)^2$ of different electronic Rydberg states of rubidium. For comparison, the corresponding hydrogenic eigenfunctions are provided as well. In Fig. 1.4(a) we present the density distributions for the $35S_{1/2}$ and $35D_{3/2}$ states, respectively. Compared to the hydrogenic distributions we clearly see a phase shift of the rubidium densities towards smaller radial distance r . This difference is caused by the quantum defect. For small r the potential seen by the rubidium valence electron is lowered compared to pure Coulomb potential of the hydrogen atom. Consequently, the kinetic energy of the rubidium valence electron is increased, leading to a decrease of the wavelength of the radial oscillations relative to the hydrogen atom. As a result, in rubidium all the nodes of the radial wave function are pulled closer to the origin than in hydrogen. This is clearly reflected in the density distributions in Fig. 1.4(a,b). In Fig. 1.4(c,d) the scaling of the probability densities with the principal quantum numbers $n = 30, 40, 50$ is depicted. Fig. 1.4(c) illustrates the low angular momentum states nS which significantly penetrate the ionic rubidium core. In contrast to this, the circular states ($l = m = n - 1$) presented in Fig. 1.4(d) have a vanishing probability density for small r .

Spin-orbit coupling

Similar to the question which model potential to use for the electron-core interaction the spin-orbit interaction depends on the considered angular momentum states as well. For the model potential $V_l(r)$ (1.13) the spin orbit term [108, 118] is given by

$$V_{\text{so}}(r) = \frac{\alpha^2}{2r} \left[1 - \frac{\alpha^2}{2} V_l(r) \right]^{-2} \frac{dV_l(r)}{dr} \mathbf{L} \cdot \mathbf{S} = \frac{\alpha^2}{2r} \left[1 - \frac{\alpha^2}{2} V_l(r) \right]^{-2} \frac{dV_l(r)}{dr} (\mathbf{J}^2 - \mathbf{L}^2 - \mathbf{S}^2), \quad (1.21)$$

where $\alpha = 1/137$ denotes the *fine structure constant*. Due to the spin-orbit coupling the quantum numbers m_l and m_s are not any longer good quantum numbers. However, by introducing the total angular momentum $\mathbf{J} = \mathbf{L} + \mathbf{S}$ a new complete set of commuting observables can be found which is given by $\{H, \mathbf{J}^2, J_z, \mathbf{L}^2, \mathbf{S}^2\}$. The relation between the old and new basis states is given by

$$|njm_j l \frac{1}{2}\rangle = \sum_{m_l m_s} \langle nlm_l \frac{1}{2} m_s | njm_j l \frac{1}{2}\rangle |nlm_l \frac{1}{2} m_s\rangle \quad (1.22)$$

The coefficients $\langle nlm_l \frac{1}{2} m_s | njm_j l \frac{1}{2}\rangle$ are the so-called *Clebsch-Gordon coefficients* [118]. Including the spin-orbit coupling, we obtain for the final Hamiltonian of the Rydberg electron

$$H = \frac{\mathbf{p}^2}{2} + V_l(r) + V_{\text{so}}(r). \quad (1.23)$$

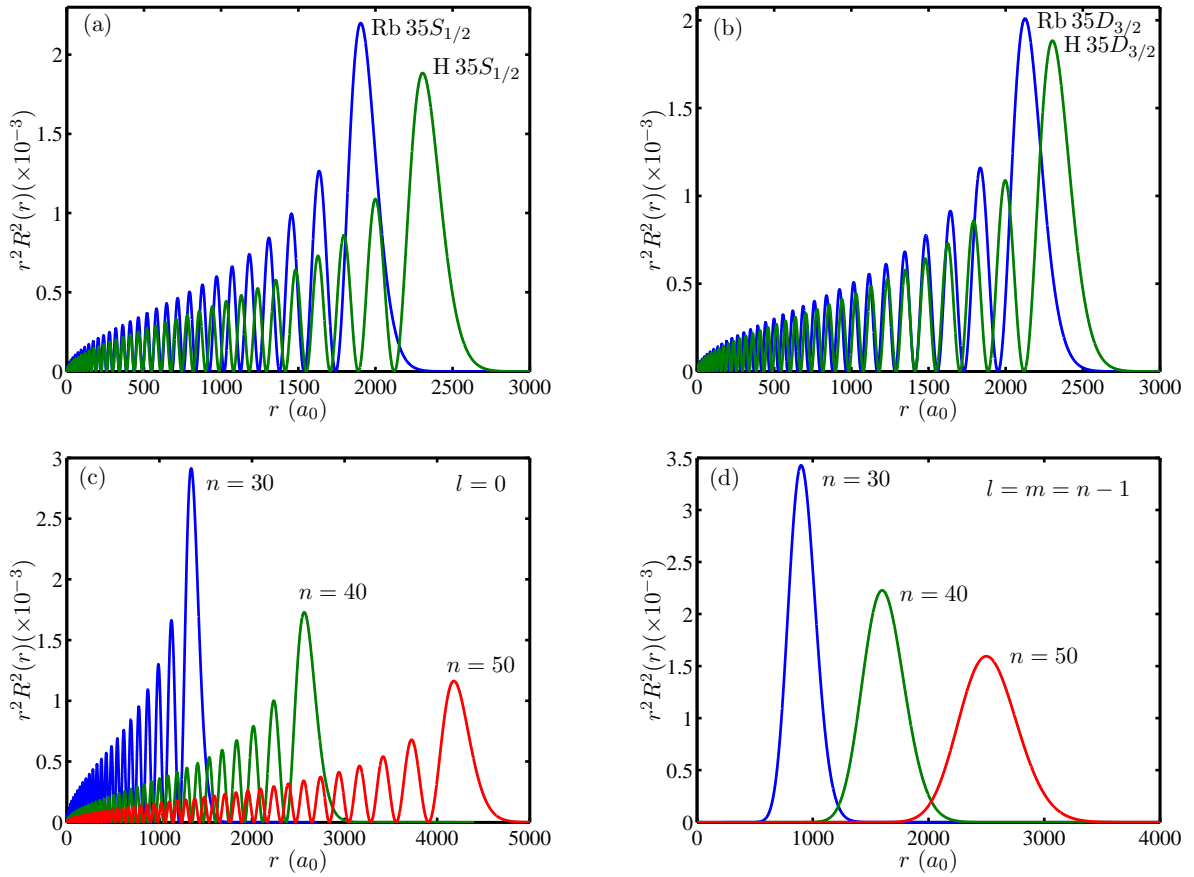


Figure 1.4: Radial probability densities $r^2 R(r)$ of different electronic Rydberg states of rubidium and hydrogen. Figure (a,b) show the density distributions for the $35S_{1/2}$ and $35D_{3/2}$ states, respectively. As expected, the influence of the finite size ionic rubidium core is less pronounced for the higher angular momentum state. Figure (c) and (d) illustrate the scaling of the radial probability densities with the angular momentum for $n = 30, 40, 50$. In case of zero angular nS states (Fig. (c)) a strong core penetration is visible. In contrast, the circular states ($l = m = n - 1$) possess vanishing probability densities for $r \rightarrow 0$, cf. panel (d).

For the hydrogen atom the energetic splitting caused by the fine structure interaction can be estimated as

$$\Delta E_{njl} \sim \frac{\alpha^2}{n^3(l + \frac{1}{2})(l + 1)l} \times \begin{cases} 0, & l = 0 \\ l, & j = l + \frac{1}{2}, l \neq 0 \\ -(l + 1), & j = l - \frac{1}{2}, l \neq 0 \end{cases}. \quad (1.24)$$

We see that for high angular momentum states the resulting fine structure splitting scales as $\sim 1/n^5$ [126], while for low angular states one encounters a scaling as $\sim 1/n^3$ (see Eq. (1.24)). In Fig. 1.5 the fine structure splitting of ΔE_{fs} between rubidium $nD_{3/2}$ and $nD_{5/2}$ states is shown as shown as a function of the principal quantum number n in the range of $25 \leq n \leq 65$ [127].

In this thesis we investigate electronic molecular states arising both from high- l (see Section 4.2) and low angular momentum states (see Chapter 7). In the case of the high- l states we neglect spin-orbit effects. In contrast, for low- l states it is essential to include those. In Section 4.2 we provide a more detailed discussion on this subject.

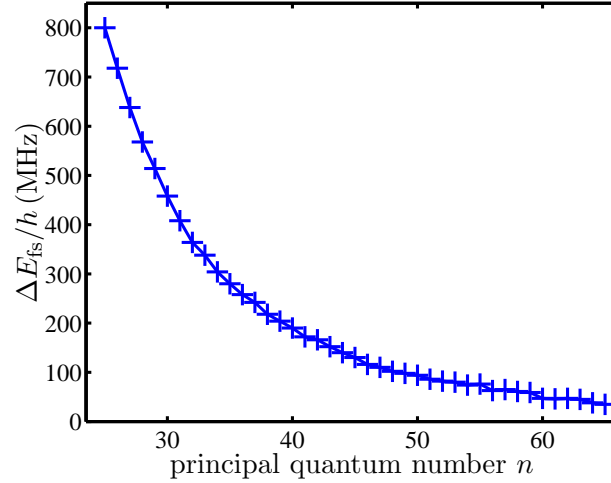


Figure 1.5: Fine structure splitting ΔE_{fs} for the Rb $nD_{3/2,5/2}$ states as function of the principal quantum number n (values taken from [127]).

1.3.3 Radiative lifetimes of Rydberg atoms

As Rydberg atoms are excited quantum objects they only possess finite lifetimes. In case of an isolated Rydberg atom we have two possible decay channels. First, the Rydberg atom interacts with the vacuum which leads to possible transitions to energetically lower levels. This process is known as spontaneous emission and the transition rate for the radiative decay Γ from an initial state $|i\rangle$ to a final state $|f\rangle$ is given by [108]

$$\Gamma_{fi}^{\text{sp}} = \frac{4}{3}\alpha^3\omega_{fi}^3|\langle f|\mathbf{r}|i\rangle|^2, \quad \omega_{fi} = \varepsilon_i - \varepsilon_f. \quad (1.25)$$

The energies $\varepsilon_{i,f}$ are the energies of the initial and final state, respectively.

$$\tau_{\text{sp}} = \left[\sum_{f, \varepsilon_f < \varepsilon_i} \Gamma_{fi}^{\text{sp}} \right]^{-1} \quad (1.26)$$

Obviously, any variation in the radial matrix element produced in a non-zero quantum defect alters the lifetimes known from the hydrogen atom. The lifetimes of Rydberg atoms have been measured with high accuracy [128–134] and can be calculated accurately [135–137]. The following relation for the n -dependence can be found

$$\tau_{\text{sp}}(nl) = \tau_0(n - \delta_{nl}^{\text{qd}})^\gamma. \quad (1.27)$$

The actual values of τ_0 and γ for the Rydberg nS , nP , nD , nF states for rubidium are presented in Tab. 1.5 together with their theoretical predictions. For all considered states, the exponent γ is close to $\gamma = 3$. The second decay channel that has to be considered is the stimulated emission and absorption due to black body radiation of temperature T [138, 139]. Similar to Eq. (1.26) the blackbody limited lifetime τ_{bb} can be written as [70]

$$\tau_{\text{bb}} = \left[\sum_{f, E_f < E_i} \frac{\Gamma_{fi}^{\text{sp}}}{\exp(\frac{\omega_{fi}}{T}) - 1} \right]^{-1} \approx \frac{3n^2}{4\alpha^3 T}. \quad (1.28)$$

states	τ_0^{th} (ns)	γ_{th}	τ_0^{exp} (ns)	γ_{exp}
nS	1.43	2.94	1.43	2.94
nP	2.76	3.02	2.80	3.01
nD	2.09	2.85	1.90	2.83
nF	0.76	2.95	—	—

Table 1.5: Theoretical [135] and experimental [132] lifetime parameters for the Rydberg quantum defect states of rubidium according to Eq. (1.27). The actual measurements had been performed with ^{85}Rb .

We see that for increasing principal quantum number n the black body decay rate exceeds the spontaneous emission rate: the latter scales as n^{-3} compared to n^{-2} scaling of τ_{bb}^{-1} . Finally, the total lifetime τ_{tot} is given by the sum of the depopulation rates due to spontaneous and stimulated decay

$$\frac{1}{\tau_{\text{tot}}} = \frac{1}{\tau_{\text{sp}}} + \frac{1}{\tau_{\text{bb}}}. \quad (1.29)$$

1.4 Rydberg atoms in external fields

In this section we present the basic effects of external static and homogeneous electric and magnetic fields, respectively. Because we are interested in the basic effects, we first neglect all finite mass effects of the ionic core, e.g. $m_{\text{ion}} \rightarrow \infty$. The effects of a finite ion mass lead to states which are known as *giant dipole states* [79]. This will be the topic of Chapter 9.

1.4.1 Rydberg atoms in electric fields

First we consider an external electric field. If the applied electric field is in z -direction we get the following Hamiltonian

$$H = \frac{\mathbf{p}^2}{2} + V_l(r) + Ez. \quad (1.30)$$

As discussed in Section 1.3 the l -dependent potential $V_l(r)$ incorporates scattering and polarization effects of the Rydberg electron with the ionic core. At this stage we ignore the spin of the electron. Obviously, the azimuthal quantum number m is a good quantum number.

Hydrogen atom

We begin this paragraph by considering the behavior of the hydrogen atom in a static and homogeneous electric field. In this case $V_l(r) = -1/r$ which is the pure Coulomb potential. The most obvious effect of the electric field is that it lifts the degeneracy of the $|nlm\rangle$ eigenstates of a particular energy $1/2n^2$. This effect is known as the *Stark effect*. The most straightforward way to treat the Stark effect is to introduce parabolic coordinates. These are defined in terms of

$$x = \sqrt{\xi\eta} \cos(\phi), \quad y = \sqrt{\xi\eta} \sin(\phi), \quad z = \frac{(\xi - \eta)}{2}. \quad (1.31)$$

In parabolic coordinates the Schrödinger equation (1.30) becomes

$$H = -\frac{\Delta_{\xi\eta}}{2} + \frac{m^2}{2\xi\eta} - \frac{2}{\xi + \eta} + E\frac{\xi - \eta}{2} \quad \text{with} \quad \Delta_{\xi\eta} = \frac{4}{\xi + \eta} \left(\frac{\partial}{\partial\xi} \left(\xi \frac{\partial}{\partial\xi} \right) + \frac{\partial}{\partial\eta} \left(\eta \frac{\partial}{\partial\eta} \right) \right). \quad (1.32)$$

In parabolic coordinates the problem remains separable and in first order degenerated perturbation theory the wave function can be written as $\psi_{nn_1n_2m}(\xi, \eta, \phi) = u_{nn_1m}(\xi)u_{nn_2m}(\eta)e^{im\phi}$ where the parabolic quantum number n_1 , n_2 fulfill $n = n_1 + n_2 + |m| + 1$. Calculating the corrections of the degenerated eigenvalue $-1/2n^2$ up to $\mathcal{O}(E^2)$ perturbatively gives

$$\varepsilon_{nn_1n_2m} = -\frac{1}{2n^2} + \frac{3}{2}En(n_1 - n_2) - \frac{E^2}{16}n^4 [17n^2 - 3(n_1 - n_2) - 9m^2 + 19]. \quad (1.33)$$

We see that states with $n_1 \neq n_2$ possess a linear energy shift in E which means that they possess a finite permanent electric dipole moment. Furthermore, the second order shift breaks the m degeneracy.

Rydberg atoms

As discussed in Section 1.3, the corrections to the Coulomb due to scattering and polarization effects of the electron with the ionic rubidium core lead to the lifting of the l -degenerated states for small angular momenta. Selection rules for the dipole operator prohibit a coupling between states with the same angular momentum l because of equal parities. In this case the second-order perturbation theory has to be employed, which results in a quadratic Stark shift. This second order energy shift can be described by a polarizability $\alpha_{\text{Ry}}^{(i)}$

$$\varepsilon_{\text{Stark}}^{(i)} = \sum_{i \neq j} \frac{|\langle i | z | j \rangle|^2}{\varepsilon_i - \varepsilon_j} E^2 =: -\frac{1}{2} \alpha_{\text{Ry}}^{(i)} E^2. \quad (1.34)$$

In the case of high angular momenta no quantum defects are considered and the manifolds for the degenerated eigenenergies possess states of different parities. In first order perturbation theory we obtain a linear Stark effect. In Fig. 1.6(a-c) we present the Stark map in the energetic vicinity of the $42D$ state of rubidium for an electric field strength up to $E = 2 \text{ V/cm}$. In the calculation of the map spin-orbit corrections were considered as well [140], the actual angular momentum state L_j is color-coded (see Fig. 1.6(a)). In Fig. 1.6(b) the energetic splitting of the hydrogenic $n = 41$ manifold is presented. We clearly see a linear dependence on the electric field strength E . In contrast to this, Fig. 1.6(c) shows the behavior of the less degenerated $42D_j$, $j = 3/2, 5/2$ states on E . For these states a quadratic Stark effect is clearly visible.

For electric fields where $\varepsilon_{\text{Stark}}^{(i)}$ is on the order of the energy difference to the neighbored dipole coupled state, the Stark effect cannot be treated perturbatively and an exact diagonalization scheme has to be employed.

1.4.2 Rydberg atoms in magnetic fields

Next we consider an external magnetic field. If the applied magnetic field is in z -direction, we get the following Hamiltonian

$$\begin{aligned} H &= \frac{(\mathbf{p} + \mathbf{A}(\mathbf{r}))^2}{2} + \mathbf{B} \cdot \mathbf{S} + V_l(r) + V_{\text{so}}(r) \\ &= \frac{\mathbf{p}^2}{2} + V_l(r) + V_{\text{so}}(r) + \underbrace{\frac{B}{2} (J_z + S_z)}_{B_{\text{para}}} + \underbrace{\frac{B^2}{8} r^2 \sin^2(\vartheta)}_{B_{\text{dia}}}. \end{aligned} \quad (1.35)$$

Here we have chosen the symmetric gauge with $\mathbf{A}(\mathbf{r}) = B/2(-y, x, 0)^T$. In addition, we have introduced spherical coordinates. We denote the paramagnetic and diamagnetic term as B_{para} and B_{dia} , respectively. Again the azimuthal quantum number m is a good quantum number and the z -parity is a conserved quantity as well.

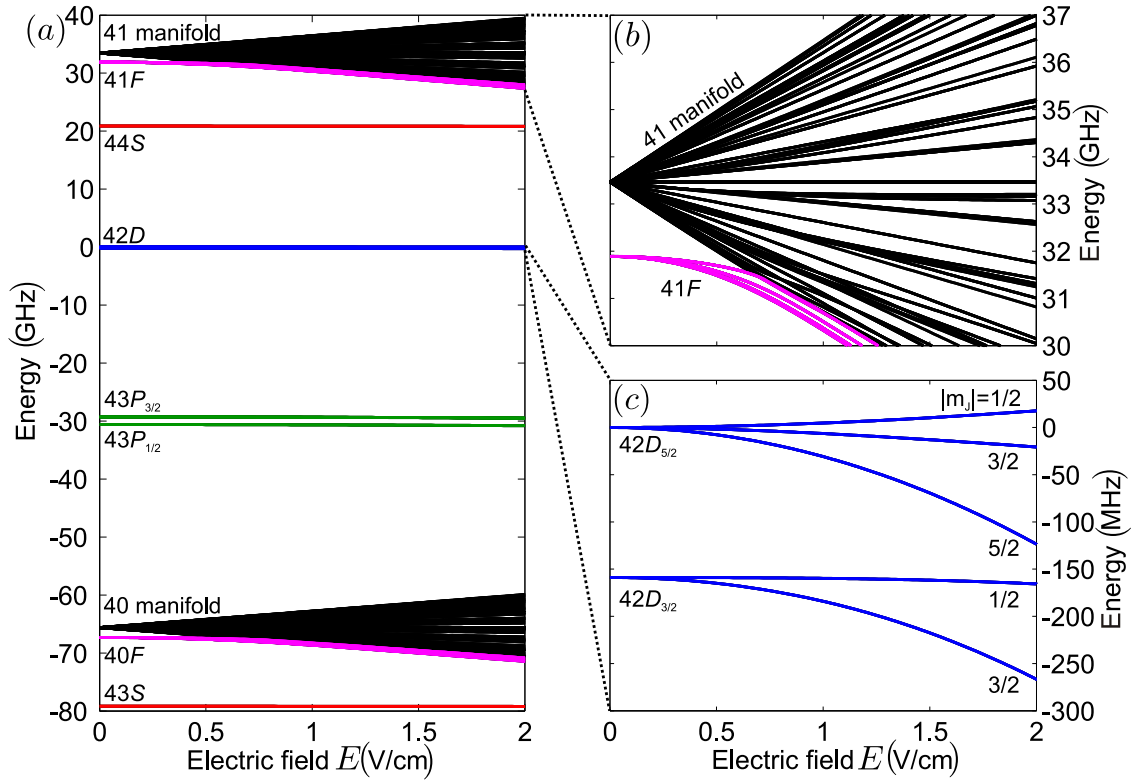


Figure 1.6: Stark maps showing the states in the energetic vicinity to the $42D$ state for electric field strengths up to 2 V/cm . In this particular setup spin-orbit coupling is considered. Figure (a) gives an overview of the Rydberg states in the vicinity of the $42D$ state, color-coded depending on their angular momentum quantum number L_j . Figure (b) shows the linear Stark effect of the degenerated hydrogenic $n = 41$ manifold. In contrast, figure (c) shows the behavior of the less degenerated $42D_j$, $j = 3/2, 5/2$ states. A quadratic Stark shift is clearly visible. (figure taken from [140]).

First we analyze the case when we still include the spin-orbit interaction. For the considered field strength we neglect the diamagnetic term. In this case we distinguish two regimes

- $B_{\text{para}} \ll V_{\text{so}}$

Here the magnetic field is only a small perturbation to the $|njm_j l \frac{1}{2}\rangle$ states. The energetic splitting ΔE induced by the magnetic field term is determined by

$$\Delta E = \frac{B}{2} m_j \left(1 \pm \frac{1}{(2l+1)} \right) \quad \text{for } j = l \pm \frac{1}{2}. \quad (1.36)$$

The degenerate nL_j manifold splits into $2j+1$ equidistant energy levels. This effect is known as the *anomalous Zeeman effect*.

- $V_{\text{so}} \ll B_{\text{para}}$

Now the spin orbit-term is just a minor perturbation. We use the eigenstates $|nlm \frac{1}{2} m_s\rangle$ to calculate the energetic splitting induced by the magnetic field and the spin-orbit term. We obtain

$$\Delta E = \frac{B}{2} (m + 2m_s) + mm_s. \quad (1.37)$$

This regime is known as the *Paschen-Back regime*.

If the spin-orbit coupling is completely neglected (as for high- l Rydberg states) the electron spin and spatial degrees of freedom are totally decoupled. For this reason we do not consider the spin

in this case. Now the Hamiltonian of the Rydberg atom in a magnetic field is given by

$$H = \frac{(\mathbf{p} + \mathbf{A}(\mathbf{r}))^2}{2} + V_l(r) = \frac{\mathbf{p}^2}{2} + V_l(r) + \frac{B}{2}L_z + \frac{B^2}{8}r^2 \sin^2(\vartheta). \quad (1.38)$$

Because L_z commutes with the field free Hamiltonian the only term causing couplings between the field free eigenstates $|nlm\rangle$ is the quadratic field term in Eq. (1.35). Expressing the Hamiltonian (1.38) in the field free states $|nlm\rangle$ we obtain

$$\langle n'l'm|H|nlm\rangle = \left(-\frac{1}{2(n - \delta_l^{\text{qd}})^2} + m\frac{B}{2} \right) \delta_{n'n} \delta_{l'l} + \langle n'l'm| \frac{B^2}{8} r^2 \sin^2(\vartheta) |nlm\rangle. \quad (1.39)$$

The only non vanishing matrix elements are given for those states for which $\Delta l = 0, \pm 2$ and $\Delta m = 0$. The explicit forms of the angular matrix elements are

$$\langle l'm| \sin^2(\vartheta) |lm\rangle = 2 \frac{l^2 + l - 1 + m^2}{(2l+3)(2l-1)} \delta_{l'l} - \sqrt{\frac{((l_{<} + 2)^2 - m^2)((l_{<} + 1)^2 - m^2)}{(2l_{<} + 5)(2l_{<} + 3)^2(2l_{<} + 1)}} \delta_{l',l\pm 2} \quad (1.40)$$

with $l_{<} := \min(l', l)$ (see Appendix B.8.1). In general, we can distinguish three different regimes

- low-field regime: $\frac{B^2}{8}n^4 \ll \frac{B}{2}n \ll 1/n^3$

In this regime the magnetic field strength B is so low that the effect of the diamagnetic term can be safely neglected. In this case the degeneracies of the $-1/2n^2$ energies are partly lifted as we get a linear spreading in the magnetic field due to the paramagnetic term. This effect is known as the (*normal*) *Zeeman effect*. Here the principal quantum number n and the angular quantum number l are still good quantum numbers and the eigenstates of (1.38) are identical to the field free eigenstates $|nlm\rangle$.

- intermediated regime $\frac{B}{2}n \ll \frac{B^2}{8}n^4 \ll 1/n^3$

In this regime the diamagnetic term significantly couples the different angular momentum states within a single n -manifold but couplings to adjacent n -manifolds can still be neglected. Due to this this regime is often referred as the *l-mixing regime*. Obviously, the only good quantum number remaining beside m is n .

- strong-field regime $1/n^3 \ll \frac{B^2}{8}n^4$

In this regime the magnetic field is such strong that it significantly couples states from adjacent n -manifolds, for this reason this regime is also referred as the *n-mixing regime*. For $n^4 \gg 2/B$ we find the situation that the paramagnetic term already causes the eigenenergies splitting linearly from different n -manifolds to overlap. In this case the *l-mixing regime* is missing and we directly go from the low into the strong field regime.

Chapter 2

Interaction of Rydberg atoms and ground state atoms

In this chapter we present the basic theoretical concepts which are required to model the interaction of a Rydberg atom with a ground state neutral perturber. In Section 2.1 we discuss the physics of low-energy electron-atom interaction which will lead to the so-called Fermi-pseudopotential approach. Within this theory the exact electron-atom interaction potential is replaced by a contact interaction which is determined by a single quantity, the so-called scattering length. In Section 2.2 the specific properties of this quantity will be discussed in detail. An alternative derivation and discussion can be found in Ref. [141].

2.1 Electron-atom interaction

The interaction of Rydberg atoms with neutral background gases is largely dominated by the scattering of the highly excited Rydberg electron from the neutral ground state atoms. In this context the first experimental studies in this direction were performed in 1934 by Amaldi and Segrè [142, 143] and independently by Füchtbauer and coworkers [144]. In their studies the effect of admixtures of various gases such as hydrogen, nitrogen and different noble gases on absorption spectra of sodium and potassium was investigated systematically. For highly excited atomic species, e.g. atomic Rydberg states, a shift and broadening of absorption lines was found. Surprisingly, both blue and red shifted lines were observed [142–144]. In general, the observed effects only depend on the type of the perturbing background gas and its density.

The explanation of the line shift was given by Enrico Fermi in 1934 [145]. In his concept the Rydberg electron in its orbital is assumed as a quasi-free particle which undergoes a scattering event with the ground state atoms at its low kinetic energy E_{kin} . In this approach the complex Rydberg electron-ground state atom interaction is reduced to a single effective parameter, the scattering length a . This model is nowadays well known as the Fermi-pseudopotential [145]. Later this concept was further refined by extending it to alkali metals perturbing gas [146] and higher electron momenta [147]. However, in order to ensure the validity of Fermi's approach some approximations have to be fulfilled. Considering a single particle incident upon a system of two or more scattering partners, these approximations in general consists of three main points [148, 149]:

1. The range of the electron-atom interaction is small compared to the atomic interparticle distance
2. The electron-atom scattering is elastic, so that there is no sizable attenuation of the incident particle by the target system. This means that, dealing with one single scattering event, the impact of the previous events can be largely neglected.
3. The single scattering event lasts short enough that binding forces during the collision are neglected.

In the field of ultracold molecular physics the Fermi-pseudopotential approach has turned out extraordinary well in providing a novel binding mechanism leading to the formation of ultralong-range Rydberg molecules [85]. For this reason, Fermi's original derivation is recapitulated in the following section. Later on in Section 2.1.2, the effect of higher order scattering terms is discussed in detail.

2.1.1 Fermi-pseudopotential

The starting point in the derivation of the Fermi-pseudopotential is the Schrödinger equation of the Rydberg valence electron wave function $\psi(\mathbf{r})$ in interaction with the ionic core and N surrounding neutral atoms

$$\left(-\frac{1}{2m_e}\Delta + U(\mathbf{r}) + \sum_{i=1}^N V_i(\mathbf{r})\right)\psi(\mathbf{r}) = E\psi(\mathbf{r}). \quad (2.1)$$

The interaction potential V_i is assumed to be short-ranged and isotropic. For large distances the neutral atom electron interaction can be considered as the induced dipole interaction of the neutral atom in the electric field of the electron

$$V_i(\mathbf{r}) = -\frac{\alpha_n}{2|\mathbf{r} - \mathbf{R}_i|^4}. \quad (2.2)$$

Here α_n denotes the ground state polarizability of a single neutral atom. The vector \mathbf{R}_i represents the position of the i -th ground state atom. The effective range r_{eff} of this approximation can be estimated by comparing it with the energy scale provided by the centrifugal potential $1/2\mu_{\text{en}}r^2$. This leads to

$$r_{\text{eff}} = \sqrt{\mu_{\text{en}}\alpha_n}, \quad (2.3)$$

where μ_{en} denotes the reduced mass of the electron-/ neutral atom system. For rubidium $^{87}\text{Rb}(5S)$, this characteristic radius is $r_{\text{eff}} = 0.96 \text{ nm}$, which is much smaller than the mean interparticle distance of $\bar{d} = \sqrt[3]{\rho^{-1}} = 1 \mu\text{m}$ at particle densities of around 10^{12} cm^{-3} typical for ultracold atomic samples. Next, the Rydberg atom is assumed to possess a low kinetic energy; in particular the de Broglie wavelength $\lambda_{\text{dB}} = h/\sqrt{2m_e E_{\text{kin}}}$ is assumed to be much larger than the effective range r_{eff} and the inter particle distance \bar{d} ; e.g. $r_{\text{eff}} \ll \bar{d} \ll \lambda_{\text{dB}}$. This assumption is invalid in the region near the ionic Rydberg core because of the increasing kinetic energy. However, this region has only little significance for the calculations in this thesis.

The essential idea in the derivation of the effective potential description is to derive a Schrödinger equation for an averaged wave function $\bar{\psi}(\mathbf{r})$. In particular, the Schrödinger equation (2.1) is averaged over a small volume which is chosen to be smaller than the de Broglie wavelength λ_{dB} but still larger than the range r_{eff} of the polarization potential (2.2) and the main inter particle distance \bar{d} . This way the local impact of the perturbing neutral atom is removed and outside the interaction region the averaged wave function $\bar{\psi}(\mathbf{r})$ resembles the wave function $\psi(\mathbf{r})$. Under this condition, the mean of the derivative of the wavefunction can be replaced by the derivative of the averaged wavefunction ($\overline{\Delta\psi(\mathbf{r})} = \Delta\bar{\psi}(\mathbf{r})$) and one obtains

$$-\frac{1}{2m_e}\Delta\bar{\psi}(\mathbf{r}) + U(\mathbf{r})\bar{\psi}(\mathbf{r}) + \sum_{i=1}^N \overline{V_i(\mathbf{r})\psi(\mathbf{r})} = E\bar{\psi}(\mathbf{r}). \quad (2.4)$$

Next we have to find an expression for $\overline{V_i(\mathbf{r})\psi(\mathbf{r})}$. For this purpose we examine the electron-perturber interaction in a region closely around a single perturbing atom, e.g. $0 < |\mathbf{r} - \mathbf{R}_i| < \lambda_{\text{dB}}$. This domain is extending over regions with vanishing and non-vanishing electron-atom interaction $V(\mathbf{r})$. In addition, we consider the mean inter particle distance to be so large that the effect of the interaction between the electron and the ionic core $U(\mathbf{r})$ of the Rydberg atom can be neglected. Since we are considering low-energy electron dynamics ($E \rightarrow 0$) we make the following ansatz for the wavefunction $\psi(\mathbf{r})$

$$\psi(r) = \frac{u(r)}{r} Y_{00} \quad \text{for } E \rightarrow 0. \quad (2.5)$$

In spherical coordinates, the Schrödinger equation for $u(r)$ is given by

$$u''(r) = 2\mu_{\text{en}}(V(r)u(r) - Eu(r)) \xrightarrow{E \rightarrow 0} u''(r) = 2\mu_{\text{en}}V(r)u(r). \quad (2.6)$$

For $r > r_{\text{eff}}$ we have $V(r) \rightarrow 0$, which means we can easily solve the last equation in (2.6) in this region:

$$u''(r) = 0 \Rightarrow u(r) = C(r - a) \text{ for } r > r_{\text{eff}}, \quad C, a \in \mathbb{R}. \quad (2.7)$$

The quantity a is known as the s -wave scattering length¹. For $a > 0$, the scattering length is the intercept of the asymptotic wave function with the abscissa. In this case a can be seen as the minimal distance the two scattering constituents approach in a low-energy scattering process. Then the scattering process can be considered as the scattering of hard sphere particles with a total scattering cross-section of $4\pi a^2$. For $r \gg |a|$, ψ is identical to the averaged wave function $\bar{\psi}$ which is, in a first approximation, a constant given by $\bar{\psi} = CY_{00}$. Finally, the averaged interaction energy stemming from a single perturber atom i can be calculated. Under the assumption that there is only a single perturbing atom inside the volume V_0 over which the wave function is averaged, one obtains

$$\overline{V_i(r)\psi(r)} = \frac{4\pi Y_{00}}{V_0} \int dr r V(r)u(r) = \frac{2\pi Y_{00}}{\mu_{\text{en}} V_0} \int_0^{r_{\text{eff}}} dr r u''(r) = \frac{2\pi a}{\mu_{\text{en}} V_0} Y_{00} C = \frac{2\pi a}{\mu_{\text{en}} V_0} \bar{\psi}. \quad (2.8)$$

The second can be solved via partial integration assuming the wave function ψ being differentiable at the position of the perturbing atom. If there is no perturbing atom within the average volume the interaction vanishes. Thus, the general result of (2.8) is given by

$$\overline{V_i(r)\psi(r)} = \frac{2\pi a}{\mu_{\text{en}}} \frac{\delta_{r_{\text{eff}}}(r)}{V_0} \bar{\psi}, \quad \text{with} \quad \frac{\delta_{r_{\text{eff}}}(r)}{V_0} = \begin{cases} 1, & \text{if } r < r_{\text{eff}} \\ 0, & \text{otherwise} \end{cases}. \quad (2.9)$$

For $r_{\text{eff}} \rightarrow 0$ we get

$$\lim_{r_{\text{eff}} \rightarrow 0} \frac{\delta_{r_{\text{eff}}}(r)}{V_0} = \delta(\mathbf{r}) \quad (2.10)$$

and the averaged interaction energy from a single atom i can be written as

$$\overline{V_i(\mathbf{r})\psi(r)} = V_{\text{pseudo}}(\mathbf{r} - \mathbf{R}_i) \bar{\psi}(r) \quad \text{with} \quad V_{\text{pseudo}}(\mathbf{r}) = \frac{2\pi a}{\mu_{\text{en}}} \delta(\mathbf{r}). \quad (2.11)$$

The potential V_{pseudo} has become known as the *zero-range Fermi-pseudopotential* in the literature [145]. The last formulation was introduced by Fermi in 1936 when he was studying the scattering of slow neutrons from hydrogen atoms [153]. However, the main parts of the derivation was already published in 1934 [145]. Here, Fermi was interested in the total effect of a large number of perturbing atoms inside the wavefunction $\psi(r)$ of the Rydberg electron. The Fermi-pseudopotential is often used instead of the exact potential in order to introduce analytical or numerical simplifications. However, one should consider the fact that this potential is too singular to be used to solve the exact three dimensional Schrödinger equation. Nevertheless, it can be very useful in perturbative or mean-field theories [154].

Finally, we summarize the level of approximations which had been introduced to derive Eq. (2.11). First, we have only considered the $l = 0$ scattering channel. In Section 2.2 we will see that it can be important to include higher order scattering terms. Second, in Eq. (2.11) the s -wave

¹The sign of a is chosen different from Fermi's original notation [145] to match today's textbook convention [150–152].

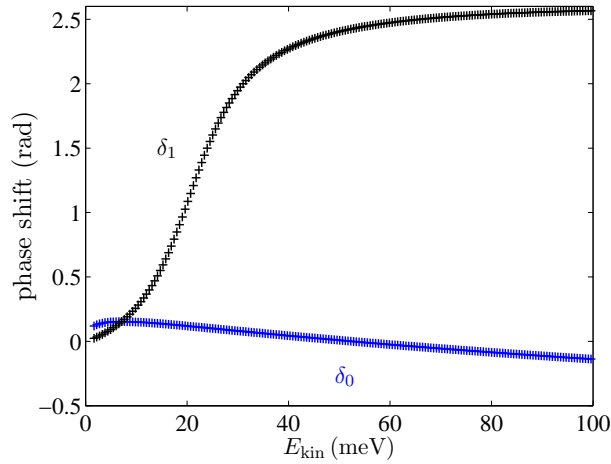


Figure 2.1: Energy dependent scattering phase shifts δ_0 (blue points) and δ_1 (black points) for e^- -Rb($5S$) scattering [155]. The phase shifts are shown as functions of the electronic kinetic energy E_{kin} .

scattering length is of constant value. However, in general this quantity is energy dependent [150]. Obtaining the value of the s -wave scattering length and its energy dependence requires a involved calculation. Depending on the atomic species and of the perturbing neutral atom and the relative orientation of the electron and atomic spin the value can be positive or negative. This facts explains the observation red and blue shifted atomic lines as the obtained line shift ΔE of the Rydberg absorption line is given by

$$\Delta E = \frac{2\pi a}{\mu_{\text{en}}}\rho, \quad (2.12)$$

where ρ is the density of ground state atoms. This result can be obtained by integrating the pseudopotential Eq. (2.11) over the Rydberg electron's density distributions $|\psi(\mathbf{r})|^2$ and over the particle density ρ which is assumed to be constant. For ^{87}Rb the triplet scattering length $a_T = -16.05a_0$ is negative while the singlet scattering length $a_s = 0.627a_0$ is one order of magnitude smaller and positive [85]. As we will see in Chapter 4 the only scattering process leading to bound molecules. Finally, we remark that any retroaction of the ground state atom on electronic Rydberg state is neglected. In general this effect is small, but in the case of rubidium dimers it has been experimentally verified that this leads to novel molecular properties such as a permanent dipole moment of homonuclear diatomic molecules [95].

The higher order terms and the energy dependencies of the electron-atom scattering length will be the topic of the next paragraph.

2.1.2 Higher order contributions

So far, the scattering of the Rydberg electron from a neutral ground state atom has only been treated in zeroth order of the electron momentum k . Higher order contributions have been calculated by A. Omont [156] by expanding the electron wavefunction in terms of Fourier transformed plain waves $e^{i\mathbf{k}\cdot\mathbf{r}}$. The general expression for the low-energy scattering potential of an electron with a neutral ground state perturber atom is given by

$$V_{\text{en}}(\mathbf{r}, \mathbf{R}) = \sum_{l=0}^{\infty} V_{\text{en}}^{(l)}(\mathbf{r}, \mathbf{R}) = 2\pi \sum_{l=0}^{\infty} (2l+1) R_l (P_l(\frac{1}{k^2} \overleftarrow{\nabla}_{\mathbf{r}} \delta(\mathbf{r} - \mathbf{R}) \overrightarrow{\nabla}_{\mathbf{r}})), \quad R_l = -\frac{\tan(\delta_l)}{k}. \quad (2.13)$$

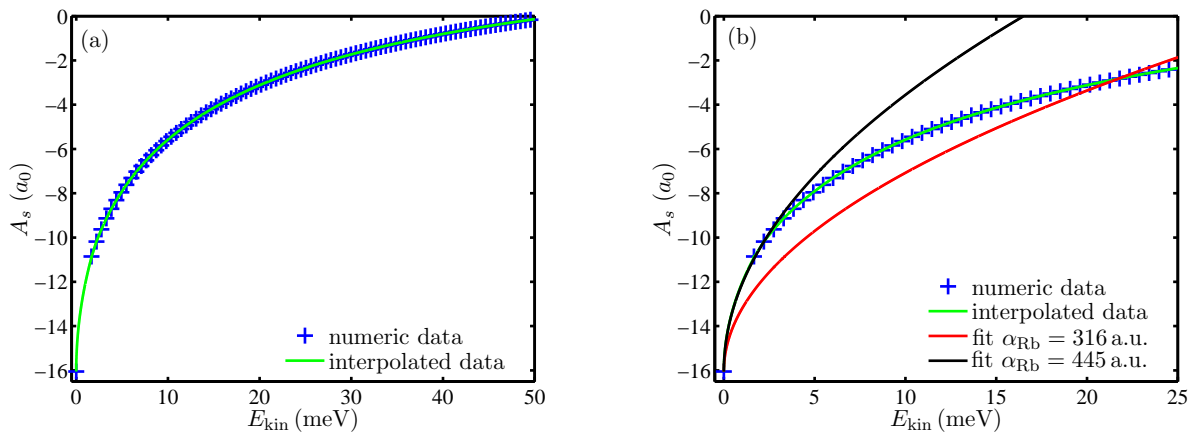


Figure 2.2: (a) Numeric data (blue points) for A_s in comparison with interpolated data (green solid curve). A cubic spline interpolation scheme was used to interpolate the numeric data. (b) Numeric and interpolated data (blue crosses and solid green line, respectively) for the s -wave scattering length. In addition the low-energy limit (Eq. (2.16)) is presented with $\alpha_{\text{Rb}} = 316$ a.u. (red solid line) and 445 a.u. (black solid line).

where P_l are the Legendre polynomials and $\delta_l(k)$ are the energy dependent phase shifts. The momentum k is related to the kinetic energy E_{kin} which is given within a semiclassical approximation

$$E_{\text{kin}} = \frac{k^2}{2} = \frac{1}{R} - \frac{1}{2(n - \delta_l^{\text{qd}})^2}. \quad (2.14)$$

The first term with $l = 0$ of the expansion (2.13) leads to

$$V_{\text{en}}^s(\mathbf{r}, \mathbf{R}) = 2\pi A_s(k) \delta(\mathbf{r} - \mathbf{R}), \quad \text{with } A_s(k) = -\frac{\tan(\delta_0(k))}{k}. \quad (2.15)$$

The quantity $A_s(k)$ is denoted as the energy dependent s -wave triplet scattering length (see Fig. 2.1). Its low-energy dependence can be expanded according to

$$A_s(k) = a_T + \frac{\pi}{6} \alpha_n k + \mathcal{O}(k^2). \quad (2.16)$$

Here α_n is again the ground state polarizability of the neutral perturber atom. The second term with $l = 1$ of the expansion (2.13) leads to

$$V_{\text{en}}^p(\mathbf{r}, \mathbf{R}) = 6\pi A_p^3(k) \overleftarrow{\nabla}_{\mathbf{r}} \delta(\mathbf{r} - \mathbf{R}) \overrightarrow{\nabla}_{\mathbf{r}}, \quad \text{with } A_p^3(k) = -\frac{\tan(\delta_1(k))}{k^3}. \quad (2.17)$$

Here the quantity $A_p^3(k)$ is denoted as the (cubed) energy dependent p -wave scattering length. Its low-energy dependence can be expanded according to

$$A_p^3(k) = -\frac{\pi \alpha_n}{15k}. \quad (2.18)$$

As we see in the relation for R_l in (2.13) the energetic dependence is determined by depends on $\tan(\delta_l)$. This means if $\delta_l = \pi/2$ the corresponding scattering terms become divergent and the description of electron-atom scattering provided with expression (2.13) breaks down. As known from scattering theory, [150] $\tan(\delta_l)$ changes rapidly from 0 to π if the incident energy E of the

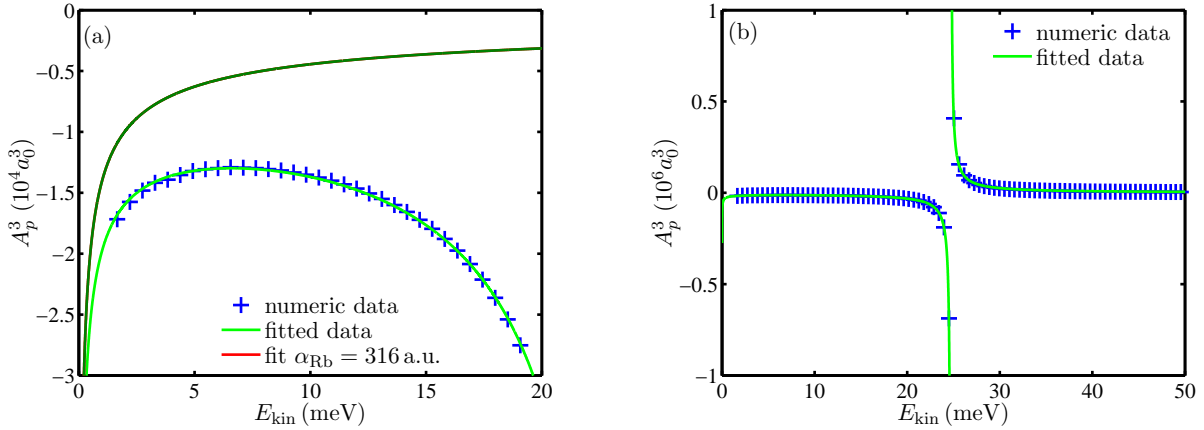


Figure 2.3: (a) Low energy data points for A_p^3 . Beside the numeric data (blue points) the low-energy limit (Eq. 2.20) is presented with a value of $\alpha_{\text{Rb}} = 316$ a.u. (red solid curve). In addition the interpolated data obtained by using a cubic spline interpolation scheme is shown as well (green solid curve). (b) The cubed p -wave scattering length A_p^3 as function of E_{kin} . The numeric data (blue points) clearly shows the existence of a resonance between 20 – 30 meV. Using the fitting function Eq. 2.20 we obtain the parameters $E_{\text{res,fit}} = 23.9 \pm 0.9$ meV and $\Gamma_{\text{fit}} = 2.2 \times 10^{-4} \pm 2 \times 10^{-5}$ a.u.. The green solid line indicates the fitted data.

incident particle matches the energy E_R of a quasi-bound state with lifetime Γ .

$$\tan(\delta_l) = -\frac{\Gamma}{E - E_{\text{res}}} \Rightarrow \tan(\delta_l) \rightarrow \infty \text{ for } E \rightarrow E_{\text{res}}. \quad (2.19)$$

This effect is known as shape resonance. As we will see in the following Section 2.2 such resonant process is important for molecule formation.

2.2 Energy dependence of the scattering phase shifts

Next we have a closer look on the specific energy dependence of the s - and p -wave scattering phase shifts $\delta_0(k)$ and $\delta_1(k)$ respectively.

In Fig. 2.1 we show the energy dependence of the triplet s - and p -wave scattering phase shifts (blue and black points, respectively) of e^- -Rb($5S$) scattering as functions of the electronic kinetic energy E_{kin} [155]. We see that $\delta_1 = \pi/2$ for $E_{\text{kin}} \approx 23 - 25$ meV which means that at this energy we hit a resonance and the associated p -wave scattering length $A_p(k)$ diverges. In Fig. 2.2(a,b) we present the energy dependent s -wave scattering lengths A_s as a function of the electronic kinetic energy E_{kin} . In both figures Fig. 2.2(a,b) the blue points indicate the scattering length derived from the numeric data of the scattering phase shifts shown in Fig. 2.1. For $E_{\text{kin}} = 0$ we have added the zero energy s -wave scattering length $A_s(k=0) = a_T = -16.05a_0$ which is taken from the literature [85, 155]. Using this data set we have performed a cubic spline interpolation scheme [157, 158]. The resulting data is indicated by the green solid line. In Fig. 2.2(b) we present a comparison of the numeric and interpolated data in the low-energy limit given by Eq. (2.16). The ground state polarizability α_{Rb} of ^{87}Rb is taken from the literature with $\alpha_{\text{Rb}} = 316$ a.u. [159]. This approximation is indicated by a red solid line. We see that this approximation does not predict the numeric data very well. Inserting a higher polarizability $\alpha_{\text{Rb}} = 445$ a.u. gives the data represented by the black solid line. This approximation fits the numeric and interpolated data better in the sense that it is more or less identical to those data sets up to a kinetic energy of $E_{\text{kin}} = 4$ meV. Beyond this value this approximation becomes less accurate for increasing kinetic energy. Although studying the common literature extensively we could not find a reasonable explanation for this deviation. We decided to use the interpolated data for our calculations.

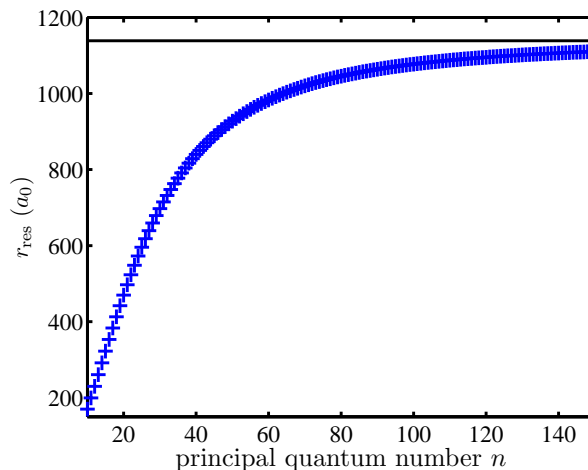


Figure 2.4: Radial position r_{res} of the triplet p -wave shape resonance. The position r_{res} was calculated according to Eq. (2.21) where a resonance energy of $E_{\text{res}} = 23.9$ meV was used. The black solid line indicates the maximal resonance position $r_{\text{res,max}} = 1139a_0$.

For the p -wave scattering data we have used the fitting function

$$A_p^3(E_{\text{kin}}) = \begin{cases} -\frac{\pi\alpha_n}{15\sqrt{2E_{\text{kin}}}}, & \text{for } E_{\text{kin}} \rightarrow 0 \\ \frac{\Gamma_{\text{fit}}}{\sqrt{2E_{\text{kin}}^{5/2}(1-E_{\text{R,fit}}/E_{\text{kin}})}}, & \text{for } E_{\text{kin}} \approx E_{\text{res}} \end{cases} \quad (2.20)$$

to fit the numeric data. In Fig. 2.3(a) we present the numeric data (blue crosses) in comparison with the low-energy limit (2.18). This approximation is indicated by the red solid curve where we have used a polarizability $\alpha_{\text{Rb}} = 316$ a.u.. We see that this approximation does not reproduce the numeric data very well. In the provided numeric data only six points with $E_{\text{kin}} < 5$ meV show a decrease in their values, which can be understood as the beginning of the $1/\sqrt{E_{\text{kin}}}$ low-energy behavior as it is predicted by Eq. (2.18) and Eq. (2.20), respectively. However, even these points are still not in the region which is purely dominated by the low-energy limit. To have any access to this specific energy range we have calculated a number of points using the expression of the low-energy approximation from Eq. (2.20) for $E_{\text{kin}} \ll 5$ meV. Including these points we have then performed a cubic spline interpolation scheme. This data is depicted by a solid green curve in Fig. 2.3(a). In Fig. 2.3(b) we present the (cubed) p -wave scattering length for electronic kinetic energies $0 \leq E_{\text{kin}} \leq 50$ meV. We clearly see a resonance for $E_{\text{kin}} \approx 23 - 25$ meV. In the region near the resonance we have used the fitting function Eq. (2.20). We obtain the fitting parameters $E_{\text{res,fit}} = 23.9 \pm 0.9$ meV and $\Gamma_{\text{fit}} = 2.2 \times 10^{-4} \pm 2 \times 10^{-5}$ a.u.. In Fig. (2.3)(b) the corresponding data is represented by a solid green curve.

For a fixed principal quantum number n the resonance energy E_{res} can be associated with a radial distance r_{res} of the Rydberg electron from the ionic core. Using the semiclassical relation Eq. (2.14) we easily derive the following expression

$$r_{\text{res}} = \frac{1}{E_{\text{res}} + \frac{1}{2n^2}}. \quad (2.21)$$

In Fig. 2.4 the relation between r_{res} and the principal quantum number n is shown. Obviously, for $n \rightarrow \infty$ it approaches a maximal value which is given by $r_{\text{res,max}} = E_{\text{res}}^{-1} \approx 1139a_0$.

Chapter 3

Basic concepts of molecular physics

Before we start to analyze the specific molecular system we repeat the essential concepts of standard molecular physics. In Section 3.1 we discuss the general Hamiltonian of atomic and molecular physics and derive a set of formally exact solutions for the molecular Schrödinger equation. After this, in Section 3.2, we present the adiabatic approximation, which is one of the most extensively used approaches in modern molecular physics. In addition, an alternative approach, the so-called diabatic approximation, is presented in Section 3.3. Finally, in Section 3.4.2 we present the standard labeling scheme for diatomic electronic molecular states.

3.1 The generic Hamiltonian of molecular physics

In case of a non-relativistic, field free molecular system we are faced with an ensemble of the atoms electrons and nuclei which interact via Coulomb interaction. Considering the atomic nuclei as positively charged point particles with charges Z_i , we obtain the following ab-initio Hamiltonian of atomic and molecular systems

$$\begin{aligned} H_{\text{mol}} = & \underbrace{\frac{1}{2m_e} \sum_{i=1}^{N_e} \mathbf{p}_i^2}_{\text{elec. kinetic energy } T_e} + \underbrace{\sum_{j=1}^{N_n} \frac{1}{2M_j} \mathbf{P}_j^2}_{\text{nuclear kinetic energy } T_n} - \underbrace{\frac{1}{2} \sum_{i,j/i \neq j}^{N_e, N_n} \frac{Z_i}{|\mathbf{R}_i - \mathbf{r}_j|}}_{\text{nuclear-electron attraction } V_{en}} \\ & + \underbrace{\frac{1}{2} \sum_{i,j/i \neq j}^{N_e} \frac{1}{|\mathbf{r}_i - \mathbf{r}_j|}}_{\text{electron-electron repulsion } V_{ee}} + \underbrace{\frac{1}{2} \sum_{i,j/i \neq j}^{N_n} \frac{Z_i Z_j}{|\mathbf{R}_i - \mathbf{R}_j|}}_{\text{nuclear-nuclear repulsion } V_{nn}}. \end{aligned} \quad (3.1)$$

Solving the molecular eigenvalue problem

$$H_{\text{mol}} \Psi_{\text{mol}}(\underline{\mathbf{r}}, \underline{\mathbf{R}}) = \mathcal{E} \Psi_{\text{mol}}(\underline{\mathbf{r}}, \underline{\mathbf{R}}), \quad \underline{\mathbf{r}} \equiv (\mathbf{r}_1, \dots, \mathbf{r}_{N_e})^T, \quad \underline{\mathbf{R}} \equiv (\mathbf{R}_1, \dots, \mathbf{R}_{N_n})^T \quad (3.2)$$

provides the full dynamics on a large variety of problems, starting from non-relativistic few particle dynamics [108, 150] going to many body phenomena (BEC and solid state physics [8, 160–162], chemical reactions [163–165]), macroscopic systems and biophysics [166, 167]¹. However, except for few physical systems (i.e. for hydrogenic atoms [150]) this point of view is very naive because a full solution of Eq. (3.2) is technically impossible with today's computational equipment. For this reason a large variety of approximative schemes such as ab-initio Molecular Dynamics (AIMD) [169, 170], Hartree-Fock based methods (HF, MCTDH) [171–176], Monte-Carlo studies (MC) [177, 178], Density Functional Theory (DFT, TDDFT) [179–182] and Coupled Cluster Approaches [183–185] have been developed.

In this chapter we present a general ansatz to solve the Schrödinger equation for problems possessing several degrees of freedom. The ansatz is particularly efficient if the considered problem provides slow and fast degrees of freedom. In our specific problems we consider molecules where the

¹It is worth recalling Dirac's comment at this point, to the effect that all of chemistry is implicit in the diagonalization of this Hamiltonian, if we could but do the arithmetic [168].

nuclei and electronic degrees of freedom are considered to be the slow and fast degrees of freedom, respectively. Starting from Eq. (3.1) we define the electronic Hamiltonian H_{el} :

$$H_{\text{mol}} = T_{\text{n}} + V_{\text{nn}}(\underline{\mathbf{R}}) + H_{\text{el}}(\underline{\mathbf{r}}; \underline{\mathbf{R}}) \quad \text{with} \quad H_{\text{el}}(\underline{\mathbf{r}}; \underline{\mathbf{R}}) \equiv T_{\text{e}} + V_{\text{ee}}(\underline{\mathbf{r}}) + V_{\text{en}}(\underline{\mathbf{r}}, \underline{\mathbf{R}}). \quad (3.3)$$

Obviously, $H_{\text{el}}(\underline{\mathbf{r}}; \underline{\mathbf{R}})$ is an operator in the electronic configuration space that parametrically depends on the nuclear coordinates $\underline{\mathbf{R}}$. Its eigenvalues $\epsilon_i(\underline{\mathbf{R}})$ and eigenfunctions $\psi_i(\underline{\mathbf{r}}; \underline{\mathbf{R}})$ thus also parametrically depend on the nuclei degrees of freedom and fulfill

$$H_{\text{el}}\psi_i(\underline{\mathbf{r}}; \underline{\mathbf{R}}) = \epsilon_i(\underline{\mathbf{R}})\psi_i(\underline{\mathbf{r}}; \underline{\mathbf{R}}). \quad (3.4)$$

We note that although the electronic Hamiltonian $H_{\text{el}}(\underline{\mathbf{r}}; \underline{\mathbf{R}})$ was introduced using the ab-initio Hamiltonian given by Eq. (3.1). Equation (3.3) is more general as the electron-nuclei interaction $V_{\text{en}}(\underline{\mathbf{r}}, \underline{\mathbf{R}})$ can be also given by an effective potential, e.g. in case of electron-atom interaction. The set of electronic eigenfunctions form a complete and orthogonal basis in the electronic space at every value of $\underline{\mathbf{R}}$

$$\sum_i \psi_i^*(\underline{\mathbf{r}}'; \underline{\mathbf{R}})\psi_i(\underline{\mathbf{r}}; \underline{\mathbf{R}}) = \delta(\underline{\mathbf{r}} - \underline{\mathbf{r}}'), \quad \langle \psi_i(\underline{\mathbf{r}}; \underline{\mathbf{R}}) | \psi_j(\underline{\mathbf{r}}; \underline{\mathbf{R}}) \rangle_{\underline{\mathbf{r}}} = \delta_{ij}. \quad (3.5)$$

Here we have introduced an abbreviation for the integration over the electronic coordinates

$$\langle \psi_i(\underline{\mathbf{r}}; \underline{\mathbf{R}}) | A | \psi_j(\underline{\mathbf{r}}; \underline{\mathbf{R}}) \rangle_{\underline{\mathbf{r}}} \equiv \int d\underline{\mathbf{r}} \psi_i^*(\underline{\mathbf{r}}; \underline{\mathbf{R}}) A \psi_j(\underline{\mathbf{r}}; \underline{\mathbf{R}}). \quad (3.6)$$

where A denotes an arbitrary operator. To solve the Schrödinger equation Eq. (3.2) for the total molecular Hamiltonian we expand the total wave function $\Psi_{\text{mol}}(\underline{\mathbf{r}}; \underline{\mathbf{R}})$ using the electronic eigenfunction:

$$\Psi_{\text{mol}}(\underline{\mathbf{r}}, \underline{\mathbf{R}}) = \sum_i \phi_i(\underline{\mathbf{R}})\psi_i(\underline{\mathbf{r}}; \underline{\mathbf{R}}). \quad (3.7)$$

This expansion is known as the *Born-Oppenheimer expansion* [186]. Formally, this expansion is exact, since the set $\{\psi_i(\underline{\mathbf{r}}; \underline{\mathbf{R}})\}$ is a complete basis. Inserting this ansatz into Eq. (3.2) and using the definition of the electronic Hamiltonian in Eq. (3.3) we obtain

$$H_{\text{mol}} \sum_i \phi_i(\underline{\mathbf{R}})\psi_i(\underline{\mathbf{r}}; \underline{\mathbf{R}}) = \mathcal{E} \sum_i \phi_i(\underline{\mathbf{R}})\psi_i(\underline{\mathbf{r}}; \underline{\mathbf{R}}) \quad (3.8)$$

$$\Rightarrow (H_{\text{el}} + T_{\text{n}} + V_{\text{nn}}(\underline{\mathbf{R}})) \sum_i \phi_i(\underline{\mathbf{R}})\psi_i(\underline{\mathbf{r}}; \underline{\mathbf{R}}) = \mathcal{E} \sum_i \phi_i(\underline{\mathbf{R}})\psi_i(\underline{\mathbf{r}}; \underline{\mathbf{R}}). \quad (3.9)$$

Multiplying from the left side with $\psi_j(\underline{\mathbf{r}}; \underline{\mathbf{R}})$ and integrating over the electronic degrees of freedom we get the following equation:

$$(T_{\text{n}} + V_{\text{nn}}(\underline{\mathbf{R}}) + \epsilon_j(\underline{\mathbf{R}}))\phi_j(\underline{\mathbf{R}}) + \sum_i \Lambda_{ji}\phi_i(\underline{\mathbf{R}}) = \mathcal{E}\phi_j(\underline{\mathbf{R}}). \quad (3.10)$$

The operators Λ_{ji} are operators in $\underline{\mathbf{R}}$ space and given by

$$\Lambda_{ji}(\ast) = \langle \psi_j(\underline{\mathbf{r}}; \underline{\mathbf{R}}) | T_{\text{n}}(\ast) | \psi_i(\underline{\mathbf{r}}; \underline{\mathbf{R}}) \rangle_{\underline{\mathbf{r}}} - \delta_{ji}T_{\text{n}}(\ast). \quad (3.11)$$

They are the so-called *nonadiabatic couplings* and they describe the dynamical interaction between the electronic and nuclear motion. As it is shown in Appendix B.7 Eq. (3.10) can be rewritten as

a matrix equation

$$[(\nabla + F)^2 + V_{\text{adia}}(\underline{\mathbf{R}})]\phi(\underline{\mathbf{R}}) = \mathcal{E}\phi(\underline{\mathbf{R}}), \quad (\nabla + F)_{ij} = -\sum_k \frac{1}{2M_k} (\vec{\nabla}_{\mathbf{R}_k} \delta_{ij} + (F_k)_{ij}) \quad (3.12)$$

with $(F_k)_{ij} = \langle \psi_i(\mathbf{r}; \underline{\mathbf{R}}) | \vec{\nabla}_{\mathbf{R}_k} | \psi_j(\mathbf{r}; \underline{\mathbf{R}}) \rangle_{\mathbf{r}}$. We see that in this approach we are left with two problems. First, we have to solve the electronic problem Eq. (3.4) to obtain the full set of electronic eigenvalues and eigenvectors. After this, these are used to set up the set of coupled differential equations 3.12 to obtain the expansion coefficients $\phi_i(\underline{\mathbf{R}})$. Up to this point, the equation Eq. (3.4) together with Eq. (3.10) defines a exact solution scheme to obtain the molecular eigenfunctions (3.7). In Section 3.2 we present two approximate schemes to reduce the level of complexity.

3.2 Adiabatic and Born-Oppenheimer approximations

As a first approximation, the so-called *adiabatic approximation*, we neglect all coupling operators Λ_{ji} in (3.11) or the derivative coupling matrix F in (3.12), respectively. In this case the Schrödinger equations for the single nuclei wave function $\phi_i(\underline{\mathbf{R}})$ are decoupled and we get

$$(T_n + V_{\text{nn}}(\underline{\mathbf{R}}) + \epsilon_i(\underline{\mathbf{R}}))\phi_i(\underline{\mathbf{R}}) = \mathcal{E}_i\phi_i(\underline{\mathbf{R}}). \quad (3.13)$$

This equation is a time-independent Schrödinger equation for the nuclei dynamics where the electronic eigenenergies $\epsilon_i(\underline{\mathbf{R}})$ serves as an additional spatial potential to the direct nuclei-nuclei interaction $V_{\text{nn}}(\underline{\mathbf{R}})$. These potential surfaces Eq. (3.13) are called the *adiabatic potential energy surfaces*. The adiabatic approximation can be understood in such a way that due to the large differences between the electron and nuclei masses ($m_e/M_i \approx 10^{-3}-10^{-5}$) the electron configuration instantaneously adapts if the nuclei positions change. This means if the nuclei are not moving too fast (i.e. having too much kinetic energy in comparison to the energy gaps between the adiabatic states), the adiabatic approximation provides a good approximation. In other words, the electrons adiabatically follows the nuclear dynamics. In this approximation, the total molecular wave function Eq. (3.7) is simply a product $\Psi_{\text{mol}}(\mathbf{r}, \underline{\mathbf{R}}) = \phi(\underline{\mathbf{R}})\psi(\mathbf{r}, \underline{\mathbf{R}})$. In this case the electronic character does not change, this means it adiabatically follows the electronic eigenstate $\psi(\mathbf{r}, \underline{\mathbf{R}})$ and the molecule remains on a specific potential energy surface $\epsilon(\underline{\mathbf{R}})$. For this reason this specific ansatz for the wave function is called the *adiabatic ansatz*.

In a second approximation we include the diagonal coupling operator Λ_{ii} in Eq. (3.10) which leads to

$$(T_n + V_{\text{nn}}(\underline{\mathbf{R}}) + \epsilon_i(\underline{\mathbf{R}}) + \Lambda_{ii})\phi_i(\underline{\mathbf{R}}) = \mathcal{E}_i\phi_i(\underline{\mathbf{R}}). \quad (3.14)$$

This can be written as

$$(T_n + V_{\text{nn}}(\underline{\mathbf{R}}) + \tilde{\epsilon}_i(\underline{\mathbf{R}}))\phi_i(\underline{\mathbf{R}}) = \mathcal{E}_i\phi_i(\underline{\mathbf{R}}). \quad (3.15)$$

with

$$\tilde{\epsilon}_i(\underline{\mathbf{R}}) = \epsilon_i(\underline{\mathbf{R}}) + \sum_{k=1}^{N_n} \frac{1}{2M_k} \int d\mathbf{r} (\vec{\nabla}_{\mathbf{R}_k} \psi_i(\mathbf{r}; \underline{\mathbf{R}}))^2. \quad (3.16)$$

The additional term in Eq. (3.16) is a finite mass correction of the nuclei on the electron dynamics. As this term is of the order of the kinetic energy of the nuclei it just provides an minor contribution to adiabatic potential surfaces in case the nuclear dynamics is sufficiently slow. In case this term is included this scheme is called the *Born-Oppenheimer approximation* [187–191]. The potential surface Eq. (3.16) are called the *Born-Oppenheimer potential surfaces*. As it is in the adiabatic

approximation the electronic character of the eigenstate is not changed and the molecule remains adiabatically on a specific potential energy surface.

Finally, we note that the notation of the different approximation schemes as they have been presented in this paragraph is not unique in the literature. In this paragraph, we have adopted the notation scheme as it is presented in [187].

3.3 Diabatic potential surfaces

As we have discussed in Section 3.2 the electronic problem Eq. (3.4) together with Eq. (3.12) provide an exact solution scheme for the molecular dynamics. However, to obtain the full nuclear dynamics one has to consider the derivative coupling matrix F which couples the different nuclear wave functions and their derivatives. Neglecting F gives the adiabatic approximation (3.13), just considering diagonal derivative couplings provides the so called Born-Oppenheimer approximation (3.16). However, both approximation schemes become invalid in case the off-diagonal derivative couplings become sufficiently strong. As we show in Appendix B.7 this is the case when two adjacent adiabatic potential surfaces $\epsilon_i(\underline{\mathbf{R}})$ approach each other, in particular if we have

$$\left| \int d\underline{\mathbf{R}} \frac{\langle \phi_j(\underline{\mathbf{R}}) | \langle \psi_j(\mathbf{r}; \underline{\mathbf{R}}) | (\vec{\nabla}_{\underline{\mathbf{R}}_k} H_{\text{el}}) | \psi_i(\mathbf{r}; \underline{\mathbf{R}}) \rangle_{\mathbf{r}} | \phi_i(\underline{\mathbf{R}}) \rangle}{\langle \phi_j(\underline{\mathbf{R}}) | \vec{\nabla}_{\underline{\mathbf{R}}_k} | \phi_i(\underline{\mathbf{R}}) \rangle (\epsilon_i(\underline{\mathbf{R}}) - \epsilon_j(\underline{\mathbf{R}}))} \right| \geq 1. \quad (3.17)$$

The basic idea of diabaticization is to perform a unitary transformation to eliminate the derivative coupling terms in Eq. (3.12). To find this unitary transformation $U(\underline{\mathbf{R}})$ we define

$$\phi(\underline{\mathbf{R}}) = U(\underline{\mathbf{R}}) \tilde{\phi}(\underline{\mathbf{R}}). \quad (3.18)$$

Inserting this into Eq. (3.12) we get (see Appendix B.7)

$$[(\nabla + \tilde{F})^2 + W(\underline{\mathbf{R}})] \tilde{\phi}(\underline{\mathbf{R}}) = \mathcal{E} \tilde{\phi}(\underline{\mathbf{R}}) \quad \text{with} \quad \tilde{F} = U^\dagger (FU + \nabla U), \quad W(\underline{\mathbf{R}}) = U^\dagger V_{\text{adia}}(\underline{\mathbf{R}}) U. \quad (3.19)$$

Obviously the transformed derivative coupling matrix \tilde{F} vanishes if the unitary transformation U fulfills the differential matrix equation

$$\nabla U = -FU. \quad (3.20)$$

We get the *diabatic* Schrödinger equation

$$[\nabla^2 + V_{\text{dia}}(\underline{\mathbf{R}})] \tilde{\phi}(\underline{\mathbf{R}}) = \mathcal{E} \tilde{\phi}(\underline{\mathbf{R}}) \quad (3.21)$$

where we have defined $W(\underline{\mathbf{R}}) \equiv V_{\text{dia}}(\underline{\mathbf{R}})$. This matrix is the so called *diabatic potential matrix*. After the unitary transformation with U the differential equations of the diabatic wave functions $\tilde{\phi}_i(\underline{\mathbf{R}})$ are still coupled because the diabatic potential matrix $V_{\text{dia}}(\underline{\mathbf{R}})$ is, in general, non-diagonal. In case the off-diagonal couplings are neglected the single diabatic nuclei functions are determined by

$$(T_n + \epsilon_{\text{dia}}^{(i)}(\underline{\mathbf{R}})) \tilde{\phi}_i(\underline{\mathbf{R}}) = \mathcal{E}_i \tilde{\phi}_i(\underline{\mathbf{R}}) \quad \text{with} \quad \epsilon_{\text{dia}}^{(i)}(\underline{\mathbf{R}}) = [V_{\text{dia}}(\underline{\mathbf{R}})]_{ii}. \quad (3.22)$$

The functions $\epsilon_{\text{dia}}^{(i)}(\underline{\mathbf{R}})$ are often referred to as the *diabatic potential surfaces*. We note that a solution U of Eq. 3.20 does not exist in general. For this reason strictly diabatic states do not exist in the general case. However, a number of approximate schemes have been developed providing so-called "pseudo-" or "quasi-diabatic potential surfaces" [192].

3.4 Diatomic molecules

3.4.1 Diatomic potential curves

As the ab-initio molecular Hamiltonian (3.1) is translational invariant the total momentum is a conserved quantity. This means that the center of mass dynamics can be separated from H_{el} . In case of a diatomic molecule we transform the electronic and nuclei degrees of freedom (\mathbf{r}, \mathbf{R}) by introducing the center of mass vector \mathbf{R}_{cm} and the relative vectors with respect to an arbitrary chosen nucleus:

$$\mathbf{R}_{\text{cm}} = \frac{1}{\mathcal{M}} \left(m_e \sum_{i=1}^{N_e} \mathbf{r}_i + \sum_{k=A,B} M_k \mathbf{R}_k \right), \quad \mathbf{R} = \mathbf{R}_A - \mathbf{R}_B, \quad \mathbf{x}_i = \mathbf{r}_i - \mathbf{R}_B, \quad \mathcal{M} = N_e m_e + M_A + M_B.$$

In the new set of coordinates the molecular Hamiltonian is given by

$$H_{\text{mol}} = \frac{\mathbf{P}_{\text{cm}}^2}{2\mathcal{M}} + \frac{\mathbf{P}^2}{2M} + \frac{\mathbf{p}^2}{2\mu} + V_{\text{nn}}(R) + V_{\text{ee}}(\mathbf{x}) + V_{\text{en}}(\mathbf{x}, \mathbf{R}) \quad (3.23)$$

with $M = M_A M_B / (M_A + M_B)$ and $\mu = m_e (M_A + M_B) / \mathcal{M}$. We note that this Hamiltonian is only an approximation as it neglects so-called mass polarization terms $\sim \mathbf{p}_i \mathbf{p}_j$. These terms describe small fluctuations in the position of the center of mass and nuclei as the electrons move around within the molecule. Obviously, the center of mass dynamics is completely decoupled from the internal degree of freedom. The Hamiltonian governing the internal molecular dynamics is given by

$$H = \frac{\mathbf{P}^2}{2M} + \frac{\mathbf{p}^2}{2\mu} + V_{\text{nn}}(R) + V_{\text{ee}}(\mathbf{x}) + V_{\text{en}}(\mathbf{x}, \mathbf{R}) \equiv \frac{\mathbf{P}^2}{2M} + V_{\text{nn}}(R) + H_{\text{el}}(\mathbf{x}, \mathbf{R}). \quad (3.24)$$

We easily verify that H commutes with the total orbital angular momentum of the internal degrees of freedom $\mathbf{L}_{\text{tot}} = \mathbf{L}_{\mathbf{R}} + \mathbf{L}_{\mathbf{x}}$. As a consequence the adiabatic potential surfaces provided by the diagonalization of $H_{\text{el}}(\mathbf{x}, \mathbf{R})$ only depend on the internuclear distance R , i.e. $\epsilon(\mathbf{R}) = \epsilon(R)$. In this case the quantization axis for the electronic problem can be chosen along the internuclear axis.

3.4.2 Labeling of diatomic electronic states

The electronic states of atoms are classified by the total orbital angular momentum \mathbf{L} of all electrons. However, in case of a diatomic molecule the electron-nuclei interaction just possesses a rotational symmetry with respect to the internuclear axis. Therefore, only the projection of the total electronic orbital angular momentum is a conserved quantity and electronic states of a diatomic molecule are labeled with respect to its absolute value which is denoted with Λ . For $\Lambda = 0, 1, 2, \dots$ the states are labeled by capital Greek letters $\Sigma, \Pi, \Delta, \dots$. The state is further characterized by the total spin \mathbf{S} of all electrons which is given as multiplicity $2S + 1$. The orbital angular momentum and spin can be combined to the total angular momentum $\mathbf{J} = \mathbf{L} + \mathbf{S}$. Similar to the atomic notation [108] the z -component of \mathbf{J} denoted by $\Omega = |\Lambda + M_s|$, $M_s = -S, \dots, S$ is used to label the electronic state. The preliminary labeling scheme reads as $^{2S+1}\Lambda_{\Omega}$.

As the general diatomic Hamiltonian commutes with several symmetry operations, the symmetry of the wave function with respect to these operators is used to classify an electronic molecular state in addition. First we verify that a diatomic molecule has one ∞ -fold rotation axis (C_{∞}) along the molecular axis. This means there exist an infinite number of mirror planes ν containing this axis. The operation appropriate to these planes is reflection σ_{ν} . As $\sigma_{\nu}^2 = 1$ the electronic wave functions possess an even/odd parity with respect to a reflection at an arbitrary plane containing the internuclear axis.

All diatomic molecules possess the reflection symmetries just discussed. When, in addition, the

molecule is homonuclear, an additional symmetry operation is present, that of inversion of all electrons at the nuclei center of mass. The corresponding operator is denoted as I . By virtue of the same sort of arguments as given for the reflection symmetries, this operation has eigenvalues ± 1 and the electronic states possess an even/odd parity with respect to the inversion operation. The parity of the wavefunction is given as subscript to the electronic state: "g" for symmetric (German "gerade") or "u" for antisymmetric (German "ungerade") states.

Finally, electronic states are also often identified by an empirical single-letter label. The ground state is labeled X , excited states of the same multiplicity are labeled in ascending order of energy with capital letters $A, B, C\dots$. Excited states having multiplicity different from the ground state are labeled with lower-case letters $a, b, c\dots$. In total the labeling scheme of a diatomic molecular state thus reads as

$$[X, A, B, a, b, \dots]^{2S+1}\Lambda_{\Omega,(g,u)}^{(\pm)}. \quad (3.25)$$

Part II

Ultralong-range molecules in external fields

Chapter 4

The molecular system

In this chapter we start the analysis of the considered molecular diatomic system. In Section 4.1 we start with the derivation of the general working Hamiltonian which will be the foundation throughout this work. Section 4.2 provides a detailed discussion of the field-free system. We derive some results which already been presented in the works of C. H. Greene *et al.* [85]. Beyond this, we present novel approaches to derive perturbative results and we discuss the results of beyond perturbation theory analysis.

4.1 The working Hamiltonian

Before we derive the Hamiltonian of ultralong-range diatomic Rydberg molecules in external fields we discuss the field-free system. If we consider a homonuclear molecules consisting of two ^{87}Rb atoms, the abinitio molecular Hamiltonian is given by Eq. (3.1) with $Z_{\text{Rb}} = 37e$, $m_{^{87}\text{Rb}} = 159,732m_e$ and $N_e = 74$. This problem is a many particle problem and the electronic states which provide the ultralong-range Rydberg molecules are of very high excitation. However, the problem can be reduced to an effective few particle problem. As discussed in Section 3.4.2 the electronic states of the Rb_2 molecule possess a defined parity denoted by “gerade” and “ungerade”. For a trilobite molecule, the gerade and ungerade states $\Sigma_{g,u}$ are nearly degenerate as the rotational constant of this molecules is small due to the huge spatial separation. Any perturbation can mix the nearly degenerate states of opposite parity. This leads to the formation of charged separated states that possess a molecular frame dipole moment. The parity splitting can be estimated by calculating the time required for the electron centered on the perturber to tunnel to the Rydberg ion core. The time required for the electron to tunnel is orders of magnitudes longer than the lifetime of the universe, indicating a ridiculously small splitting between the states of different parities ($\sim\text{kHz}$) [85]. For this reason the effective physical model is given by a highly excited Rydberg atom and ground state atom. Considering the single positively charged ionic Rydberg core as a point particle, the effective model is a three-particle system.

This means the setup considered throughout this thesis consists of a Rydberg atom and a ground state rubidium $^{87}\text{Rb}(5S)$ atom in time-independent electric and magnetic fields. In particular, the lab-frame Hamiltonian is given by

$$H_{\text{mol}} = \frac{\mathbf{p}_{\text{n}}^2}{2m_{\text{n}}} + \sum_{i=e,c} \left\{ \frac{1}{2m_i} (\mathbf{p}_i - q_i \mathbf{A}(\mathbf{r}_i))^2 + q_i \Phi(\mathbf{r}_i) + V_{\text{in}}(\mathbf{r}_i, \mathbf{r}_{\text{n}}) \right\} + V_{\text{ec}}(\mathbf{r}_e, \mathbf{r}_c). \quad (4.1)$$

Throughout this work we consider homogeneous fields. In this case the electrostatic potential Φ and the magnetic vector potential \mathbf{A} in an arbitrary gauge are given by

$$\mathbf{A}(\mathbf{r}_i) = \frac{1}{2} \mathbf{B} \times \mathbf{r}_i + \vec{\nabla}_{\mathbf{r}_i} \Lambda(\mathbf{r}_i), \quad \Phi(\mathbf{r}_i) = -\mathbf{E} \cdot \mathbf{r}_i. \quad (4.2)$$

where Λ is an arbitrary gauge function. We use $q_c = -q_e = 1$ and get

$$H_{\text{mol}} = \frac{\mathbf{p}_{\text{n}}^2}{2m_{\text{n}}} + \frac{1}{2m_c} (\mathbf{p}_c - \frac{1}{2} \mathbf{B} \times \mathbf{r}_c - \vec{\nabla}_{\mathbf{r}_c} \Lambda(\mathbf{r}_c))^2 + \frac{1}{2m_e} (\mathbf{p}_e + \frac{1}{2} \mathbf{B} \times \mathbf{r}_e + \vec{\nabla}_{\mathbf{r}_e} \Lambda(\mathbf{r}_e))^2 + \mathbf{E} \cdot (\mathbf{r}_e - \mathbf{r}_c) + V_{\text{en}}(\mathbf{r}_e - \mathbf{r}_{\text{n}}) + V_{\text{cn}}(\mathbf{r}_c - \mathbf{r}_{\text{n}}) + V_{\text{ec}}(\mathbf{r}_e - \mathbf{r}_c). \quad (4.3)$$

In the case of vanishing magnetic field the Hamiltonian (4.1) is translational invariant which leads the total momentum to be a conserved quantity. For finite magnetic field strength the translational symmetry is broken due to the spatial dependent vector potential \mathbf{A} given by Eq. (4.2). However, a novel quantity $\hat{\mathbf{K}}$ can be constructed which contains, apart the single particle momenta, magnetic field dependent terms:

$$\hat{\mathbf{K}} = \mathbf{p}_n + \mathbf{p}_e - \frac{1}{2}\mathbf{B} \times \mathbf{r}_e + \vec{\nabla}_e \Lambda(\mathbf{r}_e) + \mathbf{p}_c + \frac{1}{2}\mathbf{B} \times \mathbf{r}_c - \vec{\nabla}_c \Lambda(\mathbf{r}_c). \quad (4.4)$$

This quantity is the so-called *pseudomomentum* which commutes, by construction, with the total Hamiltonian (4.3) and defines a constant of motion. Generally, the pseudomomentum can be constructed for an arbitrary system of N charged particles with charges q_i and masses m_i . In this case it defines always a constant of motion. However, the components of $\hat{\mathbf{K}}$ do not commute, in general we have

$$[\hat{K}_\mu, \hat{K}_\nu] = i\epsilon_{\mu\nu\lambda} B_\lambda \sum_{i=1}^N q_i. \quad (4.5)$$

It is only for a neutral system ($\sum_i q_i = 0$) that the components of the pseudomomentum can be made sharp simultaneously. Obviously, this requirement is fulfilled in the considered system.

Next we transform the coordinates $\{\mathbf{r}_e, \mathbf{r}_c, \mathbf{r}_n\}$ of the three particles system into center of mass and relative coordinates. This means we transform the spatial coordinates and conjugated momenta into new quantities via

$$\{\mathbf{r}_e, \mathbf{r}_c, \mathbf{r}_n\} \rightarrow \{\mathbf{r}, \mathbf{R}, \mathbf{R}_{\text{cm}}\}, \quad \{\mathbf{p}_e, \mathbf{p}_c, \mathbf{p}_n\} \rightarrow \{\mathbf{p}, \mathbf{P}, \mathbf{P}_{\text{cm}}\}. \quad (4.6)$$

The relation between the positions and the momenta in the two systems is determined by

$$(\mathbf{r}, \mathbf{R}, \mathbf{R}_{\text{cm}})^T = X(\mathbf{r}_e, \mathbf{r}_c, \mathbf{r}_n)^T, \quad (\mathbf{p}, \mathbf{P}, \mathbf{P}_{\text{cm}})^T = (X^{-1})^T(\mathbf{p}_e, \mathbf{p}_c, \mathbf{p}_n)^T \quad (4.7)$$

with the transformation matrix $X \in \mathbb{R}^{3 \times 3}$ (see Fig. 4.1). We obtain

$$X = \begin{bmatrix} 1 & -1 & 0 \\ 0 & -1 & 1 \\ \frac{m_e}{\mathcal{M}} & \frac{m_c}{\mathcal{M}} & \frac{m_n}{\mathcal{M}} \end{bmatrix}, \quad X^{-1} = \begin{bmatrix} \frac{m_c+m_n}{\mathcal{M}} & -\frac{m_n}{\mathcal{M}} & 1 \\ -\frac{m_e}{\mathcal{M}} & -\frac{m_n}{\mathcal{M}} & 1 \\ -\frac{m_e}{\mathcal{M}} & \frac{m_e+m_c}{\mathcal{M}} & 1 \end{bmatrix} \quad (4.8)$$

where we have introduced the total mass $\mathcal{M} = m_e + m_c + m_n$. Obviously, the (\mathbf{r}, \mathbf{R}) are the relative position vectors of the electron and neutral perturber with respect to the ionic core. Throughout this thesis we denote r, ϑ, φ and R, θ, ϕ as the spherical coordinates for the electron and neutral perturber, respectively. This means

$$\mathbf{r} = \begin{pmatrix} r \sin(\vartheta) \cos(\varphi) \\ r \sin(\vartheta) \sin(\varphi) \\ r \cos(\vartheta) \end{pmatrix}, \quad \mathbf{R} = \begin{pmatrix} R \sin(\theta) \cos(\phi) \\ R \sin(\theta) \sin(\phi) \\ R \cos(\theta) \end{pmatrix}. \quad (4.9)$$

The vector \mathbf{R}_{cm} indicates the position vector of the center of mass. If we express the total molecular Hamiltonian (4.3) and the pseudomomentum $\hat{\mathbf{K}}$ in the new coordinates and use the fact that $\{H, \hat{K}_x, \hat{K}_y, \hat{K}_z\}$ forms a complete set of commuting observables we can express the total molecular wave function Ψ_{mol} as follows [79]

$$\Psi_{\text{mol}}(\mathbf{r}, \mathbf{R}, \mathbf{R}_{\text{cm}}) = \exp\left\{i \left(\mathbf{K} + \frac{1}{2}(\mathbf{B} \times \mathbf{r}) \right) \cdot \mathbf{R}_{\text{cm}} \right\} \Psi(\mathbf{r}, \mathbf{R}). \quad (4.10)$$

Here we consider, as we do throughout this thesis, the symmetric gauge $\mathbf{A} = \frac{1}{2}\mathbf{B} \times \mathbf{r}$. The vector

\mathbf{K} is the vector of eigenvalues of the components \hat{K}_i , $i = (x, y, z)$ of the pseudomomentum $\hat{\mathbf{K}}$. After some algebra (see Appendix B.2) we obtain the effective working Hamiltonian represented in the new coordinates

$$H_{\text{eff}} = \frac{\mathbf{K}^2}{2\mathcal{M}} + \frac{\mathbf{P}^2}{m_n} + \frac{1}{2m_e}(\mathbf{p} + \frac{1}{2}\mathbf{B} \times \mathbf{r})^2 + V_{\text{ec}}(\mathbf{r}) + \mathbf{E} \cdot \mathbf{r} + V_{\text{en}}(\mathbf{r}, \mathbf{R}) + V_{\text{cn}}(\mathbf{R}). \quad (4.11)$$

In this expression the first term $\mathbf{K}^2/2\mathcal{M}$ is just a constant contribution as the pseudomomentum $\hat{\mathbf{K}}$ is a constant of motion. In the following this term will be ignored. The electron-core interaction V_{ec} is simply given by the angular momentum dependent potential $V_l(r)$ which has been discussed in Section 1.3. In the case of the ionic rubidium core perturber interaction V_{cn} we consider an induced dipole interaction due to the polarization of the ground state rubidium atom in the field of the singly positive charged ionic core:

$$V_{\text{cn}}(R) = -\frac{\alpha_{\text{Rb}}}{2R^4}. \quad (4.12)$$

The quantity α_{Rb} denotes the ground state polarizability of the ground state rubidium atom. As this potential decreases as $1/R^4$ it only provides a sufficiently large contribution for small radial distances R ($R < 100$ a.u.). As we are interested in the properties of ultralong-range diatomic molecules, e.g. large internuclear separations R , we can safely ignore this term. The electron-atom interaction V_{en} is considered to be a low-energy scattering interaction as it is discussed in Chapter 2. Finally, we obtain the working Hamiltonian

$$H = \frac{\mathbf{P}^2}{m_n} + \frac{1}{2m_e}(\mathbf{p} + \frac{1}{2}\mathbf{B} \times \mathbf{r})^2 + V_l(r) + V_{\text{en}}(\mathbf{r}, \mathbf{R}) + \mathbf{E} \cdot \mathbf{r}. \quad (4.13)$$

4.2 The field-free system

In this Section we present the analysis of the field-free ultralong-range diatomic Rydberg molecules. First, we derive and discuss results considering only a pure s -wave electron-perturber interaction. These studies had been first published by C. H. Greene *et al.* in 2000 [85]. Hereafter, we consider the p -wave interaction potential as well [86]. In addition to the exact results obtained within perturbation theory we present an approximative analysis which just considers the energy dependence of the s - and p -wave phase shifts $\delta_l(k)$, $l = 0, 1$. Finally, we discuss the results of beyond perturbation theory studies.

4.2.1 Trilobite states

Before considering ultralong-range Rydberg molecules in combined external fields we first analyze the properties of the field-free species. In this case the Hamiltonian of a single molecule (see Eq. (4.13)) is given by

$$\begin{aligned} H &= \frac{\mathbf{P}^2}{m_n} + \frac{\mathbf{p}^2}{2} + V_l(r) + 2\pi A[k(R)]\delta(\mathbf{r} - \mathbf{R}) + 6\pi A_p^3[k(R)]\overleftarrow{\nabla}_{\mathbf{r}}\delta(\mathbf{r} - \mathbf{R})\overrightarrow{\nabla}_{\mathbf{r}} \\ &\equiv \frac{\mathbf{P}^2}{m_n} + H_{\text{el}}(\mathbf{r}; \mathbf{R}). \end{aligned} \quad (4.14)$$

In Fig. 4.1 we show the setup for the field-free diatomic molecule. Because $m_n/m_e \approx 1.6 \times 10^5$ we can apply the Born-Oppenheimer approximation and calculate the adiabatic potential curves $\epsilon(\mathbf{R})$ with $H_{\text{el}}(\mathbf{r}; \mathbf{R})\psi(\mathbf{r}; \mathbf{R}) = \epsilon(\mathbf{R})\psi(\mathbf{r}; \mathbf{R})$ (see Section 3.2). Because of the rotational invariance of the electronic Hamiltonian H_{el} the adiabatic potential surface only depend on the radial distance $R = |\mathbf{R}|$ between the perturber and the ionic rubidium core (see Appendix B.5.1). Due to this we chose the internuclear axis to coincide with the z -axis of the coordinate system, e.g. $\mathbf{R} = (\theta =$

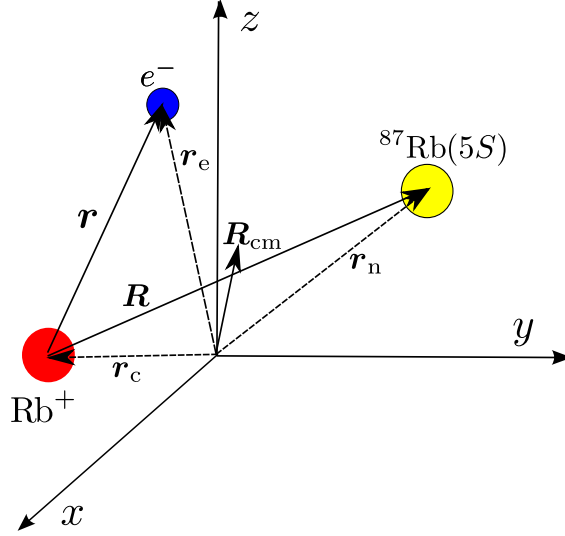


Figure 4.1: A sketch of the field-free system in the laboratory frame. The molecular constituents are a singly positive charged ionic rubidium core (Rb^+), the Rydberg electron (e^-) and a ground state rubidium atom ($^{87}\text{Rb}(5S)$).

$0, \phi = 0, R)^T$. Initially, we treat the interaction because of the neutral rubidium atom perturbatively with the high- l degenerate manifolds of the unperturbed Rydberg Hamiltonian H_0 . We calculate the adiabatic potential curve performing an exact diagonalization scheme using the hydrogenic eigenstates $\psi_{nlm}(\mathbf{r}) = R_{nl}(r)Y_{lm}(\vartheta, \varphi)$ of H_0 as a basis set to perform degenerate perturbation theory for the $-1/2n^2$ eigenenergy. Throughout the study of ultralong-range Rydberg molecules we consider the potential curves which emerge from the $n = 35$ hydrogenic manifold. The energy offset of all potential energy curves and higher dimensional surfaces is the dissociation limit of the atomic states $^{87}\text{Rb}(5S) + \text{Rb}$ ($n = 35, l \geq 3$).

Pure s-wave interaction

First we analyze the general properties of the s -wave scattering term (2.15). we calculate the matrix elements

$$\langle i | V_{\text{en}}^s(\mathbf{r}, \mathbf{R}) | j \rangle = 2\pi A_s[k(R)] \int d\mathbf{r} \phi_i^*(\mathbf{r}) \delta(\mathbf{r} - \mathbf{R}) \phi_j(\mathbf{r}) = 2\pi A_s[k(R)] \phi_i^*(\mathbf{R}) \phi_j(\mathbf{R}). \quad (4.15)$$

If we calculate the matrix representation of $V_s(\mathbf{r}, \mathbf{R})$ with respect to an arbitrary basis set $\{\phi_i(\mathbf{r})\}_{i=1, \dots, N}$ we can write this in the following way

$$V_{\text{en}}^s(\mathbf{r}, \mathbf{R}) = 2\pi A_s[k(R)] \psi(\mathbf{R}) \otimes \psi(\mathbf{R})^\dagger \quad \text{with} \quad \psi(\mathbf{R}) = (\phi_1(\mathbf{R}), \dots, \phi_N(\mathbf{R}))^T. \quad (4.16)$$

A matrix of such a form is known as a separable matrix. In Appendix B.6 we discuss and prove some basic properties of such matrices. One important result is that a separable matrix only possesses a single non zero eigenvalue where the vector $\psi(\mathbf{R})$ is the corresponding eigenvector. In the case of the s -wave scattering potential (4.15) the non zero eigenvalue ϵ_s is given by

$$\epsilon_s = 2\pi A_s[k(R)] \sum_{n=1}^N |\phi_n(\mathbf{R})|^2, \quad \psi_s(\mathbf{r}; \mathbf{R}) = \frac{1}{\sqrt{\sum_n |\phi_n(\mathbf{R})|^2}} \sum_n \phi_n^*(\mathbf{R}) \phi_n(\mathbf{r}). \quad (4.17)$$

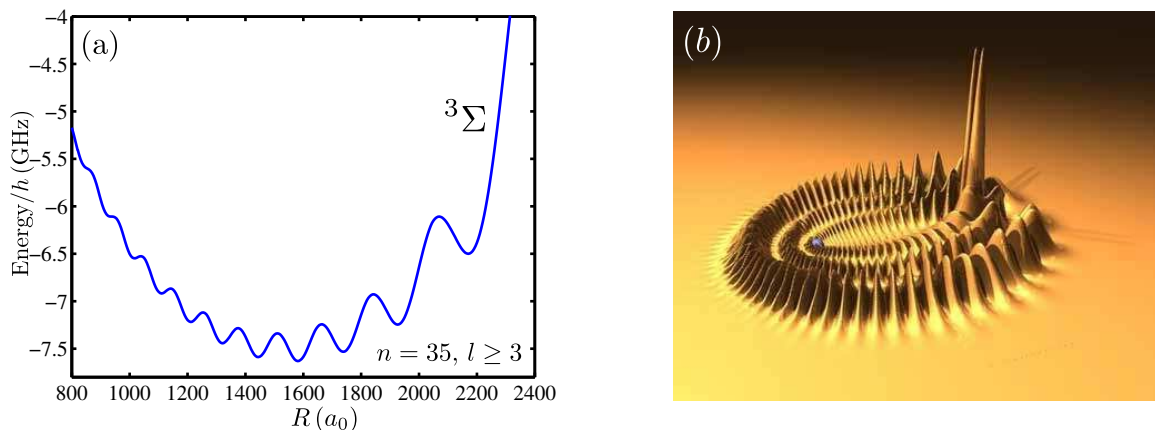


Figure 4.2: (a) Adiabatic potential curve ϵ_{35}^s for a purely s -wave dominated electron-perturber interaction. The shown curve stems from the $n = 35$, $l \geq 3$ degenerate hydrogenic manifold. The potential curve possesses a nodal structure providing potential wells with depth in the MHz regime. In (b) the electronic probability density is presented as a cylindrical surface plot $2\pi\rho|\psi_{30}^s(\rho, z, 0; \mathbf{R}_{\text{eq}})|^2$, $\mathbf{R}_{\text{eq}} = (\theta = 0, \phi = 0, R = 1232a_0)$ [85]. The position of the perturbing atom is directly underneath the density's double peak. The blueish sphere represented the Rb^+ ion.

In case we choose as an basis set to perform degenerate perturbation theory for the $-1/2n^2$ eigenenergy we have to diagonalize a matrix with following matrix elements

$$\langle \psi_{nl'm'}(\mathbf{r}) | V_{\text{en}}^s(\mathbf{r}, \mathbf{R}) | \psi_{nlm}(\mathbf{r}) \rangle_{\mathbf{r}} = 2\pi A_s[k(R)] \psi_{nl'm'}^*(\mathbf{R}) \psi_{nlm}(\mathbf{R}) \quad (4.18)$$

Because $\theta = 0$ we only obtain non zero matrix elements for $m' = m = 0$ which means the corresponding electronic state possess a $^3\Sigma$ symmetry. We get a separable matrix of dimension $n-3 \times n-3$ with eigenvalue and eigenvector

$$\epsilon_n^s(R) = \frac{1}{2} A[k(R)] \sum_{l=3}^{n-1} (2l+1) R_{nl}^2(R), \quad \psi_n^s(\mathbf{r}; \mathbf{R}) = \frac{1}{\sqrt{\sum_{lm} |\psi_{nlm}(\mathbf{R})|^2}} \sum_{lm} \psi_{nlm}^*(\mathbf{R}) \psi_{nlm}(\mathbf{r}). \quad (4.19)$$

In Fig. 4.2(a) the potential curve ϵ_{35}^s is depicted. This curves possesses a nodal structure with a global minimum at $R_{\text{eq}} \approx 1590a_0$. The depths of the single potential wells are of the order of several hundreds of MHz. The considered potential curve provided bound states with level spacings in the MHz regime [85]. The electronic density probability $|\psi_n^s(\mathbf{r}; \mathbf{R})|^2$ is characterized by a strongly oscillatory structure possessing a large density peak at the perturber position. In Fig. 4.2(b) the electronic density distribution $2\pi\rho|\psi_{30}^s(\rho, z, 0; \mathbf{R}_{\text{eq}})|^2$, $\mathbf{R}_{\text{eq}} = (\theta = 0, \phi = 0, R = 1232a_0)$ for $n = 30$ is presented as a cylindrical surface plot [85]. In order to obtain a symmetric density profile the density distribution is horizontally reflected at the z -axis. The position of the perturbing rubidium atom is directly underneath the double peak structure towards the right side of the figure. The Rb^+ ion is represented (with exaggerated size) as a small blueish sphere on the left. The region with appreciable density includes $700a_0 \leq z \leq 1700a_0$ and $\rho \leq 1200a_0$. As the probability distribution possesses the shape a trilobite¹ these states have become known as *trilobite states*.

Inclusion of p -wave interaction

In this paragraph we discuss the properties of the p -wave interaction term

$$V_p(\mathbf{r}, \mathbf{R}) = 6\pi A_p^3[k(R)] \overleftarrow{\nabla}_{\mathbf{r}} \delta(\mathbf{r} - \mathbf{R}) \overrightarrow{\nabla}_{\mathbf{r}}. \quad (4.20)$$

¹Trilobites are a fossil group of extinct marine arthropods which roamed the oceans for over 270 million years. They were among the most successful of all early animals and first appeared 571 million years ago [84].

Because the energy dependent p -wave scattering length just gives as spatial modulation we concentrate on the actual operator $\overleftarrow{\nabla}_{\mathbf{r}}\delta(\mathbf{r}-\mathbf{R})\overrightarrow{\nabla}_{\mathbf{r}}$. We calculate its matrix elements with respect to the Rydberg wave function $\psi_{nlm}(\mathbf{r}) = R_{nl}(r)Y_{lm}(\theta, \phi)$

$$\int d\mathbf{r}\psi_{n'l'm'}^*(\mathbf{r})\overleftarrow{\nabla}\delta(\mathbf{r}-\mathbf{R})\overrightarrow{\nabla}\psi_{nlm}(\mathbf{r}) = \overrightarrow{\nabla}\psi_{n'l'm'}^*(\mathbf{R}) \cdot \overrightarrow{\nabla}\psi_{nlm}(\mathbf{R}). \quad (4.21)$$

Using the spherical coordinate representation of the Nabla operator

$$\overrightarrow{\nabla} = \frac{\partial}{\partial R}\mathbf{e}_R + \frac{1}{R}\frac{\partial}{\partial\theta}\mathbf{e}_\theta + \frac{1}{R\sin(\theta)}\frac{\partial}{\partial\phi}\mathbf{e}_\phi \quad (4.22)$$

we get

$$\overrightarrow{\nabla}\psi_{nlm}(\mathbf{R}) = R'_{nl}(R)Y_{lm}(\theta, \phi)\mathbf{e}_R + \frac{R_{nl}(R)}{R}\frac{\partial}{\partial\theta}Y_{lm}(\theta, \phi)\mathbf{e}_\theta + \frac{imR_{nl}(R)Y_{lm}(\theta, \phi)}{R\sin(\theta)}\mathbf{e}_\phi. \quad (4.23)$$

In this expression we can rewrite the angular functions as follows

$$\begin{aligned} \frac{\partial}{\partial\theta}Y_{lm}(\theta, \phi) &= \frac{1}{2}\sqrt{\frac{2l+1}{4\pi}\frac{(l-m)!}{(l+m)!}}(P_{l,m+1}(\cos(\theta)) - (l+m)(l-m+1)P_{l-m+1}(\cos(\theta)))e^{im\phi} \\ &\equiv F_{lm}(\theta)e^{im\phi}, \end{aligned} \quad (4.24)$$

$$\begin{aligned} \frac{imY_{lm}(\theta, \phi)}{\sin(\theta)} &= -i\frac{1}{2}\sqrt{\frac{2l+1}{4\pi}\frac{(l-m)!}{(l+m)!}}(P_{l+1,m+1}(\cos(\theta)) \\ &\quad + (l-m+1)(l-m+2)P_{l+1,m-1}(\cos(\theta)))e^{im\phi} \\ &\equiv iH_{lm}(\theta)e^{im\phi}. \end{aligned} \quad (4.25)$$

In Appendix B.5.2 we prove the following properties of the functions F_{lm} and H_{lm}

$$F_{l,-m}(\theta) = (-1)^m F_{lm}(\theta), \quad H_{l,-m}(\theta) = (-1)^{m+1} H_{lm}(\theta). \quad (4.26)$$

We get for the matrix element Eq. (4.21)

$$\begin{aligned} \overrightarrow{\nabla}\psi_{n'l'm'}^*(\mathbf{R}) \cdot \overrightarrow{\nabla}\psi_{nlm}(\mathbf{R}) &= R'_{n'l'}(R)Y_{l'm'}^*(\theta, \phi)R'_{nl}(R)Y_{lm}(\theta, \phi) \\ &\quad + \frac{1}{R^2}R_{n'l'}(R)F_{l'm'}(\theta)R_{nl}(R)F_{lm}(\theta)e^{i(m-m')\phi} \\ &\quad + \frac{1}{R^2}R_{n'l'}(R)H_{l'm'}(\theta)R_{nl}(R)H_{lm}(\theta)e^{i(m-m')\phi}. \end{aligned} \quad (4.27)$$

All together we can write the interaction matrix $V_{\text{en}}^p(\mathbf{r}, \mathbf{R})$ as the sum off three single matrices

$$V_{\text{en}}^p(\mathbf{R}) = 6\pi A_p^3[k(R)](V_{\text{en}}^{p1}(\mathbf{R}) + V_{\text{en}}^{p2}(\mathbf{R}) + V_{\text{en}}^{p3}(\mathbf{R})). \quad (4.28)$$

We see that if we include the p -wave interaction term we have to sum up three additional matrices with matrix elements

$$\begin{aligned} 6\pi A_p^3[k(R)]\langle\psi_{n'l'm'}(\mathbf{r})|V_{\text{en}}^{p1}|\psi_{nlm}(\mathbf{r})\rangle_{\mathbf{r}} &= 6\pi A_p^3[k(R)]R'_{n'l'}(R)Y_{l'm'}^*(\theta, \phi)R'_{nl}(R)Y_{lm}(\theta, \phi), \\ 6\pi A_p^3[k(R)]\langle\psi_{n'l'm'}(\mathbf{r})|V_{\text{en}}^{p2}|\psi_{nlm}(\mathbf{r})\rangle_{\mathbf{r}} &= 6\pi A_p^3[k(R)]\frac{R_{n'l'}(R)R_{nl}(R)}{R^2}F_{l'm'}(\theta)F_{lm}(\theta)e^{i(m-m')\phi}, \\ 6\pi A_p^3[k(R)]\langle\psi_{n'l'm'}(\mathbf{r})|V_{\text{en}}^{p3}|\psi_{nlm}(\mathbf{r})\rangle_{\mathbf{r}} &= 6\pi A_p^3[k(R)]\frac{R_{n'l'}(R)R_{nl}(R)}{R^2}H_{l'm'}(\theta)H_{lm}(\theta)e^{i(m-m')\phi}. \end{aligned}$$

Because $\mathbf{R} = (\theta = 0, \phi = 0, R)^T$ we only get non-vanishing matrix elements for $m = 0, \pm 1$. Hereby the $m = 0$ and $|m| = 1$ blocks are decoupled defining the ${}^3\Sigma$ and ${}^3\Pi$ molecular symmetry sector, respectively.

- ${}^3\Sigma$ symmetry sector

In this subspace we have to diagonalize the s -wave interaction matrix as well as the first matrix of the p -wave interaction term V_{en}^{p1} .

$$[V_{\Sigma}(\mathbf{R})]_{l'l} = \frac{\sqrt{(2l'+1)(2l+1)}}{2} [A_s[k(R)]R_{nl'}(R)R_{nl}(R) + 3A_p^3[k(R)]R'_{nl'}(R)R'_{nl}(R)] \quad (4.29)$$

Obviously $V_{\Sigma}(R)$ is a sum of two separable matrices which means it is not separable itself. As a first approach we diagonalize $V_{\Sigma}(R)$ numerically. However, as $\text{rank}(V_{\text{en}}^s + V_{\text{en}}^{p1}) \leq 2$ we expect two different adiabatic potential curves. In case the energetic separation of both interaction terms is sufficiently large we can diagonalize both matrices separately. Beside the s -wave potential curve (4.19) we obtain a second potential curve ϵ_n^{p1} with

$$\epsilon_n^{p1}(R) = \frac{3}{2} A_p^3 [k(R)] \sum_{l=3}^{n-1} (2l+1)(l+1)l(R'_{nl}(R))^2 \quad (4.30)$$

and the corresponding eigenstate

$$\psi_n^{p1}(\mathbf{r}; \mathbf{R}) = \frac{1}{\sum_{lm} (R'_{nl}(R))^2 |Y_{lm}(\theta, \phi)|^2} \sum_{lm} R'_{nl}(R) Y_{lm}^*(\theta, \phi) \psi_{nlm}(\mathbf{r}). \quad (4.31)$$

In Fig. 4.3(a) we present the ${}^3\Sigma$ potential curves for the $n = 35$, $l \geq 3$ hydrogenic manifold. As expected due to the inclusion of the p -wave interaction term V_{en}^{p1} a novel potential splits away from the $n-4$ degenerate manifold. The novel potential curve which is denoted as $A^3\Sigma$ in Fig. 4.3(a) energetically moves downwards as the spatial separation R decreases for $R \geq 1400a_0$ (green solid curve). The other potential curve which is denoted by $X^3\Sigma$ is the former ϵ_{35}^s curve (blue solid line). For $R \geq 1450a_0$ the curves are energetically separated and purely dominated by s - and p -wave character, respectively. In the region around $R = 1525a_0$ we clearly see an avoided crossing of the two potential curves. This means for spatial separations $R \leq 1525a_0$ the character of the two potential curves have switched. Here $X^3\Sigma$ is p -wave dominated whereas $A^3\Sigma$ possesses a strong s -wave character.

- ${}^3\Pi$ symmetry sector

In this subspace we have to diagonalize the sum $V_{\Pi}(R)$ of the second and third p -wave interaction matrix $V_{\text{en}}^{(p2)}$ and $V_{\text{en}}^{(p3)}$ in Eq. 4.28, respectively. However, in Appendix B.5.2 we prove that

$$[V_{\text{en}}^{p2}, V_{\text{en}}^{p3}] = 0, \quad (4.32)$$

which means that these two matrices can be diagonalized simultaneously. Again, V_{en}^{p2} and V_{en}^{p3} are separable matrices and can be diagonalized analytically. We obtain a doubly degenerate potential curve with

$$\epsilon_n^{p2}(R) = \epsilon_n^{p3}(R) = \frac{3}{16\pi} A_p^3 [k(R)] \sum_{l=3}^{n-1} (2l+1)(l+1)lR_{nl}^2(R) \quad (4.33)$$

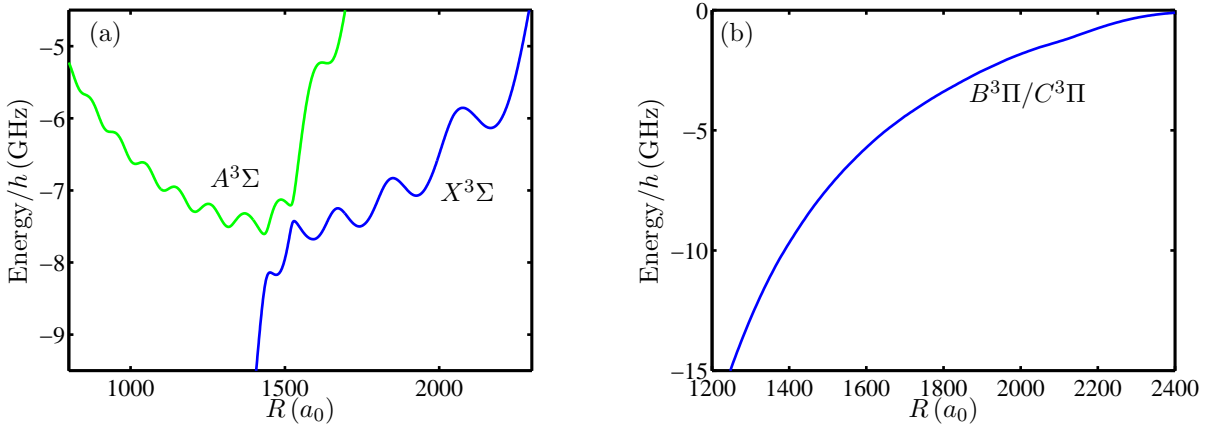


Figure 4.3: (a) $X^3\Sigma$ and $A^3\Sigma$ potential curves ϵ_{35}^s and ϵ_{35}^{p1} (blue and green lines, respectively) for the $n = 35$, $l \geq 3$ hydrogenic manifold. In the region $1400a_0 \leq R \leq 1600$ an avoided crossing is clearly visible. Figure (b) shows the $X^3\Pi$ and $A^3\Pi$ potential curves $\epsilon_{35}^{p2/3}$ which are degenerate. This curve is monotonically increasing possessing hardly any nodal structure.

and the corresponding eigenvectors

$$\psi_n^{p2}(\mathbf{r}; \mathbf{R}) = \frac{1}{\sqrt{\sum_{lm} R_{nl}^2(R) F_{lm}^2(\theta)}} \sum_{lm} R_{nl}(R) F_{lm}(\theta) e^{-im\phi} \psi_{nlm}(\mathbf{r}), \quad (4.34)$$

$$\psi_n^{p2}(\mathbf{r}; \mathbf{R}) = \frac{1}{\sqrt{\sum_{lm} R_{nl}^2(R) H_{lm}^2(\theta)}} \sum_{lm} R_{nl}(R) H_{lm}(\theta) e^{-im\phi} \psi_{nlm}(\mathbf{r}). \quad (4.35)$$

In Fig. 4.3(b) we present the $^3\Pi$ potential curve for the $n = 35$, $l \geq 3$ hydrogenic manifold. As a function of the spatial separation R this curve is monotonically increasing and possesses hardly any nodal structure.

4.2.2 Two-state analysis

In this paragraph we show that although the $^3\Sigma$ symmetry sector consists of two non commuting matrices V_{en}^s and V_{en}^{p1} the calculation of the corresponding potential curves in first order degenerate perturbation theory can be performed analytically. In Appendix B.6.2 we prove that the two potential curves $X^3\Sigma$ and $A^3\Sigma$ can be obtained analytically by the diagonalization of an effective electronic Hamiltonian $H_{\text{eff}}^{\text{el}}$ which acts on the reduced Hilbert space $\mathcal{H} = \text{span}\{|\psi_n^s(\mathbf{r}; R)\rangle, |\psi_n^{p1}(\mathbf{r}; R)\rangle\}$. Although $|\psi_n^s(\mathbf{r}; R)\rangle$, $|\psi_n^{p1}(\mathbf{r}; R)\rangle$ are linearly independent they are non orthogonal. For this reason we construct a orthonormal basis set $\{|\tilde{\psi}_n^s(\mathbf{r}; R)\rangle, |\tilde{\psi}_n^{p1}(\mathbf{r}; R)\rangle\}$ by applying the Gram-Schmidt process [193]. We get

$$|\tilde{\psi}_n^{p1}(\mathbf{r}; R)\rangle = \frac{|\psi_n^{p1}(\mathbf{r}; R)\rangle - C|\psi_n^s(\mathbf{r}; R)\rangle}{\sqrt{1 - C^2}}, \quad C = \langle\psi_n^s(\mathbf{r}; R)|\psi_n^{p1}(\mathbf{r}; R)\rangle_{\mathbf{r}}. \quad (4.36)$$

If $1_{\mathcal{H}} = |\psi_n^s(\mathbf{r}; R)\rangle\langle\psi_n^s(\mathbf{r}; R)| + |\tilde{\psi}_n^{p1}(\mathbf{r}; R)\rangle\langle\tilde{\psi}_n^{p1}(\mathbf{r}; R)|$ denotes the unity operator in the reduced Hilbert space \mathcal{H} the effective electronic Hamiltonian $H_{\text{eff}}^{\text{el}}$ is given by

$$H_{\text{eff}}^{\text{el}}(\mathbf{r}; R) = 1_{\mathcal{H}} H_{\text{el}}(\mathbf{r}; R) 1_{\mathcal{H}}.$$

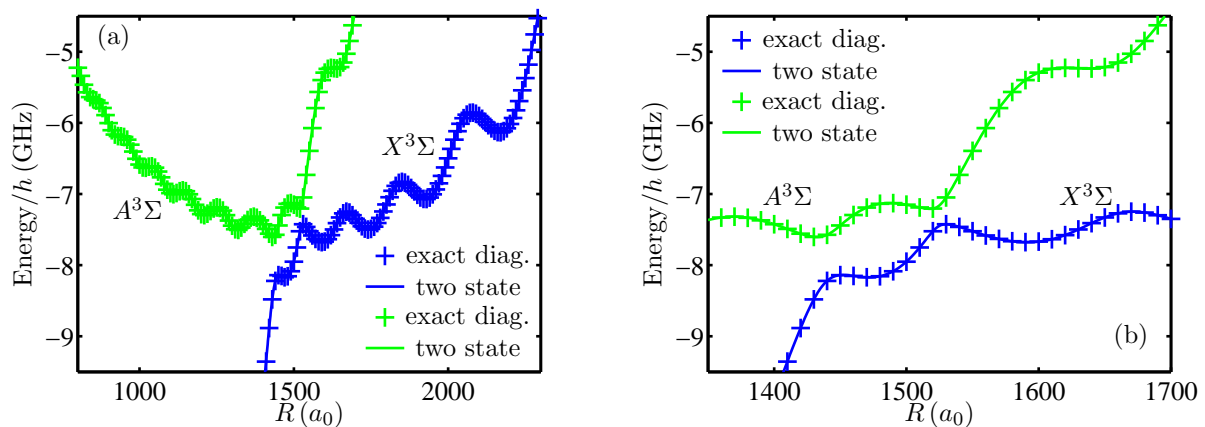


Figure 4.4: (a) shows the $X^3\Sigma$ and $A^3\Sigma$ potential curves obtained via exact diagonalization (blue and green crosses) in comparison with the potential curves obtained from the two state analysis (4.38) (blue and green solid lines). In (b) the spatial region around the avoided crossing $R \approx 1525a_0$ is enlarged. Obviously, the two state model provides a the same result as the exact diagonalization using hydrogenic eigenstates.

In the considered basis we obtain the matrix representation of $H_{\text{eff}}^{\text{el}}$

$$H_{\text{eff}}^{\text{el}} = \begin{bmatrix} \alpha_1 & g \\ g & \alpha_2 \end{bmatrix} \quad (4.37)$$

with

$$\begin{aligned} \alpha_1(R) \equiv \alpha_1 &= \epsilon_n^s + \langle \psi_n^s(\mathbf{r}; R) | V_{\text{en}}^{p_1}(\mathbf{r}; R) | \psi_n^s(\mathbf{r}; R) \rangle_{\mathbf{r}}, \\ \alpha_2(R) \equiv \alpha_2 &= \langle \tilde{\psi}_n^{p_1}(\mathbf{r}; R) | V_{\text{en}}^s(\mathbf{r}; R) + V_{\text{en}}^{p_1}(\mathbf{r}; R) | \tilde{\psi}_n^{p_1}(\mathbf{r}; R) \rangle_{\mathbf{r}}, \\ g(R) \equiv g &= \langle \psi_n^s(\mathbf{r}; R) | V_{\text{en}}^{p_1}(\mathbf{r}; R) | \tilde{\psi}_n^{p_1}(\mathbf{r}; R) \rangle_{\mathbf{r}}. \end{aligned}$$

This gives the following eigenvalues

$$\lambda_{1,2}(R) \equiv \lambda_{1,2} = \frac{\alpha_1 + \alpha_2}{2} \pm \frac{1}{2} \sqrt{(\alpha_2 - \alpha_1)^2 + 4g^2} \quad (4.38)$$

and eigenvectors

$$|\Lambda_{1,2}(R)\rangle \equiv |\Lambda_{1,2}\rangle = \frac{1}{\sqrt{(\lambda_{1,2} - \alpha_1)^2 + g^2}} \begin{bmatrix} g \\ \lambda_{1,2} - \alpha_1 \end{bmatrix}. \quad (4.39)$$

In Fig. 4.4(a,b) a comparison between the potential curves obtained via exact diagonalization (green and blue solid lines) and the curves obtained within the two state analysis (green and blue crosses) are shown. We clearly see that both approaches provide identical potential energy curves.

4.2.3 The Borodin-Kazansky model

An alternative approach to study the high angular momentum Born-Oppenheimer potential curves is to assume that due to the interaction with the neutral perturber two potential curves split away from the degenerate high- l manifold. Their expressions are obtained via the relation (1.19) between the quantum defect and the scattering phase

$$E_l^{(n)}(R) = -\frac{1}{2(n - \frac{\delta_l[k(R)]}{\pi})^2} \approx -\frac{1}{2n^2} - \frac{\delta_l[k(R)]}{\pi n^3}, \quad l = 0, 1. \quad (4.40)$$

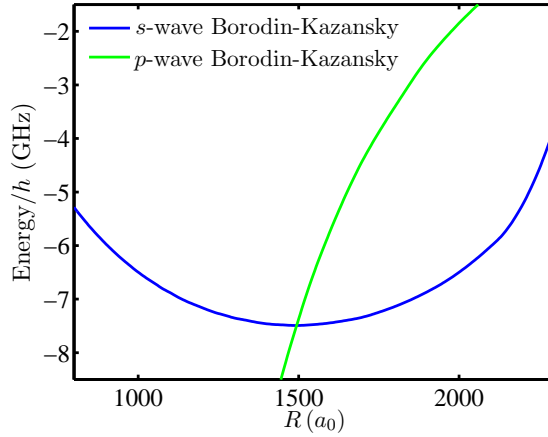


Figure 4.5: Adiabatic potential curves obtained within the Borodin-Kazansky model. The s -/ p -wave potential curve is represented by a solid blue / green line, respectively. Although the nodal structure is missing the global behavior of the potential curves is reproduced quite accurately. In Fig. 4.5 a comparison with the perturbative potential curves is shown.

This approach is known as the Borodin-Kazansky model [194]. Using Eq. (2.16) and (2.18) we obtain the following relations in the $k \rightarrow 0$ limit

$$E_0^{(n)}(R) = -\frac{1}{2n^2} + \frac{k}{\pi n^3} \left(a + \frac{\pi}{3} \alpha_n k \right), \quad E_1^{(n)}(R) = -\frac{1}{2n^2} - \frac{\alpha_n k^2}{15n^3}. \quad (4.41)$$

Using $k = \sqrt{2/R - 1/n^2}$ we get an analytic expression for the radial crossing position R_{cr}

$$k_{\text{cr}} = -\frac{3a}{2\pi\alpha_n} \Rightarrow R_{\text{cr}}^{(n)} = \frac{2n^2}{1 + \left(\frac{3a}{2\pi\alpha_n}\right)^2}. \quad (4.42)$$

We can calculate the radial position of the minimum of the s -wave potential curve as well. By differentiating Eq. (4.41) with respect to the internuclear distance R we obtain

$$\frac{d}{dR} E_0^{(n)}(R)|_{R=R_{\text{min}}} = \frac{d}{dR} \frac{k}{\pi n^3} \left(a + \frac{\pi}{3} \alpha_n k \right) |_{R=R_{\text{min}}^{(n)}} = 0 \Rightarrow R_{\text{min}}^{(n)} = \frac{2n^2}{1 + \left(\frac{3a}{2\pi\alpha_n}\right)^2}. \quad (4.43)$$

We get the interesting result that

$$R_{\text{min}}^{(n)} = R_{\text{cr}}^{(n)}. \quad (4.44)$$

This means that the two potential curves in the $^3\Sigma$ symmetry sector always possess an avoided crossing near the global minimum of the trilobite potential curve. This property is independent from the considered atomic species. In Fig. 4.5 the s - and p -wave potential curves obtained from the Borodin-Kazansky model (Eq. (4.40)) are presented for a principal quantum number $n = 35$. Within this model the nodal structure, as it is clearly visible in Fig. 4.3(a), is absent. However, the potential curves topologies are represented quite accurately. Similar to the pure s -wave scattering potential the s -wave curve (blue solid curve) possesses a global minimum at $R \approx 1500a_0$. The p -wave potential curve (green solid curve) monotonically decreases. As derived in Eq. (4.43) the two curve crosses each other exactly at the minimum of the s -wave potential curve. In the case of the Borodin-Kazansky model the s - and p -wave potential curves do not possess any avoided crossings.

In Fig. (4.6)(a,b) we present a comparison between the Borodin-Kazansky model and the potential curves obtained from perturbation theory. In Fig. 4.6(a) we clearly see that the Borodin-

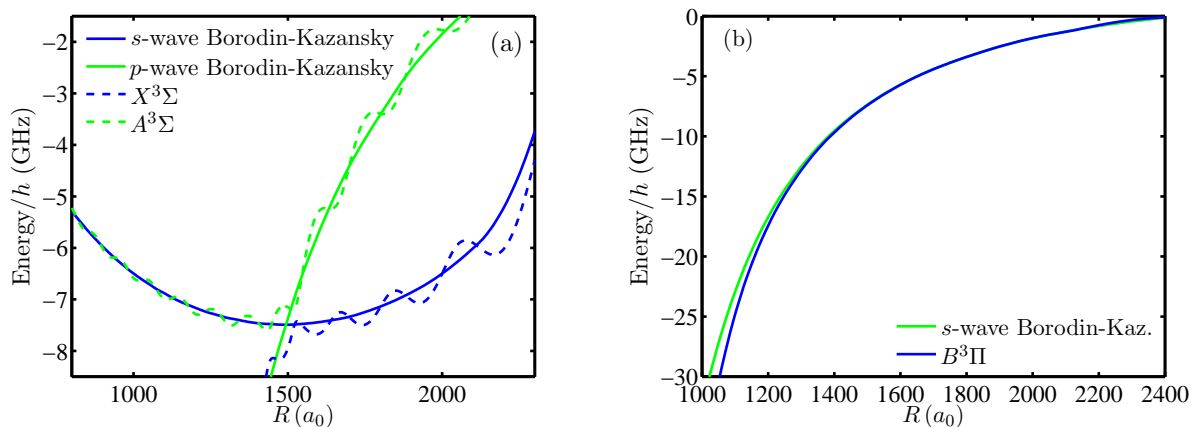


Figure 4.6: Figure (a) shows the s - and p -wave potential curves obtained within the Borodin-Kazansky model. In (b) we depict the Borodin-Kazansky curves in comparison with the potential curves in the $^3\Sigma$ symmetry sector.

Kazansky approach accurately reproduces the global behavior of the $^3\Sigma$ -curves obtained from perturbation theory. However, the strongly oscillating structure and the avoided crossing near the s -wave potential curve's minimum are not reproduced by the Borodin-Kazansky ansatz. In Fig. 4.6(b) we present the p -wave potential curve from the Borodin-Kazansky model (red solid line) with the $^3\Pi$ p -wave potential from perturbation theory (blue solid line). We clearly see that in the range of $1200a_0 \leq R \leq 2400a_0$ both potential curves match quite accurately, for $R \leq 1200a_0$ we find slight deviations between the two curves.

4.2.4 Inclusion of additional basis states

Every analysis we have performed so far was restricted to the degenerate hydrogenic manifold $n = 35$, $l \geq 3$. In this paragraph expand the considered basis set by systematically including basis states in the energetic vicinity of the considered hydrogenic manifold. For every single basis set we perform exact diagonalization in order to achieve convergence. As we are interested in studying the potential curve in the Σ symmetry sector we diagonalize $V_\Sigma = V_{\text{en}}^s + V_{\text{en}}^{p1}$ using the Rydberg wave functions $\psi_{nl0}(\mathbf{r})$. We obtain for the matrix elements

$$[V_\Sigma(\mathbf{r}, \mathbf{R})]_{n'l', nl} = \langle \psi_{n'l'0}(\mathbf{r}) | V_\Sigma(\mathbf{r}, \mathbf{R}) | \psi_{nl0}(\mathbf{r}) \rangle_{\mathbf{r}}, \quad \psi_{nl0}(\mathbf{r}) = R_{nl}(r) Y_{l0}(\vartheta, \varphi). \quad (4.45)$$

In the convergence study performed in this chapter we concentrate on the results for the $X^3\Sigma$ potential curve as the results of the $A^3\Sigma$ curve just differ quantitatively but not qualitatively.

We start our analysis by defining the basis sets (1)-(1c) in the energetic vicinity of the $n = 35$, $l \geq 3$ hydrogenic manifold as they are presented in Table 4.1. Hereby basis set (1) denotes the pure hydrogenic manifold while the other basis sets (1b) and (1c) contain the quantum defect states which lie below, respectively above the considered manifold. As discussed in Section 1.3.2 the atomic Rydberg states with $l = 0, 1, 2$ possesses a finite hyperfine splitting. However, this splitting is of the order of 200 MHz which is much less than the energetic separation of the Σ potential curves to these energy levels. For this reason, we neglect the spin-orbit coupling for these states and use the single electronic Rydberg nl states instead. In Fig. (4.7)(a) we present the potential energy curves which have been calculated using the different basis sets (1)-(1c). We see that the inclusion of the quantum defect states below and above the $n = 35$, $l \geq 3$ hydrogenic manifold hardly changes the $X^3\Sigma$ potential curve. In particular, with the inclusion of additional states, we obtain a relative deviation of 10^{-3} .

Next we start to include the neighbored degenerate hydrogenic manifolds as well as all the

basis set	hydrogenic manifold	quantum defect states
(1)	$n = 35, l \geq 3$	-
(1b)	$n = 35, l \geq 3$	$37p, 36d, 38s$
(1c)	$n = 35, l \geq 3$	$37p, 36d, 38s, 38p, 37d, 39s$

Table 4.1: Basis set (1)-(1b) in the energetic vicinity of the $n = 35, l \geq 3$ hydrogenic manifold. Basis set (1a) denote the pure hydrogenic manifold. Basis set (1b)((1c)) contain the quantum defect states which lie energetically below (above) the considered manifold.

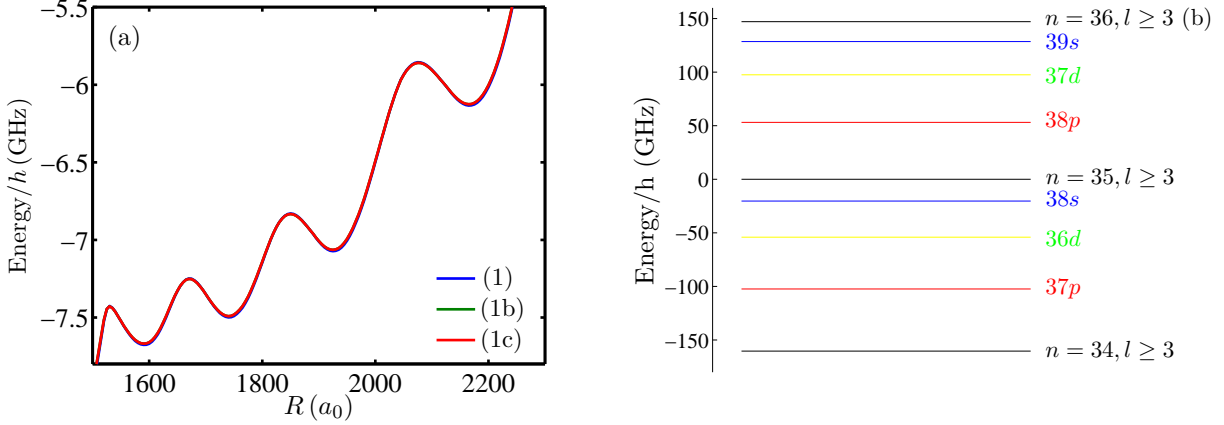


Figure 4.7: (a) Potential energy curves for the $n = 35, l \geq 3$ hydrogenic manifold calculated with the basis sets (1)-(1c) (see Table 4.1). We see that including the neighboring quantum defect states hardly changes the potential curve. Figure (b) shows the energetic level scheme for the basis set (2).

nearby quantum defect states. For this we define the basis sets (2)-(6) as they are presented in Table 4.2. These basis states are characterized by an integer number Δn which denotes the number of hydrogenic manifolds in the vicinity of the $n = 35$ manifold which are included into the basis set. For instance, $\Delta n = 1$ includes the $n = 34, l \geq 3$ till $n = 36, l \geq 3$ hydrogenic manifolds including all quantum defect states (see Section 1.3). In Fig. (4.7)(b) the energetic level scheme for the basis set (2) is shown. In Fig. 4.8 we present the potential energy curves which have been calculated using the basis sets (1)-(6). In contrast to the previous analysis now the curves show a strong energy shift with an increasing number of basis states. With increasing radial distance R the effect of including additional basis states becomes more dominant. Although we have included the states of five degenerate manifolds below and above the considered $n = 35, l \geq 3$ manifold we have not yet achieved convergence. To get a possible explanation for the observed level shift we remark

basis set	hydrogenic manifold	quantum defect states
(1)	$\Delta n = 0$	-
(2)	$\Delta n = 1$	$37p - 39s$
(3)	$\Delta n = 2$	$36p - 40s$
(4)	$\Delta n = 3$	$35p - 41s$
(5)	$\Delta n = 4$	$34p - 42s$
(6)	$\Delta n = 5$	$33p - 43s$

Table 4.2: Basis set (2)-(6) in the energetic vicinity of the $n = 35, l \geq 3$ hydrogenic manifold. The number Δn denote the range of hydrogenic manifolds which are taken into the basis set. All quantum defect states which lie between the hydrogenic manifolds are included (see 1.3 and Fig. 4.7(b)).

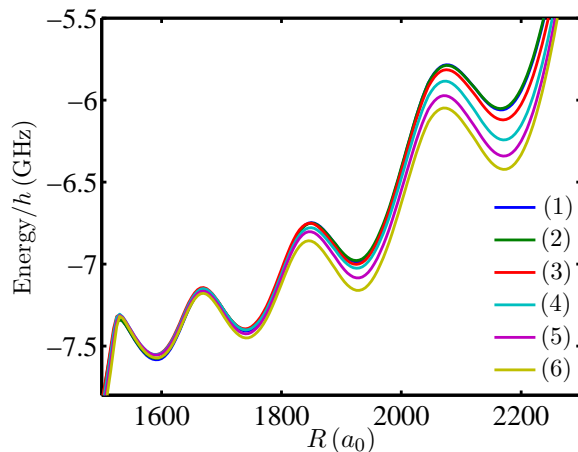


Figure 4.8: Potential energy curves calculated with the basis sets (1)-(6). With an increasing number of basis states the potential curve continues moving energetically downwards.

(a)	basis set	quantum defect states	(b)	basis set	hydrogenic manifolds
	(1)	-		(1)	$\Delta n = 0$
	(2) _{qds}	$37p - 39s$		(2) _{nqd}	$\Delta n = 1$
	(3) _{qds}	$36p - 40s$		(3) _{nqd}	$\Delta n = 2$
	(4) _{qds}	$35p - 41s$		(4) _{nqd}	$\Delta n = 3$
	(5) _{qds}	$34p - 42s$		(5) _{nqd}	$\Delta n = 4$
	(6) _{qds}	$33p - 43s$		(6) _{nqd}	$\Delta n = 5$

Table 4.3: In table (a) we present the basis sets which only include quantum defect states $n_{\min}p$ - $n_{\max}s$. In contrast table (b) only includes basis sets which contain degenerate hydrogenic manifolds with $n_{\min/\max} = 35 \pm \Delta n$.

that we can distinguish two different subsets of basis states. First, we have quantum defect states which are non degenerate. In contrast, the hydrogenic manifolds are highly degenerate possessing levels of degeneracy of $n - 3$. For this reason we conclude that the constant level shift observed in Fig. 4.8 is related to the inclusion of highly degenerate hydrogenic manifolds. To analyze this issue more systematically we perform additional studies where we define two novel basis sets which are presented in Table 4.3(a,b). The first basis set just contains the quantum defect states between the degenerate hydrogenic manifolds. The basis states are denoted as $(n)_{\text{qds}}$ (see Table 4.3(a)). The second analysis is performed with basis sets which only contain degenerate hydrogenic manifolds. These basis states are denoted as $(n)_{\text{nqd}}$ and labels the number of neighboring degenerate manifolds with minimal and maximal principal quantum number $n_{\min/\max} = 35 \pm \Delta n$ (see Table 4.3(b)). In Fig. 4.9(a) we present the potential curves which are obtained by exact diagonalization using the basis sets (1)-(6)_{qds}. Similar to the previous study using basis set (1)-(1c) (see Fig. 4.7(a)) the potential curves are hardly affected by increasing the number of basis states. Again we obtain relative deviations of 10^{-3} . In contrast in Fig. 4.9(b) we present the potential curves obtained from the diagonalization in the basis sets (1)-(6)_{nqd}. Here we obtain similar results to the study using the basis states (1)-(6). With increasing the number of degenerate hydrogenic manifolds, the potential curve continue to shift with a constant relative deviation up to 0.9. This strengthens the idea that the constant energy shift is caused by the mixing of the degenerate hydrogenic states by the contact interaction V_{en} . However, a satisfactory explanation of this behavior could not be found. For this reason we remark that this issue requires additional research. Throughout this thesis we have used a basis set consisting of the $n = 35$, $l \geq 3$ hydrogenic manifold and the $38s$, $36d$ and $37p$ states. As

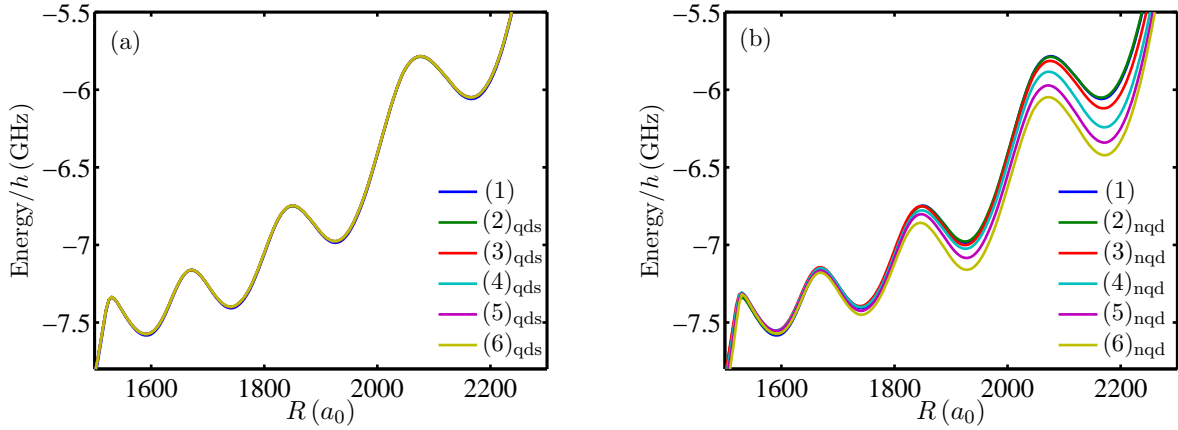


Figure 4.9: Figure (a) shows the potential curves obtained via exact diagonalization using the basis sets (1)-(6)_{qds}. Including additional basis states hardly affects the potential curves. Figure (b) shows the convergence studies using the basis states (1)-(6)_{nqd} only containing degenerate hydrogenic manifolds. Increasing the number of included hydrogenic manifolds causes the potential curves to shift energetically downwards.

we expect the Σ potential curves to lower in energy we have included the quantum defect states energetically below the hydrogenic $n = 35$, $l \geq 3$ manifold. In this case we denote the field free eigenstates as $|\Xi_i(\mathbf{r}; \mathbf{R})\rangle$, this means

$$H_{\text{el}}(\mathbf{r}; \mathbf{R})|\Xi_i(\mathbf{r}; \mathbf{R})\rangle = \epsilon_0^{(i)}(R)|\Xi_i(\mathbf{r}; \mathbf{R})\rangle. \quad (4.46)$$

For sufficiently large electric and magnetic field strengths we expect the energy level to approach cross each other. As we expect this regime to provided a plethora of interesting physics the inclusion of these states is essential.

Chapter 5

Electrically dressed ultralong-range Rydberg molecules

5.1 Introduction

In this chapter we perform a study of the impact of an electric field on the structure and dynamics of high- l ultralong-range diatomic Rubidium molecules. We hereby proceed as follows. Section 5.2 provides a formulation of the problem presenting the working Hamiltonian and a discussion of the underlying interactions. Our analysis goes beyond the s -wave approximation and takes into account the next order p -wave term of the Fermi-pseudopotential. Section 5.3 contains our methodology and a qualitative discussion of the effects of an external electric field strength. In Section 5.4 we analyze the evolution of the topology of the potential energy surfaces (PES) with varying electric field strength. Besides a numerical exact diagonalization scheme, we also study the PES in two approximative approaches. The resulting PES show a strongly oscillatory behavior with bound states in the MHz and GHz regime. With increasing field strength the diatomic molecular equilibrium distance shifts substantially in a range of the order of thousand Bohr radii. In Section 5.5 we analyze the behavior of the corresponding electric dipole moment. Thereby we realize molecular states with a dipole moment up to several kDebye. Based on these properties and the s -wave admixture via the external electric field a preparation scheme for high- l polar molecular electronic states via a two photon excitation process is presented. Finally, in Section 5.6 we provide an analysis of the vibrational spectra which exhibit spacings of the order of several MHz.

5.2 The setup

We consider a highly excited Rydberg atom interacting with a ground state neutral perturber atom (again we focus on the ^{87}Rb atom here) in a static and homogeneous electric field. The Hamiltonian treating the Rb ionic core and the neutral perturber as point particles is given by

$$H = \frac{\mathbf{P}^2}{m_n} + H_{\text{el}} + V_{\text{en}}(\mathbf{r}, \mathbf{R}), \quad H_{\text{el}} = H_0 + \mathbf{E} \cdot \mathbf{r}, \quad H_0 = \frac{\mathbf{p}^2}{2m_e} + V_l(r), \quad (5.1)$$

where $(m_n, \mathbf{P}, \mathbf{R})$ denote the atomic rubidium mass and the relative momentum and position of the neutral perturber with respect to the ionic core. $(m_e, \mathbf{p}, \mathbf{r})$ indicate the corresponding quantities for the Rydberg electron. The electronic Hamiltonian H_{el} consists of the field-free Hamiltonian H_0 and the usual Stark term of an electron in a static external \mathbf{E} -field. $V_l(r)$ is the angular momentum-dependent one-body pseudopotential felt by the valence electron when interacting with the ionic core. For low-lying angular momentum states the electron penetrates the finite ionic Rb^+ -core which leads to a l -dependence of the interaction potential $V_l(r)$ due to polarization and scattering effects [70]. Throughout this work we choose the direction of the field to coincide with the z -axis of the coordinate system, i.e. $\mathbf{E} = E\mathbf{e}_z$, $E \geq 0$. In Fig. 5.1 the setup of the molecular system is depicted. Finally, the interatomic potential V_{en} for the low-energy scattering between the Rydberg electron and the neutral perturber is described as a so-called Fermi-pseudopotential which is discussed in detail in Section 2.1.

$$V_{\text{en}}(\mathbf{r}, \mathbf{R}) = 2\pi A_s[k(R)]\delta(\mathbf{r} - \mathbf{R}) + 6\pi A_p^3[k(R)]\overleftarrow{\nabla}_{\mathbf{r}}\delta(\mathbf{r} - \mathbf{R})\overrightarrow{\nabla}_{\mathbf{r}}. \quad (5.2)$$

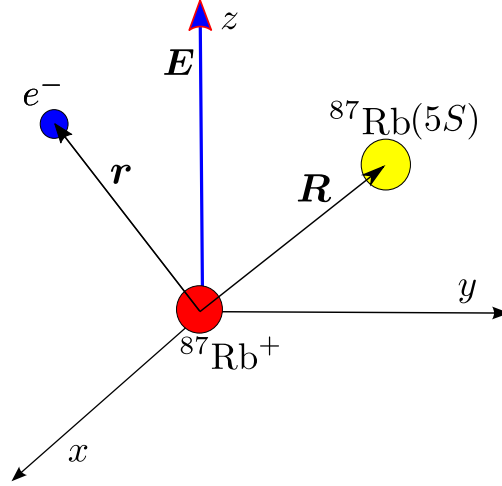


Figure 5.1: A sketch of the considered setup. An ultralong-range Rydberg molecule is exposed to an external electric \mathbf{E} -field. The molecule consists of a rubidium Rydberg atom (Rb^+ ionic core plus valence electron (e^-) and a neutral ground state atom (Rb), which interact via a low energy electron-atom scattering potential $V_{\text{en}}(\mathbf{r}, \mathbf{R})$. The \mathbf{E} -field points along the z -axis.

Here we consider the triplet ($S = 1$) scattering of the electron from the spin- $\frac{1}{2}$ ground state alkali atom. Suppression of singlet scattering events can be achieved by an appropriate preparation of the initial atomic gas. In Eq. (7.4) $A_s[k(R)] = -\tan(\delta_0(k))/k$ and $A_p^3[k] = -\tan(\delta_1(k))/k^3$ denote the energy-dependent triplet s - and p -wave scattering lengths, respectively, which are evaluated from the corresponding phase shifts $\delta_l(k)$, $l = 0, 1$. The kinetic energy $E_{\text{kin}} = k^2/2$ of the Rydberg electron at the collision point with the neutral perturber can be approximated according to $k^2/2 = 1/R - 1/2n^{*2}$. The behavior of the energy-dependent phase shifts δ_l as functions of the kinetic energy E_{kin} is shown in Fig. 2.1. If not stated otherwise, atomic units will be used throughout.

5.3 Methodology and symmetries

In order to solve the eigenvalue problem associated with the Hamiltonian (5.1) we adopt an adiabatic ansatz for the electronic and heavy particle dynamics. We write the total wave function as $\Psi(\mathbf{r}, \mathbf{R}) = \psi(\mathbf{r}; \mathbf{R})\phi(\mathbf{R})$ and obtain within the adiabatic approximation

$$[H_0 + \mathbf{E} \cdot \mathbf{r} + V_{\text{en}}(\mathbf{r}, \mathbf{R})]\psi_i(\mathbf{r}; \mathbf{R}) = \epsilon_i(\mathbf{R})\psi_i(\mathbf{r}; \mathbf{R}), \quad (5.3)$$

$$\left(\frac{\mathbf{P}^2}{m_{\text{n}}} + \epsilon_i(\mathbf{R})\right)\phi_{ik}(\mathbf{R}) = E_{ik}\phi_{ik}(\mathbf{R}), \quad (5.4)$$

where ψ_i describes the electronic molecular wave function in the presence of the neutral perturber for a given relative position \mathbf{R} and ϕ_{ik} determines the rovibrational state of the perturber. From Eqs. (5.3) and (5.4) we already deduce some symmetry properties of the states ψ , ϕ and the energies ϵ . If $P_{\mathbf{r}, \mathbf{R}, \mathbf{E}}$ denotes the generalized parity operator that transforms $(\mathbf{r}, \mathbf{R}, \mathbf{E}) \rightarrow (-\mathbf{r}, -\mathbf{R}, -\mathbf{E})$ we have $[H, P_{\mathbf{r}, \mathbf{R}, \mathbf{E}}] = [V_{\text{en}}(\mathbf{r}, \mathbf{R}), P_{\mathbf{r}, \mathbf{R}, \mathbf{E}}] = 0$. This means that the states Ψ , ψ and ϕ are parity (anti)symmetric and the PES fulfill $\epsilon(\mathbf{R}; \mathbf{E}) = \epsilon(-\mathbf{R}; -\mathbf{E})$.

To calculate the specific potential energy surfaces and analyze their properties we have applied different approaches. However, before we start with any specific analysis we try to determine the effects of the applied electric field by basic considerations. The neutral atom is point-like to a good approximation and its interaction with the Rydberg atom probes the highly excited electronic wave function locally in space, meaning that the highly oscillatory character of the Rydberg wave function is mapped onto the potential energy surface. This holds both for the absence and presence of an electric field. As discussed in Section 4.2.1 the topology of the adiabatic potential curve

is determined by the electronic density probability. In case the Rydberg electron is exposed to the electric field it feels an electrostatic force of magnitude $-E$. Due to this the electron orbits are shifted into the negative z -direction and the electron density increases in this region. As a consequence of this the former radial symmetric potential curves are rendered into two-dimensional potential energy surfaces (PES) with a global potential minimum along the negative z -direction. In addition, the PES possess an azimuthal symmetry, e.g. the vector defining the internuclear axis can, without loss of generality, be chosen to lie in the $x - z$ -plane. Throughout this chapter we are mostly interested in the properties of electrically dressed $X^3\Sigma$ potential surface. As this curve provides the known trilobite states in the field-free case (see Section 4.2.1) we denote the associated curves and two dimensional PES also as "trilobite curves" or "trilobite surfaces".

In particular, to calculate the field dressed potential energy surfaces we have first applied to approximative approaches. In the first place we analyze the one-dimensional potential curves parallel and antiparallel to the applied field direction using the analytic results from Section 4.2.2. Hereafter, we perform first order perturbation theory using the field-free states from Section 4.2.4 to analyze the complete two dimensional potential surfaces. Finally we calculate the PES by applying an exact diagonalization scheme. To calculate the specific the potential energy surface $\epsilon_i(\mathbf{R})$ we expand $\psi(\mathbf{r}; \mathbf{R})$ in the eigenbasis of H_0 , i.e. $\psi_i(\mathbf{r}; \mathbf{R}) = \sum_{nlm} C_{nlm}^{(i)}(\mathbf{R})\chi_{nlm}(\mathbf{r})$ with $H_0\chi_{nlm}(\mathbf{r}) = \varepsilon_{nl}\chi_{nlm}(\mathbf{r})$, $\chi_{nlm}(\mathbf{r}) = R_{nl}(r)Y_{lm}(\vartheta, \varphi)$. Finally, we have to solve the following eigenvalue problem

$$(\varepsilon_{nl} - \epsilon(\mathbf{R}))C_{nlm} + \sum_{n'l'm'} C_{n'l'm'}(E\langle nlm|z|n'l'm'\rangle\delta_{mm'} + \langle nlm|V_{\text{en}}(\mathbf{r}, \mathbf{R})|n'l'm'\rangle) = 0, \quad (5.5)$$

for which we use standard numerical techniques for the diagonalization of hermitian matrices.

5.4 Potential energy surfaces

5.4.1 Two-state analysis

At first we perform a two-state analysis as it is performed for the field-free molecular system in Section 4.2.2. As the spherical symmetry is broken we now have to consider the configurations $\theta = 0$ and $\theta = \pi$ separately. We use the two eigenstates $|\Lambda_1(\mathbf{r}; R, \theta)\rangle$ and $|\Lambda_2(\mathbf{r}; R, \theta)\rangle$ of the field-free system (see 4.2.2) to diagonalize the electronic Hamiltonian (5.3). Using these states we obtain two one-dimensional potential energy curves along the $\theta = 0, \pi$ direction, respectively. In particular we get

$$H_{\text{eff}}^{\text{el}}(E) = \begin{bmatrix} \lambda_1 + E\langle \Lambda_1(\mathbf{r}; R, \theta)|z|\Lambda_1(\mathbf{r}; R, \theta)\rangle_{\mathbf{r}} & E\langle \Lambda_1(\mathbf{r}; R, \theta)|z|\Lambda_2(\mathbf{r}; R, \theta)\rangle_{\mathbf{r}} \\ E\langle \Lambda_1(\mathbf{r}; R, \theta)|z|\Lambda_2(\mathbf{r}; R, \theta)\rangle_{\mathbf{r}} & \lambda_2 + E\langle \Lambda_2(\mathbf{r}; R, \theta)|z|\Lambda_2(\mathbf{r}; R, \theta)\rangle_{\mathbf{r}} \end{bmatrix} \quad (5.6)$$

We introduce the abbreviations $\langle \Lambda_i(\mathbf{r}; R, \theta)|z|\Lambda_j(\mathbf{r}; R, \theta)\rangle_{\mathbf{r}} \equiv \langle \Lambda_i|z|\Lambda_j\rangle$ and obtain the following expressions for the field dependent eigenvalues

$$\begin{aligned} \lambda_{1,2}(R; \theta, E) \equiv \lambda_{1,2}(E) &= \frac{\lambda_1 + \lambda_2 + E(\langle \Lambda_1|z|\Lambda_1\rangle + \langle \Lambda_2|z|\Lambda_2\rangle)}{2} \\ &\pm \frac{1}{2}\sqrt{(\lambda_2 - \lambda_1 + E(\langle \Lambda_1|z|\Lambda_1\rangle - \langle \Lambda_2|z|\Lambda_2\rangle))^2 + 4E^2\langle \Lambda_1|z|\Lambda_2\rangle^2} \end{aligned} \quad (5.7)$$

and eigenvectors

$$\begin{aligned} |\Lambda_{1,2}(R; \theta, E)\rangle &\equiv \quad (5.8) \\ |\Lambda_{1,2}(E)\rangle &= \frac{1}{\sqrt{(\lambda_{1,2}(E) - \lambda_1 - E\langle \Lambda_1|z|\Lambda_1\rangle)^2 + E^2\langle \Lambda_1|z|\Lambda_2\rangle^2}} \begin{bmatrix} E\langle \Lambda_1|z|\Lambda_2\rangle \\ \lambda_{1,2}(E) - \lambda_1 - E\langle \Lambda_1|z|\Lambda_1\rangle \end{bmatrix}. \end{aligned}$$

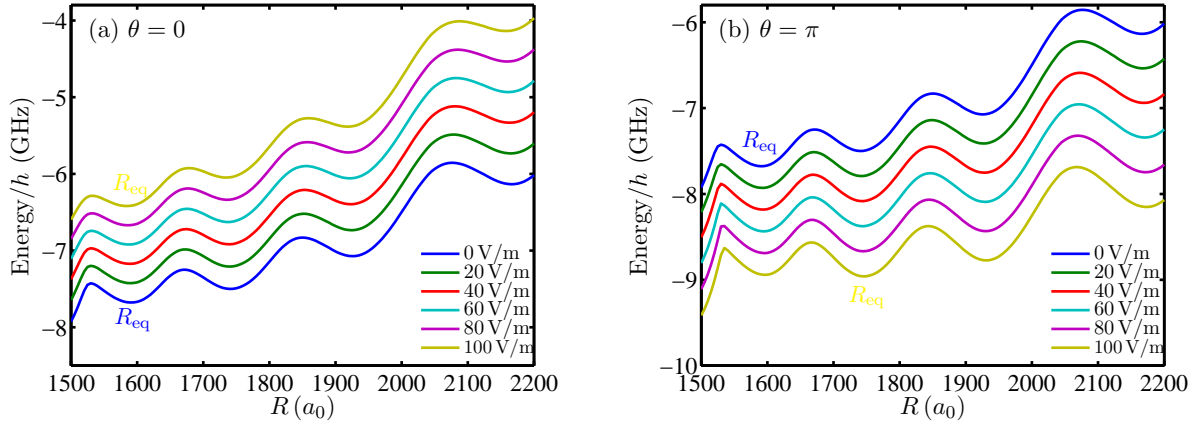


Figure 5.2: One dimensional potential curves along the $\theta = 0$ (a) and π direction (b) for applied field strength $E = 0, 20, 40, \dots, 100$ V/m obtained with the two-state model. For $\theta = 0$ the topology of the potential curves remain unchanged with increasing field strength E . The potential curves are energetically shifted by a constant factor of around 500 MHz. In contrast to this for $\theta = \pi$ the topology of the potential curve are field affected. For $E > 60$ V/m the radial equilibrium position R_{eq} is shifted.

The potential curve λ_1 corresponds to the field dressed trilobite curve in $\theta = 0$ and $\theta = \pi$ direction, respectively. In Fig. 5.2(a,b) we present $\lambda_1(E)$ calculated for electric field strengths of $E = 0, 20, 40, \dots, 100$ V/m in the $\theta = 0, \pi$ direction, respectively. In Fig. 5.2(a) we clearly see that for $\theta = 0$ the topology of the potential curves remain unchanged for the considered spatial distances $R \in [1500a_0, 2200a_0]$. As for the field-free case the region of avoided crossings is still localized near $R \approx 1525a_0$ for all applied field strength. The nodal structure of the field-free potential wells is still clearly visible, the radial positions of the local potential wells and their depths are hardly affected by the applied electric field. The potential curves are just shifted upwards by an approximately constant energy shift of around 500 MHz as the electric field strength is increased in steps of 20 V/m. This energy shift is more or less constant for all considered spatial distances $R \in [1500a_0, 2200a_0]$. In addition we indicate the equilibrium positions R_{eq} of the $E = 0$ V/m potential well (solid blue curve) and for the $E = 100$ V/m well (solid yellow curve). For all electric field strengths the global equilibrium positions of the potential wells remain constant. In Fig. 5.2(b) we see that for $\theta = \pi$ the potential curves move downwards as the electric field is increased. Up to an applied electric field strength of $E = 60$ V/m (solid cyan curve) the behavior of the shifted potential curves are qualitatively the same as for the $\theta = 0$ direction. The only difference is that in this case the potential curves are shifted by a constant magnitude of around 500 MHz downwards instead of upwards as it is can be seen in Figs. 5.2(a) and (b), respectively. However, for $E > 60$ V/m the behavior of the energetically shifted curves significantly change compared to $\theta = 0$ configuration. Beyond this particular electric field strength the global topology of the potential curves changes with increasing electric field. For instance, in case $E = 20$ V/m the topology of the field dressed potential curve (solid green curve) is still identical to the field-free curves topology (solid blue curve). For $E = 60$ V/m we recognize the first change in the curves topology in the sense that the energetic spacing between the two local potential wells at $R = 1600a_0$ and $R = 1750a_0$ has decreased (solid cyan curve). Increasing the electric field strength to $E = 80$ V/m to local potential minimum of the second curve ($R = 1750a_0$) is now deeper than the first well's potential minimum ($R = 1600a_0$). This means the energetic minimum of the PES is now provided by the second potential well and the radial equilibrium position has changed from $R_{eq} = 1600a_0$ to $R_{eq} = 1750a_0$. In Fig. 5.2(b) we again indicate the equilibrium position R_{eq} for applied field strengths of $E = 0$ V/m and 100 V/m, respectively. For $E = 100$ V/m the energetic spacing of the first two neighboring potential minima has further increases as it can be clearly seen in Fig. 5.2(b) (light yellow curve).

To understand this effect we analyze the expression of the field dependent eigenenergies 5.7 by

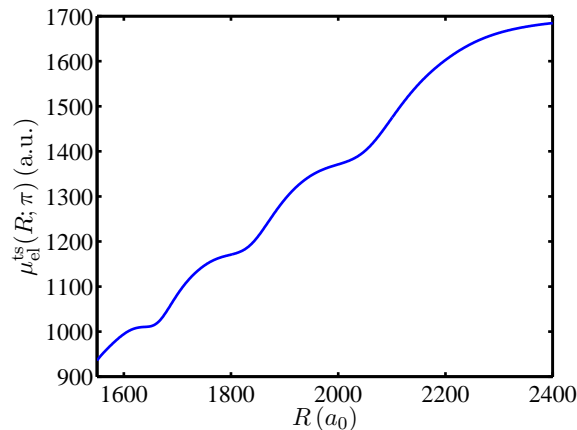


Figure 5.3: Two-state electronic dipole function $\mu_{\text{el}}^{\text{ts}}(R; \pi)$ as a function of the radial separation R . The function monotonically increases in R . For $\mu_{\text{el}}^{\text{ts}}(R; 0)$ we have $\mu_{\text{el}}^{\text{ts}}(R; 0) = -\mu_{\text{el}}^{\text{ts}}(R; \pi)$.

just keeping the linear term in E

$$\lambda_1(R, E) \approx \lambda_1 + E \langle \Lambda_1(R) | z | \Lambda_1(R) \rangle \equiv \lambda_1 - E \mu_{\text{el}}^{\text{ts}}(R; \theta). \quad (5.9)$$

In this approximation the energy shift is determined by the two-state electronic dipole function $\mu_{\text{el}}^{\text{ts}}(R; \theta)$ which is defined as

$$\mu_{\text{el}}^{\text{ts}}(R; \theta) \equiv -\langle \Lambda_1(R; \theta) | z | \Lambda_1(R; \theta) \rangle.$$

It is easy to verify that $\mu_{\text{el}}^{\text{ts}}(R; 0) = -\mu_{\text{el}}^{\text{ts}}(R; \pi)$. Obviously this approximation is identical to first order perturbation theory where the exact eigenvector is replaced by the eigenvector $|\Lambda_1\rangle$ from the two-state approximation discussed in Section 4.2.2. In Fig. 5.3 we present the electronic dipole function $\mu_{\text{el}}(R, \pi)$ as a function of the spatial separation R . We clearly see a monotonically increasing function in R . Using the electronic dipole function we can explain the behavior of the two adiabatic potential curves presented in Fig. 5.2(a,b). For $\theta = 0$ the energy shift $\Delta\varepsilon = -E\mu_{\text{el}}(R, 0)$ due to the external electric field is positive and monotonically increasing in R . The field-free potential surface is, apart its local nodal oscillations, an increasing function in R itself. This means if $\theta = 0$ the field dependent correction terms $-E\mu_{\text{el}}(R, 0)$ provides a positive correction with the same monotonic behavior as the field-free curve. Due to this the potential curve $\lambda(R; E)$ is energetically shifted upwards and the topological properties of the field-free curve remain unchanged. However, for $\theta = \pi$ the situation is slightly different. In this case the monotonic behavior of the field dependent correction is opposite to the monotony of the field-free potential curve. Due to this these terms are in competition with each other. For very low electric fields the field-free term is dominant and the field-free surface is hardly affected. With increasing field strength the impact of the correction term increases. Due to this the monotonic behavior of the potential surface changes starting with small radial positions R . By increasing the electric field strength further the imprint of the correction term becomes visible for larger R and the radial equilibrium positions change as it is observed in Fig. 5.2(b). The effect has two important consequences. First, the radial equilibrium position R_{eq} can be controlled by changing the strength of the external electric strength E . Due to this low lying rovibrational states which are localized near the minimum of the deepest potential well are stabilized because their radial distance from the region of avoided crossings ($R \approx 1525a_0$) can be increased by increasing the electric field strength E . In this case their wave functions overlap into this region is significantly reduced which reduces decay processes of wave packets probing the seam of the avoided crossings. Second, as the electron density of the valence electron is centered near the neutral perturber the charge separation between electron and the positive ionic core is

expected to increase as well. Due to this the electronic dipole moment of the field dressed molecule should be very sensitive to the applied electric field. This issue will be studied in more detail in Section 5.5.

5.4.2 Perturbation theory and exact diagonalization

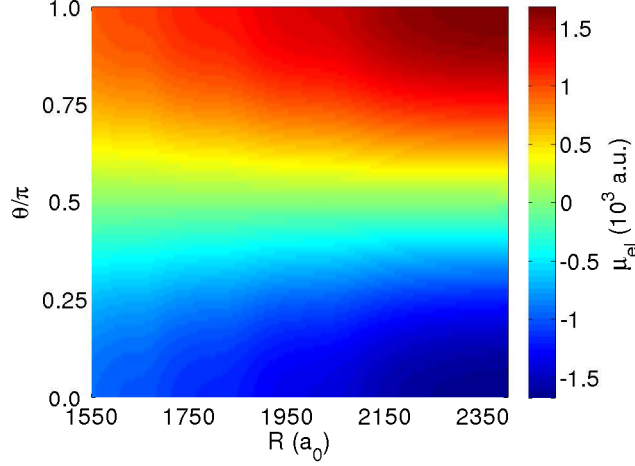


Figure 5.4: Spatial dependence of the electric dipole function $\mu_{\text{el}}(R, \theta)$. Obviously μ_{el} is antisymmetric with respect to $\theta = \pi/2$, e.g. it fulfills $\mu_{\text{el}}(R, \theta + \pi/2) = -\mu_{\text{el}}(R, \pi/2 - \theta)$.

Before we study the molecular dynamics within a numerically exact approach we analyze the two-dimensional PES in the case that the electric field just provides a minor perturbation to the field-free molecular states. In this case we apply standard first order perturbation theory for the $X^3\Sigma$ trilobite potential energy curve. In contrast to the previous two-state analysis this approach gives the complete two-dimensional PES as a function of R and θ . In addition this approach requires the field-free electronic states $|\Xi_s(\mathbf{r}; R, \theta)\rangle$ which are calculated numerically via exact diagonalization of the field-free Hamiltonian (see Section 4.2.4). We obtain for the field dressed s -wave potential surface

$$\varepsilon_s(R, \theta; E) = \varepsilon_s(R) + E \langle \Xi_s(\mathbf{r}; R, \theta) | r \cos(\vartheta) | \Xi_s(\mathbf{r}; R, \theta) \rangle_{\mathbf{r}} \equiv \varepsilon_s(R) - E \mu_{\text{el}}(R, \theta). \quad (5.10)$$

The spatial dependent energy shift is determined by the two dimensional electric dipole function

$$\mu_{\text{el}}(R, \theta) \equiv -\langle \Xi_s(\mathbf{r}; R, \theta) | r \cos(\vartheta) | \Xi_s(\mathbf{r}; R, \theta) \rangle_{\mathbf{r}}. \quad (5.11)$$

It can be shown that μ_{el} is antisymmetric with respect to $\theta = \pi/2$, e.g. it fulfills $\mu_{\text{el}}(R, \theta + \pi/2) = -\mu_{\text{el}}(R, \pi/2 - \theta)$. In Fig. 5.4 we present μ_{el} as a two dimensional function of the radial distance R and the θ angle. For any fixed $\theta > \pi/2$ the function μ_{el} is a monotonically increasing function of the radial distance R while for $\theta < \pi/2$ μ_{el} it is monotonically decreasing with respect to R . However, the function monotonically decreases in the θ coordinate for any fixed value of R . In the angular direction μ_{el} possesses its minimum at $\theta = 0$ while its maximum can be found at $\theta = \pi$. Because of these properties the potential energy surfaces given by Eq. (5.10) are expected to possess their angular equilibrium position θ_{eq} at $\theta_{\text{eq}} = \pi$. In Fig. 5.5(a,b) we present two PES for electric field strengths of $E = 0$ and $E = 50$ V/m respectively. Fig. 5.5(a) shows the field-free adiabatic potential surface as function of the radial distance R and the θ -angle. As expected this PES just possesses a radial dependence. We clearly see a nodal structure providing local potential minima with depths of the order of several hundreds of MHz. In Fig. 5.5(b) we present the PES for a finite electric field strength of $E = 50$ V/m. We clearly see that the spherical symmetry is broken

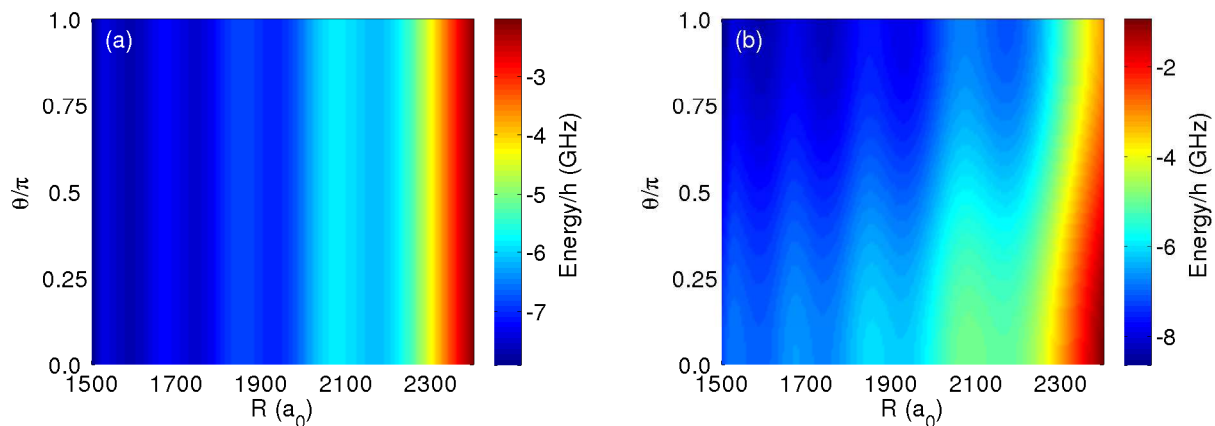


Figure 5.5: (a) Adiabatic PES for the field-free system. We clearly see a spherical symmetric potential surface with a nodal structure. The local potential wells possess depths in the order of hundreds MHz. (b) PES for a finite electric field strength of $E = 50$ V/m. We obtain a two-dimensional PES with local minima along the $\theta = \pi$ direction.

and rotational degree of freedom is turned into a vibrational one. We obtain a two-dimensional PES which possesses a global minimum at $R_{\text{eq}} = 1550a_0$, $\theta_{\text{eq}} = \pi$. Compared to the field-free system at $\theta = \pi$ the field dressed potential curve is shifted downwards with an energy of around 500 MHz while for $\theta = 0$ the PES is shifted upwards by the same amount of energy. These effects can be easily understood from the properties of the dipole function μ_{el} . As it is antisymmetric with respect to $\theta = \pi/2$ the field-free potential surface is altered according to Eq. (5.10) fulfilling the symmetry properties of the electric dipole function μ_{el} . Physically, the same effect can be easily understood by the fact that in the presence of electric field the electron experiences an external force $-E\mathbf{e}_z$. This means that the electron density increases into the negative z -direction. Because the topology of the adiabatic potential surfaces is strongly determined by the electron density the depth of the PES increases at $\theta = \pi$ while it decreases for $\theta = 0$. This feature is clearly reflected in Fig. 5.5(a,b). In Fig. 5.6 we present a surface plot of the two-dimensional PES for the $E = 50$ V/m field dressed potential surface. The potential surface clearly possesses a nodal structure providing local potential wells with depths in the range of several hundreds of MHz. The PES decreases from $\theta = 0$ to π adopting its minimum at $\theta_{\text{eq}} = \pi$. For increasing radial separation the PES increases as well.

In the following we leave the perturbative regime and focus especially electric field strengths in the regime $0 \leq E \leq 650$ V/m. To analyze the PES in this regime we have performed exact diagonalization. Again, the dissociation limits correspond to the atomic states $\text{Rb}(5s) + \text{Rb}(n = 35, l \geq 3)$. In Fig. 5.7 we present the PES for the electrically dressed polar trilobite state for $E = 150$ V/m and 300 V/m as a function θ and R . As already discussed in first order perturbation theory for a finite field strength the spherical symmetry of the field-free potential curves is broken which is clearly seen in Fig. 5.7. The potential minimum is taken for the antiparallel field configuration $\theta = \pi$. This is reasonable because the external electric fields forces the electron density to align antiparallel to its direction which leads to a higher density in the negative z -direction. The electric field therefore turns a rotational degree of freedom θ to a vibrational one. As the field strength increases a stronger confinement of the angular motion is achieved and the corresponding equilibrium distance R_{eq} increases substantially. In Fig. 5.8(a) we show intersections through the PES for the 9th to 15th excitation for a field strength of 300 V/m and $\theta = \pi$. We see that both the trilobite potential (solid blue curve) and the p -wave dominated potential cure (solid red line) possess a strongly oscillatory structure in the many hundred MHz to GHz regime. For these curves many bound vibrational states are expected to exist. The same figure also shows the adiabatic potential curve stemming from the 38s quantum defect state (green solid line). In contrast to the curves

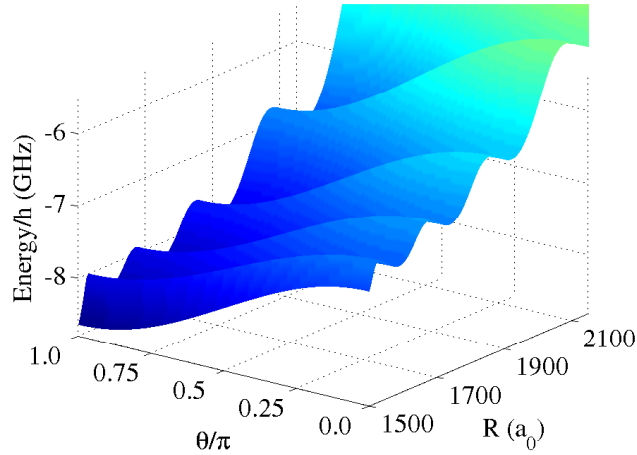


Figure 5.6: Surface plot of the two-dimensional $E = 50$ V/m field dressed PES. From $\theta = 0$ to π the potential depth clearly increases while for increasing R the depth decreases. In addition, a nodal structure providing potential wells with depth in range of hundreds of MHz are clearly visible.

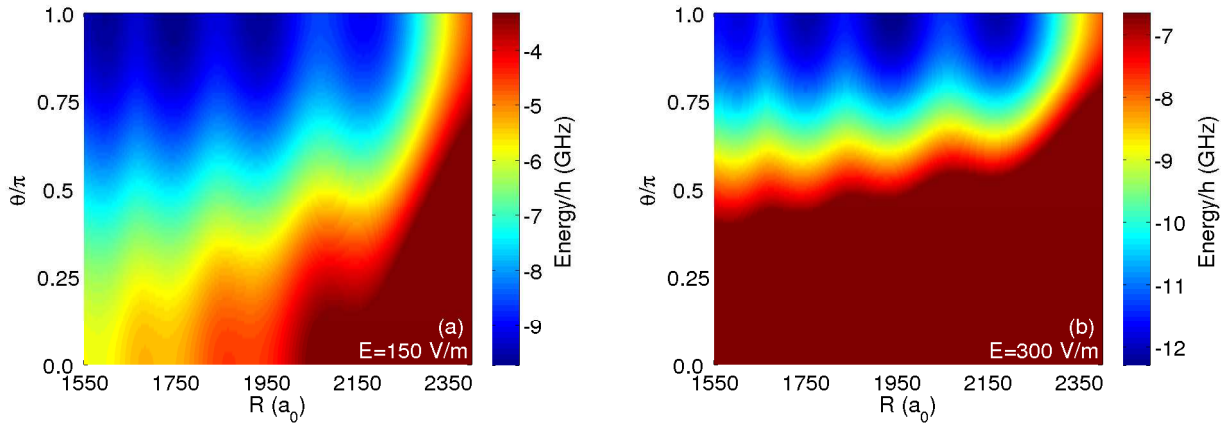


Figure 5.7: Two-dimensional potential energy surfaces for the electrically dressed polar trilobite states for $E = 150$ V/m (a) and 300 V/m (b). We observe a potential minimum at $\theta = \pi$. An increase of the electric field goes along with a stronger confinement of the angular motion and an increase of the diatomic equilibrium distance R_{eq} . Thus, the electric field stabilizes the s -wave dominated molecular states.

arising from the highly degenerate $n = 35$, $l \geq 3$ manifold the oscillations of this potential curve are of the order of several MHz. This is clearly visible in the inset (i) of Fig. 5.8(a). In this figure the $38s$ potential curve is enlarged on a MHz scale. In general, this state is much less affected by the electric field compared to the PES arising from the zero-field high- l degenerate manifold. This is reasonable since the atomic $38s$ state does not possess a substantial electric dipole moment in the presence of the field. Therefore its potential curve hardly shifts with increasing electric field strength from its field-free value of -20.284 GHz.

In Fig. 5.8(b) we show intersections for $\theta = \pi$ through the PES of the electrically dressed polar states for different field strength $E = 150$ V/m, 300 V/m and 450 V/m. We observe how the potential curve is globally shifted with increasing electric field strength. For $E \geq 700$ V/m (not shown) this trilobite PES experiences avoided crossings with the potential curve belonging to the $38s$ state. We see that the overall topology the PES does not change with varying electric field. In particular, the number of minima and their positions remain approximately constant with increasing field strength. However, the diatomic equilibrium distance R_{eq} changes strongly as E varies. This

effect has already been observed and discussed within the two-state analysis for low electric field strength in Section 5.4.1 and is still present beyond the perturbative field regime. This particular observation can be explained by the electric field giving a "spatial weight" to the PES. In contrast, the region of avoided crossings of the s - and p -wave dominated potential curves is hardly affected by the applied electric field and the PES determined mainly by the s -wave interaction. To be more specific we show the dependence of R_{eq} as a function of E in Fig. 5.9(b). We see a plateau-like structure with steps at the field strengths 100 V/m, 200 V/m and 385 V/m, where the value of R_{eq} sharply changes. This structure simply reflects the depicted effect of the electric field on the PES; i.e. by varying the electric field one changes the energetically position of the different potential wells in the oscillating PES, which leads to abrupt changes of the global equilibrium position R_{eq} . Figures 5.8(a,b) also demonstrate the with increasing field strength the avoided crossing between the p -wave and s -wave dominated states remains (approximately) localized in coordinated space whereas the energetically low-lying potential wells with bound vibrational states and in particular the one belonging to the global equilibrium position are lower in energy and are consequently well separated from this avoided crossing. In conclusion, the electric field represents an excellent tool to control the energetic positions and depths of the individual wells and to avoid destabilizing avoided crossings.

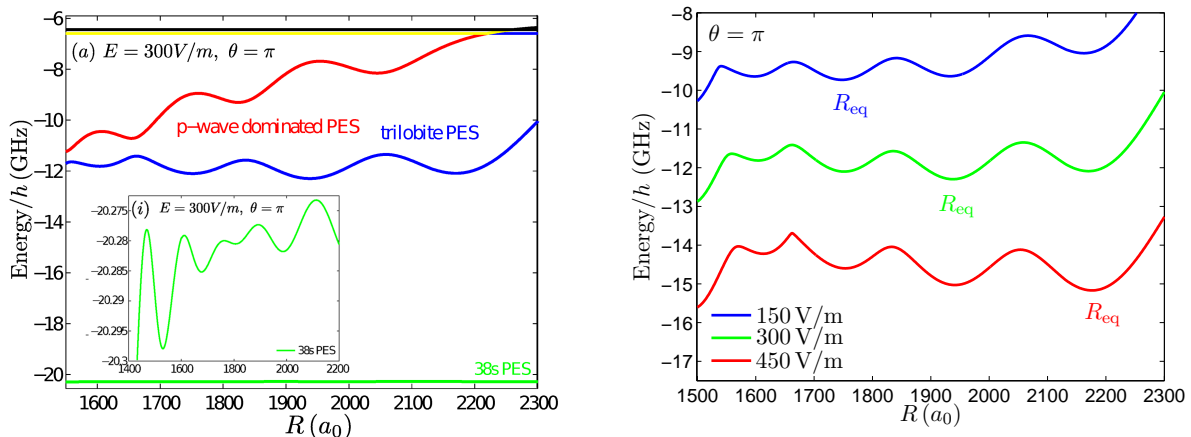


Figure 5.8: (a) Intersections through the two-dimensional PES for $\theta = \pi$ for the 9th-15th excitation for $E = 300$ V/m. For the two lowest PES arising from the high- l degenerate manifold a strongly oscillatory behavior is visible. The region of avoided crossing is clearly visible at $R \sim 1400 - 1500a_0$. (b) Same as in (a) but with varying $E = 150, 300$ and 450 V/m. The diatomic equilibrium distance R_{eq} is moving away from the region of the avoided crossing at $R = 1500a_0 - 1700a_0$.

5.5 Electric dipole moment

In Ref. [85] the authors reported on large electric dipole moments of ultralong-range polar Rydberg molecules of the order of kDebye. The zero-field permanent dipole moment for these species scales according to the semi-empirical expression $D_{\text{el}} = R_{\text{eq}} - n^2/2$. As a first approach we compare this simple expression with the result obtained from the two-state electric dipole function $\mu_{\text{el}}^{\text{ts}}(R; \theta)$ given by Eq. (5.10). We use the approximation $D_{\text{el}}(E) \approx \mu_{\text{el}}^{\text{ts}}$ for the electric dipole moment along the internuclear axis. As it was discussed in Section 5.4.1 the electric dipole moment is expected to change due to the change in the radial equilibrium position R_{eq} . Changing the electric field strength from $E = 0$ to 100 V/m we observe a single change in the value for R_{eq} . In particular, for $E \approx 92$ V/m the radial equilibrium position changes from $R_{\text{eq}} \approx 1548a_0$ to $R_{\text{eq}} \approx 1747a_0$. These values give electric dipole moments of $\mu_{\text{el}}^{\text{ts}}(1548a_0; \pi) = 2.3786$ kDebye and $\mu_{\text{el}}^{\text{ts}}(1747a_0; \pi) = 2.9776$ kDebye. The semi-empirical result gives 2.3779 kDebye and 2.8851 kDebye, respectively. The

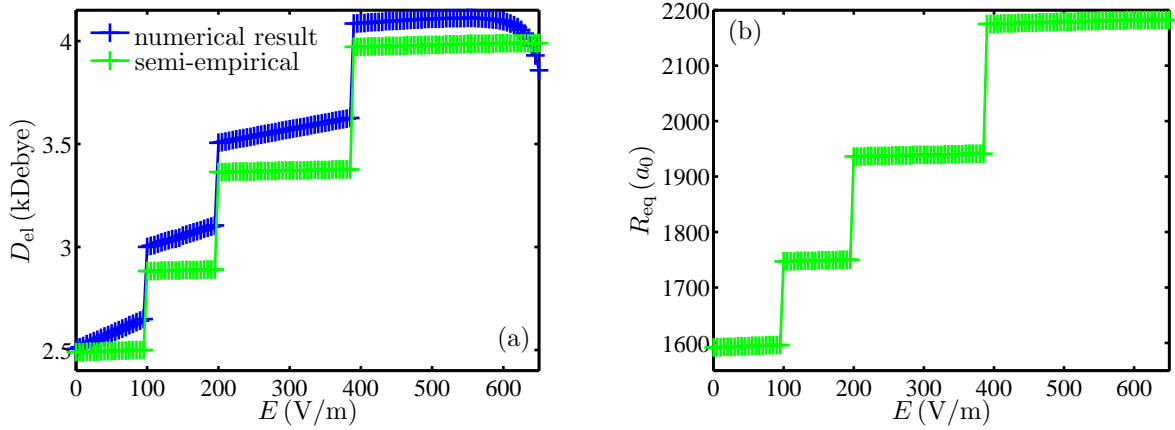


Figure 5.9: (a) The electric dipole moment as a function of the electric field E (blue points). For comparison we show a semi-classical prediction (green points). Figure (b) shows the behavior of the equilibrium distance R_{eq} with varying electric field strength.

relative deviations are 3‰ and 3%, respectively. This indicates the good agreement of the two-state approach and the semi-empirical ansatz. For the complete range of electric field strengths ($0 \text{ V/m} \leq E \leq 700 \text{ V/m}$) we have used the numerically exact electronic eigenstates $\psi(\mathbf{r}; \mathbf{R}_{\text{eq}}, \mathbf{E})$ to calculate the absolute of the electric dipole moment along the z -axis as a function of the field strength.

$$D_{\text{el}}(E) = \left| \int d^3\mathbf{r} \psi^*(\mathbf{r}; \mathbf{R}_{\text{eq}}, \mathbf{E}) z \psi(\mathbf{r}; \mathbf{R}_{\text{eq}}, \mathbf{E}) \right| = \sqrt{\frac{4\pi}{3}} \left| \sum_{nn'l'm} C_{n'l'm}^* C_{nlm} \int dr r^3 R_{n'l'}(r) R_{nl}(r) \right. \\ \left. \times \int d\Omega Y_{10}(\vartheta, \varphi) Y_{l'm}^*(\vartheta, \varphi) Y_{lm}(\vartheta, \varphi) \right|, \quad \mathbf{R}_{\text{eq}} = (0, 0, R_{\text{eq}})^T. \quad (5.12)$$

The integration over the angular degrees of freedom provides $\Delta l = \pm 1$ as a selection rule. In Fig. 5.9(a) we show the absolute value of the electric dipole moment along the z -axis as a function of the field strength. We observe that with increasing electric field also D_{el} increases up to values of around 4 kDebye. As for R_{eq} we see a sharp step structure, i.e. for field strengths at approximately 100, 200, 385 V/m its values suddenly increase in steps of roughly 500 Debye. In Fig. 5.9 we also show a comparison between the exact result calculated according to Eq. (5.12) (blue data points) and the semi-empirical approximation (green data points). For low electric fields the agreement is quite well, but differs with increasing field strength up to a deviation of around 10%. In the considered electric field regime semi-empirical result therefore still allows for a qualitative description of the behavior of D_{el} . A major deviation between the two approaches is that the numerically exact electric dipole moment also grows linearly while the semi-empirical ansatz remains constant. This effect can be explained by the fact that the exact result contains higher order contributions in E . In case R_{eq} remains constant the increasing dipole moment can be explained by contributions linear in E which are associated with electric polarizability of the ultralong-range Rydberg molecule. This issue will be discussed in Chapter 8. For $E > 570 \text{ V/m}$ we find an unexpected decrease of D_{el} . This feature can be understood if one analyzes the field-dependent spectrum of coefficients for the electronic eigenvector $\psi(\mathbf{r}; \mathbf{R}_{\text{eq}}, \mathbf{E}) = \sum_i C_i(E) \chi_i(\mathbf{r})$. In Fig. 5.10 we show the distribution $|C_i|^2$ for $E = 300 \text{ V/m}$ and 600 V/m . For $E = 300 \text{ V/m}$ the spectrum is dominated by basis states from the $n = 35, l \geq 3$ manifold. Contributions stemming from the quantum defect split states (which are placed at the outermost right edge of the spectrum at $i = 1217, \dots, 1225$) are negligible. For $E = 600 \text{ V/m}$ the situation has changed in the sense that now the main contribution is provided by the $38s$ state. This can be understood by the fact that the considered PES is approaching the $38s$ PES with increasing field strength. The latter is however barely affected by the electric

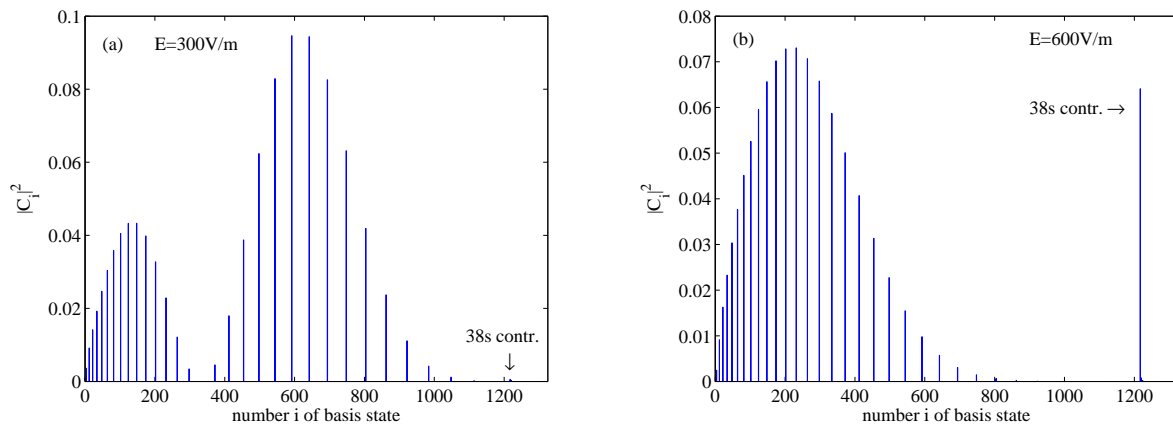


Figure 5.10: Spectrum of coefficients of the electronic eigenvector $\psi(\mathbf{r}; \mathbf{R}_{\text{eq}}, \mathbf{E})$ at $E = 300 \text{ V/m}$ (a) and 600 V/m (b). For increasing field strength the eigenstates gain a finite admixture of the quantum defect split states. For 600 V/m we clearly see a major contribution provided by the $38s$ state.

field. For $E = 600 \text{ V/m}$ the PES involve avoided crossings which causes the high- l dressed trilobite PES to acquire a major contribution from the $38s$ state. This finite admixture has two important consequences:

- Due to the $\Delta l = \pm 1$ selection rule the $38s$ state only acquires a contribution to the integral (5.12) via the $37p$ state. However, the coefficient of the latter state is negligibly small. This causes the decrease of D_{e1} for large field strengths as seen in Fig. 5.9.
- The finite $38s$ admixture provides us with the possibility to prepare high- l Rydberg molecules via a two-photon process. This goes beyond the three-photon preparation scheme suggested in [85] ($l_{\text{min}} = 3$ for the field-free case). For $E \geq 570 \text{ V/m}$ the trilobite state acquires a major $l = 0$ contribution which makes it accessible for a two-photon transition scheme. In Fig. 5.11(a,b) two possible transitions schemes are depicted. In Fig. 5.11(a) the high- l Rydberg molecules are created via a two photon process into to reach a high nd intermediated state. In particular, we have chosen the $35d$ state. Hereafter an additional microwave pulse is used to finally reach the $n = 35$, $l \geq 3$ perturbed hydrogenic state. In Fig. 5.11(b) the excitation scheme for the field dressed high- l species is depicted. Here, an intermediated np level ($n = 30$ in this case) can be used to reach the field dressed trilobite state within a two photon process. The same mechanism has been reported recently in the analysis of ultralong-range polyatomic Rydberg molecules formed by a polar perturber [88]. Field-free high- l molecular states can then in principle be accessed via an additional adiabatic switching of the electric field back to the zero value.

5.6 Rovibrational states

Because of the azimuthal symmetry of the PES we introduce cylindric coordinates (ρ, Z, ϕ) for their parametrization $\epsilon(\mathbf{R}) = \epsilon(\rho, Z)$. For the rovibrational wave functions we choose the following ansatz

$$\phi_{\nu m}(\mathbf{R}) = \frac{F_{\nu m}(\rho, Z)}{\sqrt{2\pi\rho}} \exp(im\phi), \quad m \in \mathbb{Z}, \quad \nu \in \mathbb{N}_0. \quad (5.13)$$

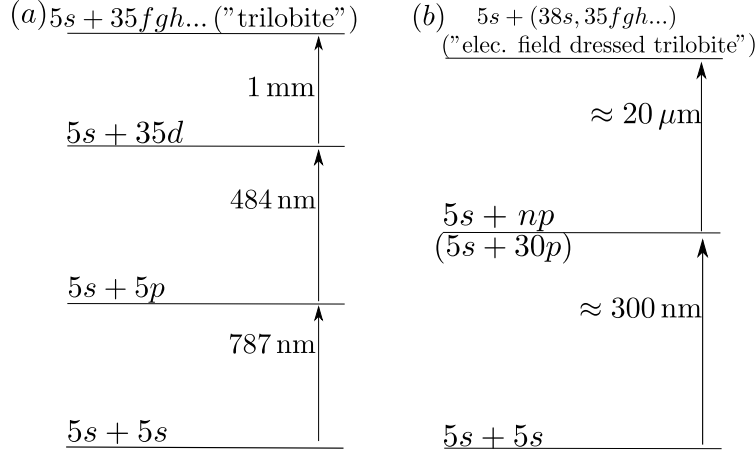


Figure 5.11: Schematic draft of possible transition schemes in order to create high- l Rydberg molecules. Figure (a) shows a two photon process to reach a nd Rydberg state followed by an additional microwave pulse. In (b) the field dressed Rydberg molecules can be reached within a two photon process via an intermediated np state.

With this we can write the rovibrational Hamiltonian in Eq. (5.4) as

$$H_{\text{rv}} = -\frac{1}{m_n}(\partial_\rho^2 + \partial_Z^2) + \frac{m^2 - 1/4}{m_n \rho^2} + \epsilon(\rho, Z). \quad (5.14)$$

We solved the corresponding Schrödinger equation for different azimuthal quantum numbers m using a fourth order finite difference method (see Appendix A.3).

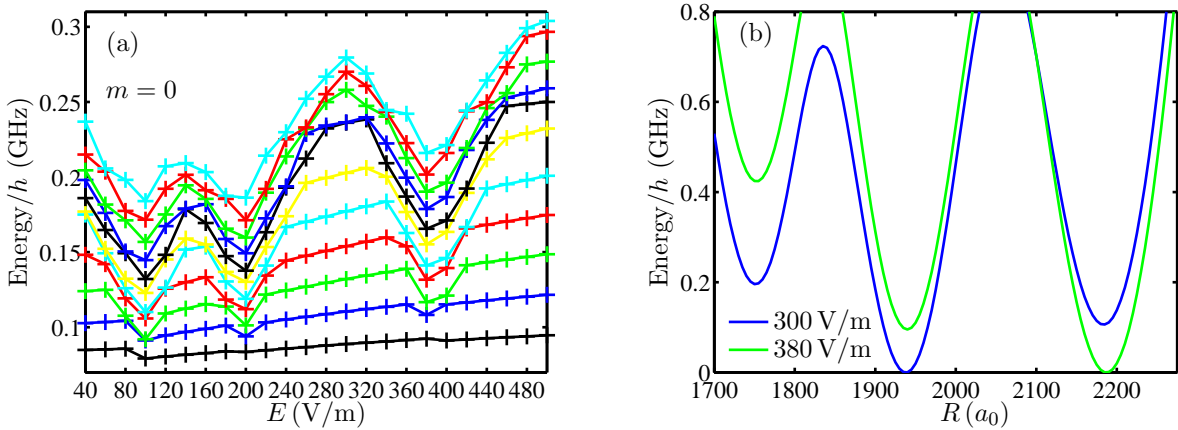


Figure 5.12: (a) shown are the eleven lowest vibrational energies as a function of the field strength E . The dips around $E = 100$, 200 and 385 V/m are caused by the change of potential wells determining the diatomic equilibrium distance R_{eq} . In figure (b) we show the offset corrected potential curves for $E = 300$ V/m and $E = 380$ V/m ($\theta = \pi$). For $E = 300$ V/m bound states in the middle well with energies larger than 200 MHz can tunnel into the neighbored potential wells. This causes a reduction of their level spacings. For $E = 380$ V/m we nearly get a double potential well and states with energies less than 200 MHz possess a higher tunneling probability. Correspondingly, this leads to a denser spectrum.

In Fig. 5.12(a) we provide the energies of the eleven lowest vibrational ($m = 0$) states living in the trilobite PES for varying field strength. In order to obtain a normalized view of the spectrum the corresponding energy of the minimum of the PES has been subtracted. In general we observe a slight increase of the level spacing with increasing field strength. The increase is due to an enhanced angular confinement of the rovibrational motion for strong fields. For $E = 100$, 200 and 385 V/m

however we encounter a dip in the rovibrational level spacing. The latter corresponds to the case of crossover of the equilibrium positions between neighboring wells and therefore an accompanying relocation of the corresponding rovibrational wave functions. This leads to enhanced tunneling probabilities between neighboring wells and therefore an increased level density. In Fig. 5.12(b) we show the offset corrected potential curves for $E = 300$ V/m (blue curve) and $E = 380$ V/m (green curve) ($\theta = \pi$). For $E = 300$ V/m the potential curve possesses a global minimum at $R = 1938a_0$ and two local minima at $R = 1750a_0$ and $2182a_0$ with an offset of 200 MHz. Bound states in the middle well with energies higher than 200 MHz can tunnel into these wells, whereby their level spacing is reduced. For increasing field strengths the right potential well is shifted downwards. This enhances the tunneling probabilities of states with energies less than 200 MHz, which correspondingly leads to a denser spectrum.

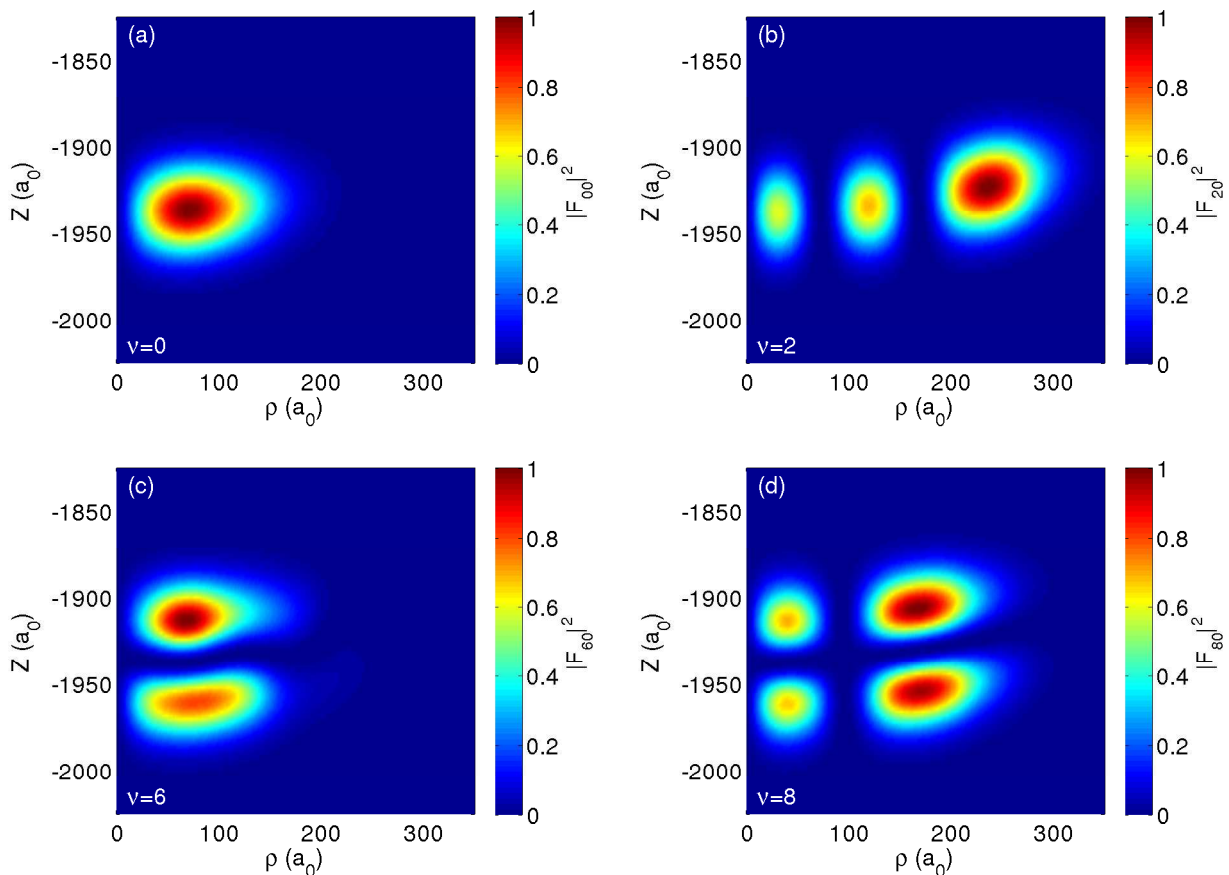


Figure 5.13: Scaled probability densities $|F_{\nu 0}(\rho, z)|^2$ for rovibrational wave functions. All four contractions belong to the trilobite PES for $E = 300$ V/m with an azimuthal quantum number $m = 0$. In (a) we observe a deformed Gaussian like density profile for the ground state ($\nu = 0$) centered at $Z = -1938a_0$ and $\rho = 72a_0$. In Z/ρ -direction the density distribution has an extension of approximately $50a_0/100a_0$. In (b) we show the density profile for the second excited state ($\nu = 2$). This density profile provided three peaks at $(Z, \rho) = (-1939a_0, 32a_0)$, $(-1934a_0, 122a_0)$ and $(-1924a_0, 234a_0)$. Figure (c) shows the density profile for the sixth excited state. We notice an asymmetric double peak structure along the Z -direction. This feature reflects the excitation of the Z -degree of freedom. Finally, in (d) we have both an excitation the angular and Z -direction which results in a density profile possessing four peaks.

In Figs. 5.13((a)-(d)) we present (scaled) probability densities $|F_{\nu 0}(\rho, z)|^2$ for $m = 0$ for the vibrational ground state ($\nu = 0$) and higher excitation ($\nu = 2, 6, 8$) for $E = 300$ V/m. The equilibrium distance for the PES is located at $Z = -1939a_0$, $\rho = 0$. The $m = 0$ ground state distribution is characterized by a deformed Gaussian profile that is localized at $Z = -1938a_0$ and $\rho = 72a_0$. In Z, ρ -direction the density distribution possesses an extension of approximately $50a_0$ and $100a_0$,

respectively. The density profile for the second excitation ($\nu = 2$) shows three separate Gaussian like density peaks with increasing intensity located at $(Z, \rho) = (-1939a_0, 32a_0)$, $(-1934a_0, 122a_0)$ and $(-1924a_0, 234a_0)$ with an extension of around $(25a_0, 30a_0)$, $(25a_0, 40a_0)$ and $(75a_0, 75a_0)$ in the Z, ρ -directions, respectively. The specific profile of the $|F_{20}(\rho, z)|^2$ density profile can be understood by considering the excitation dynamics into the θ -direction to be similar to the harmonic oscillator. In this case the density profile in Fig. 5.13(b) can be easily related to the second excited state of a harmonic oscillator. Increasing the degree of excitation we obtain a novel kind of density profile for ($\nu = 6$) as it is depicted in Fig. 5.13(c). Now the Gaussian probability density from Fig. 5.13(a) possesses a double peak structure with a node at the former peak position ($\rho = 72a_0, Z = -1939a_0$). In Fig. 5.14 this issue is presented in more detail. In this figure we present, beside the field dressed potential energy curve $\epsilon(Z, \rho_0)$, intersection through the probability densities $|F_{\nu 0}(Z, \rho_0)|^2_{\nu=0,6}$ (green and blue curve, respectively) for fixed $\rho_0 = 72a_0$ as functions of Z . In the case of the ground state rovibrational state ($\nu = 0$) the Gaussian profile is clearly visible. In the case of the excited state ($\nu = 6$) the density profile possesses a double peak structure providing a node at the peak position of the ground state density distribution ($Z_{\text{peak}} = -1939a_0$). The density profile of the excited can be understood if this excitation is considered to be a harmonic oscillator in the Z -direction instead of the angular direction. The asymmetric peak structure in Fig. 5.14 can be explained by the asymmetric potential shape. Finally, in Fig. 5.13(d) we present the rovibrational probability density $|F_{60}(Z, \rho_0)|^2$. In this case an angular mode is excited in addition to the just discussed excitation in the Z -direction. We obtain a density profile consisting of four density peaks whereby the peak high is larger for the outer peaks than the inner peaks.

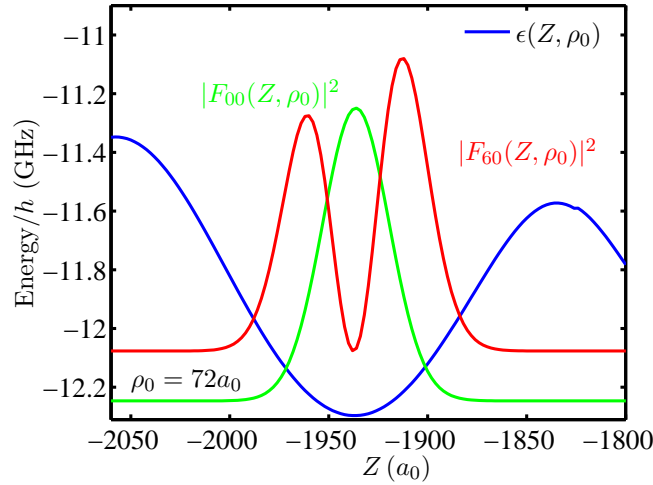


Figure 5.14: Electrically dressed trilobite potential curve $\epsilon(Z, \rho_0)$ (solid blue curve) for $E = 300$ V/m and as a function of Z and fixed $\rho_0 = 76a_0$. In addition, intersections through the (scaled) rovibrational probability densities $|F_{\nu 0}(Z, \rho_0)|^2_{\nu=0,6}$ are depicted (green and red solid curves, respectively).

5.7 Conclusion

In the present work we have therefore explored the changes the polar high angular momentum trilobite states experience if they are exposed to an electric field of varying strength. Taking into account s - and p -wave interactions it turns out that the electric field provides us with a unique know to control the topology of the adiabatic potential energy surfaces. First of all, the angular degree of freedom between the electric field and internuclear axis is converted from a rotational to a vibrational degree of freedom thereby rendering the field-free potential energy curve into a two-dimensional potential energy surface. It turns out that the global equilibrium position is always the antiparallel configuration of these two axes. The sequence of potential wells with increasing radial

coordinate, i.e. the oscillatory behavior of the potential is changed dramatically in the presence of the field. In particular we encounter an overall lowering of the energy accompanied by a subsequent crossover of the energetic order of the individual wells. Consequently, the equilibrium distance and the lowest vibrational states are systematically shifted to larger internuclear distances. The p -wave split state which, due to its resonant behavior, lowers dramatically in energy with decreasing internuclear distance and therefore crosses the polar trilobite state close to its equilibrium distance in the zero-field case, can now with increasing field strength be systematically shifted away from the energetic lowering equilibrium distance and corresponding well. In such a way the respective stability of the ground and many excited vibrational states of the polar trilobite state is guaranteed. For strong fields the interaction of the latter state with non-polar (quantum defect split) states, which are very weakly polarized in the presence of the field, leads to a strong admixture of, in our specific case, s -wave character to the polar high angular momentum states. As a consequence, a two-photon excitation process starting from the ground state of the two-atom system should be sufficient to efficiently excite these states and probe their character. The electric dipole moment, which is steadily increasing with increasing electric field strength starting from zero-field, does, due to the above admixture, decrease in the strong field regime.

To obtain an even richer topology of the potential energy surfaces of the potential surfaces which stem from the highly degenerate hydrogenic n manifold the combination of static electric and magnetic fields would be the next step. This subject will be the content of Chapter 6. The results from the studies on electrically dressed ultralong-range Rydberg molecules have been published in [3].

Chapter 6

Ultralong-range Rydberg molecules in combined electric and magnetic fields

6.1 Introduction

The impact of either magnetic or electric fields on ultralong-range molecules has been studied in previous works [3,99]. It has been shown that in the presence of an external field the angular degree of freedom between the field and the internuclear axis acquires a vibrational character resulting in two-dimensional adiabatic potential energy surfaces (PES). A pure magnetic field yields molecular states oriented perpendicular to the molecular axis and leads, with increasing field strength, to a monotonic lowering of the magnitude of the electric dipole moment [99]. In contrast, a pure electric field forces the molecule into a parallel oriented configuration with an electric dipole of growing magnitude for increasing electric field strength [3].

In the present chapter we explore the impact of combined electric and magnetic fields, and specifically the cases of parallel and crossed (perpendicular) fields, on the structure and dynamics of high- l ultralong-range diatomic rubidium molecules. Our analysis goes beyond the s -wave approximation, taking into account the next order p -wave term in the Fermi-pseudopotential [86,195,196]. Already for the case of a pure magnetic field only we demonstrate the strong impact of the p -wave contribution. Due to p -wave interactions the potential wells providing the weakly bound trilobite states vanish beyond a critical magnetic field strength and consequently no bound states exist anymore. For combined electric and magnetic fields the topology of the PES strongly depends on the specific field configuration and the applied field strengths. The resulting PES show a strong oscillatory behavior with depths up to hundreds of MHz and we find rovibrational bound states with level spacings in the MHz regime. By tuning the field parameters separately we can control the molecular orientation for the parallel field configuration from a perpendicular to an antiparallel molecular configuration with respect to the magnetic field. For the crossed field configuration the alignment can be tuned from an aligned to an antialigned molecular state. For both field configurations we present an analysis of the electric dipole moment.

In detail we proceed as follows. In Section 6.2 we present the molecular Hamiltonian and a discussion of the underlying interactions. Sections 6.3 and 6.4.1 contain the methodology and our results for the pure magnetic field configuration, respectively. In Section 6.5 we analyze the impact of the combined fields on the topology of the PES for the parallel as well as the crossed field configuration. Their rovibrational spectra are addressed in Section 6.6. A detailed study of the alignment and orientation as well as the corresponding electric dipole moment are provided in Sections 6.7 and 6.8, respectively. Finally, Section 6.9 contains our conclusions. The results from this chapter have been published in Ref. [5].

6.2 The setup

In this chapter we consider a highly excited Rydberg atom interacting with a ground state neutral atom (the 'perturber' atom) in combined static and homogeneous electric and magnetic fields. Again, we focus on the ^{87}Rb atom. The Hamiltonian treating the rubidium ionic core and the

neutral perturber as point particles is given by

$$H = \frac{\mathbf{P}^2}{m_n} + H_{\text{el}}^0 + V_{\text{en}}(\mathbf{r}, \mathbf{R}), \quad (6.1)$$

$$H_{\text{el}}^0 = H_0 + \mathbf{E} \cdot \mathbf{r} + \frac{1}{2} \mathbf{B} \cdot \mathbf{L} + \frac{1}{8m_e} (\mathbf{B} \times \mathbf{r})^2, \quad H_0 = \frac{\mathbf{p}^2}{2m_e} + V_l(r), \quad (6.2)$$

where $(m_n, \mathbf{P}, \mathbf{R})$ denote the atomic rubidium mass and the relative momentum and position of the ground state ^{87}Rb atom with respect to the ionic core.

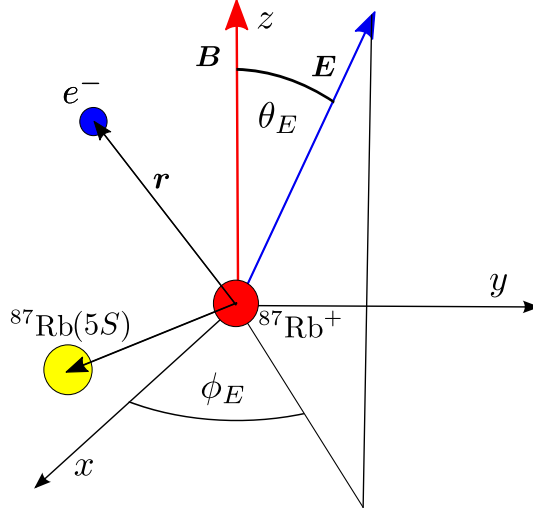


Figure 6.1: A sketch of the considered setup. An ultralong-range Rydberg molecule is exposed to external electric \mathbf{E} and magnetic \mathbf{B} -fields. The molecule consists of a rubidium Rydberg atom (Rb^+ ionic core plus valence electron (e^-)) and a neutral ground state atom (Rb) which interact via a low energy electron-atom scattering potential $V_{\text{en}}(\mathbf{r}, \mathbf{R})$. The \mathbf{B} -field points along the z -axis while the direction of the \mathbf{E} -field is specified by the angles (θ_E, ϕ_E) .

The triple $(m_e, \mathbf{p}, \mathbf{r})$ indicates the corresponding quantities for the Rydberg electron. The electronic Hamiltonian H_{el}^0 consists of the field-free Hamiltonian H_0 and the usual Stark, Zeeman and diamagnetic terms of an electron in static external \mathbf{E} -/ \mathbf{B} -fields. $V_l(r)$ is the angular momentum dependent one-body pseudopotential felt by the Rydberg electron when interacting with the ionic core [125]. For low-lying angular momentum states the electron penetrates the finite ionic Rb^+ -core. This leads to an angular momentum-dependent interaction potential $V_l(r)$ due to polarization and scattering effects [70]. In this work we choose the direction of the magnetic field to coincide with the z -axis of the coordinate system, i.e. $\mathbf{B} = B\mathbf{e}_z$. Finally, we model the interatomic potential V_{en} for the low-energy scattering between the Rydberg electron and the neutral perturber as a so-called Fermi-pseudopotential which is discussed in detail in Section 2.1.

$$V_{\text{en}}(\mathbf{r}, \mathbf{R}) = 2\pi A_s[k(R)]\delta(\mathbf{r} - \mathbf{R}) + 6\pi A_p^3[k(R)]\overleftarrow{\nabla}_r \delta(\mathbf{r} - \mathbf{R}) \overrightarrow{\nabla}_r. \quad (6.3)$$

In our setup we consider the triplet scattering ($S = 1$) of the electron from the spin-1/2 ground state alkali atom. Suppression of singlet scattering events can be achieved by an appropriate preparation of the initial atomic gas. In Eq. (7.4) the quantities $A_s[k(R)] = -\tan(\delta_0(k))/k$ and $A_p^3[k] = -\tan(\delta_1(k))/k^3$ denote the energy-dependent triplet s - and p -wave scattering lengths, respectively. They are evaluated from the corresponding phase shifts $\delta_l(k)$, $l = 0, 1$. The kinetic energy $E_{\text{kin}} = k^2/2$ of the valence electron at the collision point with the neutral perturber can be taken according to $k^2/2 = 1/R - 1/2n^*$, which represents a semiclassical approximation. If not stated otherwise, atomic units will be used throughout.

6.3 Methodology

In order to solve the eigenvalue problem associated with the Hamiltonian (6.1) we adopt an adiabatic ansatz for the electronic and heavy particle dynamics, cf. Section 3.2. We write the total molecular wave function as $\Psi(\mathbf{r}, \mathbf{R}) = \psi(\mathbf{r}; \mathbf{R})\Phi(\mathbf{R})$ and obtain within the adiabatic approximation

$$[H_0 + \mathbf{E} \cdot \mathbf{r} + \frac{1}{2}\mathbf{B} \cdot \mathbf{L} + \frac{1}{8}(\mathbf{B} \times \mathbf{r})^2 + V_{\text{en}}(\mathbf{r}, \mathbf{R})]\psi_i(\mathbf{r}; \mathbf{R}) \equiv H_{\text{el}}\psi_i(\mathbf{r}; \mathbf{R}) = \epsilon_i(\mathbf{R})\psi_i(\mathbf{r}; \mathbf{R}), \quad (6.4)$$

$$\left(\frac{\mathbf{P}^2}{M} + \epsilon_i(\mathbf{R})\right)\Phi_{ik}(\mathbf{R}) = \mathcal{E}_{ik}\Phi_{ik}(\mathbf{R}), \quad (6.5)$$

where ψ_i describes the electronic molecular wave function for a given relative position \mathbf{R} and Φ_{ik} determines the rovibrational state of the molecule. To calculate the potential energy surface $\epsilon_i(\mathbf{R})$ we expand $\psi(\mathbf{r}; \mathbf{R})$ in the eigenbasis of H_0 , i.e. $\psi_i(\mathbf{r}; \mathbf{R}) = \sum_{nlm} C_{nlm}^{(i)}(\mathbf{R})\chi_{nlm}(\mathbf{r})$ with $H_0\chi_{nlm}(\mathbf{r}) = \varepsilon_{nl}\chi_{nlm}(\mathbf{r})$, $\chi_{nlm}(\mathbf{r}) \equiv \langle \mathbf{r} | nlm \rangle = R_{nl}(r)Y_{lm}(\vartheta, \varphi)$. For $l \geq l_{\text{min}} = 3$ we neglect all quantum defects, i.e. H_0 is identical to the hydrogen problem. Finally, we have to solve the following eigenvalue problem

$$\begin{aligned} (\varepsilon_{nl} - \epsilon(\mathbf{R}) + m\frac{B}{2})C_{nlm} + \sum_{n'l'm'} C_{n'l'm'} (\langle nlm | Er \cos(\Omega) + \frac{B^2}{8}r^2 \sin^2(\vartheta) | n'l'm' \rangle \\ + \langle nlm | V_{\text{n,e}}(\mathbf{r}, \mathbf{R}) | n'l'm' \rangle) = 0, \end{aligned} \quad (6.6)$$

with $\cos(\Omega) = \sin(\theta_E) \sin(\vartheta) \cos(\phi_E - \varphi) + \cos(\theta_E) \cos(\vartheta)$. The angles (θ_E, ϕ_E) specify the direction of the electric field (see Fig. 6.1). Without loss of generality, one can choose $\phi_E = 0$. In this work we analyze the parallel ($\theta_E = 0$) and perpendicular ($\theta_E = \pi/2$) field configurations. To study the different configurations we use standard numerical techniques for the diagonalization of the resulting hermitian matrices. Throughout this work we focus on the high- l $n = 35$ manifold; for other n -quantum numbers the underlying physical processes remain similar. In the case of zero electric field this high- l manifold provides the trilobite states [85]. For the $n = 35$ trilobite manifold we used, in addition to the degenerate $n = 35$, $l \geq 3$ manifold, a basis set that includes the $38s$, $37d$, $36p$ quantum defect split states due to their energetically closeness. This basis set contains 1225 states in total.

From Eqs. (6.4) and (6.5) we already deduce some symmetry properties of the states ψ , Φ and the energies ϵ for the different field configurations. If $P_{\mathbf{r}, \mathbf{R}, \mathbf{E}}$ denotes the generalized parity operator that transforms $(\mathbf{r}, \mathbf{R}, \mathbf{E}) \rightarrow (-\mathbf{r}, -\mathbf{R}, -\mathbf{E})$ we have $[H, P_{\mathbf{r}, \mathbf{R}, \mathbf{E}}] = [V_{\text{n,e}}(\mathbf{r}, \mathbf{R}), P_{\mathbf{r}, \mathbf{R}, \mathbf{E}}] = 0$. This means that the states Ψ , ψ and Φ are parity (anti)symmetric and the PES fulfill $\epsilon_{\parallel, \perp}(\mathbf{R}; \mathbf{E}) = \epsilon_{\parallel, \perp}(-\mathbf{R}; -\mathbf{E})$ where (\parallel, \perp) denote the PES in case of parallel and perpendicular fields, respectively. In addition, if $\theta_E = 0$ (parallel configuration), the PES possess an azimuthal symmetry, e.g. $\epsilon_{\parallel}(\mathbf{R}) = \epsilon_{\parallel}(R, \theta)$ and the vector defining the internuclear axis can, without loss of generality, be chosen to lie in the x - z -plane. In contrast, if $\theta_E = \pi/2$ (perpendicular configuration), the PES depend on the azimuthal coordinate ϕ as well and possess only reflection symmetries with respect to the x - y -plane and the x - z -plane, i.e. $\epsilon_{\perp}(R, \pi - \theta, \phi) = \epsilon_{\perp}(R, \theta, \phi)$ and $\epsilon_{\perp}(R, \theta, 2\pi - \phi) = \epsilon_{\perp}(R, \theta, \phi)$. In this work the energy offset of all PES is the dissociation limit of the atomic states $\text{Rb}(5S) + \text{Rb}(n = 35, l \geq 3)$.

6.4 The pure magnetic field configuration

Before we study the combined field configurations let us analyze the system for zero electric field ($E = 0$). Such an analysis has been already performed in [99] considering only the s -wave scattering for the electron-perturber interaction. In contrast to this we here include also the p -wave interaction.

6.4.1 P -wave interaction effects

In Fig. 6.2 we show an one-dimensional cut through the s - and p -wave dominated PES (black lines) in comparison with the purely s -wave dominated potential curves (blue lines) for magnetic field strengths $B = 20$ G (dashed lines) and 100 G (solid lines). The specific cut is taken along the $\theta = \pi/2$ direction. As discussed in [99] in the case of a pure s -wave scattering potential the field-dependent terms represent a perturbation with respect to the field-free molecular Hamiltonian and the considered potential curve is just the known trilobite potential curve [85] shifted by the Zeeman splitting. The resulting PES provide, besides a global minimum between $R = 1400a_0$ and $1500a_0$, a number of local minima which are taken on for the $\theta = \pi/2$ configuration for which the internuclear axis is perpendicular to the applied field. This behavior is clearly visible in Fig. (6.2) for the blue curves which represent the purely s - wave dominated potential curves. However,

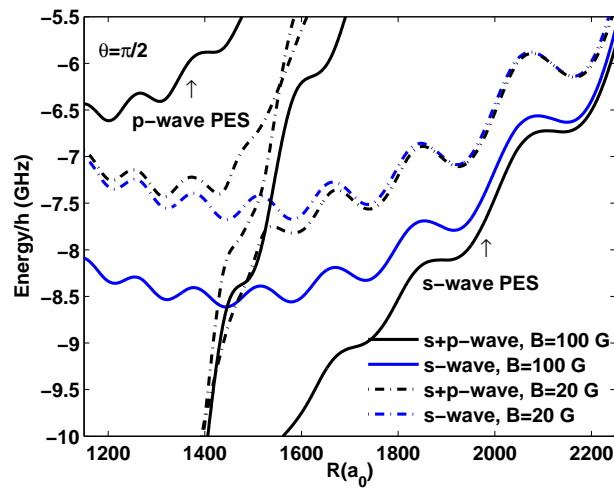


Figure 6.2: Comparison between the pure s -wave scattering dominated potential curves (blue lines) and the combined s - and p -wave potential curves (black lines). Provided are cuts for $\theta = \pi/2$ for different magnetic field strengths $B = 20$ G (dashed lines) and $B = 100$ G (solid lines).

including the p -wave scattering term changes the situation substantially. As discussed in detail in [3] in the field-free case additional potential curves arise causing avoided crossings in the vicinity of the global minimum of the s -wave trilobite curve.

As shown in Fig. 6.2 for $\theta = \pi/2$ we are faced with two additional potential curves. For $B = 20$ G (dashed, black curves) the avoided crossings in the region $R = 1400a_0 - 1600a_0$ known from the field-free case are still visible. With decreasing energetical order we first have an oscillating potential curve with a potential minimum at approximately -7.44 GHz for $R = 1312a_0$ that strongly increases for $R \geq 1400a_0$. Because it arises from the additional p -wave interaction we denote this PES as p -wave PES. Second, we find a monotonically increasing potential curve ranging from $R = 1400a_0$ to $1500a_0$. In this work this PES is not of interest because it does not exhibit any potential minima and therefore contains no bound states. The third and energetically lowest potential curve is the one providing the ultralong-range molecules ("trilobite states") from [85] in the field-free case, cf. Section 4.2.1. This potential curve does not possess a global minimum any more. It monotonically increases till $R \approx 1450a_0$ and thereafter possesses an oscillatory behavior with local potential wells of depths in the hundred MHz regime. We observe that for increasing radial distance R the s -wave character becomes more and more dominant. This curve provides metastable bound states. Although this potential curve is at least in a certain region already strongly p -wave interaction affected in the field-free case [3] we denote it as the s -wave PES. In the field-free case this surface is, at least in a certain region, strongly p -wave interaction affected [3].

Finally, the effect of an increasing field strength on the p -wave dominated potential curves can be

seen in Fig. 6.2 as well. We present the p -wave dominated potential energy curves for a magnetic field $B = 100$ G (solid black curves). An obvious consequence is that the s - and p -wave PES have moved up and down in energy, respectively, while the energetically intermediated curve is still monotonically increasing, but now in the enlarged spatial region $1400a_0 \leq R \leq 1600a_0$.

6.4.2 Three-state analysis

To explain the p -wave interaction effects we first use an analytic approach similar to the pure electric field analysis provided in Chapter 5. Again, we restrict the analytic analysis on the degenerated hydrogenic manifold $n = 35$, $l \geq 3$. To derive the conditions of this ansatz we first consider the case of low magnetic field strengths. Neglecting the diamagnetic term in Eq. (6.2) the electronic Hamiltonian H_{el}^0 possesses the same eigenstates $|nlm\rangle$ as the field free problem H_0 , the paramagnetic term $\sim L_z$ just lifts the m -degeneracy in the electronic eigenenergies. Among the states which split away from the degenerated hydrogenic n manifold the eigenstate with the lowest energy is $|n, n-1, -n+1\rangle$ with an eigenenergy of $-(B/2)(n-1)$. This state is one of the circular eigenstates of the hydrogen problem ($|m| = n-1$). These states are characterized by an electronic density distribution of toroidal structure with a single density maximum in the x - y -plane with a radial extension of $R = n(n-1)$ (see Fig. 6.1). In case the neutral perturber interacts with the Rydberg valence electron it will mix the eigenstates of the electric Hamiltonian H_{el}^0 . However, with increasing field strength the lowest potential energy surface will be determined by the circular state $|n, n-1, -n+1\rangle$. Due to this we expect the potential energy surface to be minimal along the $\theta = \frac{\pi}{2}$ direction. For this reason, we perform an analytic study to determine the potential curves for $\theta = \frac{\pi}{2}$ and $\phi = 0$.

In contrast to the electrically dressed molecules in Chapter 5 where we derived an analytical model for the $\theta = 0, \pi$ configurations, for $\theta = \pi/2$ the interaction matrix $V_{\text{en}}(R, \frac{\pi}{2}, 0)$ is non-diagonal with respect to the azimuthal m quantum number. Since

$$P_{lm}\left(\cos\left(\frac{\pi}{2}\right)\right) = P_{lm}(0) \sim \delta_{l+m, 2n}, \quad n \in \mathbb{N}_0 \quad (6.7)$$

the interaction matrix V_{en} is now diagonal with respect to $l+m$ being even or odd. In particular using Eq. (1.40) we see that the matrices $V_{\text{en}}^s(R, \pi/2, 0)$, $V_{\text{en}}^{p1}(R, \pi/2, 0)$, $V_{\text{en}}^{p3}(R, \pi/2, 0)$ only possess non zero entries if $l+m$ is even while for $V_{\text{en}}^{p2}(R, \pi/2, 0)$ the only non zero elements are found for $l+m$ to be odd. As we are mostly interested in studying the properties of the field dressed trilobite curves and the paramagnetic and diamagnetic term in Eq. 6.2 do not mix the $l+m = \text{even/odd}$ subspaces (see Section 1.40) we restrict our analysis to the $l+m = \text{even}$ subspace.

For the field-free molecular system the eigenfunctions corresponding to the non-zero eigenvalues of $V_{\text{en}}^s(R, \pi/2, 0)$, $V_{\text{en}}^{p1}(R, \pi/2, 0)$ and $V_{\text{en}}^{p3}(R, \pi/2, 0)$, given by

$$\begin{aligned} \psi_n^s\left(\mathbf{r}; R, \frac{\pi}{2}, 0\right) \equiv \psi_n^s(\mathbf{r}; R) &= \frac{1}{\sqrt{\sum R_{nl}^2(r) |Y_{lm}\left(\frac{\pi}{2}, 0\right)|^2}} \sum_{lm} R_{nl}(R) Y_{lm}\left(\frac{\pi}{2}, 0\right) \psi_{nlm}(\mathbf{r}), \\ \psi_n^{p1}\left(\mathbf{r}; R, \frac{\pi}{2}, 0\right) \equiv \psi_n^{p1}(\mathbf{r}; R) &= \frac{1}{\sqrt{\sum R_{nl}'^2(r) |Y_{lm}\left(\frac{\pi}{2}, 0\right)|^2}} \sum_{lm} R_{nl}'(R) Y_{lm}\left(\frac{\pi}{2}, 0\right) \psi_{nlm}(\mathbf{r}), \\ \psi_n^{p3}\left(\mathbf{r}; R, \frac{\pi}{2}, 0\right) \equiv \psi_n^{p3}(\mathbf{r}; R) &= \frac{1}{\sqrt{\sum R_{nl}^2(r) H_{lm}^2\left(\frac{\pi}{2}\right)}} \sum_{lm} R_{nl}(R) H_{lm}\left(\frac{\pi}{2}\right) \psi_{nlm}(\mathbf{r}), \end{aligned}$$

form a basis for the non-zero eigenvalue subspace of the electronic Hamiltonian H_{el} . Analogous to Section 4.2.2 we construct an orthonormal basis set $\{\psi_n^s(\mathbf{r}; R), \psi_n^{p1}(\mathbf{r}; R), \psi_n^{p3}(\mathbf{r}; R)\}$ by applying

the Gram-Schmidt process [193]. We obtain

$$\tilde{\psi}_n^{p1}(\mathbf{r}; R) = \frac{\psi_n^{p1}(\mathbf{r}; R) - C_1 \psi_n^s(\mathbf{r}; R)}{\sqrt{1 - C_1^2}}, \quad (6.8)$$

$$\tilde{\psi}_n^{p3}(\mathbf{r}; R) = \frac{\psi_n^{p3}(\mathbf{r}; R) - C_2 \psi_n^s(\mathbf{r}; R) - C_3 \tilde{\psi}_n^{p1}(\mathbf{r}; R)}{\sqrt{1 - C_2^2 - C_3^2}} \quad (6.9)$$

with

$$C_1 = \langle \psi_n^s(\mathbf{r}; R) | \psi_n^{p1}(\mathbf{r}; R) \rangle_{\mathbf{r}}, \quad C_2 = \langle \psi_n^s(\mathbf{r}; R) | \psi_n^{p3}(\mathbf{r}; R) \rangle_{\mathbf{r}}, \quad C_3 = \langle \psi_n^{p3}(\mathbf{r}; R) | \tilde{\psi}_n^{p1}(\mathbf{r}; R) \rangle_{\mathbf{r}}.$$

With these orthonormal basis functions we analyze the adiabatic potential curves of the magnetically dressed Rydberg molecules along the θ -direction with an effective three-state model. We get for the effective electronic Hamiltonian $H_{\text{eff}}^{\text{el}}$

$$H_{\text{eff}}^{\text{el}} = \begin{bmatrix} \alpha_1 & g_1 & g_2 \\ g_1 & \alpha_2 & g_3 \\ g_2 & g_3 & \alpha_3 \end{bmatrix} \quad (6.10)$$

with

$$\alpha_1 = \langle \psi_n^s(\mathbf{r}; R) | H_{\text{el}} | \psi_n^s(\mathbf{r}; R) \rangle_{\mathbf{r}}, \quad \alpha_2 = \langle \tilde{\psi}_n^{p1}(\mathbf{r}; R) | H_{\text{el}} | \tilde{\psi}_n^{p1}(\mathbf{r}; R) \rangle_{\mathbf{r}}, \quad \alpha_3 = \langle \tilde{\psi}_n^{p3}(\mathbf{r}; R) | H_{\text{el}} | \tilde{\psi}_n^{p3}(\mathbf{r}; R) \rangle_{\mathbf{r}},$$

$$g_1 = \langle \psi_n^s(\mathbf{r}; R) | H_{\text{el}} | \tilde{\psi}_n^{p1}(\mathbf{r}; R) \rangle_{\mathbf{r}}, \quad g_2 = \langle \psi_n^s(\mathbf{r}; R) | H_{\text{el}} | \tilde{\psi}_n^{p3}(\mathbf{r}; R) \rangle_{\mathbf{r}}, \quad g_3 = \langle \tilde{\psi}_n^{p1}(\mathbf{r}; R) | H_{\text{el}} | \tilde{\psi}_n^{p3}(\mathbf{r}; R) \rangle_{\mathbf{r}}.$$

From this matrix representation we can analytically derive the eigenfunctions and eigenenergies which correspond to the adiabatic potential curves for the magnetically dressed molecules.

Since the exact expressions of the matrix elements, eigenenergies and eigenvectors are quite complex and lengthy we abstain from presenting the exact expressions of these quantities at this point. The exact formulas for the three non-zero eigenvalues are presented, in Appendix B.9.3. In

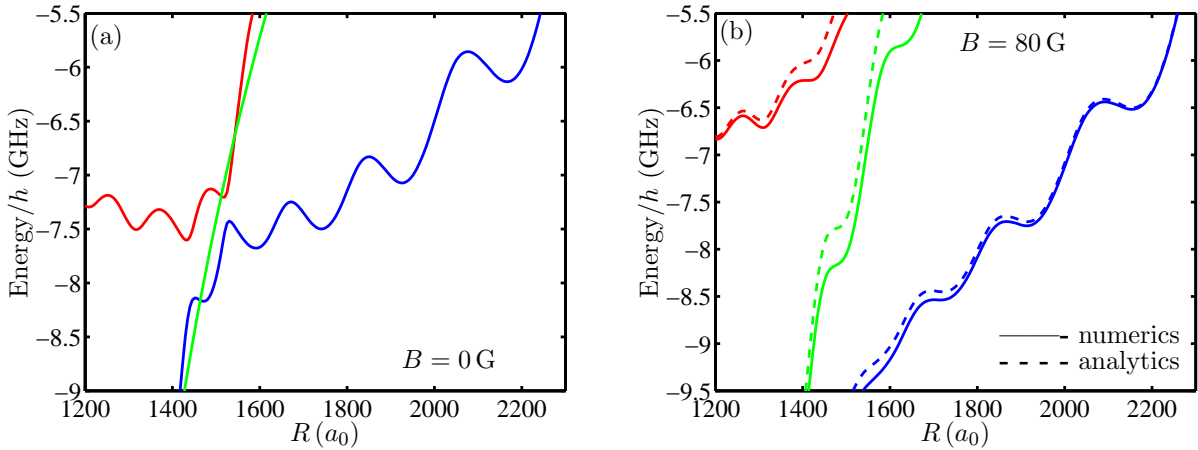


Figure 6.3: Adiabatic potential curves along the $\theta = \pi/2$ direction for applied magnetic field strengths $B = 0$ G and 80 G. In figure (a) we show the field free 3Σ curves and a single 3Π curve. In (b) we present both the potential curves obtained via exact diagonalization (solid curves) and the analytic three states (dashed curves). For the s and p -wave curves the analytic approach reproduces the numeric results quite well.

Fig. 6.3(a,b) we present a comparison between the numerically exact potential curves (solid curves) and the curves obtained from the three state analysis (dashed curves). In Fig. 6.3(a) we present

the field free curves. Obviously, in this case the three state ansatz delivers nearly identical curves to the exact diagonalization. In Fig. 6.3(b) the same curves are shown but for a finite magnetic field strength of $B = 80$ G. We see that for all three potential curves the exact diagonalization curves (solid lines) and the three-state analytic approach (dashed lines) match quite well. The largest deviations are found in the region of the field-free avoided crossings ($R \approx 1450 - 1550a_0$). For the s - and p -wave curves the energy shift and topological structure of the curves are clearly reproduced. Both Fig. 6.2 and Fig. 6.3 show that besides the energetic separation a further consequence of the p -wave interaction is the disappearance of the local potential wells in case of the s -wave curve with increasing magnetic field strength. This behavior can be understood by referring to the three-state analysis. In this approach the energy spacing between two adjacent curves is determined by the off diagonal elements g_i , $i = 1, 2, 3$. Since these terms are proportional to B the energy separation between the potential curves increases with increasing B . This feature can be understood as well by applying standard perturbation theory this feature is easily understood as well. In particular, the PES are well reproduced by the expressions

$$\epsilon_{\text{per}}^{(s,p)}(\mathbf{R}; B) = \epsilon_0^{(s,p)}(\mathbf{R}) + \frac{B}{2} \langle \Xi_{(s,p)}; \mathbf{R} | L_z | \Xi_{(s,p)}; \mathbf{R} \rangle + \frac{B^2}{4} \sum_{n \neq (s,p)} \frac{|\langle \Xi_n; \mathbf{R} | L_z | \Xi_{(s,p)}; \mathbf{R} \rangle|^2}{\epsilon_0^{(s,p)}(\mathbf{R}) - \epsilon_0^{(n)}(\mathbf{R})}, \quad (6.11)$$

where $|\Xi_n; \mathbf{R}\rangle$ and $\epsilon_0^{(n)}(\mathbf{R})$ denote the field-free adiabatic electronic eigenstates and eigenenergies from Section 4.2.4. The diamagnetic term in Eq. (6.1) can be neglected here. Obviously, the term of $\mathcal{O}(B^2)$ potentially becomes relevant in the region of avoided crossings of the field-free curves which are localized around $R \approx 1450a_0$ [3]. For increasing magnetic field strength this term in (6.11) becomes dominant in spatial regions beyond the point of the field-free avoided crossings ($R \approx 1450a_0$). This causes the PES to separate energetically in the way as it can be seen in Fig. 6.2 and Fig. 6.3(b), respectively. In Fig. 6.2 for $B = 100$ G no local potential wells are present. Instead the s -wave PES monotonically increases and possesses two plateaus at radial positions where the former two outermost potential wells had been localized. The same effect is clearly visible in Fig. 6.3(a,b). In the field-free case (see Fig. 6.3(a)) four local potential wells are clearly visible for the s -wave potential curve. However, for an applied magnetic field of $B = 80$ G the two innermost wells have vanished and the two remaining wells have decreased in depth (see Fig. 6.3(b)). Finally, both the exact diagonalization as well as the three-state approach provide the result that in case of a pure magnetic field and beyond a critical field strength of $B_{\text{cr}} = 100$ G the s -wave curve does not provide any bound states for the $\theta = \pi/2$ configuration.

6.4.3 Two-dimensional potential energy surfaces

In Fig. 6.4(a) the complete two-dimensional s -wave PES is shown as a function of (R, θ) for $B = 40$ G and for radial distances $1600a_0 \leq R \leq 2250a_0$. We observe a $\theta \rightarrow \pi - \theta$ reflection symmetric potential surface with local potential minima at $R_{\text{eq}} = 1728a_0, 1918a_0, 2159a_0$ and $\theta_{\text{eq}} = \pi/2$.

In Fig. 6.4(b) the complete two-dimensional p -wave PES is shown as a function of (R, θ) for $B = 40$ G and for radial distances $1000a_0 \leq R \leq 1500a_0$. We observe a potential surface with global equilibrium positions at $R_{\text{eq}} = 1432a_0$, $\theta_{\text{eq}} = 0, \pi$. This p -wave PES provides bound rovibrational states. The region around $R = 1500a_0$, $\theta = \pi/2$ is strongly affected by the level repulsion of the s - and p -wave PES as it has been described above. In Figs. 6.4(a) and 6.4(b) we also see that in this region the s - and p -wave PES strongly decreases and increases, respectively.

However, for $R = 1500a_0$ and θ approaching π or 0 respectively, the effect of the s - and p -wave level repulsion decreases for the s - and p -wave PES. For $\theta = 0, \pi$ this effect vanishes completely, due to the fact that the Hamiltonian (6.4) then separates into a $m = 0$ and $|m| = 1$ block. The considered s - and p -wave curves arise due to the diagonalization of the $m = 0$ subspace of the electronic problem (6.4). If we neglect the diamagnetic term in (6.4) the Zeeman interaction term does not couple the s - and p -wave curves because $L_z |n, l, 0\rangle = 0$, $\forall n, l$. Due to this the topology of

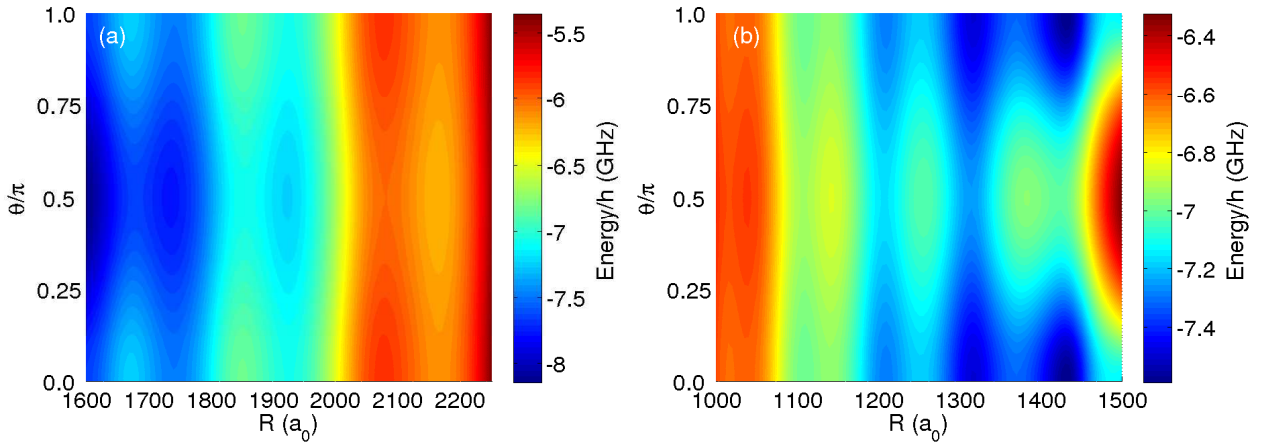


Figure 6.4: (a) The s -wave PES for $B = 40$ G for zero electric field showing a reflection symmetry with respect to $\theta = \pi/2$. (b) The p -wave PES for $B = 40$ G for zero electric field. It possesses a global minimum at $R = 1432a_0$ and $\theta = 0, \pi$. We clearly see how the region around $\theta = \pi/2$ is affected by the level repulsion with respect to the s -wave PES.

the PES is unaffected by the applied magnetic field for $\theta = 0, \pi$.

6.5 Potential energy surfaces for combined field configurations

6.5.1 Parallel field configuration

Let us begin with the analysis of the s -wave PES. We focus on the regime of field strengths $B = 0 - 100$ G and $E = 0 - 100$ V/m. As presented in [85] the s -wave PES is in absence of any external field independent of θ . For a finite electric or magnetic field strength, this spherical symmetry is broken, as it has been discussed in Refs. [3, 99]. In the case of a vanishing electric field ($\mathbf{B} = B\mathbf{e}_z$, $0 < B < B_{\text{cr}}$, $E = 0$) the s -wave PES provides a number of local minima which are realized for the perpendicular configuration $\theta = \pi/2$. In the case of a pure electric field ($E = E\mathbf{e}_z$, $E > 0$, $B = 0$) the electron density is forced to align in its negative direction, a fact that leads to a higher density in the $-z$ -direction. For this reason we find the global minimum of the s -wave PES for the antiparallel field configuration at $\theta = \pi$.

For finite parallel electric and magnetic fields we can tune the topology of the s -wave PES between the pure electric and magnetic field limits. To be specific we choose $B = 60$ G and vary the electric field strength $E = 0 - 100$ V/m. Figure 6.5(a) presents the s -wave PES for $B = 60$ G, $E = 20$ V/m. We observe three local potential minima which we label with (I_{\parallel}) , (II_{\parallel}) and (III_{\parallel}) . In the case of $E = 0$ we find these potential wells along the perpendicular configuration ($\theta = \pi/2$) with the radial minima positions at $R_{\text{I}_{\parallel}} = 1728a_0$, $R_{\text{II}_{\parallel}} = 1918a_0$ and $R_{\text{III}_{\parallel}} = 2159a_0$ respectively (see Fig. 6.4(a)). For $R \approx 1600a_0$ the s -wave potential well decreases monotonically for decreasing R which is caused by the level repulsion described in Section 6.4.1. For finite electric field strengths the topology of the s -wave PES changes in the sense that the angular positions of the minima of the the potential wells $(\text{I}_{\parallel}\text{-III}_{\parallel})$ are shifted to higher $\theta \in [\pi/2, \pi]$ values. This effect is clearly visible in Fig. 6.5(a). It can be simply explained by the fact that the electric field forces the electron density to align in its negative z -direction, which is reflected by a deeper Born-Oppenheimer potential in this region. The radial positions $R_{\text{I}_{\parallel}} - R_{\text{III}_{\parallel}}$ of the minima are less strongly affected. With increasing electric field they are transferred to the final values $1750a_0$ ($R_{\text{I}_{\parallel}}$), $1940a_0$ ($R_{\text{II}_{\parallel}}$) and $2175a_0$ ($R_{\text{III}_{\parallel}}$) for $E > 80$ V/m. Furthermore, we see that the larger the radial position R of the considered potential well from the ionic core the larger is the angular distance from $\theta = \pi/2$. This feature can be understood in a semiclassical picture where we compare the Lorenz force F_L with

the electrostatic force F_{el} on the electron. Since $F_L \sim v_{\text{el}}B \sim \sqrt{1/R - \frac{1}{2n^2}}B$ the Lorentz forces decreases with R while $F_{\text{el}} \sim E$ remains constant. Therefore the electron density further away from the ionic rubidium core is more strongly affected by the electric field. In general the depth of the potential wells ($\text{I}_{||}$ - $\text{III}_{||}$) strongly varies with the corresponding parameter values. In the case of a dominant magnetic field ($B \geq 80$ G, $E \leq 60$ V/m) the wells possess depths up to 100 MHz. For a dominant electric field ($B \leq 40$ G, $E \geq 40$ V/m) their depths are 200 – 300 MHz.

In Fig. 6.5(b) we present the p -wave PES curve for $B = 60$ G, $E = 20$ V/m. It possesses a global equilibrium position at $R = 1432a_0, \theta = \pi$ denoted by $\text{IV}_{||}$. As described in Section 6.4.1 in the case of a pure magnetic field the p -wave PES possesses a $\theta \rightarrow \pi - \theta$ symmetry (see Fig. 6.4). A finite electric field along the z -axis breaks this symmetry and tends, as above-mentioned, to enhance the electron density in the negative z -direction. As a consequence we find in case of the p -wave PES the potential minimum at $\theta = \pi$ (Fig. 6.5(b)). The depth of this potential well is approximately 300 MHz and remains roughly constant for all considered field strengths.

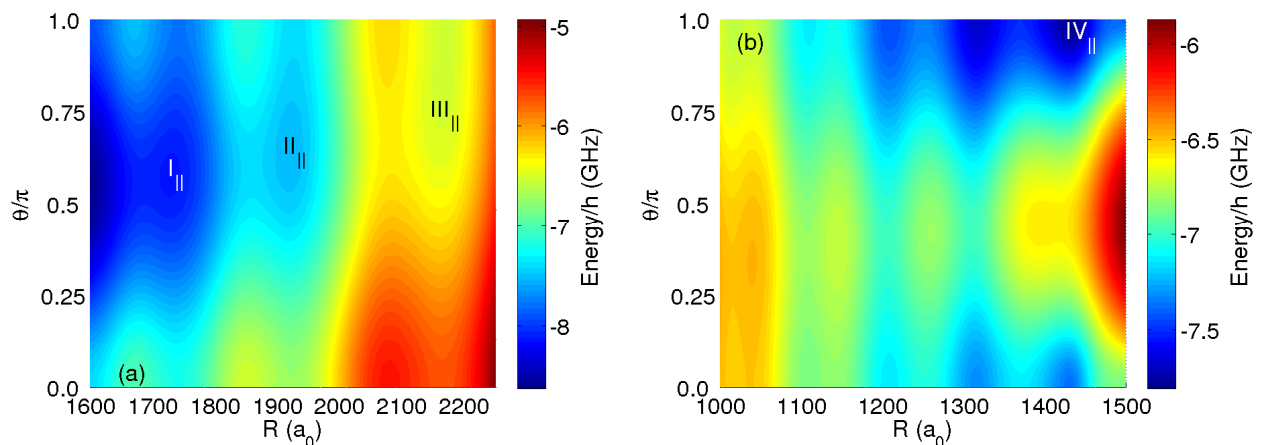


Figure 6.5: (a) s -wave PES as a function of (θ, R) ($\theta_E = 0$, $B = 60$ G, $E = 20$ V/m). We observe three local potential wells which are labeled as ($\text{I}_{||}$), ($\text{II}_{||}$) and ($\text{III}_{||}$). The wells $\text{II}_{||}$ and $\text{III}_{||}$ provide rovibrational bound states with a level spacing of 2 – 20 MHz. (b) p -wave PES as a function of (R, θ) ($\theta_E = 0$, $B = 60$ G, $E = 20$ V/m). We observe the global potential minimum at $R = 1432a_0$, $\theta = \pi$ providing bound states with a level spacing 10 – 30 MHz. Note that for a finite electric field strength the reflection symmetry with respect to $\theta = \pi/2$ is broken.

6.5.2 Perpendicular field configuration

Figure 6.6(a) shows the three-dimensional s -wave PES for the crossed field configuration $B = 100$ G, $E = 60$ V/m as a function of (R, θ, ϕ) . Because of the $\theta \rightarrow \pi - \theta$ and $\phi \rightarrow 2\pi - \phi$ symmetries (see Section 6.3) we present the potential surface in the range of $0 \leq \theta \leq \pi/2$ and $0 \leq \phi \leq \pi$. We clearly see an oscillating structure with local potential minima aligned into the negative x -direction ($\theta = \pi/2$, $\phi = \pi$). This can be understood by the fact that the electric field simply deforms the azimuthally symmetric PES for a finite magnetic field strength in the sense that it forces the electron density to align along the negative x -direction. Due to this we obtain molecular states with a well-defined orientation antiparallel to the electric field. In contrast to the parallel field configuration the orientation of these molecular states cannot be tuned by varying the electric and magnetic field strengths. In the considered parameter range tuning the field parameters just changes the depth of the local potential minima at $\theta = \pi/2$, $\phi = \pi$.

This feature is shown in detail in Fig. 6.6(b) which presents one-dimensional potential cuts for the crossed field configuration. We have fixed the magnetic field strength to $B = B_{\text{cr}} = 100$ G and vary the electric field from $E = 0 - 100$ V/m in steps of 20 V/m. As already discussed in Section

6.4.1 for $E = 0$ we obtain no potential local wells, i.e. no bound states are provided for this magnetic field strength. With increasing electric field strength we again obtain local potential wells at the minima positions $R_{I_{\perp}} = 1728a_0$, $R_{II_{\perp}} = 1918a_0$ and $R_{III_{\perp}} = 2159a_0$ respectively. Obviously, these values are very close to those obtained for the parallel field configuration (see previous subsection). Similarly to the parallel field configuration we label the wells/plateaus with (I_{\perp}) , (II_{\perp}) and (III_{\perp}) . The radial equilibrium positions increase with increasing electric field strength up to $1750a_0$ ($R_{I_{\perp}}$), $1940a_0$ ($R_{II_{\perp}}$) and $2175a_0$ ($R_{III_{\perp}}$). As we observe in Fig. 6.6(b) the wells (III_{\perp}) is affected most by the increasing electric field in the sense that its depth increases from 0 up to 140 MHz. Similarly the depths of the well (II_{\perp}) and (I_{\perp}) increase up to 100 MHz (II_{\perp}) and 40 MHz (I_{\perp}) respectively. We therefore conclude that the electric field counterbalances the effect of the p -wave interaction and leads to bound states in regimes where otherwise none would have existed. This result is reminiscent of an effect already observed for the pure electric field configuration where the electric field stabilizes as well bound molecular states of the s -wave PES [3]. For dominant electric fields in the considered field regime the depths of the potential wells increase up to a value of approximately 300 MHz.

In Fig. 6.7 we present a two-dimensional cut defined by $\phi = \pi$ through the p -wave PES for the crossed field configuration for $B = 100$ G, $E = 60$ V/m. As for the p -wave PES in the parallel field configuration, we concentrate on the potential well providing the global equilibrium position. This well is labeled with IV_{\perp} . The radial equilibrium position is again given by $R = 1432a_0$ for $\theta = 0, \pi$. In the case of a pure electric field the single existing potential minimum is localized at $R = 1432a_0$, $\theta = \pi/2, \phi = \pi$ as shown in the inset of Fig. 6.7. By increasing the magnetic field strength the angular equilibrium position is shifted from $\theta_{\text{eq}} = \pi/2$ to $\theta_{\text{eq}} = \pi/2 \pm \delta$, $\delta \in (0, \pi/2]$. This means that the topology of the p -wave PES changes from a single well to a double well PES. For all applied field strengths the depth of the well IV_{\perp} remains around *unit*300MHz.

In the table 6.1 we summarize the topological properties for both field configurations in the limit of dominant electric and magnetic field strengths.

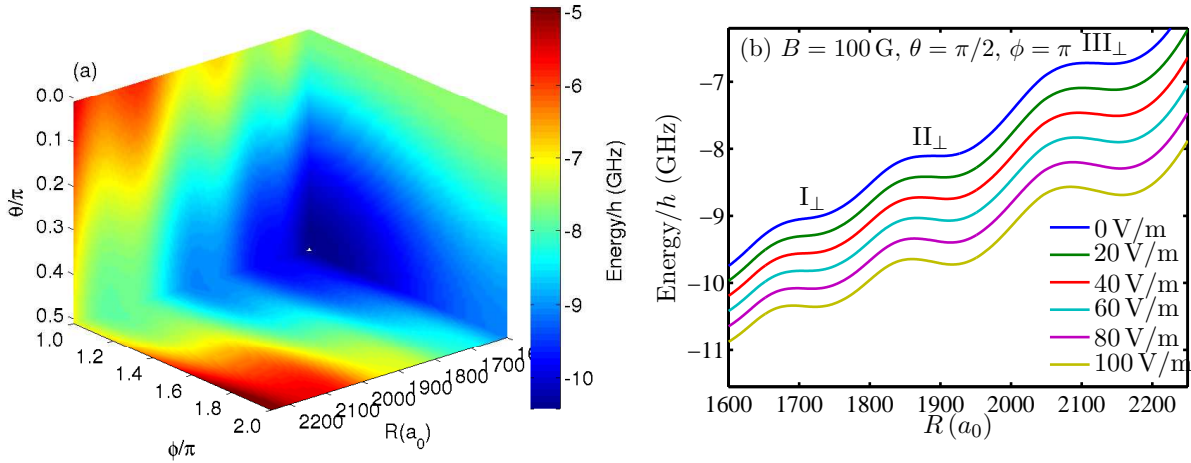


Figure 6.6: (a) Three-dimensional s -wave PES as a function of (R, θ, ϕ) ($\theta_E = \pi/2$, $B = 100$ G, $E = 60$ V/m). We find two local potential wells at $R = 2159a_0$ and $R = 1922a_0$, $\theta = \pi/2$ and $\phi = \pi$. For more details an intersection for $\theta = \pi/2$, $\phi = \pi$ is presented in Fig. 6.6(b). (b) Intersections through the s -wave PES for the perpendicular field configuration for $\theta = \pi/2$, $\phi = \pi$. The shown cuts are taken for fixed $B = 100$ G while the electric field strength E is varied from $E = 0$ to 100 V/m in steps of 20 V/m. Depending on the electric field strength we find local plateaus/potential wells at $R = 1728a_0$, $1918a_0$ and $2159a_0$ labeled by I_{\perp} , II_{\perp} and III_{\perp} . With increasing E the plateaus ($B = 100$ G) are transformed into local potential wells with depths of 40 MHz (I_{\parallel}), 100 MHz (II_{\parallel}) and 140 MHz (III_{\parallel}).

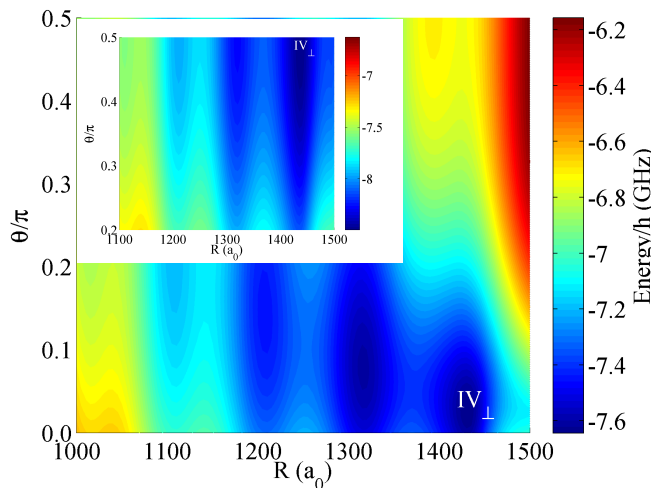


Figure 6.7: Two-dimensional p -wave PES for $\phi = \pi$ and $0 \leq \theta \leq \pi/2$ ($\theta_E = \pi/2$, $B = 100$ G, $E = 80$ V/m). The complete PES is a function of (R, θ, ϕ) and possesses a $\theta \rightarrow \pi - \theta$ symmetry. We observe several local potential wells with the energetically lowest labeled by IV_{\perp} . The inset shows the same PES but for $B = 0$, $E = 80$ V/m. In this case the p -wave PES possesses a single potential minimum IV_{\perp} at $R_{\text{eq}} = 1432a_0$, $\theta = \pi/2$, $\phi = \pi$.

Table 6.1: Topological properties of the s - and p -wave PES for both field configurations for dominant magnetic ($B \gg E$) and electric ($B \ll E$) field. The triple $(R_{\text{eq}}, \theta_{\text{eq}}, \phi_{\text{eq}})$ presents the radial and angular equilibrium positions. In the case of azimuthally symmetric PES (parallel fields) only $(R_{\text{eq}}, \theta_{\text{eq}})$ is provided. In case the considered PES possesses double well character both angular equilibrium positions are presented (e.g. $(1432a_0, (0, \pi), \pi)$ for IV_{\perp} , $B \ll E$).

	I_{\parallel}	II_{\parallel}	III_{\parallel}	IV_{\parallel}
$B \gg E$	$1728a_0, \frac{\pi}{2}$	$1918a_0, \frac{\pi}{2}$	$2159a_0, \frac{\pi}{2}$	$1432a_0, (0, \pi)$
$B \ll E$	$1750a_0, \pi$	$1940a_0, \pi$	$2175a_0, \pi$	$1432a_0, \pi$

	I_{\perp}	II_{\perp}	III_{\perp}	IV_{\perp}
$B \gg E$	$1728a_0, \frac{\pi}{2}$	$1918a_0, \frac{\pi}{2}$	$2159a_0, \frac{\pi}{2}$	$1432a_0, (0, \pi)$
$B \ll E$	$1750a_0, \pi$	$1940a_0, \pi$	$2175a_0, \pi$	$1432a_0, \pi$

6.6 Rovibrational states

6.6.1 Parallel field configuration

To analyze the rovibrational states for the parallel field configurations we introduce cylindrical coordinates (ρ, Z, ϕ) for the parametrization $\epsilon_{\parallel}(\rho, Z)$. We have $[H_{\text{rv}}, L_z] = 0$, which means the azimuthal quantum number m is a good quantum number. With this we write the rovibrational wave function $\Phi(\rho, Z, \phi) = \frac{F_{\nu m}(\rho, Z)}{\sqrt{2\pi\rho}} \exp(im\phi)$, $m \in \mathbb{Z}$, $\nu \in \mathbb{N}_0$ which transforms the Hamiltonian (6.5) into

$$H_{\text{rv}} = -\frac{1}{m_{\text{n}}}(\partial_{\rho}^2 + \partial_Z^2) + \frac{m^2 - 1/4}{m_{\text{n}}\rho^2} + \epsilon_{\parallel}(\rho, Z). \quad (6.12)$$

We solve the corresponding Schrödinger equation focusing on $m = 0$ using a fourth order finite difference method for electric field strengths in the range $0, 20, \dots, 80$ V/m and $B = 60$ G.

In Fig. 6.8 we present the ground state probability densities of the local potential wells (I_{\parallel} - III_{\parallel})

in cylindrical coordinates (ρ, Z) . We label the densities according to the applied field strengths E with a, b, c, d, e . For instance, $(\text{III}_{||}, c)$ indicates the probability density of the ground state in the well $(\text{III}_{||})$ with an applied electric field strength of $E = 40 \text{ V/m}$. As described in Section 6.5 with increasing electric field strength the wells move from the $\theta = \pi/2$ configuration to the $\theta = \pi$ direction. This feature is clearly reflected in the position of the ground state probability densities. We observe that the larger the radial separation R is the stronger the impact of the electric field on the position of the ground state density position. For instance, the ground state density $(\text{II}_{||}, e)$ is nearly at the same position as the density distributions $(\text{II}_{||}, d)$ and $(\text{III}_{||}, c)$, respectively. As the results for all three potential wells only differ quantitatively we restrict our analysis on the $\text{III}_{||}$ potential well. For field strengths beyond $E = 40 \text{ V/m}$ the position of the minimum of this particular well remains close to $\theta = \pi$. As a result there are no qualitative changes of the corresponding ground state rovibrational probability densities $(\text{III}_{||}, c)$ - $(\text{III}_{||}, e)$. The rovibrational density distributions $(\text{III}_{||}, a)$ - $(\text{III}_{||}, c)$ can be characterized by their radial ΔR and angular extension $\Delta\theta$. Typical values observed, are of the order of $\Delta R = 80a_0$ and $\Delta\theta = 250a_0$ $(\text{III}_{||}, c)$ up to $650a_0$ $(\text{III}_{||}, b)$. We see that with increasing electric field strength from $E = 0$ to 20 V/m the angular extensions of the rovibrational probability densities in $(\text{III}_{||}, a)$ and $(\text{III}_{||}, b)$ increase as well. For higher field strengths the potential well $(\text{III}_{||})$ approaches $\theta = \pi$ and the angular extension of the probability density decreases again. This is clearly visible already for $(\text{III}_{||}, c)$ in Fig. 6.8 and is caused by the potential term $-1/(4m_n\rho^2)$.

In Fig. 6.9(a) we present the the first five eigenenergies of the rovibrational states for the potential well $(\text{III}_{||})$ of the s -wave PES, relative to the minimum of the potential well. The level spacing decreases to 2 MHz for $E = 20 \text{ V/m}$ which can be explained by the minor decrease of the angular confinement. With increasing E beyond a field strength of 470 V/m the potential gets affected by the centrifugal term in Eq. (6.12) and the angular confinement increases. This leads to a larger level spacing up to 10 MHz as can be seen in Fig. 6.9(a). For the p -wave PES the level spacing is of the order of $10\text{-}30 \text{ MHz}$ as shown in Fig. 6.9(b). In the case of the low-lying states it hardly varies with increasing field strength; only the higher excited states are affected in the sense that their level spacing increases from 5 to 10 MHz . This can be explained by the fact that enhancing the electric field strength increases the angular confinement which affects the higher excited states more strongly than the energetically low-lying ones.

In Fig. 6.10(a,b) we present the (scaled) probability densities $|F_{\nu 0}|_{\nu=0,4}^2$ for the vibrational ground state ($\nu = 0$) and the fourth excitation ($\nu = 4$) for $B = 60 \text{ G}$. The equilibrium distance for the PES is located at $Z = -1435a_0$. The ground state distribution $|F_{00}(\rho, Z)|^2$ is characterized by a deformed Gaussian that is localized at $Z = -1435a_0$ and $\rho = 35a_0$. In Z/ρ -direction the density distribution possesses an extension of approximately $50a_0$ and $100a_0$, respectively. The density profile for the fourth ($\nu = 4$) shows five separate two-dimensional Gaussian like density peaks with increasing intensity located at $(Z, \rho) = (-1435a_0, 25a_0)$, $(-1432a_0, 75a_0)$, $(-1430a_0, 140a_0)$, $(-1420a_0, 200a_0)$ and $(-1405a_0, 290a_0)$, respectively.

6.6.2 Perpendicular field configuration

In the case of the crossed field configuration we have $[H_{rv}, P_Y] = [H_{rv}, P_Z] = 0$ where $P_Y : Y \rightarrow -Y$ and $P_Z : Z \rightarrow -Z$. Due to these symmetry properties the wave functions $F(\rho, Z, \phi)$ obey now $F(\rho, -Z, \phi) = \pm F(\rho, Z, \phi)$ and $F(\rho, Z, 2\pi - \phi) = \pm F(\rho, Z, \phi)$. To estimate the rovibrational level spacings we use the fact that the exact potential energy surfaces can be expanded around their equilibrium positions $(R_{\text{eq}}, \theta_{\text{eq}}, \pi)$ as

$$\epsilon_{\perp}(R, \theta, \phi) \approx \epsilon_{\perp}(R_{\text{eq}}, \theta_{\text{eq}}, \pi) + \frac{m_n}{4}\omega_R^2(R - R_{\text{eq}})^2 + \frac{m_n}{4}\omega_{\theta}^2 R_{\text{eq}}^2(\theta - \theta_{\text{eq}})^2 + \frac{m_n}{4}\omega_{\phi}^2 R_{\text{eq}}^2(\phi - \pi)^2. \quad (6.13)$$

For small extensions in the angular directions (θ, ϕ) the quantities $R_{\text{eq}}(\phi - \pi)$, $R_{\text{eq}}(\theta - \theta_{\text{eq}})$ define together with $R - R_{\text{eq}}$ a local Cartesian coordinate system. In these coordinates, Eq. (6.5) is

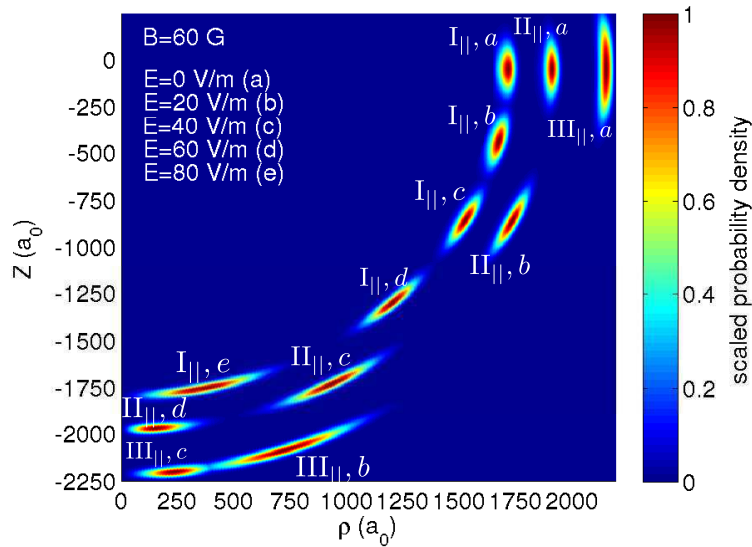


Figure 6.8: Scaled probability densities $|F_{00}(\rho, Z)|^2$ for rovibrational wave functions. Shown are the ground state probability densities in the potential wells (I_{||})-(III_{||}) for electric field strengths $E = 0, 20, \dots, 80$ V/m for the parallel field configuration with $B = 60$ G. The densities for the corresponding field strengths are labeled by a, b, c, d, e .

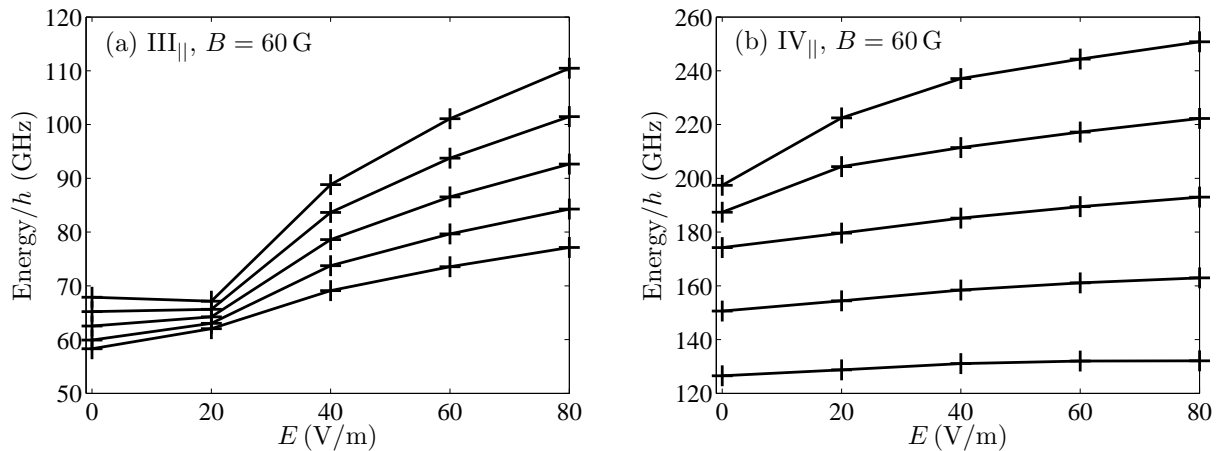


Figure 6.9: In figure (a) the rovibrational eigenenergies for the five energetically lowest states in the (III_{||}) well are shown with varying electric field strength E . The level spacing first decreases and afterwards increases up to 10 MHz. Figure (b) shows the eigenenergies for the five energetically lowest states in the (IV_{||}) well of the p -wave PES. Here the level spacings for the energetically lowest states remain constant and only for the higher excited states the increasing angular confinement causes an increase. We find a level spacing between 10-30 MHz.

reduced to three single harmonic oscillators providing level spacings ω_R , ω_θ and ω_ϕ . In Fig. 6.11 we present such an approximation scheme for the $B = 20$ G, $E = 60$ V/m crossed field configuration for the coordinates (R, ϕ) . We clearly see that the harmonic approximation (crosses) fits the exact potential quite well. From this fit the frequencies of the harmonic oscillator can be extracted

$$\omega_i = \sqrt{\frac{4\Delta V}{Ma_i^2 R_{\text{eq}}^2}}, \quad i = \theta, \phi, \quad \omega_R = \sqrt{\frac{4\Delta V}{Ma_R^2}}. \quad (6.14)$$

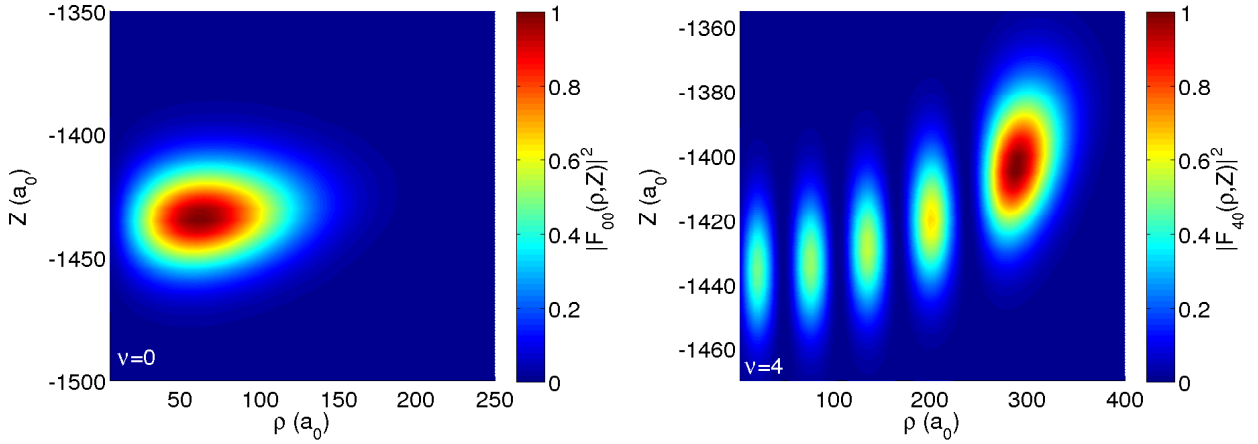


Figure 6.10: Scaled probability densities $|F_{\nu 0}(\rho, Z)|^2_{\nu=0,4}$ for the rovibrational wave functions of the p -wave potential well IV_{\perp} . In (a) we observe a for deformed Gaussian like density profile for the ground state ($\nu = 0$) centered at $Z = -1435a_0$ and $\rho = 65a_0$. In Z/ρ -direction the density distribution has an extension of approximately $50a_0/100a_0$. In (b) we show the density profile for the fourth excited state ($\nu = 4$). This density profile provides five peaks at $(Z, \rho) = (-1435, 25a_0)$, $(-1432a_0, 75a_0)$, $(-1430a_0, 140a_0)$, $(-1420a_0, 200a_0)$ and $(-1405a_0, 290a_0)$.

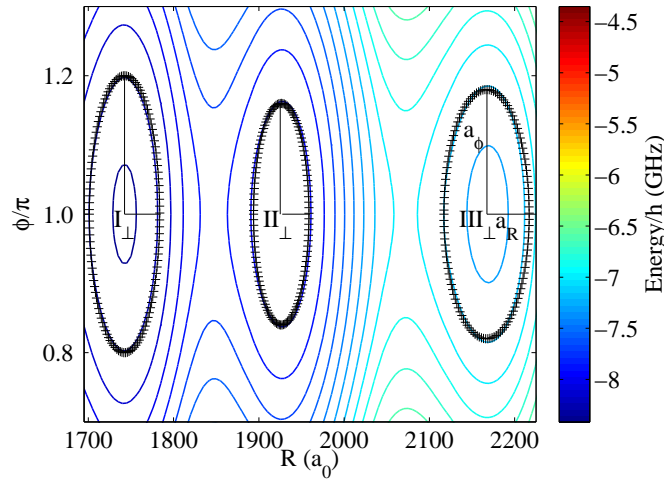


Figure 6.11: Contour plot of the s -wave PES for $\theta = \pi/2$ with applied field strengths $B = 20 \text{ G}$, $E = 60 \text{ V/m}$. ($\theta_E = \pi/2$). We clearly see the $\phi = \pi$ reflection symmetry. The ellipses indicated by the black crosses represent approximations to the exact potential surface according to Eq. (6.13). From the ellipse parameters we get a level spacing of approximately 130 MHz for the radial and 5 MHz for the angular degrees of freedom via Eq. (6.14).

where ΔV , a_i and a_R are the energy difference to the potential minimum and the fitted values for the semi-axis of the underlying ellipsoid. For the specific setup we find level spacings of $\omega_R = 130 \text{ MHz}$ (I_{\perp}), 140 MHz (III_{\perp}) and 150 MHz (II_{\perp}). This means that each potential well only provides up to one radial excitation. For the angular degrees of freedom we get $\omega_{\phi} \approx \omega_{\theta} = 5 \text{ MHz}$ for all three potential wells. In the case of the (IV_{\perp}) potential well for the p -wave PES we obtain level spacings of the order of $\omega_R \approx 200 \text{ MHz}$ in the radial and $\omega_{\theta} = 5 - 20 \text{ MHz}$, $\omega_{\phi} = 5 \text{ MHz}$ in the angular degrees of freedom.

We remark that for both field configurations and for both s - and p -wave PES the radial as well as the angular level spacings strongly depend on the applied fields. The general level structure implies a single radial excitation ($130 - 250 \text{ MHz}$) with several angular excitations ($5 - 30 \text{ MHz}$) on

top. For both field configurations the states in the wells ($I_{||}$ - $III_{||}$) and (I_{\perp} - III_{\perp}) of the s -wave PES possess a finite lifetime due to a tunneling out of the local potential wells. These lifetimes strongly depend on the considered field strengths and we get maximal lifetimes of order of microseconds.

6.7 Molecular alignment and orientation

In Section 6.5 we presented the possibility to vary the topology of the molecular PES via tuning of the electric and magnetic fields. Obviously, this provides the possibility to control the molecular orientation and alignment.

To quantify the orientation and alignment in case of the parallel field configuration we have to analyze the expectation value $\langle \cos(\theta) \rangle_{\Phi}$ and the variance $\Delta \cos(\theta) = \sqrt{\langle \cos(\theta)^2 \rangle_{\Phi} - \langle \cos(\theta) \rangle_{\Phi}^2}$. The expectation values $\langle \dots \rangle_{\Phi}$ are taken with respect to the rovibrational state $\Phi(\mathbf{R})$ for the ground states in the potential wells ($I_{||}$), ($II_{||}$) and ($III_{||}$). The closer the absolute value of $\langle \cos(\theta) \rangle_{\Phi}$ is to one, the stronger is the orientation of the state into the Z -direction and the closer $\Delta \cos(\theta)$ is to zero, the stronger is the alignment of the state. We consider the ground state probability densities in the single wells to be strongly localized such that we can approximate the expectation values according to $\langle \cos(\theta) \rangle_{\Phi} \approx \cos(\theta_{\text{eq}})$ and $\langle \cos(\theta)^2 \rangle_{\Phi} \approx \cos(\theta_{\text{eq}})^2$ where θ_{eq} denotes the angular equilibrium position of the underlying potential well (see Fig. 6.8). In this approximation we get for the variance $\Delta \cos(\theta) \approx 0$, which means that the degree of alignment is perfect.

In Fig. 6.12(a) we present the dependence of $\cos(\theta_{\text{eq}})$ of the ground state state of the potential well ($II_{||}$) on the applied field. The inset in this figure shows the same analysis but for the ($I_{||}$) well. We see that for pure magnetic and pure electric fields the state is oriented in a perpendicular (red region) and antiparallel (blue region) configuration, respectively. For both potential wells we find a crossover regime (yellow region) between these two configurations. We see that for fixed magnetic field strength the antiparallel configuration for the well ($II_{||}$) is achieved for lower electric field strengths than for ($I_{||}$). This can be explained by the fact that the electric field stronger affects the states in the well ($II_{||}$) as compared to ($I_{||}$) (see Section 6.5). In the case

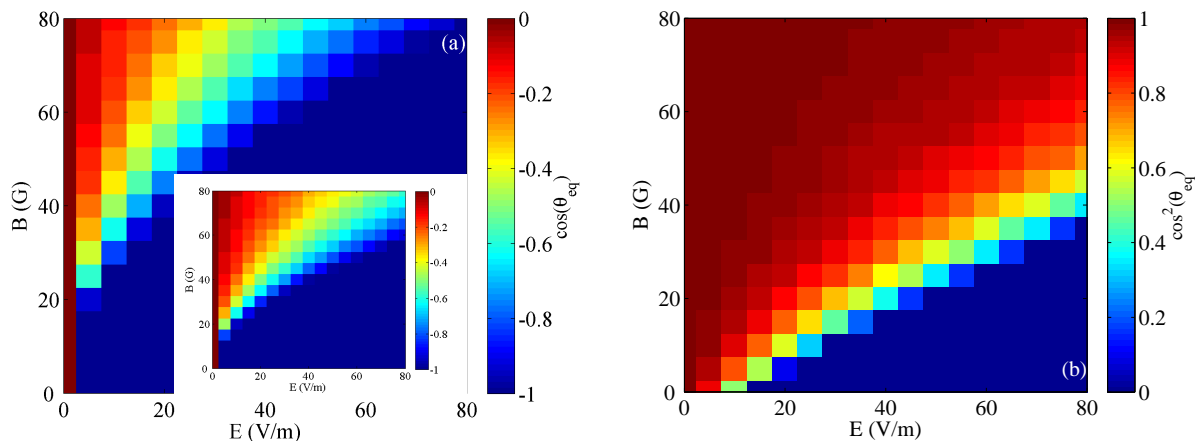


Figure 6.12: (a) Orientation $\langle \cos(\theta) \rangle_{\Phi} \approx \cos(\theta_{\text{eq}})$ of the ground state in the potential well ($II_{||}$) (main figure) and ($I_{||}$) (inset) belonging to the s -wave PES. For pure electric/magnetic fields the internuclear axis is oriented in an antiparallel/perpendicular configuration. By varying the field strengths the orientation can be tuned. For fixed magnetic field strength the antiparallel configuration for the well ($II_{||}$) is achieved for lower electric field strengths than for ($I_{||}$). (b) Alignment $\langle \cos(\theta)^2 \rangle_{\Phi} \approx \cos(\theta_{\text{eq}})^2$ of the ground state in the potential well IV_{\perp} belonging to the p -wave PES. For pure electric/magnetic fields the molecule is anti-/aligned with respect to the magnetic field.

of the crossed field configuration the rovibrational Hamiltonian (6.12) possesses a P_Z reflection symmetry i.e. we get $\langle \cos(\theta) \rangle_{\Phi} = 0$. In this case the molecular alignment is quantified by

$\langle \cos^2(\theta) \rangle \approx \cos^2(\theta_{\text{eq}})$, $\theta_{\text{eq}} \in [0, \pi/2]$ for ground rovibrational states. For the s -wave PES we have molecular states with a well-defined perpendicular configuration of the internuclear axis with respect to the z -axis. Here we have $\cos^2(\theta_{\text{eq}}) = 0$, which means they are antialigned with respect to the z -axis. For the p -wave PES and finite magnetic field strength we have potential surfaces with double well character. In this case the rovibrational states are delocalized over the double wells.

In Fig. 6.12(b) we present the field-dependent alignment of the ground states in the corresponding IV_{\perp} potential well. We see that for pure electric and magnetic field configuration we have perfectly (anti)aligned molecular states. Similar to the molecular orientation for the parallel field configuration we find a crossover regime (yellow region) where the alignment changes from antialigned (blue region) to aligned states (red region).

6.8 Electric dipole moment

Due to the impact on the molecular configuration the electric dipole moment can be readily tuned by changing the field strengths and specific field configuration. Let us analyze the dipole moments along the internuclear axis in the following

$$D_{\text{el}} = \langle \psi(\mathbf{r}; \mathbf{R}_{\text{eq}}; \mathbf{B}, \mathbf{E}) | \mathbf{n} \cdot \mathbf{r} | \psi(\mathbf{r}; \mathbf{R}_{\text{eq}}; \mathbf{B}, \mathbf{E}) \rangle, \quad (6.15)$$

where \mathbf{n} denotes the unit vector along the internuclear axis.

In Fig. 6.13 we show the electric dipole moment for the s -wave PES for the parallel field configuration as a function of E and B . We observe that with increasing B the dipole moment decreases while it increases for increasing E . This can be understood by the fact that in the absence of any contact interaction and $B \neq 0$, $E = 0$ the reflection operations $P_x \otimes P_y$ and P_z are exact symmetries of the Hamiltonian (6.4). In the presence of the neutral perturber and $B = 0$, $E = 0$ the mixing of degenerate Rydberg states leads to an electric dipole given by the semiclassical approximation $D_{\text{el}} \approx R_{\text{eq}} - \frac{n^2}{2}$ for a purely s -wave interaction dominated PES. However, with increasing magnetic field the magnetic field terms become dominant and the corresponding symmetry properties get imprinted in the quantum states [99]. For a pure strong magnetic field case the s -wave PES is approximately dominated by the $|35, 34, -34\rangle$ hydrogen state which explains the decrease of the electric dipole moment. In the case of an increasing electric field the electron cloud is more aligned into the negative field direction which causes the increase of D_{el} .

Next we perform some (semi)analytical analysis to estimate the electric dipole moment. First we check the validity of the semiclassical approximation for finite electric and magnetic field strengths. As discussed in Section 6.5 for the considered field regimes the radial positions of the potential wells is only to a minor extent affected by the external fields (see table 6.1). Therefore, we estimate the electric dipole moment as $\bar{R}_{\text{eq}} - \frac{n^2}{2}$ where \bar{R}_{eq} denotes the mean value of the minimal and maximal radial positions for a considered potential well for varying field strength. For instance, $R_{\text{eq}, I_{\parallel}} = 1728a_0$ for $B = 80$ G, $E = 0$ and $R_{\text{eq}, I_{\parallel}} = 1750a_0$ for $B = 0$ G, $E = 80$ V/m which gives $\bar{R}_{\text{eq}, I_{\parallel}} = (1728a_0 + 1750a_0)/2 = 1739a_0$ and an approximate dipole moment of $D_{\text{el}} \approx 2.85$ kDebye. This corresponds to a relative deviation of 5% compared to the exact result, which means that in the considered parameter regime this simple estimate is quite accurate.

As discussed in Section 6.5 in case of the p -wave PES its equilibrium position remains constant ($R_{\text{eq}} = 1432a_0$, $\theta_{\text{eq}} = \pi$) with respect to a variation of the field strengths. In particular, in Section 6.4.1 we have shown that the corresponding electronic eigenvector $|\psi(\mathbf{r}; \mathbf{R}_{\text{eq}}; B, E)\rangle$ is independent of the applied magnetic field. Due to this we can reduce the analysis of the dipole moment of the p -wave state to an arbitrary value of B which we choose to be $B = 0$ G. In Fig. 6.13(b) we show the electric dipole moment for the p -wave PES for $B = 0$ G as a function of E . With increasing electric field strength D_{el} grows quadratically. To verify this we present a corresponding semi-analytical result for the electric dipole moment where we expanded the state $|\psi(\mathbf{r}; \mathbf{R}_{\text{eq}}; B = 0, E)\rangle$

Table 6.2: Minimal ($D_{\text{el,min}}$) and maximal ($D_{\text{el,max}}$) electric dipole moment for the potential wells (I_{\perp} - III_{\perp}). The minimal (maximal) values are taken for $B = 80$ G, $E = 0$ V/m ($B = 0$ G, $E = 80$ V/m). For comparison we present the semiclassical approximation $\bar{R}_{\text{eq}} - \frac{n^2}{2}$.

	$D_{\text{el,min}}$	$D_{\text{el,max}}$	$\bar{R}_{\text{eq}} - \frac{n^2}{2}$
I_{\perp}	2.69	2.94	2.86
II_{\perp}	3.25	3.39	3.34
III_{\perp}	3.92	3.98	3.95

in a perturbative series up to the $\mathcal{O}(E^2)$:

$$|\psi(\mathbf{r}; \mathbf{R}_{\text{eq}}; 0, E)\rangle = |\psi_0(\mathbf{r}; \mathbf{R}_{\text{eq}})\rangle + E \sum_{n \neq 0} C_n^{(1)} |\psi_n(\mathbf{r}; \mathbf{R}_{\text{eq}})\rangle + E^2 \sum_{n \neq 0} C_n^{(2)} |\psi_n(\mathbf{r}; \mathbf{R}_{\text{eq}})\rangle. \quad (6.16)$$

In this expansion $|\psi_n(\mathbf{r}; \mathbf{R}_{\text{eq}})\rangle$ indicate the field-free electronic states and $C_n^{(1,2)}$ are the expansion coefficients given by standard perturbation theory [118]. Inserting this ansatz into (6.15) and keeping terms up to $\mathcal{O}(E)$ and $\mathcal{O}(E^2)$ we obtain the linear term (red) and quadratic term (green) approximations according to Fig. 6.13(b). We see that the exact data (blue line and crosses) are well approximated by the quadratic approximation. The semiclassical approximation gives a result of $D_{\text{el}} = 2.08$ kDebye which deviates from the obtained data by 10%. The larger deviation compared to the s -wave state can be explained by the fact that the semiclassical approximation is originally derived for s -wave interactions in the absence of any fields. Although we expect the p -wave state to possess a strong s -wave character far away from the region of avoided crossings ($R < 1450a_0$) for the region of the localized potential well ($R_{\text{eq}} = 1432a_0$) the p -wave character still provides a substantial contribution which explains the less accurate result for the resulting electric dipole moment.

For the crossed field configuration the electric dipole moments of the s -wave PES potential wells

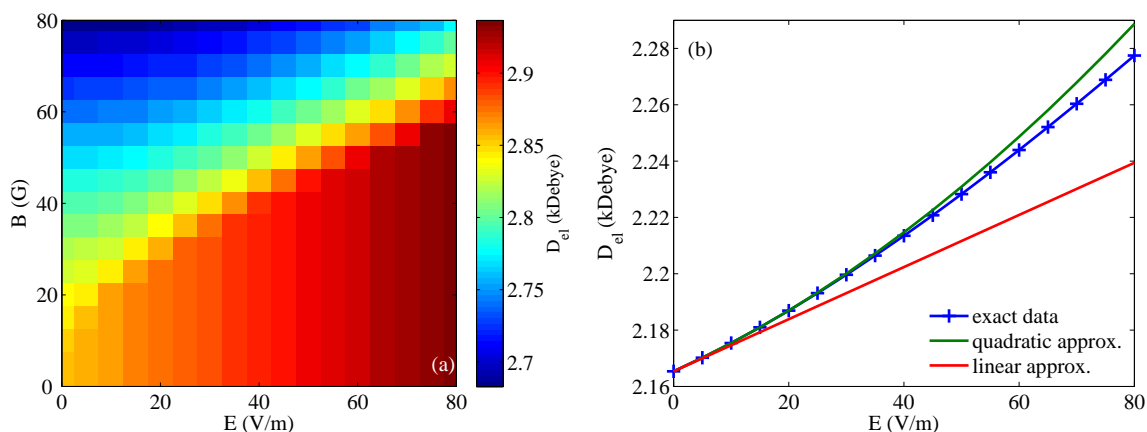


Figure 6.13: (a) shows the electric dipole moment D_{el} in the direction of the internuclear axis for the s -wave PES for the parallel field configuration. Using the mean value $\bar{R}_{\text{eq}} = 1739a_0$ the semiclassical approximation $D_{\text{el}} \approx \bar{R}_{\text{eq}} - \frac{n^2}{2}$ gives $D_{\text{el}} \approx 2.85$ kDebye. (b) shows the electric dipole moment for the p -wave PES. In addition we show a comparison with the semi-analytic expansion (6.16). The red respectively green curve indicate a linear ($\mathcal{O}(E)$) and quadratic approximation ($\mathcal{O}(E^2)$).

(I_{\perp} - III_{\perp}) show a qualitatively similar behavior as their counterparts (I_{\parallel} - III_{\parallel}) in case of the parallel configuration. For all potential wells we find a decreasing dipole moment for increasing magnetic

field strength and an increase of D_{el} for an increasing electric field strength. In table 6.2 we present the minimal ($D_{\text{el,min}}$) and maximal ($D_{\text{el,max}}$) value of the electric dipole moment (6.15) for the wells (I $_{\perp}$ -III $_{\perp}$). As for the parallel field configuration we compare these results with the semiclassical approximation $\bar{R}_{\text{eq}} - \frac{n^2}{2}$. With a maximal deviation of 1-5% the exact results are reproduced satisfactorily.

6.9 conclusion

In this work we have explored the effect of combined electric and magnetic fields on the polar high angular momentum molecular states for a parallel as well as a crossed field configuration. Taking into account both s - and p -wave interactions it turns out that for a pure magnetic field configuration strong level repulsion causes the potential wells which provide the trilobite states in the field-free case [85] to vanish. For this PES beyond a critical field strength of around 100 G no bound states are provided anymore. For finite field strengths the angular degrees of freedom are converted from rotational to vibrational degrees of freedom, thereby rendering the field-free potential energy curve into a two- and three-dimensional energy surface for parallel and crossed field configurations, respectively. We obtain oscillatory potential curves with localization in the radial and angular degrees of freedom with depths up to hundreds of MHz providing a rich topology depending on the specific degree of electronic excitation and field configuration. The resulting rovibrational level spacings are in the order of several MHz.

The parallel as well as the crossed field configuration provide unique ways to control the topology of the adiabatic potential energy surfaces. This directly leads to the possibility to control molecular orientation and alignment for the parallel and crossed field configuration, respectively. For instance, for parallel fields the molecular orientation can be tuned from a perpendicular to an antiparallel configuration by varying applied field strengths. In the case of crossed fields the molecular alignment can be changed between an aligned and anti-aligned configuration with respect to the magnetic field. In addition, the topological control of the PES provides the possibility of directly controlling the electric dipole moment as well. Apart from numerical results we have provided also a semiclassical estimate and perturbative analysis of the electric dipole moment.

The plethora of interesting effects of high- l ultralong-range Rydberg molecules in external fields keeps this particular species a promising candidate for future investigations. Because of its high sensitivity to small field strengths it is worth studying the dependence of molecular properties like electric and magnetic polarizabilities and susceptibilities. In the case of Rydberg atoms these quantities strongly depend on the Rydberg excitation. The results from this chapter have been published in Ref. [5].

Chapter 7

Alignment of ultracold $D_{5/2}$ -state Rydberg molecules

7.1 Introduction

In this chapter we show that a weak magnetic field of a dozen Gauss allows us to strongly impact and control the properties of ultralong-range $D_{5/2}$ -state Rydberg molecules. Rydberg molecules have been theoretically predicted [85, 86, 95, 99] and so far experimentally observed for Rydberg S -states [87, 90, 92], P -states [93] and recently D -states as well [94]. In this work we investigate ultralong-range D -state Rydberg rubidium molecules for two different m_J substates of the Rydberg electron with high resolution photoassociation spectroscopy. We specifically study molecular states emerging from the $D_{5/2}$, $m_J = 1/2$ and $m_J = 5/2$ electronic states for principal quantum numbers n ranging from $n = 41$ to 49. Depending on the degree of electronic excitation we obtain two different classes of D -state Rydberg molecules. These two species are characterized by aligned and antialigned molecular states. We selectively excite distinct rovibrational molecular states with specific alignments and identify them by a comparison of the binding energies with theoretical predictions. The results provided by both approaches agree well. In this chapter we mainly outline the concepts and results of the theoretical studies. We hereby proceed as follows: In Section 7.2 we present the basic aspects of the experimental setup which has been used for this work. Hereby we discuss both the applied Rydberg excitation scheme and the ion detection method. Section 7.3 provides a formulation of the problem, presenting the working Hamiltonian and a discussion of the underlying interactions. Section 7.4 contains our methodology and a review of the calculated adiabatic potential energy surfaces (PES). Hereafter, a discussion of the rovibrational energies and states is provided in Section 7.5. In Section 7.6 and 7.7 the theoretically obtained rovibrational energies are compared to experimental spectra and the alignment of the different molecular states is discussed in detail.

This work was done in collaboration with the experimental group of Prof. Dr. Tilman Pfau from the 5. Physikalisches Institut from the University of Stuttgart, Germany. Most experimental studies were performed by Alexander Krupp, Anita Gaj (PhD students) and Dr. Jonathan Balewski. The theoretical results which are mainly presented in this chapter were provided by Markus Kurz (PhD student) and Prof. Dr. Peter Schmelcher from the Center for Optical Quantum Technologies at the University of Hamburg, Germany. The results of this collaboration have been published in [4].

7.2 Experimental setup

In this section we present the basic aspects of the experimental setup which was used to create the D -state Rydberg molecules and to measure their properties such as binding energies and degree of alignment. In particular, we describe the preparation scheme of the rubidium samples and the cooling processes required to reach ultracold temperatures.

We note that this section only provides the basic concepts of the experimental setup. For more detailed information please refer to [140, 141, 197–199] and references therein.

7.2.1 Preparation of samples of ultracold rubidium atoms

In this paragraph we discuss the main processes which lead to a magnetically trapped sample of rubidium atoms at thermal or BEC temperatures.

Starting point in the preparation process is an oven in which a sample of elementary rubidium is constantly heated up to 150°C . From the heating oven the rubidium atoms fly into a Zeeman slower [200,201] which possesses a length of around 85 cm. Here the fast atoms are decelerated and guided in the main BEC chamber of the experimental setup. Here a magneto-optical trap (MOT) catches and traps the atoms possessing the right velocity. A differential pumping system is installed to provide a constant pressure gradient from 10^{-7} mbar to 10^{-11} mbar in the main chamber. The loading time of the BEC chamber is given with 2 s, during this period time a mechanical shutter separates the oven part from the vacuum chamber and blocks the hot atoms from accessing the Zeeman slower. The MOT itself consists of three pairs of orthogonal and counter propagating laser beams and a magnetic quadrupole field which is generated by two pinch coils. The laser light which is used to cool and trap the rubidium atoms is provided by a Titanium-Sapphire laser system with the main cooling transition $5S_{1/2}(F=2) \rightarrow 5P_{3/2}(F=3)$. An additionally repumping laser for the MOT and the Zeeman slower is required since the cooling transition is not closed and atoms also decay to the $5S_{1/2}(F=1)$ state. The repumping laser drives the transition $5S_{1/2}(F=1) \rightarrow 5P_{3/2}(F=2)$. Atoms in this specific hyperfine state decay with a relative probability of 50 to the $5S_{1/2}(F=2)$ state and are thus part of the cooling cycle again. More details about the laser system can be found in [199] and [197]. After a molasses cooling phase, the atoms are transferred from the MOT into a pure magnetic trap. The final step to reach the BEC

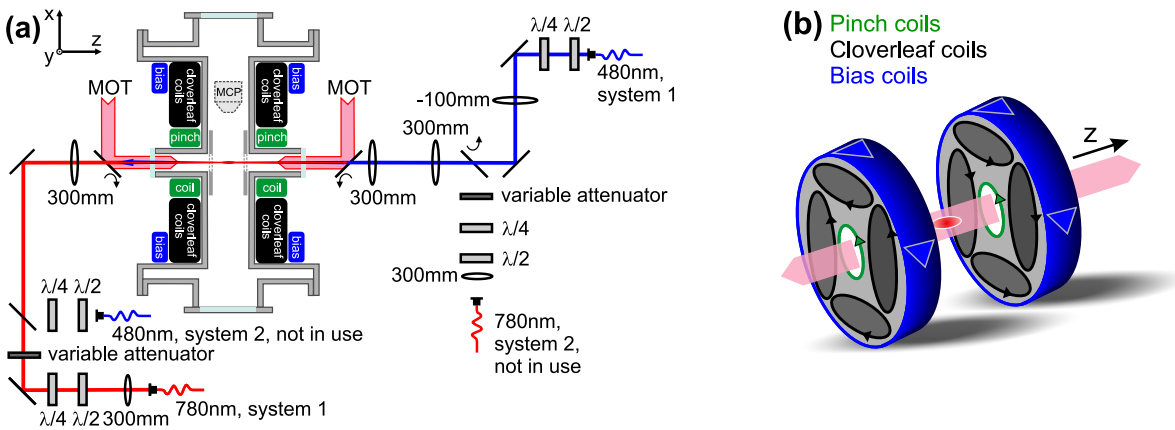


Figure 7.1: (a) Rydberg excitation laser setup as it is configured around the main vacuum chamber. The different magnetic coils (pinch (green), bias (blue) and cloverleaves (black)) are wound around the outside of the chamber. The optical paths of the MOT beams can be guided by small, pivoting mirrors. During loading the MOT the MOT beams are guided into the chamber. Afterwards they are flipped down to open the optical path for the Rydberg excitation lasers (red laser system, $\lambda = 780$ nm, blue laser system, $\lambda = 480$ nm) into the vacuum chamber. In (b) the different magnetic field coils are shown in more detail. In addition, the winding directions of the single coils are presented (picture taken from [140]).

regime is the evaporative cooling procedure to obtain temperatures in the $\mu\text{K} - \text{nK}$ regime [7]. The basic idea of this procedure is to drive the transitions between magnetically split m_F and $m_F \pm 1$ sublevels of the $5S_{1/2}(F=2)$ hyperfine state off-resonantly using a radio frequency (RF). In a scanning ramp of 40 s the radio frequency ramps down from 45 MHz to 1 MHz. Due to this atoms are transferred into the untrapped $m_F \leq 0$ states. The detuned frequency ramp is chosen in a such a way that only hot atoms at the outer parts of the magnetic trap are affected. Here the atoms experience a larger Zeeman shift and therefore are transferred into untrapped states. By losing the fastest atoms the complete ensemble of rubidium atoms rethermalizes and the overall temperature of the atomic cloud is reduced. For the evaporative cooling process it is crucial that the atomic ensemble possesses a high atomic density since this increases the efficiency of the rethermalization process due to collisions. This is essential for the cooling cycle as it generates new hot atoms again. Depending on the final frequency of the RF scanning ramp, either a cold thermal rubidium

ensemble ($\rho_{\text{peak}} \sim 10^{12} \text{ cm}^{-3}$, $T \sim 1 \mu\text{K}$) or a BEC ($\rho_{\text{peak}} \sim 10^{14} \text{ cm}^{-3}$, $T \sim 100 \text{ nK}$) can be realized. For this specific setup a typical condensate atom number is about $7 \times 10^4 - 10^5$.

After the evaporative cooling procedure the magnetic offset field at the center of the magnetic trap can be tuned from its initial value of about 0.8 G to the highest possible value of $B_0 = 13.55 \text{ G}$. This is achieved by ramping down the current of the bias coils which are used for compensation. As the Zeeman splitting increases with the magnetic field strength the radio frequency needs to be adjusted to guarantee the removal of only the hottest atoms. However, this procedure has to be performed in a very controlled way. Otherwise one might excite collective condensate modes, shape oscillations for instance, or even destroy the complete BEC.

In this work all experiments were conducted at the highest possible offset field of $B_0 = 13.55 \text{ G}$. For the considered D -state molecule this is crucial as a sufficiently large magnetic field is required to split and address different m_J states separately. For this offset field the axial trapping frequency is $\omega_z = 2\pi \times 22 \text{ Hz}$ whereas the radial trapping frequency is given by $\omega_r = 2\pi \times 82 \text{ Hz}$.

7.2.2 Rydberg excitation

The excitation of the rubidium Rydberg states is performed by a two-photon excitation process depicted in the scheme of Fig. 7.2. A σ^+ -polarized 780 nm laser drives the transition from the $5S_{1/2}(F = 2m, m_F = 2)$ ground state to the intermediated $5P_{3/2}(F = 3, m_F = 3)$ state. The upper transition is conducted by a σ^+ - or σ^- -polarized 480 nm laser to address the Rydberg D - and S -states. The red laser is $\Delta_p = 500 \text{ MHz}$ blue detuned from the intermediated state to prevent its population. This allows us to treat the three-level system as a simple two-level system, realizing a coherent coupling between ground and Rydberg state. In order to reduce Doppler broadening the blue and red laser beams for the Rydberg excitation are shone from the opposite direction onto the atomic ensemble in the main chamber. In contrast to a collinear setup this counter propagation beam setup reduces the Doppler broadening by more than a factor of three to around 19 kHz for $T \sim 1 \mu\text{K}$. To switch between the axial MOT beams, shone in during the MOT loading phase, and the two Rydberg excitation beams, two installed motorized flipping mirrors are used (see Fig. 7.1)

7.2.3 Ion detection method

The method used in this work to detect Rydberg atoms and molecules is a field ionization process. In this approach a sufficiently large voltage is applied to opposing field plates in the vacuum chamber in order to ionize the Rydberg molecules after they have been created via laser excitation. The energy needed for the ionization can be estimated by a classical calculation taking into account the Coulomb potential of the Rydberg ionic core and the Stark potential. In the resulting three dimensional potential possesses a saddle point and electrons above this local maximum become unbounded. One obtains for the classical ionization field

$$E_{\text{ion}} = \frac{1}{16n^{*4}} \quad (7.1)$$

where n^* is the effective principal quantum number. For $n = 35$ we obtain a field strength of $E_{\text{ion}} = 312 \text{ V/cm}$ which requires voltages of a few kV for the field plates. The voltage applied to ionize the Rydberg atoms and molecules is also used to accelerate the ions towards a micro channel plate (MCP) detector. A standard sequence for recording a spectrum with the ion detector is depicted in Fig. 7.3. After the cloud is prepared in the magnetic trap and cooled down to a few μK , the two excitation lasers create Rydberg atoms and molecules in the whole thermal cloud for typical time scales of 1-50 μs . Next an ionization field pulse is applied for a duration of 60 μs during which the ion signal is detected at the MCP. A complete cycle of excitation, ionization and detection is repeated 400 times using a single atomic cloud. Such a sequence is denoted as one experimental run. During a single run the red lasers frequency is changed after each cycle in

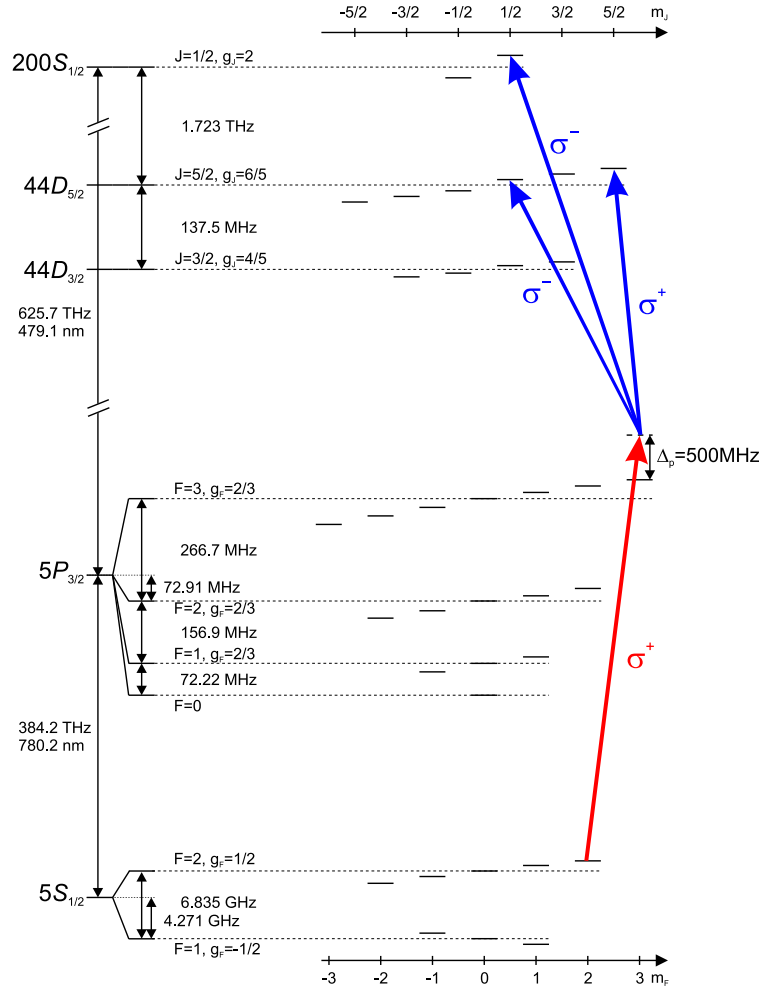


Figure 7.2: Level scheme for the Rydberg excitation of ^{87}Rb . Starting from the $5S_{1/2}$ ground state the excitation into the $44D_{3/2}$, $44D_{5/2}$ and $200S_{1/2}$ Rydberg states via the $5P_{3/2}$ intermediated state is shown exemplarily. For both the ground- and intermediate state the hyperfine splitting is presented. For the high n Rydberg states the hyperfine splitting is neglected. In addition, the splitting of the states in the presence of a finite magnetic field is indicated by the m_F quantum number (ground- and intermediate states) and m_J (Rydberg states), respectively. The Rydberg states are excited via a two-photon process using a red ($\lambda_{\text{red}} = 780\text{ nm}$) and blue ($\lambda_{\text{blue}} = 480\text{ nm}$) excitation laser. The laser are blue detuned by $\Delta_p = 500\text{ MHz}$ from the intermediated $5P_{3/2}(F = 3, m_F = 3)$ state. By changing the polarization of the upper transition (σ^- -polarization) S - and D -state Rydberg atoms (σ^+ - and σ^- -polarization) can be addressed. In the scheme only the most dominant transition path are shown (picture taken from [140]).

time steps of 6 ms. This sequence allows us to obtain a complete spectrum in a total experimental runtime of about 50 s.

7.3 The molecular Hamiltonian in a magnetic field

We start our analysis of ultralong-range D -state Rydberg molecules by considering a highly excited Rydberg atom interacting with a ground state neutral perturber atom (we will focus on the ^{87}Rb atom here) in a static and homogeneous magnetic field. The Hamiltonian treating the rubidium

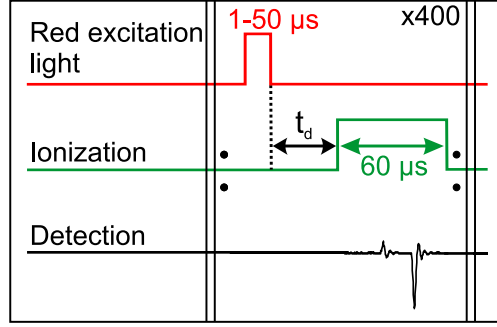


Figure 7.3: Temporal sequence for a spectroscopy measurement. A single experimental cycle consists of a 1-50 μs long laser excitation pulse and a 60 μs long ionization pulse. During this time a signal on the MCP can be detected. This cycle is repeated 400 times where every cycle possesses a slightly different laser detuning. In combination with the small laser bandwidth we obtain a high resolution spectrum (picture taken from [140]).

ionic core and the ground state atom as point particles is given by

$$H = \frac{\mathbf{P}^2}{m_n} + H_{\text{el}} + V_{n,e}(\mathbf{r}, \mathbf{R}), \quad (7.2)$$

$$H_{\text{el}} = H_0 + \frac{1}{2}\mathbf{B}(\mathbf{L} + 2\mathbf{S}) + \frac{1}{8}(\mathbf{B} \times \mathbf{r})^2, \quad H_0 = \frac{\mathbf{p}^2}{2} + V_l(r) + H_{\text{fs}} \quad (7.3)$$

where $(m_n, \mathbf{P}, \mathbf{R})$ denote the atomic rubidium mass and the relative momentum and position of the ground state atom with respect to the ionic core. The vector \mathbf{r} indicates the relative position of the Rydberg electron to the ionic core. The electronic Hamiltonian H_{el} consists of the field-free Hamiltonian H_0 of the Rydberg atom and the paramagnetic and diamagnetic terms of an electron in a static external magnetic field. The Hamiltonian H_0 includes the Rydberg quantum defects due to the angular momentum dependent electron-core potential $V_l(r)$ and the fine structure term H_{fs} . In addition, H_{el} contains the Zeeman-interaction terms of the angular momenta (spin and orbital) with the external field. We choose $\mathbf{B} = B\mathbf{e}_z$. The interatomic potential $V_{n,e}$ for the low-energy scattering between the Rydberg electron and the ground state atom is described as a Fermi-pseudopotential

$$V_{n,e}(\mathbf{r}, \mathbf{R}) = 2\pi A_s[k(R)]\delta(\mathbf{r} - \mathbf{R}) + 6\pi A_p^3[k(R)]\overleftarrow{\nabla}_r\delta(\mathbf{r} - \mathbf{R})\overrightarrow{\nabla}_r.$$

In our analysis we consider the triplet scattering of the electron from the ground state alkali atom. $A_s(k) = -\tan[\delta_0(k)]/k$ and $A_p^3(k) = -\tan[\delta_1(k)]/k^3$ denote the energy-dependent triplet s - and p -wave scattering lengths whereas $\delta_{l=0,1}(k)$ are the energy dependent phase shifts (see Fig. 2.1). The wave number $k(R)$ is determined by the semiclassical relation $k(R)^2/2 = E_{\text{kin}} = -1/2n^{*2} + 1/R$ where n^* is the effective principal quantum number.

We introduce the total electronic angular momentum $\mathbf{J} = \mathbf{L} + \mathbf{S}$ and write the total wave function as

$$\Psi_{\nu m}^{(nm,J)}(\mathbf{r}, \mathbf{R}) = \psi_{nm,J}(\mathbf{r}; \mathbf{R})\phi_{\nu m}^{(nm,J)}(\mathbf{R}). \quad (7.4)$$

where $\psi_{nm,J}(\mathbf{r}; \mathbf{R})$ describes the electronic molecular wave function in the presence of the ground state atom for a given relative position \mathbf{R} and $\phi_{\nu m}^{(nm,J)}$ determines the rovibrational state of the relative motion. Because $L = 2$, $s = 1/2$ we have $J = 3/2, 5/2$. Within the adiabatic approximation

we obtain

$$[H_0 + \frac{B}{2}(J_z + S_z) + \frac{B^2}{8}(x^2 + y^2) + V_{n,e}(\mathbf{r}, \mathbf{R})]\psi_{nm_J}(\mathbf{r}; \mathbf{R}) = \epsilon_{nm_J}(\mathbf{R})\psi_{nm_J}(\mathbf{r}; \mathbf{R}), \quad (7.5)$$

$$\left(\frac{\mathbf{P}^2}{m_n} + \epsilon_{nm_J}(\mathbf{R})\right)\phi_{\nu m}^{(nm_J)}(\mathbf{R}) = E_{\nu m}^{(nm_J)}\phi_{\nu m}^{(nm_J)}(\mathbf{R}). \quad (7.6)$$

The experimental field strength of $B_0 = 13.55$ G was used for the calculations. For such a field strength the diamagnetic term in (7.5) can be neglected. Furthermore, the adiabatic potential energy surfaces (PES) $\epsilon_{\nu m_J}(\mathbf{R})$ possess rotational symmetry around the z -axis, which means they depend on the angle of inclination Θ between the field vector and the internuclear axis and the radial distance R , i.e. $\epsilon_{nm_J}(\mathbf{R}) = \epsilon_{nm_J}(R, \Theta)$. In cylindrical coordinates the PES are then functions of (Z, ρ) .

7.4 Potential energy surfaces

In this work we have calculated the PES and analyzed the rovibrational dynamics of $D_{5/2}$ -Rydberg molecules with principal quantum numbers n ranging from 41 to 49 and the magnetic substates $m_J = 1/2$ and $m_J = 5/2$. To calculate the adiabatic potential surfaces we have expanded the electronic wave function $\psi_{nm_J}(\mathbf{r}; \mathbf{R})$ in terms of the eigenfunctions $\langle \mathbf{r} | nJm_J, L = 2, s = 1/2 \rangle \equiv \chi_{nJm_J}(\mathbf{r})$ of the field free Hamiltonian H_0 . Because of their energetic closeness the used basis set includes all states from the $J = 3/2$ and $J = 5/2$ manifold. In total the used basis set consists of ten states. We have

$$\begin{aligned} \chi_{nJm_J}(\mathbf{r}) &= R_{nJ2}(r) \left(\pm \sqrt{\frac{\frac{5}{2} \pm m_J}{5}} Y_{2, m_J - \frac{1}{2}}(\vartheta, \phi) | \uparrow \rangle + \sqrt{\frac{\frac{5}{2} \mp m_J}{5}} Y_{2, m_J + \frac{1}{2}}(\vartheta, \phi) | \downarrow \rangle \right) \\ &\equiv R_{nJ2}(r) \left(\pm \alpha_{\pm}(m_J) Y_{2, m_J - \frac{1}{2}}(\vartheta, \phi) | \uparrow \rangle + \alpha_{\mp}(m_J) Y_{2, m_J + \frac{1}{2}}(\vartheta, \phi) | \downarrow \rangle \right) \end{aligned} \quad (7.7)$$

The quantities $\alpha_{\pm}(m_J)$ are the Clebsch-Gordon coefficients and $| \uparrow \rangle, | \downarrow \rangle$ indicate the two different spin states. If we insert the expansion

$$\langle \mathbf{r}; R, \theta | \psi_{nm_J} \rangle = \sum_{Jm_J} C_{Jm_J}(R, \theta) \langle \mathbf{r} | nJm_J Ls \rangle \quad (7.8)$$

into Eq. (7.5) we obtain the following eigenvalue problem for the PES

$$[\epsilon_{nm_J}^0 - \epsilon_{nm_J}(R, \theta)] \delta_{JJ'} \delta_{m_J m_J'} + \sum_{J'm_J'} \langle nJ'm_J' Ls | \frac{B}{2}(J_z + S_z) + V_{n,e}(\mathbf{r}, R, \theta) | nJm_J Ls \rangle_{\mathbf{r}} = 0. \quad (7.9)$$

In Fig. 7.4(a) we present the PES for the $42D_{5/2}$, $m_J = 1/2$ states as a two-dimensional function of the spherical coordinates (R, θ) for $2000a_0 \leq R \leq 3500a_0$. This potential surface possesses two global potential minima at $\theta = 0, \pi$, $R \approx 3180a_0$ with a depth of around 18 MHz. In addition, a more shallow well with a depth of around 6 MHz can be identified at $\theta = \pi/2$, $R \approx 3180a_0$. Beside these three potential minima we find additional wells along the $\theta = 0, \pi/2$ and π direction. These wells are spatially separated by a radial distance of around $500a_0$. With decreasing R the depths of those potential wells decrease as well. In Fig. 7.4(b) the PES for the $42D_{1/2}$, $m_J = 5/2$ state is depicted. In contrast to the $m_J = 1/2$ potential surface this potential only possesses a single global maximum at $R \approx 3180a_0$, $\theta = \pi/2$ with a depth of around 10.3 MHz. As before we find a number of additional local potential minima which are aligned along the $\theta = \pi/2$ direction and which are separated by a radial spacing of around $500a_0$. As for the $m_J = 1/2$ PES the depths of these potential wells decrease with decreasing radial distance R . In general all calculated

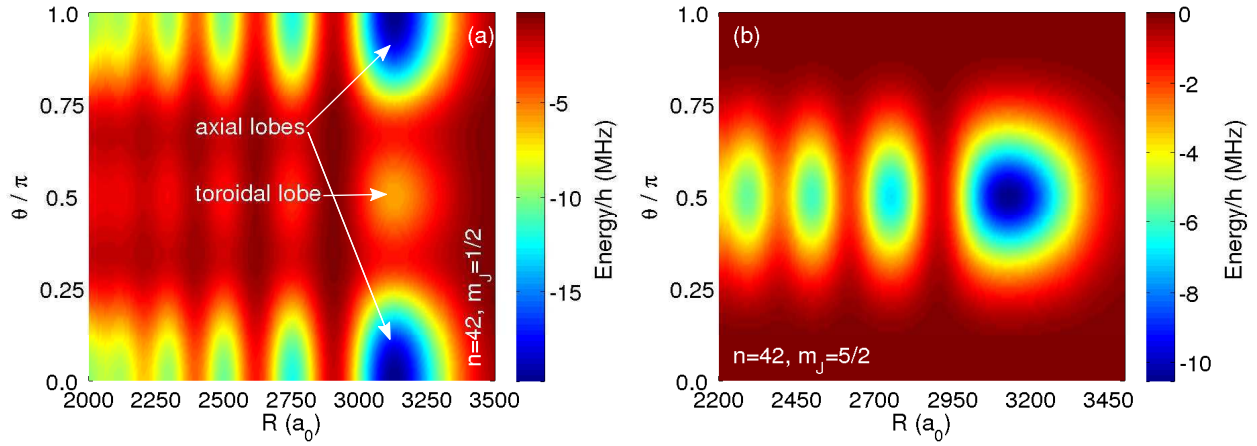


Figure 7.4: (a) $42D_{1/2}$, $m_J = 1/2$ adiabatic potential surface as a two-dimensional function of the spherical coordinates (R, θ) for $2000a_0 \leq R \leq 3500a_0$. We clearly detect two global potential minima at $\theta = 0, \pi$, $R \approx 3180a_0$ with a depth of around 18 MHz. In addition, a more shallow well with a depth of around 6 MHz can be identified at $\theta = \pi/2$, $R \approx 3180a_0$. Figure (b) shows the PES for the $42D_{5/2}$, $m_J = 1/2$ state. Here the global potential minimum ($R \approx 3180a_0$, $\theta = \pi/2$) with a depth of around 10.3 MHz is provided by a single potential well.

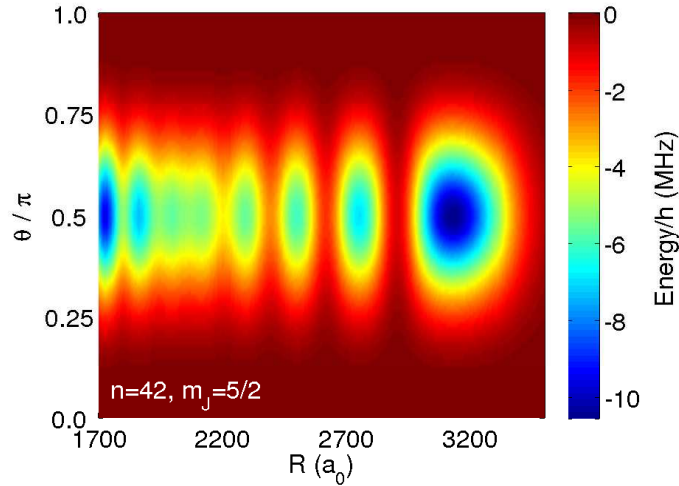


Figure 7.5: $42D_{1/2}$, $m_J = 1/2$ adiabatic potential surface as a two-dimensional function of the spherical coordinates (R, θ) for $1700a_0 \leq R \leq 3500a_0$. For $R < 2200a_0$ the PES strongly oscillates due to the increasing impact of the p -wave scattering potential.

$nD_{5/2}$, $m_J = 1/2, 5/2$ PES possess the same topology as it was just described for the $42D_{5/2}$ states. This can be understood qualitatively by considering the angular dependence of the bare electronic orbitals which dominate the topology of the potential surfaces. For $m_J = 1/2, 5/2$ the angular topology PES are mainly determined by $|Y_{20}(\theta, \phi)|^2$ and $|Y_{22}(\theta, \phi)|^2$, shown in Fig. 7.6(b) and (c), respectively. In addition, Fig. 7.6(a) shows the angular dependence of the electronic $l = m = 0$ orbital which determines the PES of the ultralong-range S -state Rydberg molecules. These species have been studied in detail theoretically [85,86] as well as experimentally [91,202]. Obviously, their potential surfaces are spherically symmetric. In contrast to this, the angular dependence of the electron density distribution of the two different D -states deviate tremendously from each other and from the S -state. In case of the $l = 2$, $m = 0$ state (see Fig. 7.6(b)) the electronic density features the shape of a dumbbell with a small torus in the equatorial plane. However, the electronic density of the $l = 2$, $m = 2$ state (Fig. 7.6(c)) only possesses a single toroidal shaped structure.

This means that the PES of the $nD_{5/2}$ molecular state do not possess a spherical symmetry as the S -states as the corresponding electronic density probabilities are θ -dependent. As the calculated

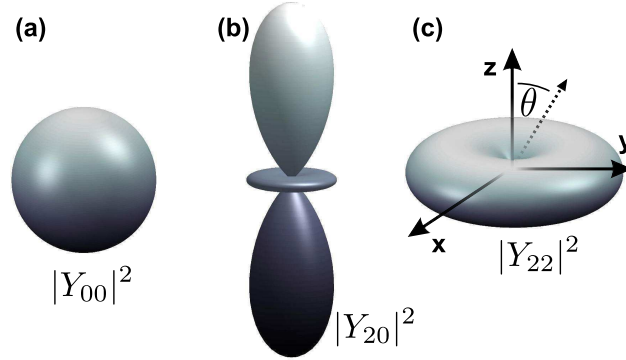


Figure 7.6: Absolute values of different spherical harmonic functions. The angular dependence of the S -state PES [202] is determined by $|Y_{00}|^2$ which is presented in (a). Obviously, this function is spherically symmetric. The D -state PES are determined by $|Y_{20}|^2$ ($m_J = 1/2$) and $|Y_{22}|^2$ ($m_J = 5/2$) which are depicted in Fig. (b) and (c), respectively. These electronic density distributions possess both a dumbbell structure in Z -direction with a small torus in the equatorial plane (see Fig. (b)) and a purely toroidal structure as it can be seen in (c).

PES of the $nD_{5/2}$, $m_J = 1/2, 5/2$ states provide several potential minima with depths in the MHz regime (see, for instance, Fig. 7.4(a,b)) we expect to find several bound rovibrational states, which are localized within these potential wells. The calculation of their specific properties and dynamics will be the content of Section 7.5.

In Fig. 7.5 we present the two-dimensional PES for the $42D_{5/2}$, $m_J = 5/2$ state with radial distances for $1700a_0 \leq R \leq 3500a_0$. In contrast to Fig. 7.4(b), where the same PES is shown but for $1700a_0 \leq R \leq 3500a_0$, we find that below radial separations of approximately $1700a_0$ the PES starts to oscillate widely with an increasing amplitude for decreasing R . This feature can be explained by the fact that with decreasing radial distance R the electrons kinetic energy increases and approaches the resonance energy of the p -wave scattering length A_p (see Section 2.2) which is given with $E_{\text{res}} \approx 23.9 \text{ meV}$. As the p -wave potential is directly proportional to A_p^3 the PES becomes more and more p -wave dominated as R decreases and the divergent behavior of the p -wave scattering length is reflected in the PES topology of all $nD_{5/2}$ states. In Fig. 7.7 we present the PES for the $42D_{5/2}$, $m_J = 5/2$ state for $1700a_0 \leq R \leq 3500a_0$ as a three-dimensional contour plot. We see a sequence of local potential well along the $\theta = \pi$ direction with a spatial separation of $500a_0$. At $R \approx 3180a_0$, $\theta = \pi/2$ a local potential minimum with a depth of around 10.3 MHz is clearly visible. For $R < 1700a_0$ the PES starts to oscillate widely as the divergent p -wave potential character determines the PES topology.

However, for all considered potential surfaces the radial separation of the outer potential wells is in the range of several thousand Bohr radii. As we are mostly interested in the molecular properties of the lowest rovibrational excitations and these are well localized within the outer potential minima, we expect the rovibrational wave functions to be hardly affected by the strong oscillating region of the PES. Depending on the specific potential well we distinguish between two kind of molecular states. In case the rovibrational wave function is localized in the axial lobes of the $m_J = 1/2$ potential surfaces we denote these as *axial (molecular) states*. In case the states are localized in a toroidal potential well these states are denoted *toroidal (molecular) states*. Obviously, toroidal states can be found for both $nD_{5/2}$, $m_J = 1/2$ and $m_J = 5/2$ PES.

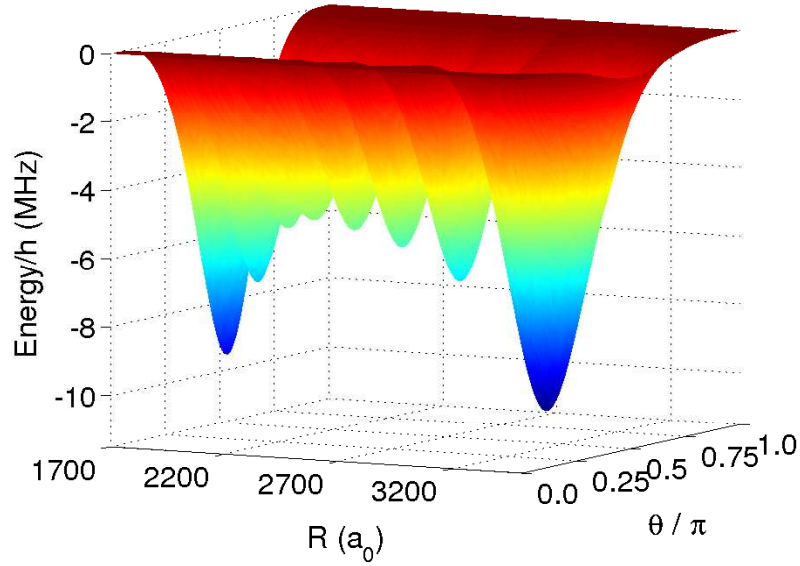


Figure 7.7: $42D_{5/2}$, $m_J = 5/2$ contour plot for $1700a_0 \leq R \leq 3500a_0$. For $R < 1700a_0$ the potential surface starts to oscillate widely as the divergent p -wave character becomes dominant.

7.5 Rovibrational states and binding energies

In order to solve the rovibrational Schrödinger equation (7.6) we express the wave function $\phi_{\nu m}^{(nmJ)}(R, \theta)$ as follows

$$\phi_{\nu m}^{(nmJ)}(R, \theta) = \frac{F_{\nu m}^{(n,mJ)}(\rho, Z)e^{im\phi}}{\sqrt{2\pi\rho}}, \quad m \in \mathbb{Z}, \quad \nu \in \mathbb{N}_0. \quad (7.10)$$

Inserting this into Eq. (7.6) gives the following differential equation for $F_{\nu m}^{(n,mJ)}$:

$$\left(-\frac{\partial_\rho^2 + \partial_Z^2}{m_n} + \frac{m^2 - 1/4}{m_n \rho^2} + \epsilon_{nmJ}(\rho, Z) \right) F_{\nu m}^{(nmJ)}(\rho, Z) = E_{\nu m}^{(nmJ)} F_{\nu m}^{(nmJ)}(\rho, Z). \quad (7.11)$$

We see that the number m indicates the degree of rovibrational rotation as the PES are azimuthal symmetric. The number ν labels the different rovibrational excitation for a given set of (n, m, m_J) . As the PES fulfill the relation $\epsilon_{nmJ}(\rho, Z) = \epsilon_{nmJ}(\rho, -Z)$ the function $F_{\nu m}^{(n,mJ)}$ are eigenstates of P_Z parity operator, e.g. $F_{\nu m}^{(n,mJ)}(\rho, -Z) = \pm F_{\nu m}^{(n,mJ)}(\rho, Z)$. For this reason the corresponding probability densities possess a reflection symmetry with respect to the x - y -plane, this means $|F_{\nu m}^{(n,mJ)}(\rho, -Z)|^2 = |F_{\nu m}^{(n,mJ)}(\rho, Z)|^2$. In our calculations we set $m = 0$ and solved the corresponding Schrödinger equation using a finite difference method (see Appendix A.3). The molecular binding energies $E_B^{(nmJ)}$ are given as the energy difference between the eigenenergies and the dissociation limit of the consider potential surface. As the PES are always defined with respect to the dissociation limit the binding energies we have $E_B^{(nmJ)} = E_{\nu m}^{(nmJ)}$.

$42D_{5/2}$, $m_J = 5/2$ toroidal states

In Fig. 7.8(a) the the $42D_{5/2}$, $m_J = 5/2$ PES is presented in cylindrical coordinates for $2000a_0 \leq \rho \leq 3300a_0$ and $-1500a_0 \leq Z \leq 1500a_0$. At $\rho \approx 3150a_0$, $Z = 0$ this potential surface possesses a toroidal shaped minimum with a depth of around 10.3 MHz. In addition we find further potential wells with are equally separated by a radial distance of approximately $400a_0$. In Fig. 7.8(b)-(d) we

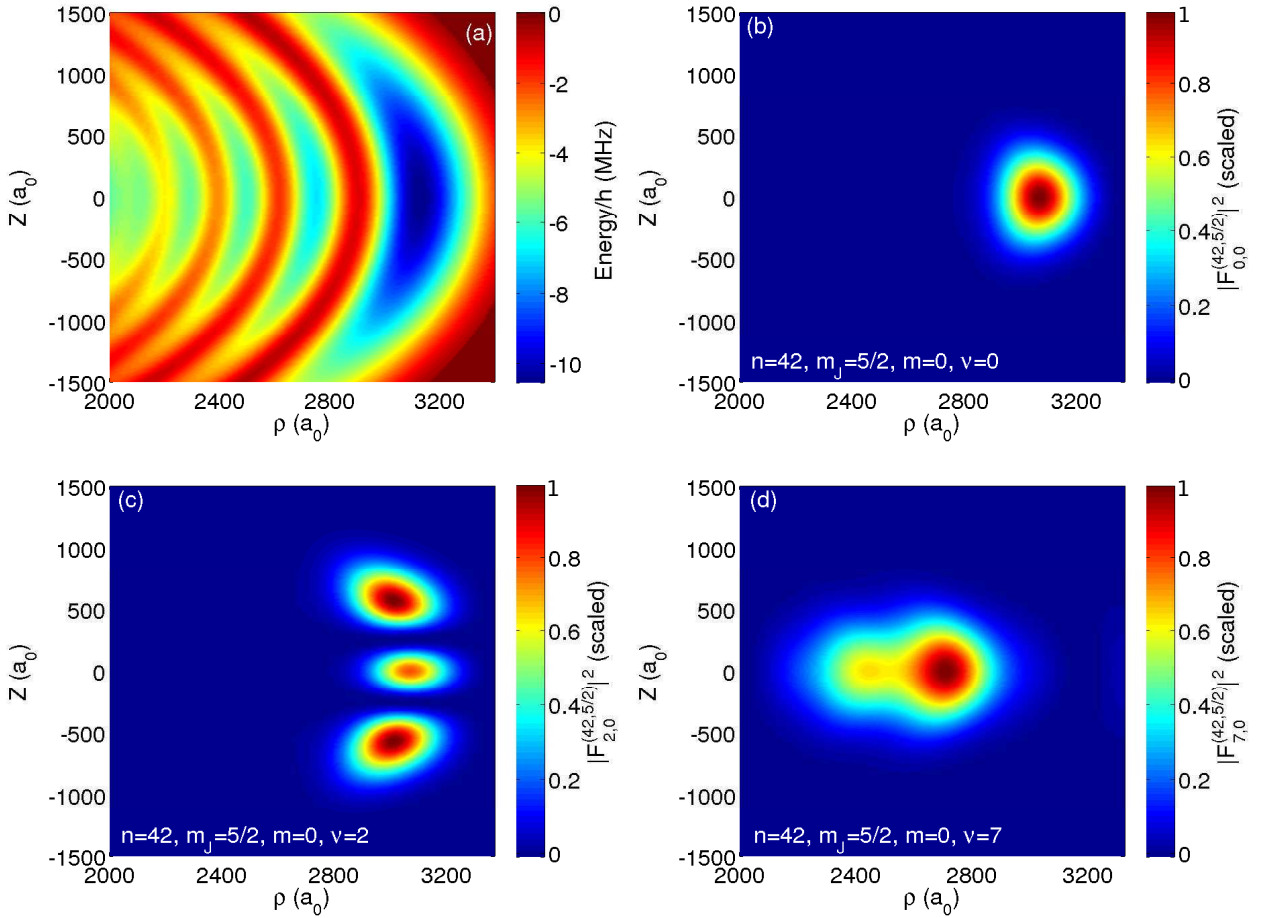


Figure 7.8: (a) $42D_{5/2}$, $m_J = 5/2$ PES as a function of cylindrical coordinates (ρ, Z) . A toroidal potential minimum is localized at $\rho \approx 3000a_0, Z = 0$ with a depth of around 12 MHz. In addition we find several wells. The figures (b)-(c) show the (scaled) probability densities $|F_{\nu 0}^{(42,5/2)}|^2$ with excitation number $\nu = 0, 1, 7$. In panel (a) we observed a deformed Gaussian-like density profile for the ground state ($\nu = 0$) centered at $\rho \approx 3000a_0, Z = 0$. (c) shows the density profile for the second excitation ($\nu = 2$). This density profile possesses two nodes with three separate Gaussian-like density peaks located at $\rho \approx 3000a_0, Z = 0$ and $\rho \approx 2900a_0, Z \approx \pm 600a_0$, respectively. Figure (c) shows the density profile for the seventh excitation ($\nu = 7$).

present the (scaled) probability densities $|F_{\nu 0}^{(42,5/2)}|^2$ of the toroidal rovibrational states which are provided by the potential wells in Fig. 7.8(a). These states are labeled with excitation numbers $\nu = 0, 2$ and $\nu = 7$. Fig. (7.8)(b) shows a slightly deformed Gaussian-like density profile for the ground state ($\nu = 0$) centered at $\rho \approx 3150a_0, Z = 0$ with a spatial extension of around $200a_0$. The density profile for the second excitation ($\nu = 2$) which is depicted in Fig. 7.8(c) shows three separate Gaussian-like density peaks located at $\rho \approx 3150a_0, Z = 0$ and $\rho \approx 3050a_0, Z \approx \pm 600a_0$, respectively. As the density peaks located $Z = \pm 600a_0$ are of equal intensity the probability density of the third peak localized $Z = 0$ is of reduced intensity. Finally, Fig. 7.8(d) shows the density profile for the seventh excitation ($\nu = 7$). Obviously, this rovibrational probability density possesses a novel intensity profile. This density profile possesses a major peak at $\rho \approx 2750a_0, Z = 0$ with a single side peak at $\rho \approx 2400a_0, Z = 0$. We find extensions of $450a_0$ in ρ and $1000a_0$ in Z -direction, respectively. All three density profile presented in Fig. 7.8(b)-(d) can be understood by considering the topology of the potential providing these bound states (see Fig. 7.8(a)). In a first approximation the potential around the minimum located at $\rho \approx 3150a_0, Z = 0$ can be understood a two separated harmonic oscillators, one in the θ -direction and the second one in the

ρ -direction. Since the rovibrational dynamics is spatially less confined in the θ -direction as it is in the ρ -direction the excitation modes in the angular direction are first excited. This is clearly visible in the density profiles presented in Fig. 7.8(b) and (c) as they possess the spatial characteristics of harmonic oscillators eigenstates such as a Gaussian-shaped ground state distribution and the appearance of density nodes for higher excitations where the number of the nodes is identical to the degree of excitation. In case of the seventh excitation ($\nu = 7$) we find an excitation in the first neighbored potential well beside the potential minimum. This causes the change in the profiles' topology.

$42D_{5/2}$, $m_J = 1/2$ axial and toroidal states

Next we analyze the rovibrational states which are provided by the PES of the $42D_{5/2}$, $m_J = 1/2$ state. As already discussed in Section 7.4 this potential surface possesses two different potential well which have to be analyzed separately. In Fig. 7.9 we show the considered PES for $1700a_0 \leq \rho, Z \leq 3500a_0$ as a function of cylindrical coordinates (ρ, Z). As the potential surface is reflection symmetric with respect to the x - y plane we only present the PES for positive Z . As discussed in Section 7.4 we are interested in the rovibrational states located in the outermost axial and toroidal potential wells (see Fig. 7.4). For this reason the potential surface for $R = \sqrt{\rho^2 + Z^2} \leq 1700a_0$ is of minor interest as in this region the PES is strongly oscillating since it is dominated by the divergent p -wave scattering potential. For this reason we do not present this part of the PES in Fig. 7.9 and the potential surface is put to zero artificially. In order to calculate the rovibrational levels

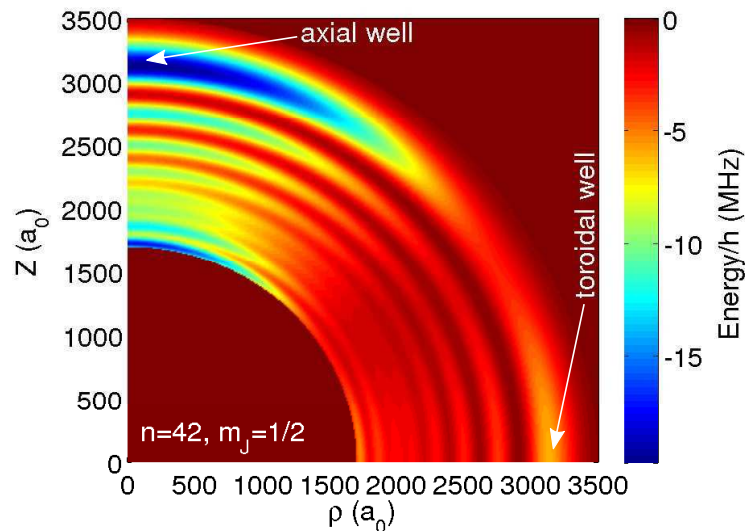


Figure 7.9: Two-dimensional PES for the $42D_{5/2}$, $m_J = 1/2$ state in cylindrical coordinates. Because of symmetry reasons the PES is only presented for $Z \geq 0$. As we are interested in the rovibrational states in the two outermost potential wells (axial and toroidal well) the PES is only calculated for $1700a_0 \leq R = \sqrt{\rho^2 + Z^2} \leq 3500a_0$. For $R \leq 1700a_0$ the potential is set to zero.

for the $m_J = 1/2$ potential surfaces we performed two separate calculations for the associated PES. For instance, for $n = 42$ we have calculated the PES around the axial potential well for $1700a_0 \leq Z \leq 3500a_0$ and $0 \leq \rho \leq 2000a_0$. In case of the toroidal potential well we used the potential for $|Z| \leq 1500a_0$ and $1700a_0 \leq \rho \leq 3500a_0$. For both potential surfaces we again use a finite difference method to solve the corresponding differential equation (7.11). In Fig. 7.10 we present a qualitatively picture of the scaled probability densities of the axial and toroidal rovibrational states for different degrees of excitation. We remark that Fig. 7.10 is just an illustration and that the spatial positions and extensions are not true to scale. In Fig. 7.10(a) the $42D_{1/2}$, $m_J = 1/2$ toroidal ground state ($\nu = 0$) as well as the second axial excited state ($\nu = 1$) are depicted. We

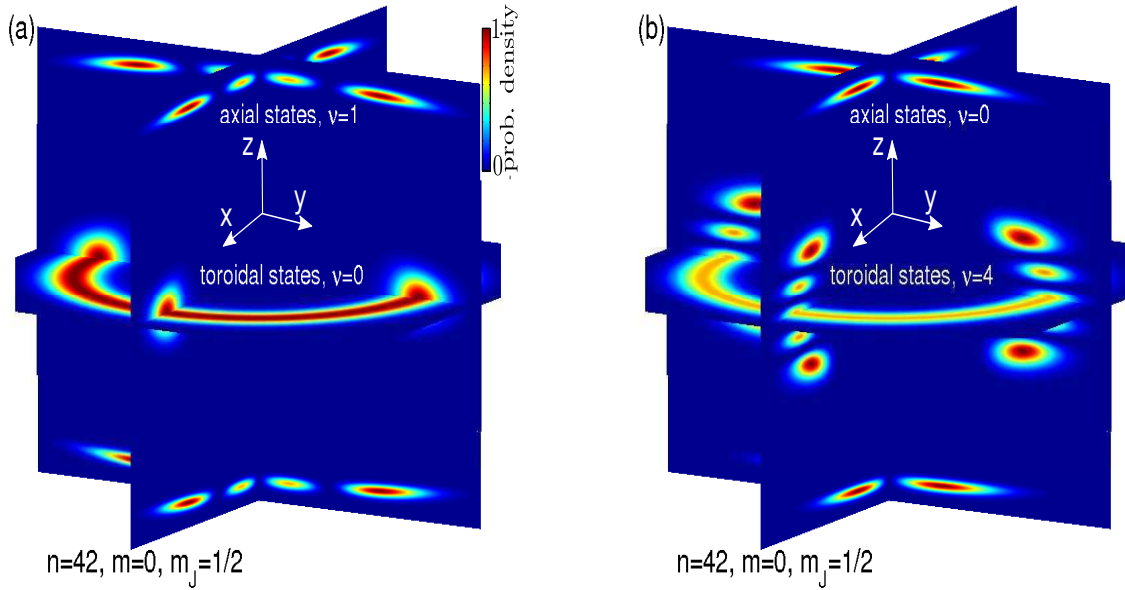


Figure 7.10: Qualitatively 3d-dimensional plots of the scaled rovibrational probability densities of axial and toroidal states (figures are not true to scale). Figure (a) shows the scaled probability densities of the $\nu = 1$ axial and $\nu = 0$ toroidal states, in (b) the scaled probability densities of the $\nu = 0$ axial and $\nu = 4$ toroidal molecule is depicted.

clearly see how the rovibrational wave functions are localized in the axial and toroidal potential lobes of the PES shown in Fig. 7.9. In Fig. 7.10(b) the fourth toroidal excitation ($\nu = 4$) as well as the axial ground state ($\nu = 0$) are shown. We see how the toroidal probability density spreads in the Z -direction with increasing degree of excitation. On the other hand the axial states are created far out in the Z -direction advancing into radial direction for higher excitation numbers ν . In Tab. 7.1 we present the binding energies of the $42D_{5/2}$, $m_J = 1/2$ axial and toroidal states, respectively. As the axial potential lobes are much deeper than the toroidal lobe the binding energies are higher and more axial states can be excited. For this reason we have calculated the rovibrational states for the axial potential lobe up to $\nu = 20$ while in case of the toroidal potential lobe we restricted the calculation up to $\nu = 5$. However, one has to be careful by calculating the rovibrational states in the axial lobes for several reasons. Increasing the degree of excitation we encounter two different kinds of molecular states. The first species are states which rovibrational probability density is localized within the outermost axial well and is unaffected from the boundary conditions which have been introduced to solve the rovibrational Schrödinger equation. These states are of main interest and they can be considered to be well converged. The second species, however, are states which are ground excitations of neighboring potential wells besides the axial lobe with minima positions $1700a_0 \leq Z \leq 3000a_0$. As those states are closer to the artificial boundary condition set at $R = 1700a_0$ these states are stronger effected by this which has a direct influence on the calculated wave functions and binding energies. In addition, the oscillations of the considered potential start to increase as R approaches to artificial boundary at $R = 1700a_0$. To obtain reliable results the fineness of the calculated potential grid should be increased. However, as we are mostly interested in the outermost rovibrational excitations we did not perform these steps as this would increase the amount of required computational time and memory. For this reason the binding energies in Tab. 7.1 of the states which have to be treated with caution and are indicated by bold numbers in the binding energy list for the axial rovibrational levels.

$42D_{5/2}$	$m_J = 1/2$ axial states	$m_J = 1/2$ toroidal states	$m_J = 5/2$ toroidal states
ν	E_B (MHz)	E_B (MHz)	E_B (MHz)
0	-14.42	-3.27	-7.05
1	-13.24	-2.78	-6.42
2	-12.04	-2.31	-5.74
3	-10.84	-1.85	-5.18
4	-9.64	-1.39	-4.60
5	-8.47	-0.93	-4.01
6	-7.32		-3.69
7	-6.90		-3.58
8	-6.48		-3.04
9	-6.20		-2.79
10	-5.93		
11	-5.83		
12	-5.37		
13	-5.12		
14	-4.87		
15	-4.77		
16	-4.31		
17	-4.21		
18	-4.10		
19	-3.83		
20	-3.47		

Table 7.1: Rovibrational binding energies of the $42D_{5/2}$, $m_J = 1/2, 5/2$ states. As the axial lobe is much deeper than the toroidal lobes more bound states can be calculated. The energies printed in bold numbers are related to rovibrational states which are not localized within the axial potential well (see Fig. 7.9). These values have to be treated with caution (more details in the text).

7.6 Experimental spectra

As already discussed in Section 7.2 in this experiment we investigate the formation of ultralong-range Rydberg D -state molecules via photoassociation and high resolution spectroscopy in an ultracold cloud of rubidium atoms. In contrast to previous investigated S -state molecules the considered D -state molecules in an external magnetic field of $B = 13.55$ G provide novel and interesting features. The main difference between these two molecular species is the different angular dependence of the behavior of the corresponding PES (see Section 7.4). For S -states the potential surfaces are completely isotropic, whereas in case of the D -state molecules the PES possess a θ -dependence (see Section 7.4). Due to the additional angular confinement in the θ -direction the rovibrational level spacing increases. For this reason we expect to resolve a larger number of molecular lines compared to the previous S -state measurements.

In the concrete measurements we have studied the diatomic D -molecules for principal quantum numbers n ranging from $n = 41$ to 49 addressing the $m_J = 1/2, 5/2$ substates by changing the polarization of the 480 nm laser: the $m_J = 1/2$ states by using σ^- and the $m_J = 5/2$ states by using σ^+ -polarized light. The experiment was performed in a magnetically trapped thermal cloud ($T_{\text{cloud}} \sim 2 \mu\text{K}$) of ^{87}Rb with a typical peak density of 10^{12} cm^{-3} . Since the main properties of the $nD_{5/2}$, $m_J = 1/2, 5/2$ molecular states arising from different n quantum numbers are qualitatively comparable we only present two states exemplary here: the $44D_{5/2}$, $m = 1/2$ and the $42D_{5/2}$, $m_J = 5/2$ molecular state. In Fig. 7.11(a,b) we present the photoassociation spectra

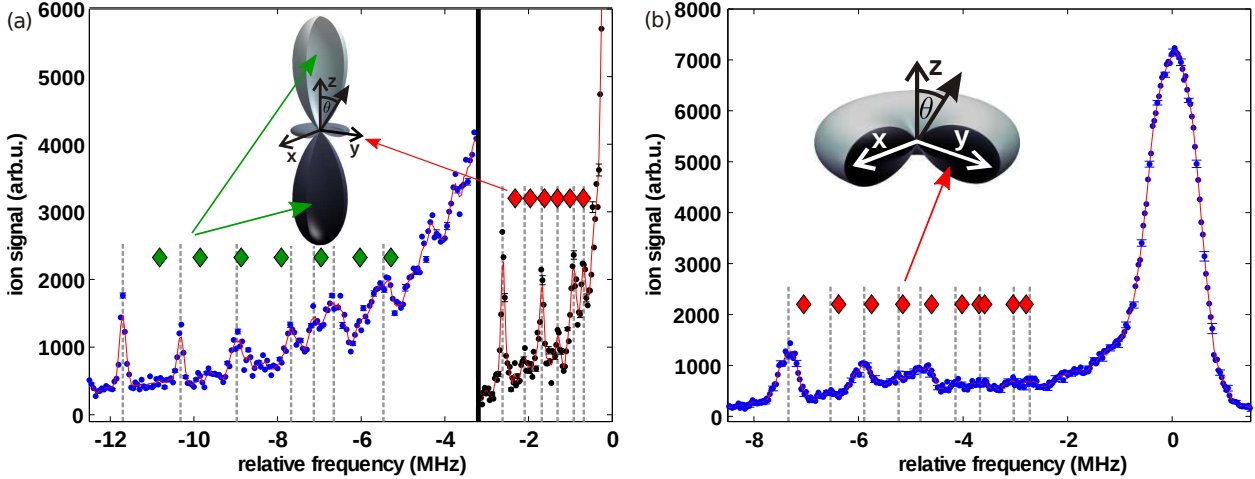


Figure 7.11: Molecular spectra of the $44D_{5/2}$, $m_J = 1/2$ (a) and $42D_{5/2}$, $m_J = 5/2$ state (b). The ion detector signal is plotted versus the frequency of the excitation laser. The laser frequency is given relative to the atomic transition. Apart from the photoassociation spectra the angular distributions $|Y_{2,(0,2)}|^2$ (a,b) of the atomic electron orbitals relevant for the topological structure of the PES are depicted as insets in both figures. In (a) we present two individual spectra taken with different laser intensities which are separated by a solid line at a frequency of -3.2 MHz. The experimental data are represented by blue and black points, respectively. In addition, a moving average (red line) is included to provide a better visibility. The dashed gray line mark the experimental peak positions whereas colored diamonds indicate the calculated binding energies of the axial (green) and toroidal (red) molecular states. In spectrum (b) only toroidal molecular states were detected.

of the $44D_{5/2}$, $m = 1/2$ and $42D_{5/2}$, $m_J = 5/2$, respectively. For both states the molecular lines appear energetically below the dissociation limit of the molecules which defines the energy offset. In Fig. 7.11(a) the two spectra for the $m_J = 1/2$ are shown. The two spectra, which are separated by a solid black line at a relative frequency of -3.2 MHz, indicate the binding energies of bound molecular states which are localized in the axial (left spectrum) and toroidal well (right spectrum), respectively. The measured ion signals are indicated by blue points (left spectrum) and black dots (right spectrum). For a better visibility a moving average (red solid line) was included in both spectra. In addition, gray dashed lines mark the experimental peak positions whereas colored diamonds indicate the calculated binding energies of the axial (green) and toroidal (red) molecular states. As the Franck-Condon factors are much smaller for the axial states than for the toroidal states the measured ion signal in the axial spectrum (left) is smaller than in the toroidal (right) if it had been recorded with the same laser power. For this reason a higher laser power had been applied to resolve the axial molecular states. As we can see the binding energies of the axial states are much larger as the binding energies of the corresponding toroidal states. By considering the angular part of the PES to be given by the simple relation $3/5|Y_{2,0}(\theta)|^2$ we can estimate the axial potential well to be approximately four times deeper than the toroidal well. From this simple estimation one can expect the binding energies of the axial rovibrational levels to be four times larger than the toroidal states and five times larger than the binding energies of the S -state molecular molecules. Both estimates are in quite good agreement with the experimental results.

In Fig. 7.11(b) the spectrum of the $42D_{5/2}$, $m_J = 5/2$ state is depicted. As before for the axial molecular states, the measured ion signal is indicated by blue points and the experimental peak positions are indicated by gray dashed lines. The calculated binding energies are indicated by red diamonds. The molecular ground state has a binding energy of -7.4 MHz. As the radial electronic wave functions are about the same for the S - and D -state molecules we can correlate their binding energies by comparing the angular parts of their wave functions. We get $|Y_{22}(\theta = \pi/2)|^2/|Y_{00}|^2 = 1.88$ which explains well the deeper bound D -state molecules. As we see in Fig. 7.11(b) the calculated binding energies reproduce the measured data quite satisfactory.

In Fig. 7.14 and Fig. 7.15 we present a comparison between the experimentally measured data points (dots) and the theoretically calculated binding energies (diamonds) over a wide range of principal quantum numbers n . In Fig. 7.14 the comparison is shown for the $m_J = 5/2$ states. We see that the numerics reproduces the measured data sufficiently well. However, with increasing principal quantum number n the binding energies decrease as the corresponding PES become more and more shallow. For this reason the molecular spectral lines move closer to the atomic line until at high n we end up with a non-resolvable flank on the red side of the atomic lines. Because of this hardly any spectral lines could be identified for the higher rovibrational excitations in the spectra for high n , which means those points are missing in Fig. 7.14. In addition, the figure provides the scaled probability densities of certain rovibrational states for ρ and Z as well ranging from $2000a_0$ to $3300a_0$ and from $-1500a_0$ to $1500a_0$, respectively.

In Fig. 7.15(a,b) we present the same analysis for the $m_J = 1/2$ axial and toroidal molecular states, respectively. In Fig. 7.15(a) it is clearly visible that the largest difference between theoretical calculated and experimental measured values for the binding energies can be found for the axial molecules. One possible explanation for this might be the uncertainty in the determination of atomic and molecular line positions. Due to the high laser power, needed to resolve the outermost axial states, the atomic lines are highly broadened which complicates the exact determination of the binding energies for the axial molecules. Furthermore, in the experiments only molecular lines down to binding energies of around -12 MHz can be measured, since -13 MHz the atomic lines of the $m_J = -1/2$ state is localized. Thus the outermost axial molecular lines of the $m_J = 1/2$ state for low n cannot be resolved since they overlap with the $m_J = -1/2$ atomic line. As for the previously discussed $m_J = 5/2$ molecular states (see Fig. 7.14), we depict the scaled probability densities of specific rovibrational states in the ρ - and z -direction.

Finally, we remark that so far no analysis has been performed on the profiles of the measured signals. For such an analysis the specific Frank-Condon factors have to be calculated. This procedure is very demanding as one has to consider the correct ground state distribution of the atoms and how this affects the overlap integrals between the excited Rydberg and ground state atom wave function.

7.7 Alignment of $D_{5/2}$ -state Rydberg molecules

The control of molecular alignment and orientation is of major importance in a number of molecular processes and properties such as photoelectron angular distribution [203–206], molecular dissociation [207–210], pathways of chemical reactions including stereo-chemistry [211–214] and diffractive imaging of molecules [215, 216]. Recently, the quantum stereodynamics of ultracold bimolecular reactions has been probed [217].

An experimental way to align molecules is to use external electric, magnetic and light fields [218, 219]. These procedures have been used in a variety of technical applications such as hexapole focusing [220–222], strong ac pulsed fields [223–225], combined ac and dc electric fields [226–234] and brute force orientation [235]. For instance, strong magnetic fields crucially influence the adiabatic electronic potential surfaces which determine the rovibrational dynamics [236]. This results in the emergence of novel equilibrium positions [237], novel binding and chemical reaction mechanisms [238, 239] as well as field induced rovibrational interacting pathways, for instance via conical intersections of adiabatic PES [240].

The $D_{5/2}$ -state Rydberg molecules considered in this work, created in an external magnetic field of $B = 13.55$ G, are aligned due to the specific properties of their electronic structure which is reflected in their PES (see Section 7.5). By changing the detuning and polarization of the used excitation lasers one can selectively excite a specific molecular state with an certain alignment.

Quantitatively the alignment $A_\nu^{(nm_J)}$ of a molecular state $\phi_{\nu 0}^{(nm_J)}$ is defined as

$$A_\nu^{(nm_J)} = \langle \phi_{\nu 0}^{(nm_J)} | \cos^2(\theta) | \phi_{\nu 0}^{(nm_J)} \rangle. \quad (7.12)$$

If $A = 1$ a molecular state is called *aligned* with respect to the z -axis, in case $A = 0$ the molecular state is called *antialigned*. In Fig. 7.12(a,b) we present the alignment of the $42D_{5/2}$, $m_J = 1/2, 5/2$

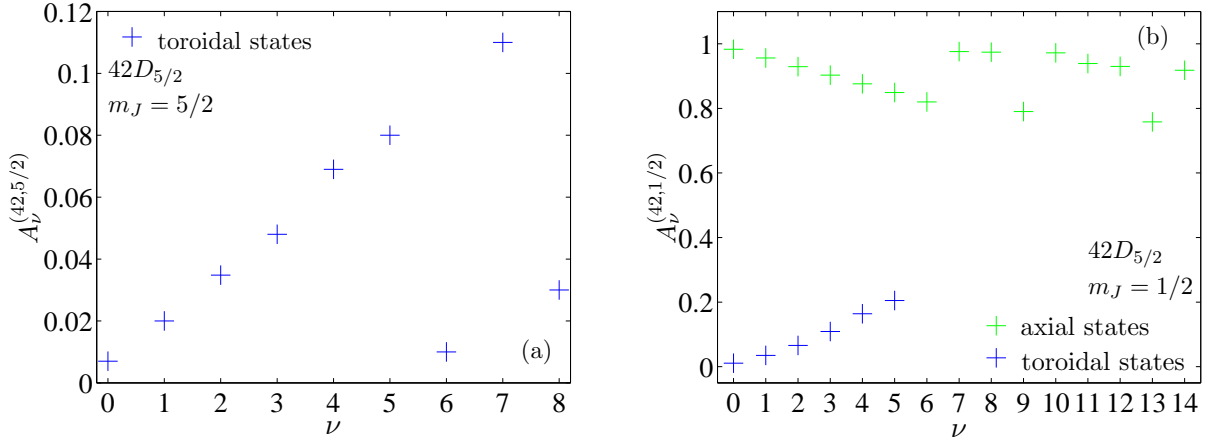


Figure 7.12: Molecular alignment A_{ν}^{42, m_J} plotted versus the rovibrational excitation number ν . In (a) and (b) the alignment is presented for the $m_J = 1/2$ and $m_J = 5/2$ states, respectively. In figure (b) we also distinguish between the alignment of the axial (green crosses) and the toroidal states (blue crosses). The abrupt changes in the molecular alignments are related to topological changes in the wave functions' density distributions.

states as function of the excitation number ν . In Fig. 7.12(a) we clearly see that the alignment of the toroidal $m_J = 5/2$ rovibrational states linearly increases up to an excitation number of $\nu = 6$. For this specific degree of excitation we see a sudden drop in the molecular alignment. For $\nu = 7$ the alignment increases, but drops again for $\nu = 8$. This behavior can be easily understood by considering the rovibrational probability densities which have been discussed in detail in Section 7.5. In Fig. 7.8(b-d) we see how the topology of the rovibrational probability density change with the considered excitation number ν . Till $\nu = 5$ only angular modes are excited and the rovibrational densities spread around the $\theta = \pi/2$ angle. As the different density profiles possess their maximal value at the outermost peaks the molecular alignment determined by Eq. (7.12) increases. However, for $\nu = 7$ the rovibrational density profile changes as a radial mode is excited. In this case the density's peaks is localized at $\theta = \pi/2$ again. For this reason the molecular alignment undergoes a sudden drop as it is observed in Fig. 7.12(a). In Fig. 7.12(b) we present the alignment for both the $m_J = 1/2$ axial (green crosses) and toroidal states (blue crosses). For the toroidal states we observe the same behavior as for the $m_J = 5/2$ toroidal states. As we have only considered toroidal excitations up to $\nu = 5$ we do not observe any sudden change in the molecular alignments. However, in case of the axial states we find a different behavior. For low excited states the rovibrational states are deeply localized in the axial lobes as presented in Fig. 7.9. Obviously, these states are well aligned along the z -axis and $A_{\nu}^{(42, 1/2)} \approx 1$. With increasing excitation number ν the probability densities of the rovibrational states spread away from the $\theta = 0$ configuration and the molecular alignment decreases. This is clearly seen in Fig. 7.13(a) where the densities profile $|F_{6,0}^{(42, 1/2)}|^2$ of the sixth excitation is depicted. However, for $\nu = 7$ an excitation in one of the neighboring potential wells beside the axial lobe is excited. The density profiles $|F_{7,0}^{(42, 1/2)}|^2$ of this state is depicted in Fig. 7.13(b). Obviously, the peak of this probability density is again located near the Z -axis, which means the corresponding alignment is close to one again. This behavior is clearly reflected in Fig. 7.12(b) where we see a sudden increase in the molecular alignment for the axial states as the excitation number changes from $\nu = 6$ to $\nu = 7$. For larger ν we have a change between axial states possessing density profiles which are localized far away from or close to the Z -axis. For this reason we find a rapid change in the corresponding molecular alignments which is clearly reflected in Fig. 7.12.

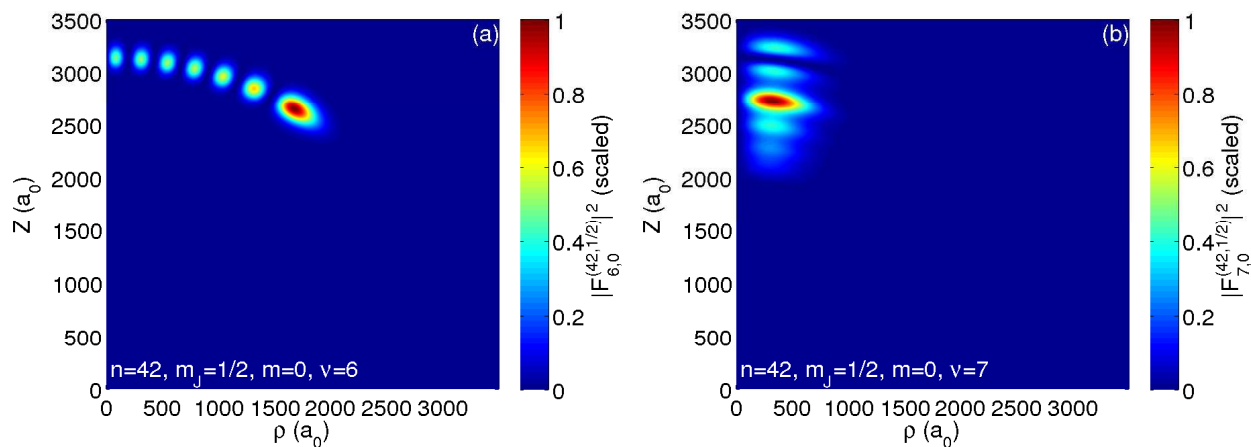


Figure 7.13: (Scaled) probability densities $|F_{6,0}^{(42,1/2)}|^2$ (a) and $|F_{7,0}^{(42,1/2)}|^2$ (b) for the axial potential well of the $n = 42$, $m_J = 1/2$ PES (see Fig. 7.9). In (a) the rovibrational wave function is localized inside the outermost potent well of the potential surface (see Fig. 7.9). The rovibrational state can be understood as a higher excitation in the θ -direction. In contrast, the rovibrational state in (b) is an excitation in a neighboring well.

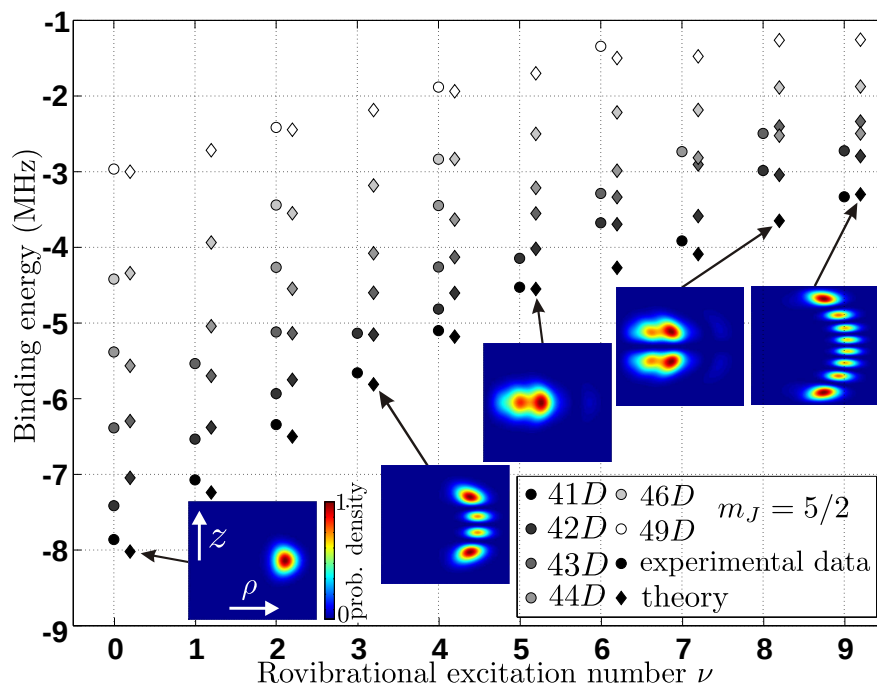


Figure 7.14: Experimental and theoretical molecular binding energies of the $m_J = 5/2$ toroidal states plotted versus the rovibrational excitation number ν . The principal quantum number n ranges from $n = 41$ to 49 . The experimental (theory) data points are represented by solid dots (solid diamonds). With increasing n their color change from black ($n = 41$) to white ($n = 49$). To improve the readability the theory points possess a slight horizontal offset with respect to the experimental data. The several insets show the (scaled) probability densities of certain excitation numbers for $2000a_0 \leq \rho \leq 3300a_0$ and $|Z| \leq 1500a_0$.

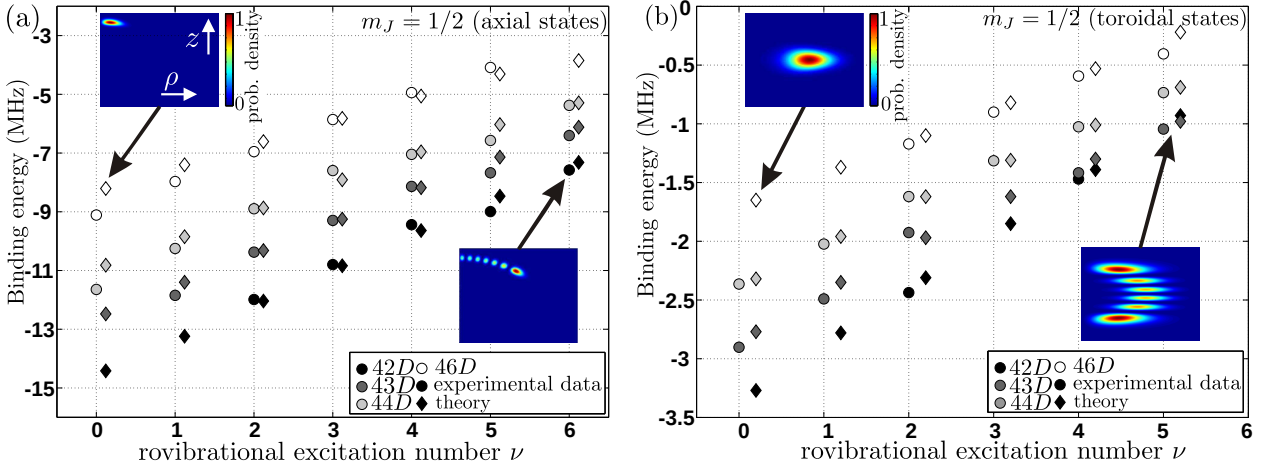


Figure 7.15: Experimental and theoretical molecular binding energies of the $m_J = 1/2$ states plotted versus the rovibrational excitation number ν for principal quantum numbers n ranging from $n = 42$ to 46 . In figure (a) and (b) we present the binding energies for the axial and toroidal states, respectively. In both figures the experimental (theory) data points are represented by solid dots (solid diamonds). With increasing n their color change from black ($n = 41$) to white ($n = 46$). To improve the readability the theory points possess a slight horizontal offset with respect to the experimental data. In both figures the insets depict the (scaled) probability densities of selected rovibrational states in cylindrical coordinates (ρ, Z) . In case of the axial states (a) the insets show image sections with $0 \leq \rho \leq 3500a_0$ and $0 \leq Z \leq 3500a_0$. For the toroidal states (b) the insets show image sections with $2700a_0 \leq \rho \leq 3500a_0$ and $|Z| \leq 2250a_0$.

7.8 Conclusion

In conclusion, this chapter reports on the observation of ultralong-range D -state molecules exposed to small magnetic fields in high resolution spectroscopy. The $m_J = 1/2$ and $m_J = 5/2$ electronic Rydberg states lead, due to their different electronic configuration, to adiabatic PES with different topologies. For the $m_J = 1/2$ the two dimensional potential surfaces $\epsilon(R, \theta)$ exhibit a number of radial wells at $\theta = 0, \pi$ and a series of shallower potential wells for $\theta = \pi/2$. These are caused by the corresponding electronic orbitals and lead to aligned and antialigned rovibrational states. On the contrary, the $m_J = 5/2$ PES only possesses a single local well at $\theta = \pi/2$ which lead to antialigned molecular states. Spectroscopically the molecular states are observed as a sequence of peaks for off and close by to the atomic Rydberg transition. Changing the principal quantum number n only introduces qualitatively changes in the measured spectra. For all studies the theoretical and experimental results show a satisfactory agreement.

In general, this work opens the doorway to the control of molecular Rydberg structures and even chemical reaction dynamics by external fields. In case of several polyatomic states, i.e. several neutral perturber, it can be conjectured external fields can be used to strongly change the molecular geometry applying weak field strengths, which is otherwise impossible both for ground state molecules. In addition, the design of conical intersections [240, 241] yielding ultrafast decay or predissociation processes comes into the reach of experimental progress in the field of ultracold molecular physics.

Chapter 8

Polarizability and susceptibility of ultralong-range Rydberg molecules

In this chapter we provide a brief introduction into the theory of electronic response properties of field-dressed ultralong range Rydberg molecules. In particular, we are interested in the electric polarizability/magnetic susceptibility for magnetically/electrically dressed molecular states.

8.1 Molecular response properties in the adiabatic approximation

We our analysis be studying a molecule which is exposed to an external field \mathbf{F} (which can be either an electric or magnetic field, respectively). In general the molecular eigenenergies \mathcal{E} are field dependent, e.g. $\mathcal{E} = \mathcal{E}(\mathbf{F})$. If $\Psi_{\text{mol}}(\mathbf{r}_{\text{el}}, \mathbf{r}_{\text{n}}; \mathbf{F})$ denotes the corresponding eigenfunction we have

$$\mathcal{E}(\mathbf{F}) = \langle \Psi_{\text{mol}}(\mathbf{r}_{\text{el}}, \mathbf{r}_{\text{n}}; \mathbf{F}) | \underbrace{H_{\text{mol}}(\mathbf{r}_{\text{el}}, \mathbf{r}_{\text{n}}; \mathbf{F})}_{\equiv H_{\text{mol}}(\mathbf{F})} | \Psi_{\text{mol}}(\mathbf{r}_{\text{el}}, \mathbf{r}_{\text{n}}; \mathbf{F}) \rangle_{\mathbf{r}_{\text{el}}, \mathbf{r}_{\text{n}}} \quad (8.1)$$

In the presence of an external field the dipole moment $\boldsymbol{\mu}$ (permanent+induced) is defined as $\boldsymbol{\mu}_{\text{mol}}(\mathbf{F}) \equiv -\vec{\nabla}_{\mathbf{F}} \mathcal{E}(\mathbf{F})$. According to the Feynman-Hellman theorem [242, 243] this can be expressed as

$$\boldsymbol{\mu}_{\text{mol}}(\mathbf{F}) = -\langle \Psi_{\text{mol}}(\mathbf{r}_{\text{el}}, \mathbf{r}_{\text{n}}; \mathbf{F}) | \vec{\nabla}_{\mathbf{F}} (H_{\text{mol}}(\mathbf{F})) | \Psi_{\text{mol}}(\mathbf{r}_{\text{el}}, \mathbf{r}_{\text{n}}; \mathbf{F}) \rangle_{\mathbf{r}_{\text{el}}, \mathbf{r}_{\text{n}}}. \quad (8.2)$$

If we apply the adiabatic approximation for the molecular wave function

$$\Psi_{\text{mol}}(\mathbf{r}_{\text{el}}, \mathbf{r}_{\text{n}}; \mathbf{F}) = \psi(\mathbf{r}_{\text{el}}; \mathbf{r}_{\text{n}}; \mathbf{F}) \phi(\mathbf{r}_{\text{n}}; \mathbf{F}) \quad (8.3)$$

we obtain

$$\begin{aligned} \boldsymbol{\mu}_{\text{mol}}(\mathbf{F}) &= -\langle \phi(\mathbf{r}_{\text{n}}; \mathbf{F}) | \langle \psi(\mathbf{r}_{\text{el}}; \mathbf{r}_{\text{n}}; \mathbf{F}) | \vec{\nabla}_{\mathbf{F}} (H_{\text{mol}}(\mathbf{F})) | \psi(\mathbf{r}_{\text{el}}; \mathbf{r}_{\text{n}}; \mathbf{F}) \rangle_{\mathbf{r}_{\text{el}}} | \phi(\mathbf{r}_{\text{n}}; \mathbf{F}) \rangle_{\mathbf{r}_{\text{n}}} \\ &\equiv -\langle \phi(\mathbf{r}_{\text{n}}; \mathbf{F}) | \boldsymbol{\mu}_{\text{el}}(\mathbf{r}_{\text{n}}; \mathbf{F}) | \phi(\mathbf{r}_{\text{n}}; \mathbf{F}) \rangle_{\mathbf{r}_{\text{n}}}. \end{aligned} \quad (8.4)$$

We denote the quantity $\boldsymbol{\mu}_{\text{el}}(\mathbf{r}_{\text{n}}; \mathbf{F})$ defined in the Eq. (8.4) as the *electronic dipole kernel*.

Next we are interested in the case of $\mathbf{F} \rightarrow 0$, which means that the external field just provides a minor perturbation to the molecular system. In this case we expand the molecular dipole moment $\boldsymbol{\mu}$ up to $\mathcal{O}(F^2)$

$$\boldsymbol{\mu}_{\text{mol}}(\mathbf{F}) \equiv \boldsymbol{\mu}_{\text{mol}} + \boldsymbol{\alpha}_{\text{mol}}^{(F)} \mathbf{F} \quad \text{with} \quad (\boldsymbol{\alpha}_{\text{mol}}^{(F)})_{ij} = \frac{\partial}{\partial F_i} (\boldsymbol{\mu}_{\text{mol}}(\mathbf{F}))_j |_{\mathbf{F}=0}. \quad (8.5)$$

The first term is known as the *permanent molecular dipole moment*. The quantity $\boldsymbol{\alpha}_{\text{mol}}^{(F)}$ is, in general, known as the second order tensor hyperpolarizability. In case the external field $\mathbf{F} = \mathbf{E}$ $\boldsymbol{\alpha}_{\text{mol}}^{(E)} \equiv \boldsymbol{\alpha}_{\text{mol}}$ is denoted as the (*molecular*) *electric polarizability*, if $\mathbf{F} = \mathbf{B}$ the tensor $\boldsymbol{\alpha}_{\text{mol}}^{(B)} \equiv \boldsymbol{\chi}_{\text{mol}}$ is called the (*molecular*) *magnetic susceptibility*. To derive the expressions for the molecular dipole moment and the hyperpolarizabilities we use Eq. (8.4). We expand the rovibrational state $\phi(\mathbf{r}_{\text{n}}; \mathbf{F})$

and the electronic kernel $\boldsymbol{\mu}_{\text{el}}(\mathbf{r}_n; \mathbf{F})$ according to

$$\phi(\mathbf{r}_n; \mathbf{F}) = \phi(\mathbf{r}_n) + \mathbf{F} \cdot \sum_{k \neq i} \mathbf{C}_k \phi_k(\mathbf{r}_n), \quad \boldsymbol{\mu}_{\text{el}}(\mathbf{r}_n; \mathbf{F}) = \boldsymbol{\mu}_{\text{el}}(\mathbf{r}_n) + \boldsymbol{\alpha}_{\text{el}}(\mathbf{r}_n) \mathbf{F}. \quad (8.6)$$

The coefficient vector \mathbf{C}_k is obtained within Rayleigh Schrödinger perturbation theory. Inserting the latter expressions into Eq. (8.4) and just keeping terms up to $\mathcal{O}(F)$ we obtain

$$\boldsymbol{\mu}_{\text{mol}} = \langle \phi(\mathbf{r}_n) | \boldsymbol{\mu}_{\text{el}}(\mathbf{r}_n) | \phi(\mathbf{r}_n) \rangle_{\mathbf{r}_n}, \quad \boldsymbol{\alpha}_{\text{mol}}^{(F)} = \boldsymbol{\alpha}_{\text{mol,el}}^{(F)} + \boldsymbol{\alpha}_{\text{mol,rv}}^{(F)} \quad (8.7)$$

with

$$\boldsymbol{\alpha}_{\text{mol,el}}^{(F)} = \langle \phi(\mathbf{r}_n) | \boldsymbol{\alpha}_{\text{el}}(\mathbf{r}_n) | \phi(\mathbf{r}_n) \rangle, \quad \boldsymbol{\alpha}_{\text{mol,rv}}^{(F)} = 2\text{Re} \left(\sum_{k \neq i} \langle \phi_i(\mathbf{r}_n) | \boldsymbol{\mu}_{\text{el}}(\mathbf{r}_n) | \phi_k(\mathbf{r}_n) \rangle * \mathbf{C}_k^T \right). \quad (8.8)$$

We see that the molecular tensor polarizabilities consist of two terms. We denote the first term $\boldsymbol{\alpha}_{\text{mol,el}}^{(F)}$ as the *electronic (hyper)polarizability* because it merely contains the effect of the external field on the electrons. The second term takes into account the effect on the nuclei degrees of freedom. For this reason we denote this term the *rovibrational (hyper)polarizability*.

8.2 Magnetically dressed Rydberg molecules

In this paragraph we consider the molecular dipole moments and electronic hyperpolarizability of field-dressed ultralong-range diatomic Rydberg molecules.

Molecular dipole moment and polarizability

We start our analysis with the permanent molecular dipole moment and electric polarizability of magnetically dressed ultralong-range diatomic Rydberg molecules. We write the molecular Hamiltonian (4.13) as

$$H_{\text{mol}}(\mathbf{r}, \mathbf{R}; \mathbf{B}; \mathbf{E}) = \frac{\mathbf{P}^2}{m_n} + H_{\text{el}}(\mathbf{r}, \mathbf{R}; \mathbf{B}) + \mathbf{E} \cdot \mathbf{r}. \quad (8.9)$$

whereby $H_{\text{el}}(\mathbf{r}, \mathbf{R}; \mathbf{B})$ is given by Eq. (6.4). For this specific Hamiltonian we have $\vec{\nabla}_{\mathbf{E}}(H_{\text{mol}}(\mathbf{E})) =$

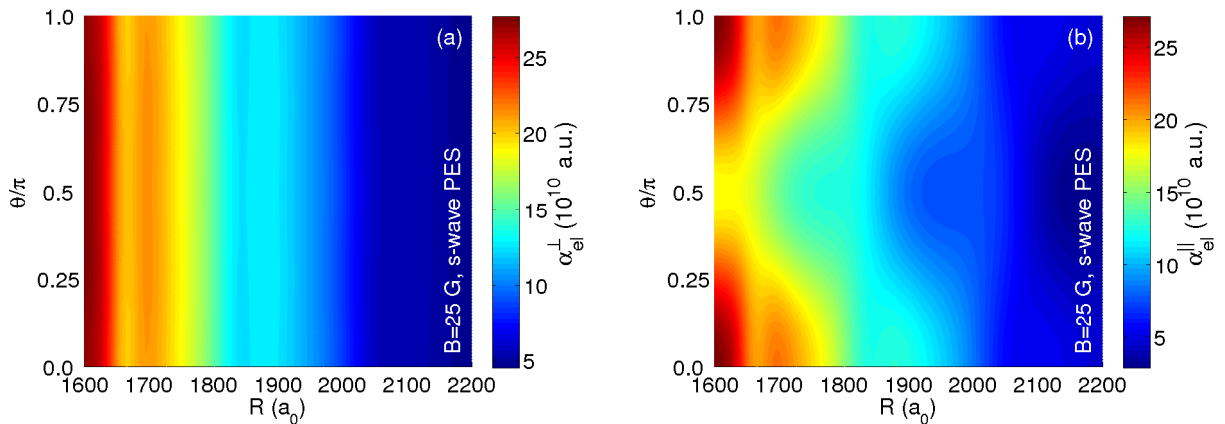


Figure 8.1: (a) Electronic polarizability $\alpha_{\text{el}}^{\parallel}$ as a function of θ and R . The applied magnetic field strength is $B = 25$ G. In (b) $\alpha_{\text{el}}^{\perp}$ is shown for identical magnetic field strength.

\mathbf{r} . In case of ultralong-range Rydberg diatomic molecules Hamiltonian one can express the elec-

tronic degree of freedom as a linear combination $\mathbf{n} = \mathbf{r}_{\parallel} + \mathbf{r}_{\perp}$ with $\mathbf{r}_{\parallel,\perp} = (\mathbf{r} \cdot \mathbf{n}_{\parallel,\perp}) \mathbf{n}_{\parallel,\perp}$. The vectors $\mathbf{n}_{\parallel,\perp}$ are the unit vectors either parallel or perpendicular to the internuclear axis, respectively. We obtain for the electronic dipole kernel of the magnetically dressed system

$$\boldsymbol{\mu}_{\text{el}}^{\parallel,\perp}(\mathbf{R}; \mathbf{B}) = \langle \psi(\mathbf{r}; \mathbf{R}; \mathbf{B}) | \mathbf{n}_{\parallel,\perp} \cdot \mathbf{r} | \psi(\mathbf{r}; \mathbf{R}; \mathbf{B}) \rangle_{\mathbf{r}} \mathbf{n}_{\parallel,\perp}. \quad (8.10)$$

Next we consider the electronic polarizability kernel. Due to symmetry arguments the polarizability tensor just possesses two independent components which are the polarizabilities either parallel or perpendicular to the internuclear axis

$$\alpha_{\text{el}}^{\parallel,\perp}(\mathbf{R}; \mathbf{B}) = 2 \sum_{k \neq i} \frac{|\langle \psi_k(\mathbf{r}; \mathbf{R}; \mathbf{B}) | \mathbf{n}_{\parallel,\perp} \cdot \mathbf{r} | \psi_i(\mathbf{r}; \mathbf{R}; \mathbf{B}) \rangle_{\mathbf{r}}|^2}{\varepsilon_i(\mathbf{R}; \mathbf{B}) - \varepsilon_k(\mathbf{R}; \mathbf{B})}. \quad (8.11)$$

In Fig. 8.1 we present the electronic polarizability functions $\alpha_{\text{el}}^{\parallel}$ and $\alpha_{\text{el}}^{\perp}$ as two-dimensional functions of the polar angle θ and the spatial separation R .

8.3 Electrically dressed Rydberg molecules

Magnetic dipole moment

Next we analyze the magnetic susceptibility of electrically dressed ultralong-range molecules. Analogous to the electrically dressed species we start with expressing the electric Hamiltonian as

$$H_{\text{mol}}(\mathbf{r}, \mathbf{R}) = \frac{\mathbf{P}^2}{m_{\text{n}}} + H_{\text{el}}(\mathbf{r}; \mathbf{R}; \mathbf{E}) + \frac{1}{2} \mathbf{B} \cdot \mathbf{L} + \frac{1}{8} (\mathbf{B} \times \mathbf{r})^2. \quad (8.12)$$

In contrast to the electric field Hamiltonian Eq. (8.9) we have two field dependent terms which are known as the diamagnetic and paramagnetic terms. For this specific Hamiltonian we have $\vec{\nabla}_{\mathbf{B}}(H_{\text{mol}}(\mathbf{B})) = \mathbf{L}/2 + (\mathbf{B}r^2 - (\mathbf{B} \cdot \mathbf{r})\mathbf{r})/4$ which can be expanded as follows

$$\vec{\nabla}_{\mathbf{B}}(H_{\text{mol}}(\mathbf{B})) = \frac{\mathbf{L}}{2} + \mathcal{H}\mathbf{B} \quad \text{with} \quad (\mathcal{H})_{ij} = \frac{1}{4}(\delta_{ij}r^2 - r_i r_j). \quad (8.13)$$

Analogous to Eq. (8.10) we define here the magnetic dipole kernel parallel and perpendicular to the internuclear axis

$$\boldsymbol{\eta}_{\text{el}}^{(\parallel,\perp)}(\mathbf{R}; \mathbf{E}) = \langle \psi(\mathbf{r}; \mathbf{R}; \mathbf{E}) | \mathbf{n}_{\parallel,\perp} \cdot \mathbf{L} | \psi(\mathbf{r}; \mathbf{R}; \mathbf{E}) \rangle_{\mathbf{r}} \mathbf{n}_{\parallel,\perp}. \quad (8.14)$$

The second order hyperpolarizability is known as the magnetic susceptibility tensor $\boldsymbol{\chi}$. In contrast to the magnetically dressed molecules (see section 8.2) we now have two contributions to the magnetic susceptibility. The first one corresponds to the contribution from the paramagnetic term in Eq. (8.12) which is the reason to denote this terms as the paramagnetic susceptibility $\boldsymbol{\chi}_{\text{para}}$. As in the case of the electric polarizability this quantity possesses two independent components with are the components parallel respectively perpendicular to the internuclear axis. We get

$$\boldsymbol{\chi}_{\text{para}}^{\text{el},(\parallel,\perp)}(\mathbf{R}; \mathbf{E}) = \frac{1}{2} \sum_{k \neq i} \frac{|\langle \psi_k(\mathbf{r}; \mathbf{R}; \mathbf{E}) | \mathbf{n}_{\parallel,\perp} \cdot \mathbf{L} | \psi_i(\mathbf{r}; \mathbf{R}; \mathbf{E}) \rangle_{\mathbf{r}}|^2}{\varepsilon_i(\mathbf{R}; \mathbf{E}) - \varepsilon_k(\mathbf{R}; \mathbf{E})}. \quad (8.15)$$

The second contribution emerges from the diamagnetic term in Eq. (8.12). We denote this term as the diamagnetic susceptibility $\boldsymbol{\chi}_{\text{dia}}$ and its components parallel and perpendicular to the internuclear axis are given by

$$\boldsymbol{\chi}_{\text{dia}}^{\text{el},(\parallel,\perp)}(\mathbf{R}; \mathbf{E}) = \frac{1}{4} \langle \psi_i(\mathbf{r}; \mathbf{R}; \mathbf{E}) | r^2 - (\mathbf{n}_{\parallel,\perp} \cdot \mathbf{r})(\mathbf{n}_{\parallel,\perp} \cdot \mathbf{r}) | \psi_i(\mathbf{r}; \mathbf{R}; \mathbf{E}) \rangle_{\mathbf{r}}. \quad (8.16)$$

Chapter 9

Giant dipole states

9.1 Introduction

An exotic species of Rydberg atoms in crossed electric and magnetic fields are the so-called giant dipole states (GDS), which have been explored theoretically [79, 244–246] and experimentally [247, 248] firstly in the 1990s. Opposite to the usual Rydberg states, the GDS are of decentered character and possess a huge electric dipole moment. More precisely, in Ref. [79] it was shown that the total potential of the electronic motion possesses a gauge invariant term which leads to an outer potential well that supports weakly bound decentered states. The mathematical origin of these effects is the non-separability of the center of mass and electronic motion in the presence of the external fields [249, 250]: translation symmetry and conservation of the total momentum in field-free space is replaced by a phase space translation symmetry and the conservation of the total pseudo momentum. Applications to the Positronium atom have demonstrated that metastable matter-antimatter states with a lifetime of many years can be formed [251]. More recently, giant dipole resonances of multiply excited atoms in crossed fields have been shown to exist and the corresponding electronic configurations as well as their stability have been analyzed [252, 253].

In the present chapter we combine the concepts of atomic giant dipole states and field-free ultra-long-range diatomic molecules: We show the existence of ultra-long-range giant dipole molecules emanating from giant dipole states. They exist in a variety of different configurations with simple to complex three-dimensional potential energy surfaces such as Gaussian, elliptical or toroidal wells. For higher excited states the potential energy surfaces of energetically neighboring states come close in configuration space and form higher-dimensional seams of avoided crossings that could lead to rapid decay processes of vibrational wave packets. In contrast to previous chapters, energies are presented in $\text{Energy}/\hbar = 2\pi \times \text{Energy}/h$.

9.2 The model Hamiltonian

We consider a highly excited hydrogen atom interacting with a ground state neutral perturber atom (we will focus on the ^{87}Rb atom here) in crossed static homogeneous electric \mathbf{E} and magnetic \mathbf{B} fields. The hydrogen atom is considered to be in a giant dipole state. For this reason corresponding Hamiltonian reads

$$H = \frac{\mathbf{p}_n^2}{2m_n} + H_{\text{GD}} + V_{\text{nGD}}, \quad (9.1)$$

where ‘n’ labels the neutral perturber and where the first term is the kinetic energy of the perturber atom followed by the giant dipole Hamiltonian of the hydrogen atom and the interaction term between the GDS and the neutral perturber. The hydrogen atom in crossed external fields has been discussed in detail in Ref. [79] and Appendix B.3. In this section it was shown that the giant dipole Hamiltonian can be transformed into an effective single particle problem in a magnetic field in the presence of a generalized potential $V(\mathbf{r}; \{\mathbf{E}, \mathbf{B}\}) = \frac{1}{2M}(\hat{\mathbf{K}} + \mathbf{B} \times \mathbf{r})^2 - \frac{1}{r}$ which parametrically depends on the external fields and the pseudomomentum $\hat{\mathbf{K}}(\mathbf{E}, \mathbf{B})$ and contains both the motional

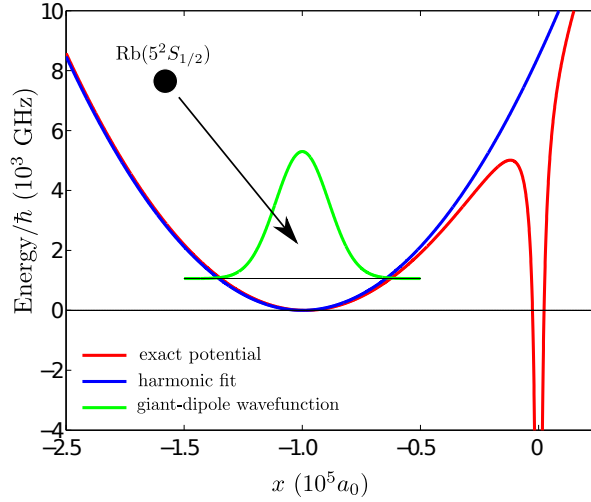


Figure 9.1: Sketch of the considered setup. A hydrogen atom is excited into a giant dipole state. The exact single particle potential (red curve) possesses an outer potential well at $x_0 \approx -10^5 a_0$, $y_0 = z_0 = 0$, around this minimum the potential can be expanded up to quadratic order (blue curve). The bound states within this potential well are called giant dipole states (green curve). The giant dipole wavefunctions are perturbed by a ground state $\text{Rb}(5^2S_{1/2})$ perturber.

and external electric field Stark terms,

$$H_{\text{GD}} = \frac{1}{2\mu}(\mathbf{p} + \frac{q}{2}\mathbf{B} \times \mathbf{r})^2 + V(\mathbf{r}; \{\mathbf{E}, \mathbf{B}\}), \quad (9.2)$$

with $\mu = \frac{m_e m_p}{m_e + m_p}$, $q = \left(\frac{m_e - m_p}{m_e + m_p}\right)$ where m_e, m_p, M are the electron, proton and atomic mass, respectively. \mathbf{r}, \mathbf{p} represent the coordinate and canonical momentum of the Rydberg electron. For sufficiently strong electric fields the potential V exhibits an outer well containing many bound GDS which are decentered from the proton at distances of about $10^5 a_0$, a_0 being the Bohr radius. The latter leads to a huge electric dipole moment typically of the order of many ten thousand Debye for strong electric and magnetic laboratory field strengths. In Fig. 9.1 we show the generalized potential for field strengths of $E = 50 \text{ V/m}$ and $B = 2 \text{ T}$ for $x = z = 0$ (red curve). We clearly see an outer potential at $x \approx -10^5 a_0$. Expanding $V(\mathbf{r}; \{\mathbf{E}, \mathbf{B}\})$ up to second order around the minimum of the outer well and performing a corresponding gauge centering [79,254] we arrive at the second order giant dipole Hamiltonian which represents a charged (effective) particle in a magnetic field and an anisotropic three-dimensional harmonic potential,

$$H_{\text{GD}} = \frac{1}{2\mu}(\mathbf{p} - \frac{q}{2}\mathbf{B} \times \mathbf{r})^2 + \frac{\mu}{2}\omega_x^2 x^2 + \frac{\mu}{2}\omega_y^2 y^2 + \frac{\mu}{2}\omega_z^2 z^2, \quad (9.3)$$

where the frequencies $\omega_x = \sqrt{\frac{2}{\mu}(\frac{B^2}{2M} + \frac{1}{x_0^3})}$, $\omega_y = \sqrt{\frac{1}{\mu}(\frac{B^2}{M} - \frac{1}{x_0^3})}$ and $\omega_z = 1/\sqrt{|\mu x_0^3|}$ characterize the anisotropy of the outer well. In this representation, \mathbf{r}, \mathbf{p} denote the electronic variables with respect to the outer minimum $(x_0, 0, 0)$ with $x_0 \approx -|\mathbf{K}|/B$. Our working Hamiltonian therefore reads

$$H = \frac{\mathbf{p}_n^2}{2m_n} + \frac{1}{2\mu}(\mathbf{p} + \frac{q}{2}\mathbf{B} \times \mathbf{r})^2 + \frac{\mu}{2}\omega_x^2 x^2 + \frac{\mu}{2}\omega_y^2 y^2 + \frac{\mu}{2}\omega_z^2 z^2 + V_{\text{nGD}}(\mathbf{r}, \mathbf{r}_n), \quad (9.4)$$

where V_{nGD} again represents the interaction of the neutral perturber atom with the giant dipole electronic Rydberg state. For deeply bound states in the outer well the electron possesses a low kinetic energy and it is legitimate to describe the interaction with the neutral perturber by a

Fermi-type pseudopotential [85, 156], namely, a s -wave contact potential

$$V_{\text{nGD}}(\mathbf{r}, \mathbf{r}_n) = 2\pi A_{\text{T}}[k(\mathbf{r})]\delta^{(3)}(\mathbf{r} - \mathbf{r}_n). \quad (9.5)$$

Here $A_{\text{T}}(k)$ is the energy-dependent triplet s -wave scattering length for electron collisions with the ground state Rb atom. \mathbf{r}_n denotes the position of the neutral perturber with respect to the minimum of the outer well. The electron wave number k is provided by the kinetic energy of the Rydberg electron $E_{\text{kin}} = k^2/2$ when it collides with the neutral perturber [85]. In a semiclassical approximation the kinetic energy is given by

$$E_{\text{kin}} = \epsilon_{n_-, n_+, n_z} - \frac{\mu}{2}\omega_x^2 x^2 - \frac{\mu}{2}\omega_y^2 y^2 - \frac{\mu}{2}\omega_z^2 z^2. \quad (9.6)$$

9.3 Methodology

In order to solve the eigenvalue problem associated with Hamiltonian (9.4) we adopt an adiabatic ansatz for the neutral ground state and the giant dipole atom. We write the total wave function as $\Psi(\mathbf{r}, \mathbf{r}_n) = \phi(\mathbf{r}_n)\psi(\mathbf{r}; \mathbf{r}_n)$ and yield

$$[H_{\text{GD}} + V_{\text{nGD}}(\mathbf{r}, \mathbf{r}_n)]\psi_i(\mathbf{r}; \mathbf{r}_n) = \epsilon_i(\mathbf{r}_n)\psi_i(\mathbf{r}; \mathbf{r}_n), \quad (9.7)$$

$$\left[\frac{\mathbf{p}_n^2}{2m_n} + \epsilon_i(\mathbf{r}_n) \right] \phi_k^i(\mathbf{r}_n) = E_k^i \phi_k^i(\mathbf{r}_n), \quad (9.8)$$

where ψ describes the electronic wave function of the decentered GDS in the presence of the neutral perturber for a given position \mathbf{r}_n and ϕ determines the vibrational state of the neutral perturber. To calculate the potential energy surfaces (PES) $\epsilon_i(\mathbf{r}_n)$ we expand $\psi_i(\mathbf{r}; \mathbf{r}_n)$ in the eigenbasis of H_{GD} , i.e., $\psi_i(\mathbf{r}; \mathbf{r}_n) = \sum_j C_j^i(\mathbf{r}_n)\chi_j(\mathbf{r})$ with $H_{\text{GD}}\chi_j(\mathbf{r}) = \epsilon_j\chi_j(\mathbf{r})$, and solve the corresponding eigenvalue problem associated with Eq. (9.7) using standard numerical techniques for the diagonalization of Hermitian matrices. In [79] it was shown that the eigenenergies and eigenfunctions of H_{GD} are determined by the three quantum numbers $n_-, n_+, n_z = 0, 1, 2, \dots$ [$\chi_j(\mathbf{r}) \equiv \chi_{n_-, n_+, n_z}(\mathbf{r})$], where $\epsilon_{n_-, n_+, n_z} = \omega_-(n_- + \frac{1}{2}) + \omega_+(n_+ + \frac{1}{2}) + \omega_z(n_z + \frac{1}{2})$ with $\omega_{\pm} = \frac{1}{\sqrt{2}}[\omega_x^2 + \omega_y^2 + \omega_c^2 \pm \text{sgn}(\omega_x^2 - \omega_y^2)\sqrt{(\omega_x^2 + \omega_y^2 + \omega_c^2)^2 - 4\omega_x^2\omega_y^2}]^{1/2}$ and $\omega_c = -qB/\mu$. To ensure convergence for our numerical approach we vary the number of orbitals associated with the quantum numbers n_-, n_+, n_z independently finally achieving a relative accuracy of 10^{-5} for the energy. To do so for the energetically lowest fifteen excitations a basis set of approximately 1500 states is needed, cf. Section 9.4. In addition to the numerically exact treatment we determine the PES in first order perturbation theory, leading to

$$\epsilon_j^{\text{pt}}(\mathbf{r}_n) = \epsilon_j + 2\pi A_{\text{T}}[k(\mathbf{r}_n)]|\chi_j(\mathbf{r}_n)|^2. \quad (9.9)$$

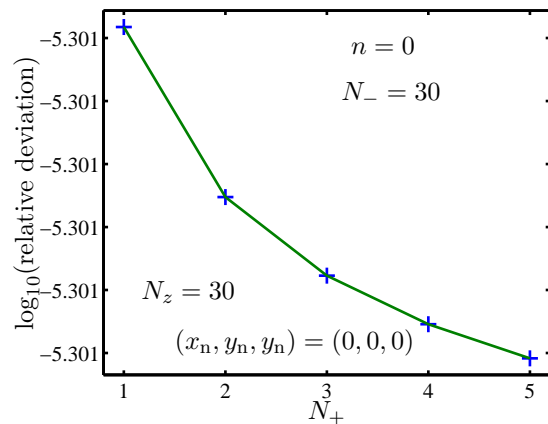
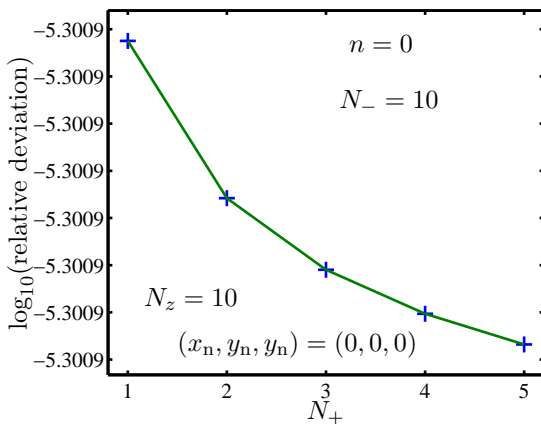
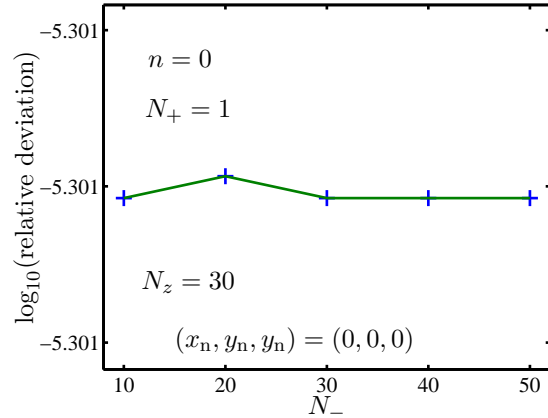
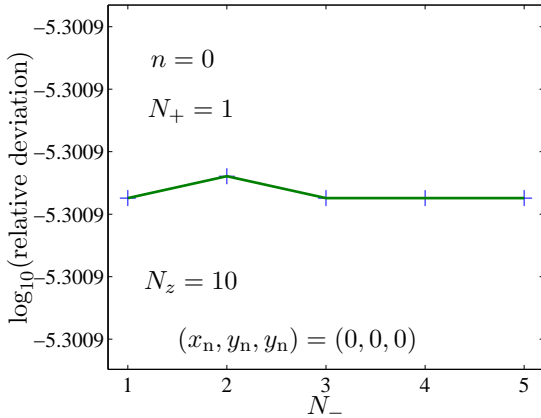
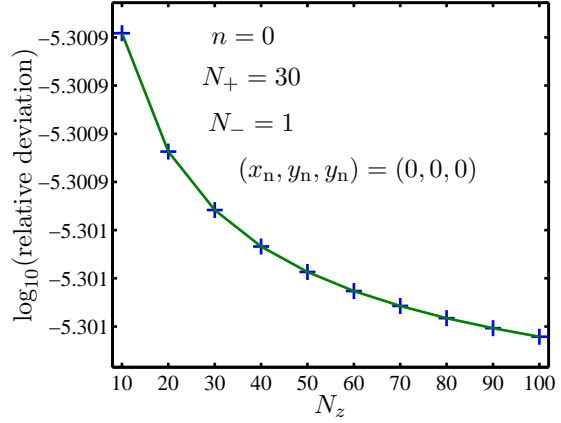
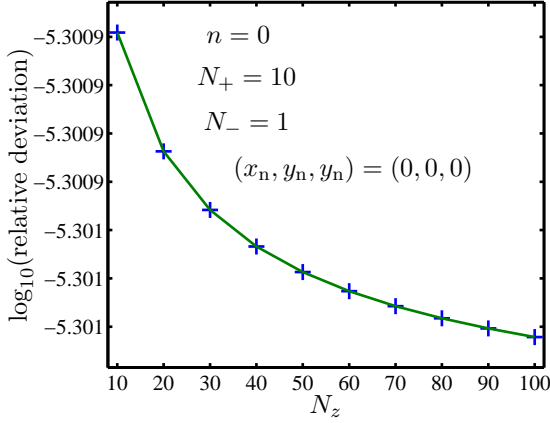
From eqs. (9.4)-(9.8) we can already deduce some symmetry properties of the states Ψ , ϕ and the energies $\epsilon(\mathbf{r})$. If $P_{\mathbf{r}, \mathbf{r}_n}$ denotes the parity operator that transforms $(\mathbf{r}, \mathbf{r}_n) \rightarrow (-\mathbf{r}, -\mathbf{r}_n)$ we have $[H, P_{\mathbf{r}, \mathbf{r}_n}] = [V_{\text{nGD}}(\mathbf{r}, \mathbf{r}_n), P_{\mathbf{r}, \mathbf{r}_n}] = 0$. This means that the states Ψ , ψ and ϕ are parity (anti)symmetric and the PES are symmetric, i.e., $\epsilon(\pm\mathbf{r}_n) = \epsilon(\mathbf{r}_n)$.

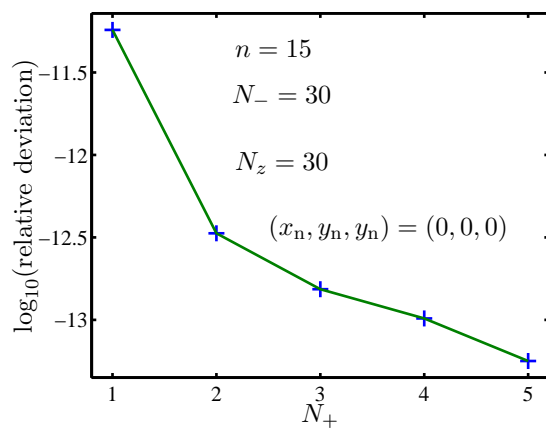
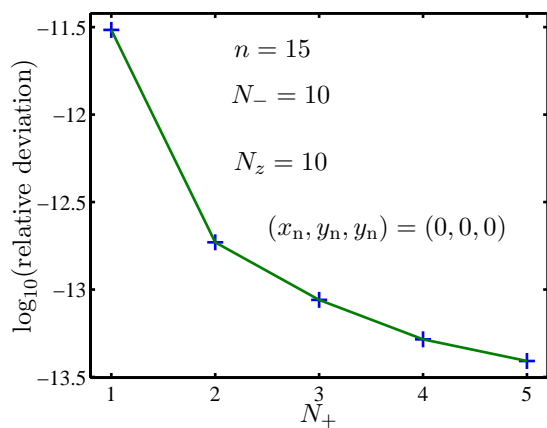
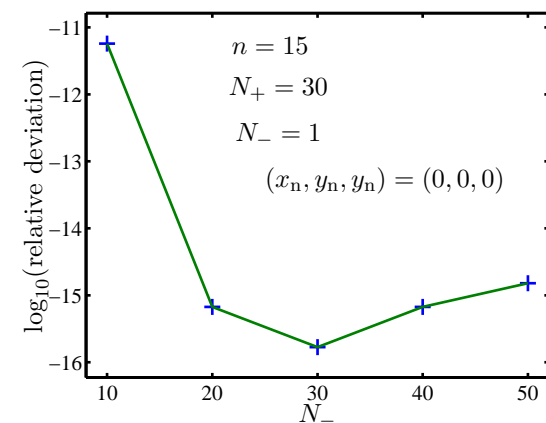
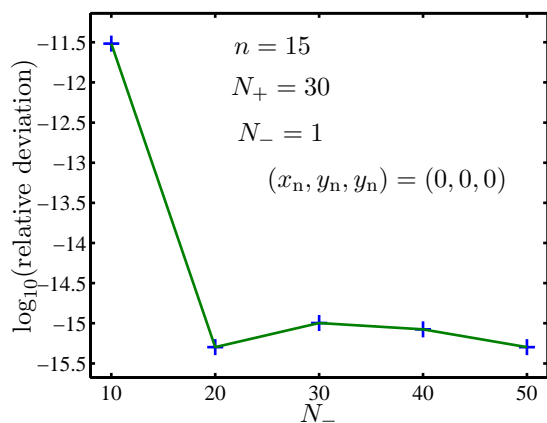
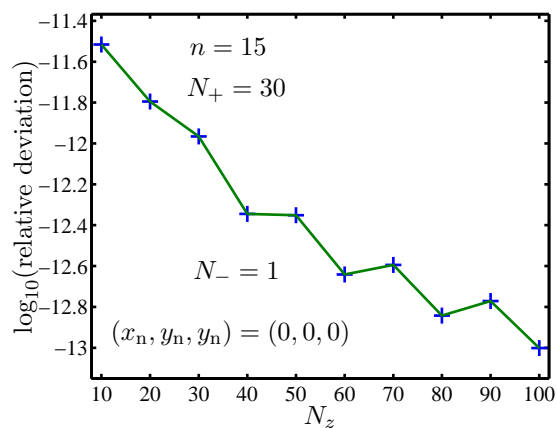
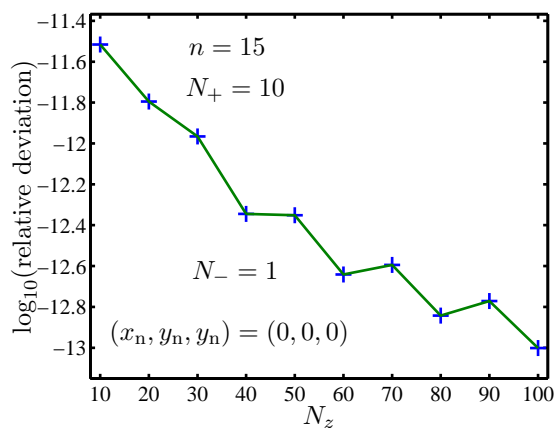
Throughout this work we use the exemplary field configuration $E = 50$ V/cm and $B = 2.35$ T. This gives giant dipole level spacings of $\omega_- = 223$ MHz, $\omega_+ = 413$ GHz and $\omega_z = 1.35$ GHz. For such fields, it is justified to neglect all interaction terms due to the induced dipole of the Rb atom.

9.4 Convergence studies

To ensure convergence of the adiabatic potential energy surfaces we perform convergence studies in the quantum numbers n_+, n_-, n_z characterizing the giant dipole state. The free parameters

of these studies are the upper bound N_i , $i = \{+, -, z\}$ of a certain quantum number n_i . In particular, for every convergence study we have fixed two quantum numbers and expanded the number of included states for the third one until the relative deviation between two following diagonalization steps undergoes an upper limit of 10^{-5} . This procedure is performed on a spatial grid of $-1500a_0 : 200a_0 : 1500a_0$ for the x_n and y_n coordinate, respectively. In the case of the z -coordinate we choose a grid of $-10000a_0 : 1000a_0 : 10000a_0$. We expand the basis set such large until we achieve convergence of the first fifteen excited states. In this Section exemplarily present the convergence studies for $\mathbf{r}_n = (0, 0, 0)^T$.





We see that a convergence of the relative deviation between two following diagonalization steps can be achieved by choosing a basis set of $N_z = 50$, $N_- = 30$ and $N_+ = 1$.

9.5 Molecular ground state potential surfaces

In first order perturbation theory the molecular giant dipole ground state PES is given by

$$\epsilon_{000}^{\text{pt}}(\mathbf{r}_n) = \epsilon_{000} + 2\pi A_{\text{T}}[k(\mathbf{r}_n)] C_0 e^{-ax_n^2 - by_n^2 - cz_n^2}, \quad (9.10)$$

where the constants $C_0, a, b, c > 0$ are given in [79]. This potential represents a single well 3d-potential and since $A_T[k(\mathbf{r}_n)] < 0 \forall \mathbf{r}_n$ the minimum is located at $\mathbf{r}_{n,\min} = 0$ with a depth of $\Delta\epsilon_{000}/\hbar \equiv [\epsilon_{000} - \epsilon_{000}^{\text{pt}}(\mathbf{r}_{n,\min})]/\hbar = 591$ MHz. In the present case we have $A_T[k(\mathbf{r}_n)] \approx A_T(x_n^2 + y_n^2, z_n^2)$ and $a \approx b$, which means that the giant dipole ground state PES possesses an approximate φ_n -rotational symmetry and $(L_z)_n$ is an approximately conserved quantity. A harmonic fit $V_h(\mathbf{r}_n) = \frac{1}{2}m_n\omega_x^2x_n^2 + \frac{1}{2}m_n\omega_y^2y_n^2 + \frac{1}{2}m_n\omega_z^2z_n^2$ around this minimum provides harmonic oscillator states with a level spacing of $\omega_x = \omega_y = 39.2$ MHz and $\omega_z = 12.4$ MHz. The numerical exact PES is presented in Fig. 9.2. The employed basis set consists of $N_- = 30$, $N_+ = 1$, $N_z = 50$ states. As in perturbation theory the potential possess a minimum located at $\mathbf{r}_{n,\min} = 0$ and is φ_n -rotationally symmetric. A harmonic fit provides here a depth of $\Delta\epsilon_{000}/\hbar = 788$ MHz and level spacing of $\omega_x = \omega_y = 20$ MHz, $\omega_z = 6.5$ MHz.

In Fig. 9.3 we show a comparison between the perturbative and the exact ground state potential for $y_n = z_n = 0$. In addition, the harmonic fitting curves and the parameters ω_x^{pt} and ω_x^{ex} are presented as well. Comparing the analytic solution Eq. (9.10) with the numerically exact result, one finds that for the exact PES the depth possesses a 165 MHz larger value while the width of the well increases by a factor of two. Furthermore, for the perturbative PES the harmonic approximation is valid in a region between $x_n \approx \pm 200a_0$, while for the exact potential it is valid up to $x_n \approx \pm 800a_0$. Hence, while providing a good qualitative prediction, the perturbative

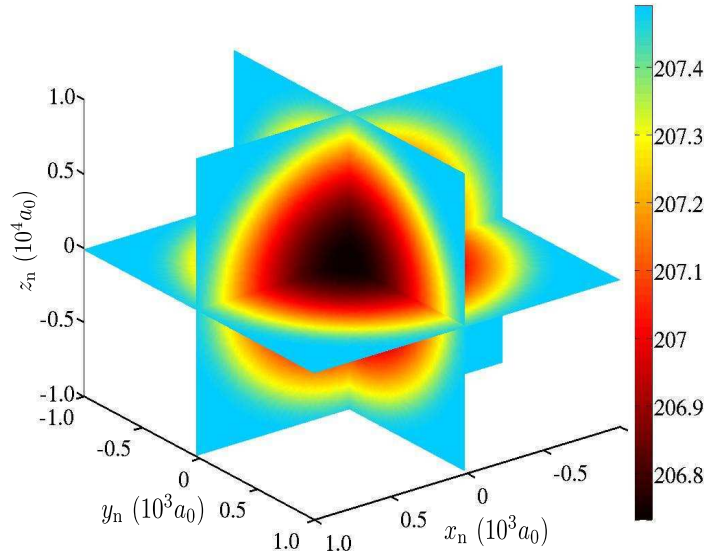


Figure 9.2: Ground state potential energy surfaces calculated via exact diagonalization. The employed basis set consists of $N_- = 30$, $N_+ = 1$, $N_z = 50$ states. The energy scale is given in GHz.

approach cannot be used to discuss quantitative details. The deviation between the exact and the perturbative result can be understood by analyzing the coupling of the giant dipole ground state to excited states of the unperturbed system. For first order perturbation theory to hold, these couplings need to be much smaller than the energetic separation of the involved levels. In our case, this amounts to the requirement

$$\gamma_{n_-n_+n_z} := 4 \left| \frac{\langle 000 | V_{\text{nGD}}(\mathbf{r}, \mathbf{r}_n) | n_-n_+n_z \rangle_{\mathbf{r}}}{\epsilon_{000}^{\text{pt}}(\mathbf{r}_n) - \epsilon_{n_-n_+n_z}^{\text{pt}}(\mathbf{r}_n)} \right|^2 \ll 1 \quad (9.11)$$

where n_- , n_+ and n_z label the quantum number of the excited state. In our case, we find, e.g., $\gamma_{100} \approx 4.5$ and $\gamma_{002} \approx 0.1$. Hence, it is not surprising that first order perturbation theory yields qualitatively but not quantitatively reliable results. This is in contrast to the trilobite systems

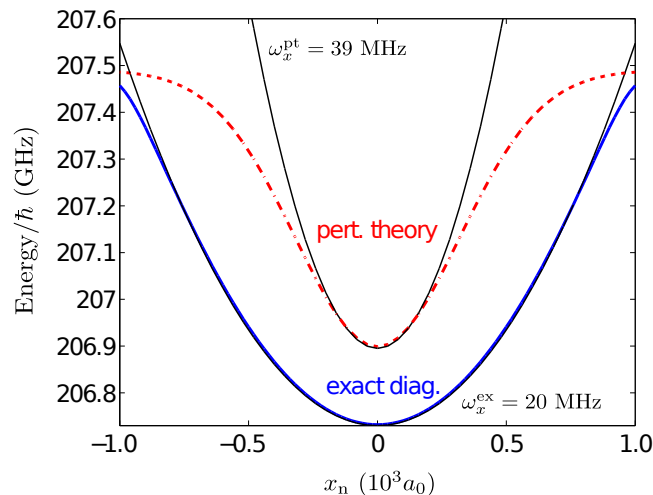


Figure 9.3: Comparison between perturbative (dashed-dotted line) and exact (solid line) ground state potential for $y_n = z_n = 0$. In addition, the harmonic fitting curves (thin lines) together with the corresponding trap frequencies ω_x^{pt} and ω_x^{ex} are shown.

[85] where degenerate first order perturbation theory within a given Rydberg n -manifold provides satisfactory results (depending on n , the splitting of adjacent manifolds is in the GHz-THz regime compared to $\omega_- = 223$ MHz in our case). We remark that the vibrational states obtained by the potential given in Fig. 9.2 are localized at internuclear distances in the range of $10^5 a_0$. To our knowledge, these molecules belong, together with recently investigated Rydberg macrodimers [255], to the largest diatomic molecules ever predicted.

9.6 Potential surfaces of excited states

In perturbation theory the PES for the lowest excitations are determined by the states $|n_-00\rangle$, $n_- = 1, 2, 3$. Introducing cylindrical coordinates ρ_n , φ_n , z_n and extracting the dominant terms in perturbation theory, the PES are approximately given by

$$\epsilon_{n_-00}^{\text{pt}}(\mathbf{r}_n) \approx \epsilon_{n_-00} + 2\pi A_{\text{T}}[k(\mathbf{r}_n)] C_{n_-} e^{-a\rho_n^2 - cz_n^2} \rho_n^{2n_-}. \quad (9.12)$$

Due to the weak dependence of $A_{\text{T}}[k(\mathbf{r}_n)]$ on k in our case, this well represents a φ_n -rotationally symmetric torus with minima at $\mathbf{r}_{n,\text{min}}^{(n_-)} = \rho_{\text{min}}^{(n_-)} \mathbf{e}_\rho$. The positions $\rho_{\text{min}}^{(n_-)}$ and depths $\Delta\epsilon_{n_-00}$ of these minima are approximately given by

$$\begin{aligned} \rho_{\text{min}}^{(n_-)} &\approx \sqrt{n_-/a}, \\ \Delta\epsilon_{n_-00} &\approx 2\pi |A_{\text{T}}[k(\mathbf{r}_{n,\text{min}}^{(n_-)})]| \frac{C_{n_-}}{e^{n_-}} \left(\frac{n_-}{a}\right)^{n_-}. \end{aligned} \quad (9.13)$$

In Fig. 9.4 the exact PES for the first excited state is shown. The toroidal structure as predicted by perturbation theory is clearly visible. Fig. 9.5(a) shows a two-dimensional intersection for $z_n = 0$ of the same PES: A “Mexican hat” like potential well is obtained with the one-dimensional manifold of the minimum lying on a circle. For sufficiently small displacements from the minima the PES can be described by a harmonic approximation, i.e., a decentered oscillator potential $V_{\text{h}}(\mathbf{r}_n) = \frac{1}{2}m_n\omega_\rho^2(\rho_n - \rho_{\text{min}})^2 + \frac{1}{2}m_n\omega_z^2z_n^2$. One therefore arrives at a free rotational motion of the

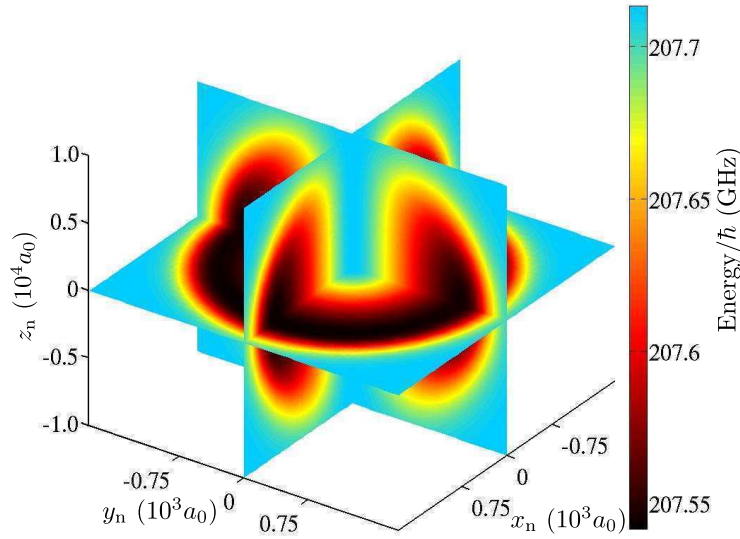


Figure 9.4: Three-dimensional representation of the first excited potential surface. To achieve convergence we use a set of $N_- = 10$, $N_+ = 1$, $N_z = 30$ basis functions.

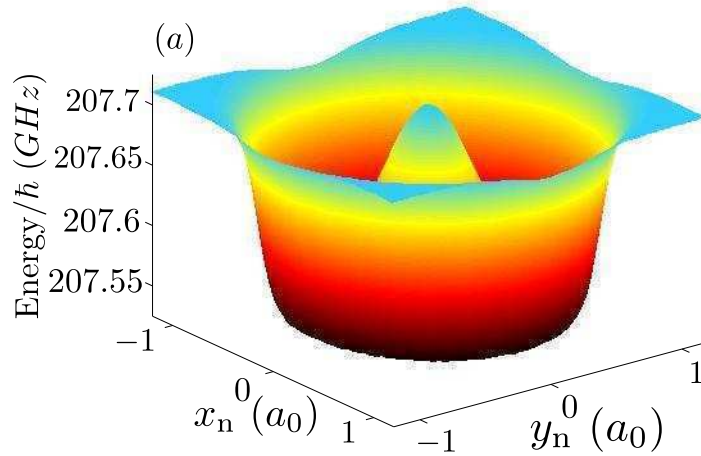


Figure 9.5: Two-dimensional intersection of the first excited potential surface for $z_n = 0$. The energy scale is given in GHz.

Rb-atom in the φ_n -direction. In perturbation theory the frequencies ω_ρ and ω_z are given by

$$\omega_\rho^{(n_-)} \approx 2\sqrt{\frac{2\pi a|A[k(\mathbf{r}_{n,\min}^{(n_-)})]|C_{n_-}}{m_{\text{Rb}}e^{n_-}} \left(\frac{n_-}{a}\right)^{n_-}}, \quad (9.14)$$

$$\omega_z^{(n_-)} \approx 2\sqrt{\frac{\pi c|A[k(\mathbf{r}_{n,\min}^{(n_-)})]|C_{n_-}}{m_{\text{Rb}}e^{n_-}} \left(\frac{n_-}{a}\right)^{n_-}}. \quad (9.15)$$

The corresponding eigenfunctions are given by the product $A(\rho_n)e^{im\varphi_n}\phi_l(z_n)$, $m \in \mathbb{Z}$ and $l \in \mathbb{N}_0$, where ϕ_l denotes the l -th eigenfunction of the harmonic oscillator and $A(\rho_n)$ are, apart from a Gaussian, the biconfluent Heun functions [256–267]. In table 9.1 the parameters ρ_{\min} , ω_ρ and ω_z

	exc. 1		exc. 2		exc. 3	
	pt	ex	pt	ex	pt	ex
ρ_{\min} / a_0	450	825	637	971	785	1050
$\Delta\epsilon_{n-00} / \text{MHz}$	221	170	162	155	134	127
ω_ρ / MHz	33	27	29	25	26	24
ω_z / MHz	1.9	0.86	1.7	0.89	1.5	1.2

Table 9.1: Parameters ρ_{\min} , $\Delta\epsilon_{n-00}$, ω_ρ and ω_z for the first three excited potential surfaces. For the numerically exact potentials (ex) the parameters are taken from a harmonic fitting. For the perturbative potentials (pt), the parameters are extracted from Eqs. (9.13)-(9.15).

for the first three excited PES, both exact and perturbative, are listed. We see that the largest difference between perturbation theory and the numerically exact result is obtained for the ρ_{\min} and ω_z parameters with a deviation of around 50% for the first excitation and 20% for the third excitation. However, for ω_ρ and $\Delta\epsilon_{n-00}$ both results are more comparable with a maximum deviation of 20%. For all quantities the exact and perturbative results are more comparable with increasing excitation.

9.7 Avoided crossings of potential surfaces

While for the first few excitations first order perturbation theory provides a reasonable prediction of the qualitative behavior of the PES, for higher excitations first order perturbation theory is not capable of describing even the qualitative behavior of the PES. For example, in Fig. 9.6 we show the PES for the fifth excitation. In addition to the toroidal well described above we get two new three-dimensional elliptical potential wells centered at $x_n = y_n = 0$, $z_n \approx \pm 6500a_0$. As a consequence the former rotationally symmetric global minimum represent now a local minimum and the two new global minima are the centers of these elliptical wells. The bound states in the toroidal well become metastable and can in principle decay into bound vibrational states in the elliptical wells. For the fifth and sixth excited PES a harmonic approximation around the global minima yields

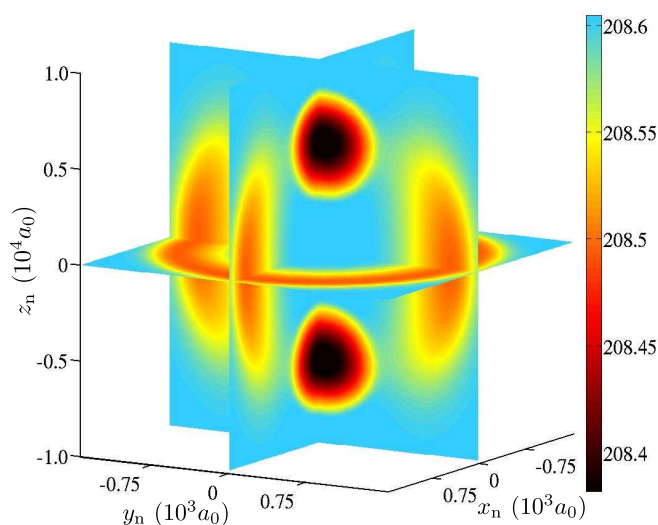


Figure 9.6: Potential surface for the fifth excitation. The additional elliptical wells arise due to avoided crossings with adjacent potential surfaces. The energy scale is given in GHz.

a vibrational level spacing of approximately 20 MHz. The additional elliptical wells arise due to

avoided crossing with neighboring PES. To confirm this, Fig. 9.7 shows intersections for the fifth, sixth and seventh PES for $x_n = 0$, $y_n = 200a_0$. Avoided crossings of the PES are encountered, e.g., at $z \approx \pm 8.5 \times 10^3 a_0$ and $z \approx \pm 5.5 \times 10^3 a_0$ for the fifth and sixth excited PES. A more global view

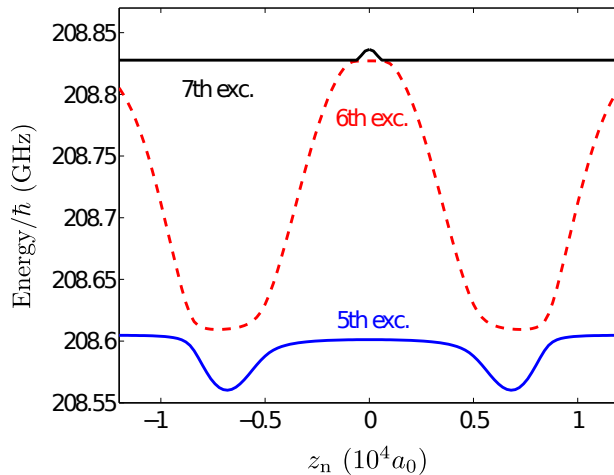


Figure 9.7: Intersections of the fifth, sixth and seventh excited potential surfaces for $x_n = 0$, $y_n = 200a_0$ are shown. Avoided crossings of the potentials are encountered. The spacing between the fifth and sixth surface at the avoided crossings is approximately 9 MHz.

of the geometry of the higher excited PES and their avoided crossings is provided with Fig. 9.8. It shows the PES obtained via perturbation theory, i.e., $\epsilon_{500}^{\text{pt}}(\mathbf{r}_n)$, $\epsilon_{600}^{\text{pt}}(\mathbf{r}_n)$ and $\epsilon_{001}^{\text{pt}}(\mathbf{r}_n)$ for fixed $x_n = 0$. The potential $\epsilon_{001}(\mathbf{r}_n)$ is obtained by raising the quantum number n_z and is given by

$$\epsilon_{001}^{\text{pt}}(\mathbf{r}_n) = \epsilon_{001} + 2\pi A_{\text{T}}[k(\mathbf{r}_n)]\tilde{C}z^2 e^{-a\rho_n^2 - cz_n^2}. \quad (9.16)$$

In contrast to $\epsilon_{500}^{\text{pt}}(\mathbf{r}_n)$ and $\epsilon_{600}^{\text{pt}}(\mathbf{r}_n)$ this potential curve possess two minima at $z = \pm 5542a_0$. Because the depth of these minima (≈ 450 MHz) is larger than the level spacing of the unperturbed giant dipole levels [$(\epsilon_{001} - \epsilon_{600})/\hbar \approx 9$ MHz, $(\epsilon_{001} - \epsilon_{500})/\hbar \approx 250$ MHz] the PES $\epsilon_{001}^{\text{pt}}(\mathbf{r}_n)$ intersects neighboring PES. Due to the coupling between the different PES this leads to avoided crossings for the exact PES and consequently novel geometries of the potentials. In the vicinity of the avoided crossing the adiabatic approximation fails and we expect a strong rovibronic interaction mixing different electronic giant dipole states. As a consequence fast decay processes of wave packets probing the seam of the avoided crossings will take place. Finally we note that the radiative lifetimes of the excited states are for our chosen parameter values of the order of several days and therefore much longer than the typical vibrational frequencies in the excited PES: it should therefore be possible to probe the vibrational dynamics belonging to the complex geometry of the molecular PES of the excited giant dipole states. We remark that the occurrence of avoided crossing will be even more prominent in heavier giant dipole systems. Considering rubidium instead of hydrogen, for example, reduces the smallest level spacing by $m_p/M_{\text{Rb}} \approx 10^{-2}$, which yields $\omega_- = 2.5$ MHz. The depths of the potential surfaces, on the other hand, do not change significantly. As a result, already the ground state shows avoided crossings with neighboring potential surfaces.

9.8 Conclusion

Bringing together the concepts underlying atomic giant dipole states in external fields and ultra-long-range molecules, we demonstrated the existence of ultra-long-range giant dipole diatomic molecules. In particular, the exotic atomic state underlying these molecules give rise to novel

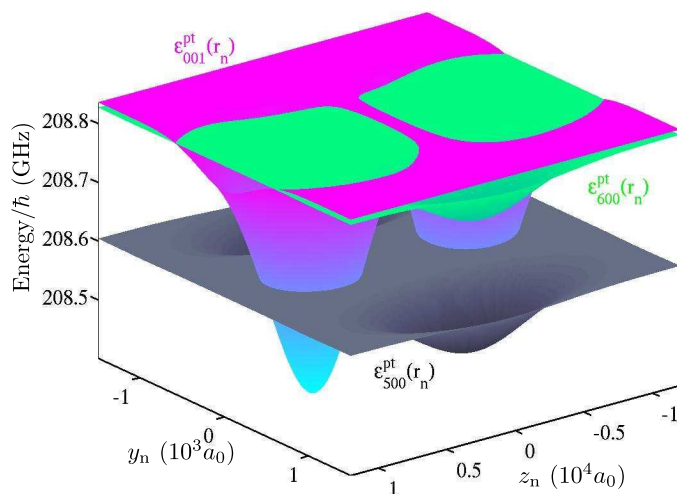


Figure 9.8: Two dimensional intersections of the perturbatively calculated PES for $x_n = 0$. We clearly see intersections of the perturbative potential surfaces.

properties such as a plethora of different quantum states with complex three-dimensional energy landscapes and rich rovibrational dynamics. The resulting molecules possess very large rovibrational bound states at internuclear distances in the range of $10^5 a_0$.

For their experimental preparation the 'best of two worlds' has to be combined. The preparation of giant dipole states is known to be possible starting from 'traditional' Rydberg states in magnetic fields and applying a sequence of electric field switches which brings the electron into low-lying outer well states [268]. Driven radio-frequency transitions in the outer well as an additional tool might help to prepare definite outer well states. Starting from these, one could overlap the GDS with a dense cloud of ultracold rubidium atoms and use radio- / microwave induced transitions to form the envisaged giant dipole molecular states. One of the main differences to standard cold atom experiments is certainly the regime of field strengths necessary to address the giant dipole states, which corresponds to strong static magnetic and electric fields. The results from this chapter have been published in Ref. [2].

Chapter 10

Summary and conclusions

We finally conclude by summarizing the results and providing a brief outlook on future research directions in the field of ultralong-range Rydberg molecules in external fields.

Field-free ultralong-range Rydberg molecules

The foundation of this thesis is based on a thorough derivation of the theory of ultracold Rydberg molecules in combined electric and magnetic fields. At first the properties of the molecular constituents, namely Rydberg atoms and ground state atoms, were discussed in detail. In particular the specific properties of Rydberg atoms and the electron-perturber interaction were discussed in detail. A detailed examination of all the ingredients necessary to adequately describe high and low angular momentum Rydberg states of an alkali atom has been provided. The coupling between the electronic and ground state atom was modeled as the Fermi-pseudopotential approach providing an effective contact interaction potential. In this particular field-dressed molecular system the translation symmetry and conservation of the total momentum in field-free space is replaced by a phase-space translation symmetry and the conservation of the pseudomomentum. Introducing center of mass and relative coordinates as well as a suitable phase-space unitary transformation considerably simplifies the ab-initio molecular Hamiltonian. In particular, the derived working Hamiltonian is an effective two-particle problem describing a Rydberg-electron and relative heavy particle motion in electric and magnetic fields. The remaining couplings between the relative and nuclei particle dynamics are treated as an adiabatic approach reminiscent of the Born-Oppenheimer separation in molecular physics. The initial problem of coupled nuclei and electron degrees of freedom is thereby reduced to the determination of adiabatic electronic energy surfaces that serve as an external potential for the nuclei dynamics. Reexamining the field-free molecular properties an analytical approach was introduced to obtain the adiabatic potential energy curves. While this approach relies on several approximations, it provides accurate results and a profound understanding of the underlying physics.

Ultralong-range Rydberg molecules in external fields

As the main subject of the present work we have explored the changes the polar high-angular momentum trilobite states experience when exposed to a purely electric, magnetic as well as combined external field configurations. Taking into account both s - and p -wave interactions it turns out that both electric and magnetic fields provide a unique way to control the topology of the adiabatic potential energy surfaces. In case ultralong-range diatomic Rydberg molecules are exposed to single external fields, the angular degree of freedom between the external electric or magnetic field and the internuclear axis is converted from a rotational to a vibrational degree of freedom, thereby rendering the field-free potential energy curve into a two-dimensional potential energy surface.

In the case of pure electric and magnetic fields the oscillatory behavior of the potential surfaces is changed dramatically in the presence of the fields. In the case of the electric field it turns out that the global equilibrium position is always in the antiparallel configuration with respect to the applied external field. Along the internuclear axis we find a sequence of potential wells with increasing radial coordinate. Increasing the electric field strength we encounter an overall lowering of the

energy accompanied by a subsequent crossover of the energetically order of individual potential wells. Consequently, the equilibrium distance and the lowest rovibrational states are systematically shifted to larger internuclear distances. This means that with increasing electric field strength the low lying molecular states can be progressively shifted away from the region of the avoided crossing of the p -wave split state which crosses the trilobite state near its equilibrium distance in the field-free case. In this manner the respective stability of the ground state and of many excited vibrational states is guaranteed. For strong fields the interaction of the electrically field dressed trilobite state with quantum defect states leads to a strong admixture of atomic s -state character to the high- l states. For this reason a two-photon excitation process starting from a two-atom system should be sufficient to create field-dressed ultralong-range Rydberg molecules.

Beside combined electric and magnetic fields we also studied a pure magnetic field configuration. This study extends a previous work by Lesanovsky *et al.* [99] where only pure s -wave interaction was considered. Taking into account both s - and p -wave interactions it turns out that strong level repulsion causes the potential wells which provide the trilobite states in the field-free case to vanish. Beyond a critical field strength of 100 G the trilobite potential energy surface (PES) does not provide any bound states anymore. In the case of combined electric and magnetic fields the field-free potential curve can even be rendered into a three-dimensional surface choosing appropriate angles of inclination between the two external field vectors. Depending on the specific degree of electronic excitation and field configuration we obtain oscillatory potential curves possessing rich topologies with localization in the radial and angular degrees of freedom and depths up to hundreds of MHz. Both the parallel and crossed field configurations provide unique ways to control the topology of the adiabatic potential surfaces. This leads to the possibility to directly control molecular orientation and alignment for both field configurations. In addition, the topological control of the PES provides the control of the electric dipole moment as well. The results from these studies have been published in Ref. [3, 5].

Alignment of ultracold $D_{5/2}$ -state Rydberg molecules

In this part we analyzed the properties of ultracold $D_{5/2}$ -state Rydberg molecules exposed to an external magnetic field of $B = 13.55$ G. In this project, which was conducted in collaboration with Prof. Tilman Pfau, Dr. Alexander Krupp and coworkers at the University of Stuttgart, ultracold Rydberg molecules were created from a thermal cloud of ultracold rubidium atoms with densities of 10^{12} cm^{-3} via a two-photon excitation process. This study is in line with a number of remarkable experimental studies of the nature of ultralong-range Rydberg molecules. For instance, in 2009 V. Bendowsky and coworkers for the first time created this novel molecular species which had been predicted by Prof. C. H. Greene in 2000 [85] using nearly the same experimental setup as it was used in Ref. [4]. However, these studies were conducted for S -state molecules whose molecular structure is determined by a spherically symmetric electronic s -orbital. In our work these studies were extended to $nD_{5/2}$ -state molecules. Exposing D -state molecules into a homogeneous magnetic field energetically splits the degenerate m_J sublevels. In contrast to the S -state molecular species these electronic states depend, besides the radial distance R , on the angle θ with respect to the applied magnetic field axis. For this reason the resulting adiabatic potential energy surfaces provide a richer topology beyond spherical symmetry. In this work two distinct species of D -state molecules have been studied, the $nD_{5/2}$, $m_J = 1/2, 5/2$ molecules for principal quantum numbers ranging from $n = 41$ to 50. Both the adiabatic potential energy surfaces and molecular binding energies were calculated and compared to the experimental data. In addition to the ground state molecules higher excited molecular states were detected as well. These states can be selectively excited by choosing the appropriate laser detuning. We discovered two different types of molecules. The first species is characterized by a high degree of molecular alignment parallel to the magnetic field axis. They stem from axial lobes in the electronic density distribution. These molecular states are denoted as axial states. In contrast, the second molecular species are determined by toroidal electron

density around the magnetic field axis, these states are denoted as toroidal states. The measured binding energies of both molecular species and the theoretically calculated data match satisfactorily. Deviations in the data sets were explained by an oversimplified model used to mimic the molecular dynamics and limitations in the excitation and detection techniques. As the two distinct D -state molecular species are determined by different electronic density profiles the molecular states differ in their alignment with respect to the applied magnetic field axis. The alignment of molecules is of central importance as it strongly influences their interaction and chemical reaction dynamics. Normally strong external electric, magnetic and light fields are required to create aligned molecules. In contrast, magnetically dressed D -state Rydberg molecules are intrinsically aligned due to their creation process in a weak magnetic fields. Rotational degrees of freedom are hardly excited as the created molecules possess large internuclear separations which results in a large moment of inertia. For this reason the molecules can be considered as stationary because they hardly rotate during their lifetime of around $10\mu\text{s}$. The results from this collaboration have been published in Ref. [4].

Ultralong-range giant dipole molecules in crossed electric and magnetic fields

The last part of this thesis contains the first results that had been published from our studies in Ref. [2]. In this work we show the existence of ultralong-range giant dipole molecules formed by a neutral alkali ground state atom that is bound to the decentered electronic wave function of a giant dipole atom. Besides the normal ground state atom these molecular species contain an exotic constituent, so-called atomic giant-dipole states. Opposite to the usual Rydberg states, the giant dipole states are of decentered character and possess a huge electric dipole moment. Their existence is related to the non-separability of the center of mass and electronic motion in the presence of the external fields. In contrast to Chapter 5 and Chapter 6, in this work the constituents of the ultralong-range diatomic molecular species only exist for finite field strengths. This means that these molecules cannot be understood as a field dressed version of a field-free diatomic molecule as the existence of these exotic molecular species is strongly related to the applied field strength of the electric and magnetic fields. Since the interaction of a giant dipole atom with a neutral ground state perturber can be described by a low-energy electron-atom scattering potential we apply the Fermi pseudopotential approach. The adiabatic potential surfaces emerging from the interaction of the ground state atom with the giant dipole electron possess a rich topology depending on the degree of electronic excitation. Depending on the applied field strength the resulting molecules are truly giant with internuclear distances up to several micrometers.

Outlook

Although ultralong-range diatomic Rydberg molecules have been studied intensively for almost fifteen years both theoretical and experimentally, this research field still provides a number of possibilities to extend the knowledge in the field of ultracold molecules.

A rather natural extension of the present work would be the investigation of polyatomic Rydberg molecules [87, 96] in both electric and magnetic fields. In case the Rydberg electron binds several ground state atoms the specific PES depend on the relative orientation of the ground state atoms. The higher dimensional energy surfaces are expected to provide a complex structure of oscillatory potential wells and avoided crossings. In addition, one can also consider the case where several ground state atoms from different species are bound by the Rydberg electron. Such molecules have become known as Borromean molecules as they only exist as polyatomic species due to mutual stabilization of their molecular bonds [97]. It would be interesting to explore the impact of electric and magnetic fields on the stability of these particular molecular species. Obviously, for both kind

of polyatomic species, combined external fields constitute a logical extension thereof. In addition, the properties of polyatomic giant dipole Rydberg molecules is still an open question.

Another very promising direction of research is the study of higher order electric and magnetic polarizabilities and susceptibilities. Because of their high sensitivity to small field strengths in Rydberg atoms these quantities strongly depend on the Rydberg excitation. For instance, the electric polarizability of single Rydberg atoms scales as n^7 . As the molecular properties both depend on the electron and nuclei degrees of freedom it is worth to extend the studies from Chapter 8 and to analyze these properties in more detail. Furthermore, the study of higher order polarizabilities can be easily extended to other molecular Rydberg species as polyatomic molecules and ultralong-range triatomic polar Rydberg molecules [241].

Finally, one can consider novel approaches to solve the electronic Schrödinger equation. A number of previous works [97,269] have already discussed the possibility to determine the adiabatic potential curves via the Green function approach. This approach is considered to be more robust compared to exact diagonalization. For this reason we expect it to provide reliable results in regimes where both exact diagonalization and the adiabatic approximation fail, for instance in the vicinity of avoided crossings.

Part III

Appendix

Appendix A

Numerical concepts

A.1 Construction of the interaction matrix

Next we present an efficient method to create the matrix representation of the interaction potential $V_{\text{en}}(\mathbf{r}; \mathbf{R})$. As discussed in Section 3.2 in order to determine the adiabatic potential surfaces we have to calculate the electronic eigenenergies $\varepsilon(\mathbf{R})$ as a function of the perturber position \mathbf{R} . In case of the present problem this means that we have to diagonalize a non sparse matrix of the dimension $\sim N^2$ at every position \mathbf{R} of the considered grid. Although the number of grid points might decrease significantly due to symmetry properties it is crucial to use an efficient way to construct the matrix representation of V_{en} due to limitations in CPU-time and memory.

At first we can use the fact that $V_{\text{en}}(\mathbf{R})$ is a sum of four separable matrices, cf. Section 4.2.1 and 4.2.1). As discussed in B.6 a separable $N \times N$ \mathbb{C} -matrix is a matrix that can be written as the matrix product of two $N \times 1$ \mathbb{C} -vectors. In our case we have

$$V_{\text{en}}^{s,p_i}(\mathbf{R}) = \boldsymbol{\psi}(\mathbf{R}) \otimes \boldsymbol{\psi}^\dagger(\mathbf{R}), \quad i = 1, 2, 3 \quad (\text{A.1})$$

with

$$\boldsymbol{\psi}(\mathbf{R}) = (\psi_{n,,m}(\mathbf{R}), \psi_{n,0,-1}(\mathbf{R}), \psi_{n,1,0}(\mathbf{R}), \psi_{n,-1,1}(\mathbf{R}), \dots, \psi_{n',n'-1,n'-1}(\mathbf{R}))^T \quad (\text{A.2})$$

Due to this the number of matrix elements that has to be calculated significantly reduces from $N(N+1)/2$ to N . However, we are still left with the fact that every function $\psi_{nlm}(\mathbf{R})$ depends on three spatial coordinates. For a large number of grid points this is might still lead to a large amount of data that has to stored and read into the used programs again.

To reduce the complexity of this problem we use the fact that in spherical coordinates R, θ, ϕ the functions $\psi_{nlm}(R, \theta, \phi)$ are given as a product of three separate functions, i.e.

$$\psi_{nlm}(R, \theta, \phi) = R_{nl}(R)F_{lm}(\theta)e^{im\phi} \quad \text{with} \quad F_{lm}(\theta) = \sqrt{\frac{2l+1}{4\pi} \frac{(l-m)!}{(l+m)!}} P_{lm}(\cos(\theta)) \quad (\text{A.3})$$

We can use this form to construct the interaction matrix V_{en} in a very elegant way. First we introduce a grid for the spherical coordinates, this means

$$[R_{\min}, R_{\max}] \rightarrow R_{\min} : \Delta R : R_{\max}, \quad (0, \pi] \rightarrow 0 : \Delta\theta : \pi, \quad (0, 2\pi] \rightarrow 0 : \Delta\phi : 2\pi.$$

In our problem R_{\max} has to be a least as large as the classical outer turning point of the electron of energy $-1/2n^2$ in the Coulomb potential, which leads to $R_{\max} = 2n^2$. For $n = 35$ this gives $R_{\max} = 2450a_0$. Finally, we have chosen $R_{\min} = 0$, $R_{\max} = 3000a_0$, $\Delta R = a_0$. In case of the angular grid we choose $\Delta\theta = \Delta\phi = 0.01\pi$. This means we get a grid of 3001 points in radial direction and 101 / 201 points in both the θ and ϕ component, respectively.

A.1.1 S-wave matrix construction

First we calculate five different files, each for every coordinate R, θ and and two for the ϕ angle. We denote these files "Radialfile" and "Thetafile" for the R and θ component and "RealPhifile"

/ "ImagPhifile" for the ϕ component. Each file contains a matrix where the columns contain the functions R_{nl} , F_{lm} and $\text{Re}(e^{im\phi}) = \cos(m\phi)$, $\text{Im}(e^{im\phi}) = \sin(m\phi)$ evaluated at a specific grid point. More precisely, in the vertical direction the quantum number n, l, m vary according to the used basis set at a fixed position while in the horizontal direction the positions R_j , θ_j and ϕ_j are varied while the quantum numbers are fixed. In particular the three files are structured as follows

$$\text{Radialfile} = \begin{bmatrix} R_{nl}(0) & \cdots & R_{nl}(R_j) & \cdots & R_{nl}(R_{\max}) \\ \vdots & \cdots & \vdots & \cdots & \vdots \\ R_{n'l'}(0) & \cdots & \underbrace{R_{n'l'}(R_j)}_{(j+1)\text{th column}} & \cdots & R_{nl}(R_{\max}) \end{bmatrix},$$

$$\text{Thetafile} = \begin{bmatrix} F_{lm}(0) & \cdots & F_{lm}(\frac{j\pi}{100}) & \cdots & F_{lm}(\pi) \\ \vdots & \cdots & \vdots & \cdots & \vdots \\ F_{l'm'}(0) & \cdots & \underbrace{F_{l'm'}(\frac{j\pi}{100})}_{(j+1)\text{th column}} & \cdots & F_{l'm'}(\pi) \end{bmatrix},$$

$$\text{RealPhifile} = \begin{bmatrix} 1 & \cdots & \cos(\frac{j m \pi}{100}) & \cdots & 1 \\ \vdots & \cdots & \vdots & \cdots & \vdots \\ 1 & \cdots & \underbrace{\cos(\frac{j m' \pi}{100})}_{(j+1)\text{th column}} & \cdots & 1 \end{bmatrix}, \quad \text{ImagPhifile} = \begin{bmatrix} 1 & \cdots & \sin(\frac{j m \pi}{100}) & \cdots & 1 \\ \vdots & \cdots & \vdots & \cdots & \vdots \\ 1 & \cdots & \underbrace{\sin(\frac{j m' \pi}{100})}_{(j+1)\text{th column}} & \cdots & 1 \end{bmatrix}.$$

Before we continue in constructing the interaction matrix we define a mapping " \odot " that maps two vectors $\mathbf{v}, \mathbf{w} \in \mathbb{C}^{n \times 1}$ in the following way

$$\odot : \mathbb{C}^{n \times 1} \times \mathbb{C}^{n \times 1} \rightarrow \mathbb{C}^{n \times 1} : (\mathbf{v}, \mathbf{w}) \rightarrow \mathbf{v} \odot \mathbf{w} \equiv (v_1 w_1, \dots, v_n w_n)^T.$$

Obviously, this mapping is just the element wise multiplication of the matrix elements of \mathbf{v}, \mathbf{w} to a new vector $\mathbf{v} \odot \mathbf{w}$.

Next we introduce the following notation for the i -th column of an arbitrary Matrix A

$$A(:, i) \equiv i\text{-th column of matrix } A$$

and we define the index function of a quantity η_i

$$\text{index}(\eta_i) = \frac{\eta_i}{\Delta\eta} + 1.$$

Using this mapping function we can set up the following algorithm to construct the interaction matrix $V_{\text{en}}^s(\mathbf{R})$:

1.) Choose a grid point $\mathbf{R} = (R_i, \theta_j, \phi_k)$

2.) Determine the indices of R_i, θ_j and ϕ_k

$$\text{index}(R_i) = i + 1, \quad \text{index}(\theta_j) = j + 1, \quad \text{index}(\phi_k) = k + 1.$$

3.) Load the files Radialfile, Thetafile, RealPhifile and ImagPhifile and read out the columns

from the matrices according to the indices. We define

$$\begin{aligned} \text{columnR} &\equiv \text{Radialfile}(:, i + 1), & \text{columnTheta} &\equiv \text{Thetafile}(:, j + 1), \\ \text{columnRePhi} &\equiv \text{RealPhifile}(:, k + 1), & \text{columnImPhi} &\equiv \text{ImagPhifile}(:, k + 1). \end{aligned}$$

The just defines quantities are $N \times 1$ \mathbb{C} -vectors.

4.) Using the just defined vectors we construct the vector "wavefunction" via

$$\text{wavefunction} \equiv \text{columnR} \odot \text{columnTheta} \odot \text{columnRePhi} \odot \text{columnImPhi}$$

5.) Finally we construct $V_{\text{en}}^s(\mathbf{R})$:

$$V_{\text{en}}^s(\mathbf{R}) = \text{wavefunction} \otimes \text{wavefunction}^\dagger.$$

A.1.2 P-wave matrix construction

As discussed in section 4.2.1 the matrix representation of the p -wave interaction term consists of three separable matrices. Analogous to the s -wave matrix construction one can construct every single matrix. For this we define three additional data files denoted as "DiffRadialfile", "DiffLegendrefile" and "Legendre2file". Again, the three files contain matrices where the columns now contain the functions $R'_{nl}(R)$, $F_{lm}(\theta)$ and $H_{lm}(\theta)$

$$\text{DiffRadialfile} = \begin{bmatrix} R'_{nl}(0) & \cdots & R'_{nl}(R_j) & \cdots & R'_{nl}(R_{\text{max}}) \\ \vdots & \cdots & \vdots & \cdots & \vdots \\ R'_{n'l'}(0) & \cdots & \underbrace{R'_{n'l'}(R_j)}_{(j+1)\text{th column}} & \cdots & R'_{n'l'}(R_{\text{max}}) \end{bmatrix},$$

$$\text{DiffLegendrefile} = \begin{bmatrix} F_{lm}(0) & \cdots & F_{lm}(\frac{j\pi}{100}) & \cdots & F_{lm}(\pi) \\ \vdots & \cdots & \vdots & \cdots & \vdots \\ F_{l'm'}(0) & \cdots & \underbrace{F_{l'm'}(\frac{j\pi}{100})}_{(j+1)\text{th column}} & \cdots & F_{l'm'}(\pi) \end{bmatrix},$$

$$\text{Legendre2file} = \begin{bmatrix} H_{lm}(0) & \cdots & H_{lm}(\frac{j\pi}{100}) & \cdots & H_{lm}(\pi) \\ \vdots & \cdots & \vdots & \cdots & \vdots \\ H_{l'm'}(0) & \cdots & \underbrace{H_{l'm'}(\frac{j\pi}{100})}_{(j+1)\text{th column}} & \cdots & H_{l'm'}(\pi) \end{bmatrix}.$$

To construct the p -wave interaction matrices we follow the steps (1) – (2) as we did in the previous paragraph. In the next step (3) we define, beside the vectors columnRePhi and columnImPhi , the vectors DiffcolumnR , $\text{DiffcolLegendreTheta}$, Legendre2theta via

$$\begin{aligned} \text{DiffcolumnR} &\equiv \text{DiffRadialfile}(:, i), \\ \text{DiffcolLegendreTheta} &\equiv \text{DiffLegendrefile}(:, j), \\ \text{Legendre2colTheta} &\equiv \text{Legendre2file}(:, j). \end{aligned}$$

We define the vectors p1wavefunc, p2wavefunc, p3wavefunc as

$$\begin{aligned} \text{p1wavefunc} &\equiv \text{DiffcolumnR} \odot \text{columnTheta} \odot \text{columnRePhi}, \\ \text{p2wavefunc} &\equiv \text{columnR} \odot \text{DiffcolLegendreTheta} \odot \text{columnRePhi}, \\ \text{p3wavefunc} &\equiv \text{columnR} \odot \text{Legendre2colTheta} \odot \text{columnRePhi}. \end{aligned}$$

and construct the corresponding interaction matrices $V_{\text{en}}^{p_i}(\mathbf{R})$, $i = 1, 2, 3$:

$$\begin{aligned} V_{\text{en}}^{p_1}(\mathbf{R}) &= \text{p1function} \otimes \text{p1function}^\dagger, \\ V_{\text{en}}^{p_2}(\mathbf{R}) &= \text{p2function} \otimes \text{p2function}^\dagger, \\ V_{\text{en}}^{p_3}(\mathbf{R}) &= \text{p3function} \otimes \text{p3function}^\dagger. \end{aligned}$$

The final p -wave interaction matrix is finally given by

$$V_{\text{en}}^p(\mathbf{R}) = 6\pi A_p^3(k(R))(V_{\text{en}}^{p_1}(\mathbf{R}) + V_{\text{en}}^{p_2}(\mathbf{R}) + V_{\text{en}}^{p_3}(\mathbf{R})).$$

A.2 Numerov integration method

A.2.1 General integration scheme

In order to calculate the low angular momentum Rydberg wave functions $R_{njl}(r)$ we have used a Numerov integration method [270]. In general, the Numerov method can be used to solve one dimensional problems of kind

$$\left(\frac{\partial^2}{\partial x^2} + V(x)\right)y(x) = 0. \quad (\text{A.4})$$

The potential $V(x)$ is sampled in the interval $[a, b]$ at equidistant points x_n . Starting from function values at two consecutive samples x_{n-1} and x_n the remaining function values can be calculated iteratively as

$$y(x_{n+2}) = \frac{(2 - \frac{5}{6}h^2V(x_{n+1}))y(x_{n+1}) - (1 + \frac{1}{12}h^2V(x_n))y(x_n)}{1 + \frac{h^2}{12}V(x_{n+2})}. \quad (\text{A.5})$$

Here $h = x_{n+1} - x_n$ is the distance between two consecutive points.

A.2.2 Application to Rydberg wave functions

We can use the Numerov integration method to solve the radial Schrödinger equation (1.23)

$$\left(\frac{\partial^2}{\partial r^2} + V_{\text{eff}}(r)\right)u_{njl}(r) = 0 \quad \text{with} \quad V_{\text{eff}}(r) = 2(E_{njl} - V_l(r) - V_{\text{so}}(r)) - \frac{l(l+1)}{r^2}. \quad (\text{A.6})$$

With the potential $V_{\text{eff}}(r)$ the radial equation can be numerically integrated in order to obtain the radial wave function $R_{njl}(r)$. Since the model potential does not reproduce the short range behavior near the origin correctly, care must be taken when choosing the boundary conditions. We introduce an inner radius r_i at which the calculated wave function should be truncated. The integration to $r \rightarrow \infty$ might also be truncated at an outer radius r_o where $R(r_o)$ has decayed sufficiently. To minimize the errors in the calculation of the radial wave function due to the core potential just being modeled approximative, the integration should be carried out inwards, beginning at the outer starting point r_o . For $r \rightarrow \infty$ we expect $u_{njl}(r)$ to decay exponentially like the hydrogen radial wave

function. For this reason we choose

$$u_0 \equiv u_{njl}(r_o) = (-1)^{n-l-1} e^{-r_o}, \quad u_1 \equiv u_{njl}(r_o - dr) = (-1)^{n-l-1} e^{-(r_o-dr)}. \quad (\text{A.7})$$

to be the initial points for the Numerov integration (see A.2.1). The radial spacing dr was varied from a_0 to $a_0/20$ and finally fixed to $dr = a_0/10$. The truncated wave function has to be normalized after calculation such that

$$\int_{r_i}^{r_o} u_{njl}^2(r) = 1. \quad (\text{A.8})$$

It turns out that good values are $r_o = 2n(n+15)$ and $r_i = \sqrt[3]{\alpha_c}$. Alternatively, the cutoff values $r_c(l)$ of the polarization potential can be used as well, cf. Table 1.4. Finally, it is important to note that the Numerov integration scheme does not provide any eigenenergies E_{njl} . These have to be calculated using different methods or provided by experimental measurements. In this work we have used experimental data provided by [127].

A.3 Finite difference method

In order to calculate the rovibrational wave function we will use the so called finite difference method. In general, the finite-difference method is a numerical method for approximating the solutions to differential equations using finite difference equations to approximate derivatives.

A.3.1 One-dimensional problems

First we consider one dimensional eigenvalue problems of kind

$$\left(\frac{\partial^2}{\partial x^2} + V(x)\right)f(x) = Ef(x). \quad (\text{A.9})$$

In case of the finite-difference method the basic idea is to express the second derivatives and the potential $V(x)$ on a grid and transfer the second order differential equation (A.9) into an algebraic eigenvalue problem. In a first step the first derivative is expressed as

$$\frac{d}{dx}f(x) \approx \frac{f(x+h) - f(x-h)}{2h}. \quad (\text{A.10})$$

Obviously, there are different possibilities to approximate the first derivative:

- forward finite difference

$$\frac{d}{dx}f(x) \approx \frac{f(x+h) - f(x)}{h},$$

- backward finite difference

$$\frac{d}{dx}f(x) \approx \frac{f(x) - f(x-h)}{h},$$

- central finite difference

$$\frac{d}{dx}f(x) \approx \frac{f(x+h) - f(x-h)}{2h}.$$

Within this thesis we use the central finite difference scheme only. In case of the second derivative representation one gets

$$f''(x_0) = \frac{f(x_0 + h) - 2f(x_0) + f(x_0 - h))}{h^2}.$$

The accuracy of a grid representation can be increased by expressing the derivatives using a larger number of grid points. For instance, the first derivative $f'(x_0)$ can be expressed using the next to next grid points $x_0 \pm 2h$ as well

$$\begin{aligned} f'(x_0) &= \frac{1}{h} \left(-\frac{1}{12}f(x_0 + 2h) + \frac{2}{3}f(x_0 + h) - \frac{2}{3}f(x_0 - h) + \frac{1}{12}f(x_0 - 2h) \right) \\ f''(x_0) &= \frac{1}{h^2} \left(-\frac{1}{12}f(x_0 + 2h) + \frac{4}{3}f(x_0 + h) - \frac{5}{2}f(x_0) + \frac{4}{3}f(x_0 - h) + \frac{1}{12}f(x_0 - 2h) \right) \end{aligned}$$

In this case the accuracy of the derivatives is of the order of h^4 . It is conventional to present the coefficients in front of the $f(x_0 \pm nh)$ for the derivatives in a table as follows. By representing the

Derivative	Accuracy	$x_0 - 2h$	$x_0 - h$	x_0	$x_0 + h$	$x_0 + 2h$
1	h^2	0	-1/2	0	1/2	0
1	h^4	1/12	-2/3	0	2/3	-1/12
2	h^2	0	1	-2	1	0
2	h^4	-1/12	4/3	-5/2	4/3	1/12

Table A.1: Central finite difference coefficients of for the first and second derivative up to an accuracy of h^2 and h^4 .

derivatives as finite differences we can now transfer the second order differential equation Eq. (A.9) into an algebraic problem. Using the grid representation up to $\mathcal{O}(h^2)$. Obviously, the expansion to higher orders in h is straight forward. We obtain

$$\underbrace{\begin{bmatrix} \frac{2}{h^2} + V(x_0) & -\frac{1}{h^2} & 0 & \cdots & 0 \\ -\frac{1}{h^2} & \frac{2}{h^2} + V(x_1) & \ddots & \vdots & \vdots \\ 0 & \ddots & \ddots & \vdots & \vdots \\ \vdots & \cdots & \cdots & \ddots & -\frac{1}{h^2} \\ 0 & \cdots & \cdots & -\frac{1}{h^2} & \frac{2}{h^2} + V(x_n) \end{bmatrix}}_{\equiv M_1} \begin{bmatrix} f(x_0) \\ f(x_1) \\ \vdots \\ \vdots \\ f(x_n) \end{bmatrix} = E \begin{bmatrix} f(x_0) \\ f(x_1) \\ \vdots \\ \vdots \\ f(x_n) \end{bmatrix}. \quad (\text{A.11})$$

This is an eigenvalue problem where the Hamiltonian is represented by an $(n + 1)^2$ dimensional real and symmetric band structured matrix. Depending on the degree of accuracy k the number of non zero bands is given with $2k + 1$. However, the structure of the Hamilton matrix remains simple and the corresponding eigenvalue problem can easily be solved with standard numerical tools.

Finally we introduce a compact notation to represent band structured matrices in general. For this purpose we label the n -th row of a matrix with negative integers $-(n - 1)$ and the columns with positive integers $n - 1$. In this case we write a general band structured matrix A that consists of vectors $\mathbf{a}_1, \dots, \mathbf{a}_n$ and $\mathbf{b}_1, \dots, \mathbf{b}_m$ with $A_{N_1 1} = [\mathbf{a}_k]_1$, $A_{1 M_1} = [\mathbf{b}_k]_1$ respectively as

$$A \equiv \text{band} \begin{bmatrix} \mathbf{a}_n & \mathbf{a}_{n-1} & \cdots & \mathbf{b}_{m-1} & \mathbf{b}_m \\ -N_n + 1 & -N_{n-1} + 1 & \cdots & M_{m-1} - 1 & M_m - 1 \end{bmatrix}. \quad (\text{A.12})$$

In this case the matrix M_1 in Eq. (A.11) can be written as

$$M_1 = \text{band} \begin{bmatrix} \mathbf{h} & \mathbf{V}_1 & \mathbf{h} \\ -1 & 0 & 1 \end{bmatrix}. \quad (\text{A.13})$$

with $\mathbf{V}_1 = (2/h^2 + V(x_0), \dots, 2/h^2 + V(x_n))^T$ and $\mathbf{h} = (-1/h^2, \dots, -1/h^2)^T$.

A.3.2 Multi-dimensional problems

In this paragraph we expand the concept of finite differences on multi-dimensional problems of kind

$$\left(\sum_{ij} \frac{\partial^2}{\partial x_i \partial x_j} + V(\mathbf{x}) \right) f(\mathbf{x}) = E f(\mathbf{x}). \quad (\text{A.14})$$

Because the following concepts can easily be expanded to arbitrary dimensions we restrict our analysis to the two dimensional case, e.g. $f(\mathbf{x}) = f(x, y)$. Analogous to the one-dimensional problem the grid representation of the partial derivatives is given by

$$\begin{aligned} f_x(x_0, y_0) &= \frac{f(x_0 + h_x, y_0) - f(x_0 - h_x, y_0)}{2h_x}, & f_y(x_0, y_0) &= \frac{f(x_0, y_0 + h_y) - f(x_0, y_0 - h_y)}{2h_y}, \\ f_{xx}(x_0, y_0) &= \frac{f(x_0 + h_x, y_0) - 2f(x_0, y_0) + f(x_0 - h_x, y_0)}{h_x^2}, \\ f_{yy}(x_0, y_0) &= \frac{f(x_0, y_0 + h_y) - 2f(x_0, y_0) + f(x_0, y_0 - h_y)}{h_y^2}, \\ f_{xy}(x_0, y_0) &= \frac{1}{4h_x h_y} (f(x_0 + h_x, y_0 + h_y) - f(x_0 + h_x, y_0 - h_y) \\ &\quad - f(x_0 - h_x, y_0 + h_y) + f(x_0 - h_x, y_0 - h_y)). \end{aligned}$$

Again, these derivatives can be expanded to higher orders in h_x and h_y respectively. Analogous to Section A.3.1 the differential equation (A.14) can be transferred into an eigenvalue problem. If we restrict the degree of accuracy on $\mathcal{O}(h^2)$ and assume all mixed partial derivatives to vanish we get a matrix of order $((N_x + 1)(N_y + 1))^2$ where N_x , N_y are the number of grid points in the x and y variable, respectively. The obtained real, symmetric and sparse matrix now contains of 2 off diagonal bands with non zero elements.

Next we analyze the case when all mixed partial derivatives are zero.

$$M_2 \begin{bmatrix} f(x_0, y_0) \\ f(x_0, y_1) \\ \vdots \\ \vdots \\ f(x_{n_x}, y_{n_y-1}) \\ f(x_{n_x}, y_{n_y}) \end{bmatrix} = E \begin{bmatrix} f(x_0, y_0) \\ f(x_0, y_1) \\ \vdots \\ \vdots \\ f(x_{n_x}, y_{n_y-1}) \\ f(x_{n_x}, y_{n_y}) \end{bmatrix},$$

where the matrix M_2 is expressed as

$$M_2 = \text{band} \begin{bmatrix} \mathbf{h}_y & \mathbf{h}_x & \mathbf{V}_2 & \mathbf{h}_x & \mathbf{h}_y \\ -N_y + 1 & -1 & 0 & 1 & N_y - 1 \end{bmatrix} \quad (\text{A.15})$$

with $\mathbf{h}_{x/y} = (-1/h_{x/y}^2, \dots, -1/h_{x/y}^2)^T$ and $\mathbf{V}_2 = (\frac{2}{h_x^2} + \frac{2}{h_y^2} + V(x_0, y_0), \dots, \frac{2}{h_x^2} + \frac{2}{h_y^2} + V(x_{N_x}, y_{N_y}))^T$.

Appendix B

Auxiliary calculations

B.1 Atomic units

In atomic and molecular physics it is convenient to express the physical quantities in so-called *atomic units*. There are two different kinds of atomic units, *Hartree atomic units* and *Rydberg atomic units*, which differ in the choice of the unit of mass and charge. This thesis deals with Hartree atomic units. The following four fundamental constants form the basis of the atomic units:

- electron mass m_e
- elementary charge e
- Bohr radius a_0
- angular momentum \hbar .

Quantity	Atomic unit	SI unit	CGS unit
mass	m_e	$9.10938215 \times 10^{-31}$ kg	$9.10938215 \times 10^{-28}$ g
charge	e	$1.602176487 \times 10^{-19}$ C	$4.80267655 \times 10^{-10}$ Fr
length	a_0	$5.2917720859 \times 10^{-11}$ m	$5.2917720859 \times 10^{-9}$ cm
angular momentum	\hbar	$1.054571628 \times 10^{-34}$ Js	$1.0545716 \times 10^{-27}$ ergs
energy	$E_h = \hbar^2/m_e a_0^2$	$4.35974394 \times 10^{-18}$ J	$4.35974394 \times 10^{-11}$ erg
velocity	$v_h = a_0 E_h / \hbar$	2.1876912541×10^6 m/s	2.1876912541×10^8 cm/s
momentum	\hbar/a_0	$1.992851565 \times 10^{-24}$ kgm/s	$1.992851565 \times 10^{-29}$ gcm/s
magnetic field strength	\hbar/ea_0^2	2.350517382×10^5 T	2.350517382×10^9 G
magnet field gradient	\hbar/ea_0^3	4.441834×10^{15} T/m	4.441834×10^{17} G/cm
magnetic dipole moment	$\hbar e/m_e$	$1.854801830 \times 10^{-23}$ J/T	$1.854801830 \times 10^{-20}$ erg/G
electric dipole moment	ea_0	$8.47835281 \times 10^{-30}$ Cm	$2.543630749 \times 10^{-18}$ Fr cm
electric field	E_h/ea_0	$5.14220632 \times 10^{11}$ V/m	1.5416117×10^{12} statV/cm
time	\hbar/E_h	$2.418884326505 \times 10^{-17}$ s	$2.418884326505 \times 10^{-17}$ s
speed of light	v_h/α	2.99792458×10^8 m/s	$2.99792458 \times 10^{10}$ cm/s

Table B.1: Various physical quantities expressed in atomic units, SI units and CGS units.

In Table B.1 we present some physical quantities expressed in atomic units. In addition, the corresponding values in both SI units and CGS units are provided. We note that in case of the electric dipole moment it is common to use the “Debye”¹ as standard unit. Its relation to the other units one Debye is given by

$$1 \text{ Debye} = 2.543630749ea_0 = 10^{-18} \text{ Fr cm} = 3.33564 \times 10^{-30} \text{ Cm}. \quad (\text{B.1})$$

In the literature atomic units are often abbreviated “a.u.” or “au”, not to be confused with the same abbreviation used also for astronomical units, arbitrary units, and absorbance units in different contexts.

¹In honor of the physicist and physical chemist Peter J. W. Debye (1884-1966).

B.2 Derivation of the working Hamiltonian

In this section we derive the working Hamiltonian of diatomic Rydberg molecules in external fields.

B.2.1 Coordinate and momentum transformation

The transformation of the generalized coordinates and the Jacobi coordinates can be written as

$$(\mathbf{r}, \mathbf{R}, \mathbf{R}_{\text{cm}})^T = X(\mathbf{r}_e, \mathbf{r}_c, \mathbf{r}_n)^T, \quad X = \begin{bmatrix} 1 & -1 & 0 \\ 0 & -1 & 1 \\ \frac{m_e}{\mathcal{M}} & \frac{m_c}{\mathcal{M}} & \frac{m_n}{\mathcal{M}} \end{bmatrix} \quad (\text{B.2})$$

The transformation matrix X is invertible which leads to

$$(\mathbf{r}_e, \mathbf{r}_c, \mathbf{r}_n)^T = X^{-1}(\mathbf{r}, \mathbf{R}, \mathbf{R}_{\text{cm}})^T, \quad X^{-1} = \begin{bmatrix} \frac{m_c+m_n}{\mathcal{M}} & -\frac{m_n}{\mathcal{M}} & 1 \\ -\frac{m_e}{\mathcal{M}} & -\frac{m_n}{\mathcal{M}} & 1 \\ -\frac{m_e}{\mathcal{M}} & \frac{m_e+m_c}{\mathcal{M}} & 1 \end{bmatrix} \quad (\text{B.3})$$

We define $\underline{\mathbf{r}} = (\mathbf{r}_e, \mathbf{r}_c, \mathbf{r}_n)^T$ and $\underline{\mathbf{R}} = (\mathbf{r}, \mathbf{R}, \mathbf{R}_{\text{cm}})^T$ and write the last expression as

$$\underline{\mathbf{r}}_i = \sum_k (X^{-1})_{ik} \underline{\mathbf{R}}_k, \quad \Rightarrow \quad \frac{\partial \underline{\mathbf{r}}_i}{\partial \underline{\mathbf{R}}_k} = (X^{-1})_{ik}. \quad (\text{B.4})$$

This expression we can use to find the transformation relation between the conjugated momenta. We define $\underline{\mathbf{p}} = (\mathbf{p}_e, \mathbf{p}_c, \mathbf{p}_n)^T$ and $\underline{\mathbf{P}} = (\mathbf{p}, \mathbf{P}, \mathbf{P}_{\text{cm}})^T$ and obtain

$$\underline{\mathbf{P}}_i = -i \vec{\nabla}_{\underline{\mathbf{R}}_i} = \sum_k \frac{\partial \underline{\mathbf{r}}_k}{\partial \underline{\mathbf{R}}_i} \underline{\mathbf{p}}_k = \sum_k (X^{-1})_{ki} \underline{\mathbf{p}}_k = \sum_i ((X^{-1})^T)_{ik} \underline{\mathbf{p}}_k. \quad (\text{B.5})$$

In matrix notation this reads

$$(\underline{\mathbf{p}}, \underline{\mathbf{P}}, \underline{\mathbf{P}}_{\text{cm}})^T = (X^{-1})^T (\underline{\mathbf{p}}_e, \underline{\mathbf{p}}_c, \underline{\mathbf{p}}_n)^T, \quad (\text{B.6})$$

with

$$(X^{-1})^T = \begin{bmatrix} \frac{m_c+m_n}{\mathcal{M}} & -\frac{m_e}{\mathcal{M}} & -\frac{m_e}{\mathcal{M}} \\ -\frac{m_n}{\mathcal{M}} & -\frac{m_n}{\mathcal{M}} & \frac{m_e+m_c}{\mathcal{M}} \\ 1 & 1 & 1 \end{bmatrix}. \quad (\text{B.7})$$

B.2.2 Hamiltonian algebra

Next we derive the working Hamiltonian. As the results will not depend on the specific gauge [79] we chose the symmetric gauge with $\mathbf{A} = (\mathbf{B} \times \mathbf{r})/2$. In relative coordinates the pseudomomentum $\hat{\mathbf{K}}$ is given by

$$\hat{\mathbf{K}} = \mathbf{P}_{\text{cm}} - \frac{1}{2}(\mathbf{B} \times \mathbf{r}). \quad (\text{B.8})$$

$$\begin{aligned} H_{\text{mol}} &= \frac{1}{2m_e} \left(\frac{m_e}{\mathcal{M}} \mathbf{P}_{\text{cm}} + \mathbf{p} + \frac{1}{2} \mathbf{B} \times \left(\mathbf{R}_{\text{cm}} + \frac{m_n + m_c}{\mathcal{M}} \mathbf{r} + \frac{m_n}{\mathcal{M}} \mathbf{R} \right) \right)^2 \\ &+ \frac{1}{2m_c} \left(\frac{m_c}{\mathcal{M}} \mathbf{P}_{\text{cm}} - \mathbf{p} - \mathbf{P} - \frac{1}{2} \mathbf{B} \times \left(\mathbf{R}_{\text{cm}} - \frac{m_e}{\mathcal{M}} \mathbf{r} - \frac{m_n}{\mathcal{M}} \mathbf{R} \right) \right)^2 + \frac{1}{2m_n} \left(\frac{m_n}{\mathcal{M}} \mathbf{P}_{\text{cm}} + \mathbf{P} \right)^2 \\ &+ V_{\text{ec}}(\mathbf{r}) + V_{\text{cn}}(\mathbf{r}, \mathbf{R}) + V_{\text{cn}}(\mathbf{R}) \\ &\equiv T_{\text{mol}} + \mathbf{E} \cdot \mathbf{r} + V_{\text{ec}}(\mathbf{r}) + V_{\text{cn}}(\mathbf{r}, \mathbf{R}) + V_{\text{cn}}(\mathbf{R}). \end{aligned} \quad (\text{B.9})$$

Here we have introduced to kinetic energy operator T_{mol} . Next we transform the molecular wave function Ψ_{mol} via a unitary transformation U :

$$\Psi_{\text{mol}}(\mathbf{x}) = U(\mathbf{r}, \mathbf{R}_{\text{cm}})\psi_{\text{mol}}(\mathbf{r}, \mathbf{R}) \quad \text{with} \quad U(\mathbf{r}, \mathbf{R}_{\text{cm}}) = \exp\{i(\mathbf{K} + \frac{1}{2}\mathbf{B} \times \mathbf{r}) \cdot \mathbf{R}_{\text{cm}}\}$$

Obviously the unitary transformation U commutes with the potentials in the molecular Hamiltonian in Eq. B.9. For this reason only the transformation of the kinetic energy operator has to be considered. We define

$$T = U^{-1}T_{\text{tot}}U \tag{B.10}$$

and use

$$U^{-1}\mathbf{p}U = \mathbf{p} - \frac{1}{2}\mathbf{B} \times \mathbf{R}_{\text{cm}}, \quad U^{-1}\mathbf{P}U = \mathbf{P}, \quad U^{-1}\mathbf{P}_{\text{cm}}U = \mathbf{P}_{\text{cm}} + \mathbf{K} + \frac{1}{2}\mathbf{B} \times \mathbf{r}.$$

By construction \mathbf{R}_{cm} is eliminated from the the Hamiltonian, which means it is unnecessary to keep the momentum operator \mathbf{P}_{cm} . We get

$$\begin{aligned} T &= \frac{1}{2m_e} \left(\frac{m_e}{\mathcal{M}} \mathbf{K} + \mathbf{p} + \frac{1}{2} \mathbf{B} \times \left(\mathbf{r} - \frac{m_n}{\mathcal{M}} \mathbf{R} \right) \right)^2 + \frac{1}{2m_n} \left(\frac{m_n}{\mathcal{M}} \mathbf{K} + \mathbf{P} + \frac{m_n}{2\mathcal{M}} \mathbf{B} \times \mathbf{r} \right)^2 \\ &\quad + \frac{1}{2m_c} \left(\frac{m_c}{\mathcal{M}} \mathbf{K} - \mathbf{p} - \mathbf{P} + \frac{1}{2} \mathbf{B} \times \left(\frac{m_e + m_c}{\mathcal{M}} \mathbf{r} + \frac{m_n}{\mathcal{M}} \mathbf{R} \right) \right)^2 \\ &= \frac{m_e}{2\mathcal{M}^2} \mathbf{K}^2 + \frac{\mathbf{K}}{\mathcal{M}} \left(\mathbf{p} + \frac{1}{2} \mathbf{B} \times \left(\mathbf{r} - \frac{m_n}{\mathcal{M}} \mathbf{R} \right) \right) + \frac{1}{2m_e} \left(\mathbf{p} + \frac{1}{2} \mathbf{B} \times \left(\mathbf{r} - \frac{m_n}{\mathcal{M}} \mathbf{R} \right) \right)^2 \\ &\quad + \frac{m_c}{2\mathcal{M}^2} \mathbf{K}^2 - \frac{\mathbf{K}}{\mathcal{M}} \left(\mathbf{p} + \mathbf{P} - \frac{1}{2} \mathbf{B} \times \left(\frac{m_e + m_c}{\mathcal{M}} \mathbf{r} + \frac{m_n}{\mathcal{M}} \mathbf{R} \right) \right) \\ &\quad + \frac{1}{2m_c} \left(\mathbf{p} + \mathbf{P} - \frac{1}{2} \mathbf{B} \times \left(\frac{m_e + m_c}{\mathcal{M}} \mathbf{r} + \frac{m_n}{\mathcal{M}} \mathbf{R} \right) \right)^2 + \frac{m_n}{2\mathcal{M}^2} \mathbf{K}^2 \\ &\quad + \frac{\mathbf{K}}{\mathcal{M}} \left(\mathbf{P} + \frac{m_n}{2\mathcal{M}} \mathbf{B} \times \mathbf{r} \right) + \frac{1}{2m_n} \left(\mathbf{P} + \frac{m_n}{2\mathcal{M}} \mathbf{B} \times \mathbf{r} \right)^2 \\ &= \frac{\mathbf{K}^2}{2\mathcal{M}} + \frac{\mathbf{K}}{2\mathcal{M}} \left(\mathbf{B} \times \left(\mathbf{r} - \frac{m_n}{\mathcal{M}} \mathbf{R} + \frac{m_c + m_e}{\mathcal{M}} \mathbf{r} + \frac{m_n}{\mathcal{M}} \mathbf{r} + \frac{m_n}{\mathcal{M}} \mathbf{R} \right) \right) \\ &\quad + \frac{1}{2m_e} \left(\mathbf{p} + \frac{1}{2} \mathbf{B} \times \left(\mathbf{r} - \frac{m_n}{\mathcal{M}} \mathbf{R} \right) \right)^2 + \frac{1}{2m_n} \left(\mathbf{P} + \frac{m_n}{2\mathcal{M}} \mathbf{B} \times \mathbf{r} \right)^2 \\ &\quad + \frac{1}{2m_c} \left(\mathbf{p} + \mathbf{P} - \frac{1}{2} \mathbf{B} \times \left(\frac{m_n + m_c}{\mathcal{M}} \mathbf{r} + \frac{m_n}{\mathcal{M}} \mathbf{R} \right) \right)^2 \\ &= \frac{\mathbf{K}^2}{2\mathcal{M}} + \frac{\mathbf{K}}{\mathcal{M}} \left(\mathbf{B} \times \mathbf{r} \right) + \frac{1}{2\mathcal{M}} \left(\mathbf{B} \times \mathbf{r} \right)^2 - \frac{1}{2\mathcal{M}} \left(\mathbf{B} \times \mathbf{r} \right)^2 \\ &\quad + \frac{1}{2m_e} \left(\mathbf{p} + \frac{1}{2} \mathbf{B} \times \left(\mathbf{r} - \frac{m_n}{\mathcal{M}} \mathbf{R} \right) \right)^2 + \frac{1}{2m_n} \left(\mathbf{P} + \frac{m_n}{2\mathcal{M}} \mathbf{B} \times \mathbf{r} \right)^2 \\ &\quad + \frac{1}{2m_c} \left(\mathbf{p} + \mathbf{P} - \frac{1}{2} \mathbf{B} \times \left(\frac{m_e + m_c}{\mathcal{M}} \mathbf{r} + \frac{m_n}{\mathcal{M}} \mathbf{R} \right) \right)^2 \\ &= \frac{1}{2\mathcal{M}} \left(\mathbf{K} + \mathbf{B} \times \mathbf{r} \right)^2 - \frac{1}{\mathcal{M}} \left(\mathbf{B} \times \mathbf{r} \right)^2 + \frac{1}{2\mathcal{M}} \left(\mathbf{B} \times \mathbf{r} \right)^2 \\ &\quad + \frac{1}{2m_e} \left(\mathbf{p} + \frac{1}{2} \mathbf{B} \times \left(\mathbf{r} - \frac{m_n}{\mathcal{M}} \mathbf{R} \right) \right)^2 + \frac{1}{2m_n} \left(\mathbf{P} + \frac{m_n}{2\mathcal{M}} \mathbf{B} \times \mathbf{r} \right)^2 \\ &\quad + \frac{1}{2m_c} \left(\mathbf{p} + \mathbf{P} - \frac{1}{2} \mathbf{B} \times \left(\left(1 - \frac{m_n}{\mathcal{M}} \right) \mathbf{r} + \frac{m_n}{\mathcal{M}} \mathbf{R} \right) \right)^2 \end{aligned}$$

$$\begin{aligned}
&= \frac{1}{2\mathcal{M}}(\mathbf{K} + \mathbf{B} \times \mathbf{r})^2 + \frac{1}{2m_c}(\mathbf{p} + \mathbf{P} - \frac{1}{2}\mathbf{B} \times ((1 - \frac{m_n}{\mathcal{M}})\mathbf{r} + \frac{m_n}{\mathcal{M}}\mathbf{R}))^2 \\
&\quad + \frac{1}{2m_e}(\mathbf{p} + \frac{1}{2}\mathbf{B} \times (\mathbf{r} - \frac{m_n}{\mathcal{M}}\mathbf{R}))^2 + \frac{1}{2m_n}(\mathbf{P} + \frac{m_n}{2\mathcal{M}}\mathbf{B} \times \mathbf{r})^2 \\
&\quad + (\mathbf{p} + \mathbf{P} + \frac{1}{2}(\mathbf{B} \times \frac{m_n}{\mathcal{M}}\mathbf{r}) - \frac{1}{2}(\mathbf{B} \times \frac{m_n}{\mathcal{M}}\mathbf{R}) - \frac{1}{2}\mathbf{B} \times \mathbf{r})(\frac{1}{\mathcal{M}}\mathbf{B} \times \mathbf{r}) \\
&\quad - (\mathbf{p} + \frac{1}{2}\mathbf{B} \times (\mathbf{r} - \frac{m_n}{\mathcal{M}}\mathbf{R}) + \mathbf{P} + \frac{1}{2}(\mathbf{B} \times \frac{m_n}{\mathcal{M}}\mathbf{r}))(\frac{1}{\mathcal{M}}\mathbf{B} \times \mathbf{r}) \\
&\quad + \frac{m_e + m_n + m_c}{2\mathcal{M}^2}(\mathbf{B} \times \mathbf{r})^2 \\
&= \frac{1}{2m_e}((\mathbf{p} + \frac{1}{2}\mathbf{B} \times (\mathbf{r} - \frac{m_n}{\mathcal{M}}\mathbf{R}))^2 - 2\frac{m_e}{\mathcal{M}}(\mathbf{p} + \frac{1}{2}\mathbf{B} \times (\mathbf{r} - \frac{m_n}{\mathcal{M}}\mathbf{R}))(\mathbf{B} \times \mathbf{r}) \\
&\quad + \frac{m_e^2}{\mathcal{M}^2}(\mathbf{B} \times \mathbf{r})^2) + \frac{1}{2\mathcal{M}}(\mathbf{K} + \mathbf{B} \times \mathbf{r})^2 \\
&\quad + \frac{1}{2m_c}((\mathbf{p} + \mathbf{P} - \frac{1}{2}\mathbf{B} \times ((1 - \frac{m_n}{\mathcal{M}})\mathbf{r} + \frac{m_n}{\mathcal{M}}\mathbf{R}))^2 \\
&\quad + 2\frac{m_c}{\mathcal{M}}(\mathbf{p} + \mathbf{P} - \frac{1}{2}\mathbf{B} \times ((1 - \frac{m_n}{\mathcal{M}})\mathbf{r} + \frac{m_n}{\mathcal{M}}\mathbf{R}))(\mathbf{B} \times \mathbf{r}) + \frac{m_c^2}{\mathcal{M}^2}(\mathbf{B} \times \mathbf{r})^2) \\
&\quad + \frac{1}{2m_n}((\mathbf{P} + \frac{m_n}{2\mathcal{M}}\mathbf{B} \times \mathbf{r})^2 - 2\frac{m_n}{\mathcal{M}}(\mathbf{P} + \frac{m_n}{2\mathcal{M}}\mathbf{B} \times \mathbf{r})(\mathbf{B} \times \mathbf{r}) \\
&\quad + \frac{m_n^2}{\mathcal{M}^2}(\mathbf{B} \times \mathbf{r})^2) \\
&= \frac{1}{2\mathcal{M}}(\mathbf{K} + \mathbf{B} \times \mathbf{r})^2 + \frac{1}{2m_e}(\mathbf{p} + \frac{1}{2}\mathbf{B} \times \mathbf{r} - \frac{1}{2}\mathbf{B} \times (\frac{m_e}{\mathcal{M}}\mathbf{r} + \frac{m_n}{\mathcal{M}}\mathbf{R}))^2 \\
&\quad + \frac{1}{2m_c}((\mathbf{p} + \mathbf{P} - \frac{1}{2}\mathbf{B} \times ((1 - \frac{m_n}{\mathcal{M}} - \frac{m_c}{\mathcal{M}})\mathbf{r} + \frac{m_n}{\mathcal{M}}\mathbf{R}))^2 \\
&\quad + \frac{1}{2m_n}(\mathbf{P} - \frac{1}{2\mathcal{M}}\mathbf{B} \times \mathbf{r})^2
\end{aligned}$$

We neglect all terms $\sim B/\mathcal{M}$ and momentum polarization terms

$$\begin{aligned}
T &\approx \frac{\mathbf{K}^2}{2\mathcal{M}} + \frac{1}{2m_e}(\mathbf{p} + \frac{1}{2}\mathbf{B} \times \mathbf{r})^2 + \frac{1}{2}(\frac{1}{m_c} + \frac{1}{m_n})\mathbf{P}^2 + \frac{1}{2m_c}(\mathbf{p} - \frac{1}{2}\mathbf{B} \times \mathbf{r})^2 \\
&= \frac{1}{2}(\frac{1}{m_c} + \frac{1}{m_e})\mathbf{p}_1^2 + (\frac{1}{m_e} - \frac{1}{m_c})\mathbf{p}(\mathbf{B} \times \mathbf{r}) + \frac{1}{2}(\frac{1}{m_c} + \frac{1}{m_n})(\mathbf{B} \times \mathbf{r})^2 \\
&\quad + \frac{1}{2}(\frac{1}{m_c} + \frac{1}{m_n})\mathbf{P}^2.
\end{aligned}$$

We introduce the masses μ and M as well as the charge q

$$\mu = \frac{m_e m_c}{m_e + m_c}, \quad M = \frac{m_n m_c}{m_c + m_n}, \quad q = \frac{m_e - m_c}{m_c + m_e}.$$

In this case we obtain the transformed the kinetic energy operator

$$T = \frac{\mathbf{K}^2}{2\mathcal{M}} + \frac{\mathbf{P}^2}{2M} + \frac{1}{2\mu}(\mathbf{p} - \frac{q}{2}\mathbf{B} \times \mathbf{r})^2. \quad (\text{B.11})$$

Finally, use $\mu \approx m_e$, $M \approx m_n/2$ and $q \approx -1$. In this case the transformed molecular Hamiltonian H reads

$$H = \frac{\mathbf{K}^2}{2\mathcal{M}} + \frac{\mathbf{P}^2}{m_n} + \frac{1}{2m_e}(\mathbf{p} + \frac{1}{2}\mathbf{B} \times \mathbf{r})^2 + \mathbf{E} \cdot \mathbf{r} + V_{\text{ec}}(\mathbf{r}) + V_{\text{cn}}(\mathbf{r}, \mathbf{R}) + V_{\text{cn}}(\mathbf{R}). \quad (\text{B.12})$$

B.3 Hydrogenic giant dipole states

The Hamiltonian of a neutral two body system in homogeneous and static electric and magnetic field reads

$$H = \frac{1}{2m_e}(\mathbf{p}_1 + \frac{1}{2}\mathbf{B} \times \mathbf{r}_e)^2 + \mathbf{E} \cdot \mathbf{r}_e + \frac{1}{2m_p}(\mathbf{p}_2 - \frac{1}{2}\mathbf{B} \times \mathbf{r}_p)^2 - \mathbf{E} \cdot \mathbf{r}_p + V(\mathbf{r}_e - \mathbf{r}_p)$$

Similar to the three-particles problem in Section B.2.2 we introduce the center of mass coordinate \mathbf{R} and the relative vector \mathbf{r}

$$\mathbf{R} = \frac{1}{M}(m_e\mathbf{r}_e + m_p\mathbf{r}_p), \quad M = m_e + m_p, \quad \mathbf{r} = \mathbf{r}_e - \mathbf{r}_p. \quad (\text{B.13})$$

Analogous to the previous section this system possesses a pseudomomentum $\hat{\mathbf{K}}$ with

$$\hat{\mathbf{K}} = \mathbf{P} - \frac{1}{2}\mathbf{B} \times \mathbf{r} \quad (\text{B.14})$$

which is a conserved quantity. The quantities \mathbf{P} and \mathbf{p} are the conjugated momenta to the coordinates \mathbf{R} and \mathbf{r} respectively. Again we eliminate the total momenta \mathbf{P} via the unitary transformation

$$\Psi(\mathbf{R}, \mathbf{r}) = U(\mathbf{R}, \mathbf{r})\psi(\mathbf{r}), \quad U(\mathbf{R}, \mathbf{r}) = \exp\left(i\mathbf{K} \cdot \mathbf{R} + i\frac{1}{2}(\mathbf{B} \times \mathbf{r}) \cdot \mathbf{R}\right). \quad (\text{B.15})$$

and we get the following transformed Hamiltonian

$$H = \frac{1}{2\mu}\left(\mathbf{p} - \frac{q}{2}\mathbf{A}(\mathbf{r})\right)^2 + \frac{1}{2M}(\mathbf{K} + \mathbf{B} \times \mathbf{r})^2 + \mathbf{E} \cdot \mathbf{r} + V(\mathbf{r}) \quad (\text{B.16})$$

We have defined the effective mass $\mu = m_em_p/(m_e + m_p)$ and $q = (m_e - m_p)/(m_e + m_p)$. This is an effective one-particle Hamiltonian for the internal motion of the two-particle system. It depends only on the operators \mathbf{p}, \mathbf{r} of the relative coordinates and momenta but is linked to the center of mass motion via the eigenvalue \mathbf{K} of the pseudomomentum. The external electric field can be absorbed by shifting the vector of the eigenvalues $\mathbf{K} \rightarrow \mathbf{K} - M\frac{\mathbf{E} \times \mathbf{B}}{B^2}$. Neglecting an unimportant constant we obtain

$$H = \frac{1}{2\mu}\left(\mathbf{p} - \frac{q}{2}\mathbf{A}(\mathbf{r})\right)^2 + \frac{1}{2M}(\mathbf{K} + \mathbf{B} \times \mathbf{r})^2 - \frac{1}{r} \equiv \frac{1}{2\mu}\left(\mathbf{p} - \frac{q}{2}\mathbf{A}(\mathbf{r})\right)^2 + V_{\text{GD}}(\mathbf{r}) \quad (\text{B.17})$$

The potential $V_{\text{GD}}(\mathbf{r})$ is called giant dipole potential. Since all components of \mathbf{K} parallel to \mathbf{B} result in an energy shift only [79] we chose $\mathbf{B} = B\mathbf{e}_z$ $\mathbf{K} = K\mathbf{e}_y$. This gives

$$V_{\text{GD}}(\mathbf{r}) = \frac{1}{2M}(\mathbf{K} + \mathbf{B} \times \mathbf{r})^2 - \frac{1}{r} = \frac{K^2}{2M} + \frac{B^2}{2M}(x^2 + y^2) + \frac{BK}{M}x - \frac{1}{r}. \quad (\text{B.18})$$

The giant dipole potential possesses a outer well at $x_0 < 0, y_0 = 0, z_0 = 0$ which is determined by the cubic equation

$$x_0^3 + \frac{K}{M}x_0^2 - \frac{M}{B^2} = 0. \quad (\text{B.19})$$

The outer well only exist if $K^3 > 27BM/4$ [79]. In the case the potential minimum exists the giant dipole potential can be approximated by a three-dimensional harmonic potential $V_{\text{GD}}(\mathbf{r}) \approx V_{\text{h}}(\mathbf{r})$ with

$$V_{\text{h}}(\mathbf{r}) = \frac{\mu}{2}(\omega_x^2x^2 + \omega_y^2y^2 + \omega_z^2z^2) \quad (\text{B.20})$$

and

$$\omega_x = \sqrt{\frac{2}{\mu} \sqrt{\frac{B^2}{2M} + \frac{1}{x_0^3}}}, \quad \omega_y = \sqrt{\frac{1}{\mu} \sqrt{\frac{B^2}{2M} - \frac{1}{x_0^3}}}, \quad \omega_z = \sqrt{-\frac{1}{\mu x_0^3}}. \quad (\text{B.21})$$

The resulting Hamiltonian H_{GD} is given by

$$H_{\text{GD}} = \frac{1}{2\mu} \left(\mathbf{p} - \frac{q}{2} \mathbf{A}(\mathbf{r}) \right)^2 + \frac{\mu}{2} (\omega_x^2 x^2 + \omega_y^2 y^2 + \omega_z^2 z^2) \quad (\text{B.22})$$

and just reflects a particle of charge q and mass μ is an three-dimensional harmonic potential. The harmonic potential provided bound states which are characterized by a large electron-proton separation. As these states possess a large permanent dipole moment these states are called *giant dipole states*.

B.4 Finite difference representation

To derive the finite difference representation for an arbitrary derivative and accuracy we start with the Taylor expansion of a function $f(x)$ around an arbitrary point x_i

$$f(x) = \sum_{i=0}^{\infty} \frac{f^{(i)}(x_i)}{i!} (x - x_i)^i. \quad (\text{B.23})$$

$$f(x_i \pm mh) = \sum_{n=0}^{\infty} (\pm)^n \frac{f^{(n)}(x_i)}{n!} (mh)^n.$$

First we derive the first the finite difference representation for the first derivative in lowest order. We make the ansatz

$$f'(x_i) = \frac{\alpha_1 f(x_i + h) + \alpha_0 f(x_i) + \alpha_{-1} f(x_i - h)}{h}$$

and insert equation (B.24)

$$\frac{\alpha_1 (f(x_i) + hf'(x_i)) + \alpha_0 f(x_i) + \alpha_{-1} (f(x_i) - hf'(x_i))}{h} \quad (\text{B.24})$$

$$\Rightarrow \alpha_1 + \alpha_0 + \alpha_{-1} = 0 \quad \wedge \quad \alpha_1 - \alpha_{-1} = 1. \quad (\text{B.25})$$

We get $\alpha_0 = 0$, $\alpha_1 = -\alpha_{-1} = 1/2$. The truncation error is given with

$$\frac{1}{2h} (f(x_i + h) - f(x_i - h)) - f'(x_i) = \sum_{n=1}^{\infty} \frac{f^{(2n)}(x_i)}{(2n)!} h^{2n} \quad (\text{B.26})$$

We see that the truncation error is of order $\mathcal{O}(h^2)$.

Next we derive the equations to represent an arbitrary derivative $f^{(n)}(x_i)$, $n \in \mathbb{N}$ up to an arbitrary order accuracy. We start by expressing $f^{(n)}(x_i)$ via N neighbored points around x_i .

$$f^{(n)}(x_i) = \sum_{m=-N}^N \frac{\alpha_m f(x_i + mh)}{h^n} = \sum_{l=0}^{\infty} \frac{f^{(l)}(x_i)}{l!} h^{l-n} \sum_{m=-N}^N \alpha_m m^l. \quad (\text{B.27})$$

Obviously, the coefficients α_m have to satisfy the relation

$$\sum_{m=-N}^N \alpha_m m^l = n! \delta_{nl}, \quad l = 0, \dots, 2N. \quad (\text{B.28})$$

In this case the first non zero term on the right hand side of Eq. (B.27) is the desired derivative $f^{(n)}(x_i)$. From equation (B.28) we can derive the following relations of the coefficients α_m

$$\sum_{m=-N}^N \alpha_m m^{n-1} = \sum_{m=1}^N (\alpha_{-m} (-1)^{n-1} + \alpha_m) m^{n-1} = 0 \Rightarrow \alpha_{-m} = (-1)^n \alpha_m, \quad (\text{B.29})$$

and from $l = 0$ we get

$$\sum_{m=-N}^N \alpha_m = 0. \quad (\text{B.30})$$

Next we assume $l = 2N + k$ to be the first non vanishing term in (B.27) it is

$$\sum_{m=-N}^N \alpha_m m^{2N+k} = \sum_{m=1}^N ((-1)^{k+n} + 1) \alpha_m m^{2N+k} = 0 \Leftrightarrow n + k \text{ odd}. \quad (\text{B.31})$$

Then we get

$$\sum_{m=-N}^N \frac{\alpha_m f(x_i + mh)}{h^n} = f^{(n)}(x_i) + \mathcal{O}(h^{2N+k-n}) \quad (\text{B.32})$$

Because $k - n$ is even the order of the truncation error is always $\mathcal{O}(h^{2L})$, $L \in \mathbb{N}$. Obviously $K = 1 + \delta_{n,\text{even}}$ which gives the connection between the number of chosen points N and the order of accuracy $2L$ that we get for the finite difference calculation of a specific derivative $f^{(n)}(x_i)$

$$N = \frac{2L - 1 + n + \delta_{n,\text{even}}}{2}. \quad (\text{B.33})$$

B.5 Field-free Hamiltonian

B.5.1 Rotational symmetry properties

In this paragraph we prove some symmetry properties of the adiabatic potential curves for the field free Hamiltonian. For this we define the total angular momentum $\mathbf{L} = \mathbf{L}_r + \mathbf{L}_R$ and use the quantum mechanical rotation of an arbitrary angle

$$\exp(i\mathbf{L}\varphi)\Psi(\mathbf{r}, \mathbf{R}) = \Psi(\mathbf{r}', \mathbf{R}')$$

We get for a general electronic Born-Oppenheimer Schrödinger equation

$$\begin{aligned} H_{\text{el}}(\mathbf{r}; \mathbf{R})\Psi(\mathbf{r}; \mathbf{R}) &= \varepsilon(\mathbf{R})\Psi(\mathbf{r}; \mathbf{R}) \\ \Rightarrow \exp(i\mathbf{L}\varphi)H_{\text{el}}(\mathbf{r}; \mathbf{R})\Psi(\mathbf{r}; \mathbf{R}) &= \exp(i\mathbf{L}\varphi)\varepsilon(\mathbf{R})\Psi(\mathbf{r}; \mathbf{R}) \\ \Rightarrow H_{\text{el}}(\mathbf{r}'; \mathbf{R}')\Psi(\mathbf{r}'; \mathbf{R}') &= \varepsilon(\mathbf{R}')\Psi(\mathbf{r}'; \mathbf{R}') \end{aligned}$$

If $[H_{\text{el}}(\mathbf{r}; \mathbf{R}), \mathbf{L}] = [H_{\text{el}}(\mathbf{r}; \mathbf{R}), \exp(i\mathbf{L}\varphi)] = 0$ we have $H_{\text{el}}(\mathbf{r}'; \mathbf{R}') = H_{\text{el}}(\mathbf{r}; \mathbf{R})$ and $\Psi(\mathbf{r}'; \mathbf{R}') = a_M \Psi(\mathbf{r}; \mathbf{R})$, $a \in \mathbb{C}$, $|a| = 1$. In this case we get the following result:

$$\begin{aligned} aH_{\text{el}}(\mathbf{r}; \mathbf{R})\Psi(\mathbf{r}; \mathbf{R}) &= a\varepsilon(\mathbf{R}')\Psi(\mathbf{r}; \mathbf{R}) \\ \Rightarrow \varepsilon(\mathbf{R}') &= \varepsilon(\mathbf{R}). \end{aligned}$$

We see that for every electronic Hamiltonian H_{el} which fulfills $[H_{\text{el}}(\mathbf{r}; \mathbf{R}), \mathbf{L}] = 0$ the adiabatic potential surfaces $\varepsilon(\mathbf{R})$ only depend on the radial distance $R = |\mathbf{R}|$.

$$[H_{\text{el}}(\mathbf{r}; \mathbf{R}), \mathbf{L}] = 0 \quad \Rightarrow \quad \varepsilon(\mathbf{R}) = \varepsilon(R). \quad (\text{B.34})$$

B.5.2 P-wave function symmetry properties

$$\begin{aligned} F_{l,-m}(\theta) &= \frac{1}{2} \sqrt{\frac{2l+1}{4\pi} \frac{(l+m)!}{(l-m)!}} (P_{l,-m+1}(\cos(\theta)) - (l-m)(l+m+1)P_{l,-(m+1)}(\cos(\theta))) \\ &= \frac{1}{2} \sqrt{\frac{2l+1}{4\pi} \frac{(l+m)!}{(l-m)!}} (P_{l,-(m-1)} - (l-m)(l+m+1)(-1)^{m+1} \\ &\quad \frac{(l-m)!}{(l+m)!} P_{l,m+1}(\cos(\theta))) \\ &= \frac{1}{2} \sqrt{\frac{2l+1}{4\pi} \frac{(l+m)!}{(l-m)!}} ((-1)^{m+1} \frac{(l-(m-1))!}{(l+m-1)!} P_{l,m-1}(\cos(\theta)) \\ &\quad - (-1)^{m+1} \frac{(l-m)!}{(l+m)!} P_{l,m+1}(\cos(\theta))) \\ &= \frac{(-1)^m}{2} \sqrt{\frac{2l+1}{4\pi} \frac{(l+m)!}{(l-m)!}} \left(\frac{(l-m)!}{(l+m)!} P_{l,m+1}(\cos(\theta)) - \frac{(l-m+1)!}{(l+m-1)!} P_{l,m-1}(\cos(\theta)) \right) \\ &= \frac{(-1)^m}{2} \sqrt{\frac{2l+1}{4\pi} \frac{(l-m)!}{(l+m)!}} (P_{l,m+1}(\cos(\theta)) - (l-m+1)(l+m)P_{l,m-1}(\cos(\theta))) \\ &= (-1)^m F_{lm}(\theta), \end{aligned}$$

$$\begin{aligned} H_{l,-m}(\theta) &= -\frac{1}{2} \sqrt{\frac{2l+1}{4\pi} \frac{(l+m)!}{(l-m)!}} (P_{l+1,-m+1}(\cos(\theta)) \\ &\quad + (l+m+1)(l+m+2)P_{l+1,-(m+1)}(\cos(\theta))) \\ &= -\frac{1}{2} \sqrt{\frac{2l+1}{4\pi} \frac{(l+m)!}{(l-m)!}} ((-1)^{m+1} \frac{(l-m+2)!}{(l+m)!} P_{l+1,m-1}(\cos(\theta)) \\ &\quad + (l+m+1)(l+m+2) \frac{(l-m)!}{(l+m+2)!} P_{l+1,m+1}(\cos(\theta))) \\ &= (-1)^{m+1} \left(-\frac{1}{2}\right) \sqrt{\frac{2l+1}{4\pi} \frac{(l-m)!}{(l+m)!}} (P_{l+1,m+1}(\cos(\theta)) \\ &\quad + (l-m+1)(l-m+2)P_{l+1,m-1}(\cos(\theta))) \\ &= (-1)^{m+1} H_{lm}(\theta). \end{aligned}$$

Proof of commutator p -wave matrices commutator relations:

$$\begin{aligned}
\langle l'1|V_{\text{en}}^{p_2}V_{\text{en}}^{p_3}|l''\pm 1\rangle &= \sum_{l,m=\pm 1} \langle l'1|V_{\text{en}}^{p_2}|lm\rangle \langle lm|V_{\text{en}}^{p_3}|l''\pm 1\rangle \\
&= \sum_l \langle l'1|V_{\text{en}}^{p_2}|l,-1\rangle \langle l,-1|V_{\text{en}}^{p_3}|l''\pm 1\rangle + \langle l'1|V_{\text{en}}^{p_2}|l1\rangle \langle l1|V_{\text{en}}^{p_3}|l''\pm 1\rangle \\
&= \sum_l -\langle l'1|V_{\text{en}}^{p_2}|l1\rangle \langle l,1|V_{\text{en}}^{p_3}|l''1\rangle + \langle l'1|V_{\text{en}}^{p_2}|l1\rangle \langle l1|V_{\text{en}}^{p_3}|l''1\rangle = 0. \\
\Rightarrow V_{\text{en}}^{p_2}V_{\text{en}}^{p_3} &= 0 \quad \Rightarrow [V_{\text{en}}^{p_2}, V_{\text{en}}^{p_3}] = 0.
\end{aligned}$$

B.6 Separable matrices

Because the interaction terms $V_{\text{en}}^{p_i}$, $i = \{1, 2, 3\}$ (see Eq. 4.28) can be represented by separable matrices we provide and prove some of their properties. We start with the definition:

B.6.1 General properties**Definition B.1** *Separable Matrix*

A $m \times n$ \mathbb{C} -matrix M is called a separable matrix if it can be expressed as

$$M = \mathbf{v} * \mathbf{w}^\dagger, \quad \mathbf{v} = (v_1, \dots, v_m)^T \in \mathbb{C}^{m \times 1}, \quad \mathbf{w} = (w_1, \dots, w_n)^T \in \mathbb{C}^{n \times 1}.$$

In this equation $*$ indicates the standard matrix multiplication and $\mathbf{w}^\dagger \equiv (\mathbf{w}^*)^T$. Next we consider the case $\mathbf{v} = \mathbf{w} \in \mathbb{C}^{n \times 1}$ and $\mathbf{v}, \mathbf{w} \neq 0$.

Lemma B.1 Let M be a separable $m \times n$ \mathbb{C} -matrix with $M \neq 0$. Then it is

$$\text{rank}(M) = 1.$$

Proof: Because of $M \neq 0$ and $M = \mathbf{v} * \mathbf{w}^\dagger$ we have $\text{rank}(M) > 0$ and $\mathbf{v}, \mathbf{w} \neq 0$. Then we get

$$\text{rank}(M) = \text{rank}(\mathbf{v} * \mathbf{w}^\dagger) \leq \min\{\underbrace{\text{rank}(\mathbf{v})}_{=1}, \underbrace{\text{rank}(\mathbf{w}^\dagger)}_{=1}\} = 1.$$

From $0 < \text{rank}(M) \leq 1$ it follows $\text{rank}(M) = 1$.

q.e.d.

Lemma B.2 Let M be a separable $n \times n$ \mathbb{C} -matrix. Then it is

$$\det(M) = 0.$$

Proof: We use Def. B.1 and rewrite it in the following way:

$$M = \mathbf{v} * \mathbf{w}^\dagger = \mathbf{v} * (\mathbf{1}^\dagger * \mathbf{1}) * \mathbf{w}^\dagger = (\mathbf{v} * \mathbf{1}^\dagger) * (\mathbf{1} * \mathbf{w}^\dagger) = (\mathbf{v} * \mathbf{1}^\dagger) * (\mathbf{w} * \mathbf{1}^\dagger)^\dagger \equiv V * W^\dagger.$$

The matrix V is given with

$$V = \mathbf{v} * \mathbf{1}^\dagger = \left(\begin{array}{c|ccc} & \vdots & \vdots & \vdots \\ \mathbf{v} & 0 & 0 & 0 \\ & \vdots & \vdots & \vdots \end{array} \right), \quad W = \mathbf{w} * \mathbf{1}^\dagger = \left(\begin{array}{c|ccc} & \vdots & \vdots & \vdots \\ \mathbf{w} & 0 & 0 & 0 \\ & \vdots & \vdots & \vdots \end{array} \right), \quad \Rightarrow \det(V) = \det(W) = 0.$$

This immediately leads to

$$\det(M) = (VW^\dagger) = \underbrace{\det(V)}_{=0} \cdot \underbrace{\det(W^\dagger)}_{=0} = 0.$$

q.e.d.

Lemma B.3 Let $M = \mathbf{v} * \mathbf{w}^\dagger$ be a separable $n \times n$ \mathbb{C} -matrix. In this case M has a single eigenvalue ε with

$$\varepsilon = \sum_i w_i^* v_i$$

and \mathbf{v} being the corresponding eigenvector.

Proof: From Lemma B.1 and B.2 that there can only be one nonzero eigenvalue ε . In order to find this we multiply M with the vector \mathbf{v}

$$M * \mathbf{v} = (\mathbf{v} * \mathbf{w}^\dagger) * \mathbf{v} = \mathbf{v} * (\mathbf{w}^\dagger * \mathbf{v}) = \left(\sum_i w_i^* v_i \right) \mathbf{v} \equiv \varepsilon \mathbf{v}.$$

q.e.d.

Obviously, in case $\mathbf{v} = \mathbf{w}$ the separable matrix M possesses a single nonzero eigenvalue with $\varepsilon = \sum_i |v_i|^2$.

B.6.2 Rank of separable matrices

Lemma B.4 Let A_1, \dots, A_N separable $n \times n$ \mathbb{C} -matrices. Then the rank of the matrix $\sum_m A_m$ is given by

$$\text{rank} \left(\sum_{m=1}^N A_m \right) \leq N. \quad (\text{B.35})$$

Proof:

$$\text{rank} \left(\sum_{m=1}^N A_m \right) \leq \sum_{m=1}^N \underbrace{\text{rank}(A_m)}_{=1} = N. \quad (\text{B.36})$$

Because a unitary transformation does not change the rank of a matrix, the rank of a matrix is equal to the number of nonzero eigenvalues. For this reason and Lemma B.4 the maximal number of nonzero eigenvalues of $\sum_m A_m$ is given by $\min(n, N)$.

B.7 Nonadiabatic coupling terms

We analyze the nonadiabatic coupling terms in Eq. (3.11). Using

$$T_n = \sum_{j=1}^{N_n} \frac{1}{2M_j} \mathbf{P}_j^2 = - \sum_{j=1}^{N_n} \frac{1}{2M_j} \Delta_{\mathbf{R}_j} \quad (\text{B.37})$$

we get

$$\begin{aligned}\Lambda_{ji}\phi_i(\underline{\mathbf{R}}) &= \langle \psi_j(\underline{\mathbf{R}}) | T_n(\phi_i(\underline{\mathbf{R}}) | \psi_i(\underline{\mathbf{R}}) \rangle_{\underline{\mathbf{r}}} - \delta_{ji} T_n \phi_i(\underline{\mathbf{R}}) \\ &= - \sum_{k=1}^{N_n} \frac{1}{2M_k} \left(\int d\underline{\mathbf{r}} \psi_j^*(\underline{\mathbf{r}}, \underline{\mathbf{R}}) \Delta_{\mathbf{R}_j}(\phi_i(\underline{\mathbf{R}}) \psi_i(\underline{\mathbf{r}}, \underline{\mathbf{R}})) - \delta_{ji} T_n \phi_i(\underline{\mathbf{R}}) \right).\end{aligned}\quad (\text{B.38})$$

Because

$$\Delta_{\mathbf{R}_k}(\phi_i(\underline{\mathbf{R}}) \psi_i(\underline{\mathbf{r}}, \underline{\mathbf{R}})) = \Delta_{\mathbf{R}_k} \phi_i(\underline{\mathbf{R}}) + 2 \vec{\nabla}_{\mathbf{R}_k} \phi_i(\underline{\mathbf{R}}) \vec{\nabla}_{\mathbf{R}_k} \psi_i(\underline{\mathbf{r}}, \underline{\mathbf{R}}) + \phi_i(\underline{\mathbf{R}}) \Delta_{\mathbf{R}_k} \psi_i(\underline{\mathbf{r}}, \underline{\mathbf{R}})$$

we get

$$\Lambda_{ji} = - \sum_{k=1}^{N_n} \frac{1}{2M_k} (2 \langle \psi_j(\underline{\mathbf{R}}) | \vec{\nabla}_{\mathbf{R}_k} | \psi_i(\underline{\mathbf{R}}) \rangle_{\underline{\mathbf{r}}} \vec{\nabla}_{\mathbf{R}_k} + \langle \psi_j(\underline{\mathbf{R}}) | \Delta_{\mathbf{R}_k} | \psi_i(\underline{\mathbf{R}}) \rangle_{\underline{\mathbf{r}}}). \quad (\text{B.39})$$

Using the expression Eq. (B.37) we can rewrite the kinetic energy operator of the nuclei as follows

$$- \sum_{k=1}^{N_n} \frac{1}{2M_k} (\Delta_{\mathbf{R}_j} + 2 \langle \psi_j(\underline{\mathbf{R}}) | \vec{\nabla}_{\mathbf{R}_k} | \psi_i(\underline{\mathbf{R}}) \rangle_{\underline{\mathbf{r}}} \vec{\nabla}_{\mathbf{R}_k} + \langle \psi_j(\underline{\mathbf{R}}) | \vec{\nabla}_{\mathbf{R}_k} | \psi_i(\underline{\mathbf{R}}) \rangle_{\underline{\mathbf{r}}}^2) \quad (\text{B.40})$$

$$= - \sum_{k=1}^{N_n} \frac{1}{2M_k} (\vec{\nabla}_{\mathbf{R}_k} + \langle \psi_j(\underline{\mathbf{R}}) | \vec{\nabla}_{\mathbf{R}_k} | \psi_i(\underline{\mathbf{R}}) \rangle_{\underline{\mathbf{r}}})^2. \quad (\text{B.41})$$

The novel term appearing in the gradient of the nuclei degrees of freedom is called *derivatives coupling terms*. It couples the nuclei wave functions via the interaction with the electrons. Next we formulate a matrix expression of the nuclei Schrödinger equation. For this we introduce a matrix operator $\nabla + F$ with

$$(\nabla + F)_{ij} = - \sum_k \frac{1}{2M_k} (\vec{\nabla}_{\mathbf{R}_k} \delta_{ij} + (F_k)_{ij}) \quad \text{and} \quad (F_k)_{ij} = \langle \psi_i(\underline{\mathbf{R}}) | \vec{\nabla}_{\mathbf{R}_k} | \psi_j(\underline{\mathbf{R}}) \rangle_{\underline{\mathbf{r}}}. \quad (\text{B.42})$$

We emphasize that the elements of a single matrix F_k are vectors, namely the previously defined derivative coupling terms. We also define a diagonal matrix $(V_{\text{adia}}(\underline{\mathbf{R}}))_{ij} \equiv (\epsilon_i(\underline{\mathbf{R}}) + V_{\text{nn}}(\underline{\mathbf{R}})) \delta_{ij}$ and a vector that contains the nuclei wave functions $(\phi(\underline{\mathbf{R}}))_i = \phi_i(\underline{\mathbf{R}})$. Now the Schrödinger equation for the nuclei dynamics can be written in a compact form

$$[(\nabla + F)^2 + V_{\text{adia}}(\underline{\mathbf{R}})] \phi(\underline{\mathbf{R}}) = \mathcal{E} \phi(\underline{\mathbf{R}}). \quad (\text{B.43})$$

Finally we analyze the coupling terms in more detail:

$j = i$:

$$\Lambda_{ii} = - \sum_{k=1}^{N_n} \frac{1}{2M_k} (2 \langle \psi_i(\underline{\mathbf{R}}) | \vec{\nabla}_{\mathbf{R}_k} | \psi_i(\underline{\mathbf{R}}) \rangle_{\underline{\mathbf{r}}} \vec{\nabla}_{\mathbf{R}_k} + \langle \psi_i(\underline{\mathbf{R}}) | \Delta_{\mathbf{R}_k} | \psi_i(\underline{\mathbf{R}}) \rangle_{\underline{\mathbf{r}}}). \quad (\text{B.44})$$

If we assume the electronic wave functions to be real the first terms vanishes and we get

$$\Lambda_{ii} = \sum_{k=1}^{N_n} \frac{1}{2M_k} \int d\underline{\mathbf{r}} (\vec{\nabla}_{\mathbf{R}_k} \psi_i(\underline{\mathbf{r}}, \underline{\mathbf{R}}))^2. \quad (\text{B.45})$$

$j \neq i$:

We use $H_{\text{el}}|\psi_i(\mathbf{R})\rangle = \epsilon_i(\mathbf{R})|\psi_i(\mathbf{R})\rangle$ to rewrite the first term in Eq. (B.39):

$$\begin{aligned} \langle \psi_j(\mathbf{R}) | \vec{\nabla}_{\mathbf{R}_k} (H_{\text{el}} |\psi_i(\mathbf{R})\rangle_{\mathbf{r}}) &= \langle \psi_j(\mathbf{R}) | \vec{\nabla}_{\mathbf{R}_k} (\epsilon_i(\mathbf{R}) |\psi_i(\mathbf{R})\rangle_{\mathbf{r}}) \\ \Rightarrow \langle \psi_j(\mathbf{R}) | \vec{\nabla}_{\mathbf{R}_k} |\psi_i(\mathbf{R})\rangle_{\mathbf{r}} &= \frac{\langle \psi_j(\mathbf{R}) | (\vec{\nabla}_{\mathbf{R}_k} H_{\text{el}}) |\psi_i(\mathbf{R})\rangle_{\mathbf{r}}}{\epsilon_i(\mathbf{R}) - \epsilon_j(\mathbf{R})} \quad \text{for } \epsilon_i(\mathbf{R}) \neq \epsilon_j(\mathbf{R}) \end{aligned} \quad (\text{B.46})$$

We receive the important result that in case the Born-Oppenheimer potential surfaces approach each other the nonadiabatic coupling terms provide a major contribution. In case $\epsilon_i(\mathbf{R}) = \epsilon_j(\mathbf{R})$ these terms diverge and the Born-Oppenheimer approximation is illdefined.

B.8 Matrix elements of hydrogen states

$$\langle nlm | \mathbf{r} | n'l'm' \rangle = \langle nlm | r \hat{\mathbf{r}} | n'l'm' \rangle = \langle nlm | x e_x + y e_y + z e_z | n'l'm' \rangle$$

$$x = r \sin(\theta) \cos(\phi), \quad y = r \sin(\theta) \sin(\phi), \quad z = r \cos(\theta)$$

$$\psi_{nlm}(\mathbf{r}) = R_{nl}(r) Y_{lm}(\theta, \phi), \quad \langle nlm | r \hat{\mathbf{r}} | n'l'm' \rangle = \langle nl | r | n'l' \rangle_r \langle ml | \hat{\mathbf{r}} | l'm' \rangle_{\Omega}$$

$$\langle nl | r | n'l' \rangle_r = \int_0^{\infty} dr r^2 R_{nl}(r) R_{n'l'}(r), \quad \langle lm | \hat{\mathbf{r}} | l'm' \rangle_{\Omega} = \int_0^{2\pi} \int_{-1}^1 d\phi d \cos(\theta) Y_{lm}^*(\theta, \phi) \hat{\mathbf{r}} Y_{l'm'}(\theta, \phi)$$

B.8.1 Angular matrix elements

To calculate angular matrix elements we use the following integral theorem of spherical harmonic functions

$$\int d\Omega Y_{l_1 m_1}(\Omega) Y_{l_2 m_2}(\Omega) Y_{l_3 m_3}(\Omega) = \sqrt{\frac{(2l_1 + 1)(2l_2 + 1)(2l_3 + 1)}{4\pi}} \begin{pmatrix} l_1 & l_2 & l_3 \\ 0 & 0 & 0 \end{pmatrix} \begin{pmatrix} l_1 & l_2 & l_3 \\ m_1 & m_2 & m_3 \end{pmatrix}.$$

where the bracket terms are Wigner 3j-symbols [118]. The general form of an angular matrix element is

$$\langle l'm' | f(\theta, \phi) | lm \rangle = \int d\Omega Y_{l'm'}^*(\Omega) f(\theta, \phi) Y_{lm}(\Omega),$$

Dependent of the electric or magnetic field terms we have the following angular dependent functions $f(\theta, \phi)$.

Stark term

In case of the Stark term we have the following matrix elements

$$\begin{aligned}
\cos(\theta) &= \sqrt{\frac{4\pi}{3}} Y_{10}(\Omega) \\
\Rightarrow \langle l'm' | \cos(\theta) | lm \rangle &= \sqrt{\frac{(l_< + m + 1)(l_< - m + 1)}{(2l_< + 1)(2l_< + 3)}} \delta_{l', l \pm 1} \delta_{m'm}, \\
\sin(\theta) \cos(\phi) &= \sqrt{\frac{2\pi}{3}} (Y_{-10}(\Omega) - Y_{10}(\Omega)) \\
\Rightarrow \langle l'm' | \sin(\theta) \cos(\phi) | lm \rangle &= \frac{1}{2} \left[\sqrt{\frac{(l-m)(l-m-1)}{4l^2-1}} \delta_{l', l-1} \delta_{m', m+1} \right. \\
&\quad - \sqrt{\frac{(l+m)(l+m-1)}{4l^2-1}} \delta_{l', l-1} \delta_{m', m-1} \\
&\quad + \sqrt{\frac{(2l+1)(l+m+2)}{(2l+3)(l+m+1)}} \left(\frac{l-m}{2l+1} - 1 \right) \delta_{l', l+1} \delta_{m', m+1} \\
&\quad \left. - \sqrt{\frac{(2l+1)(l-m+2)}{(2l+3)(l-m+1)}} \left(\frac{l+m}{2l+1} - 1 \right) \delta_{l', l+1} \delta_{m', m-1} \right], \\
\sin(\theta) \sin(\phi) &= i \sqrt{\frac{2\pi}{3}} (Y_{10}(\Omega) + Y_{-10}(\Omega)) \\
\Rightarrow \langle l'm' | \sin(\theta) \sin(\phi) | lm \rangle &= \frac{1}{2i} \left[\sqrt{\frac{(l-m)(l-m-1)}{4l^2-1}} \delta_{l', l-1} \delta_{m', m+1} \right. \\
&\quad + \sqrt{\frac{(l+m)(l+m-1)}{4l^2-1}} \delta_{l', l-1} \delta_{m', m-1} \\
&\quad + \sqrt{\frac{(2l+1)(l+m+2)}{(2l+3)(l+m+1)}} \left(\frac{l-m}{2l+1} - 1 \right) \delta_{l', l+1} \delta_{m', m+1} \\
&\quad \left. + \sqrt{\frac{(2l+1)(l-m+2)}{(2l+3)(l-m+1)}} \left(\frac{l+m}{2l+1} - 1 \right) \delta_{l', l+1} \delta_{m', m-1} \right].
\end{aligned}$$

Diamagnetic term

$$\begin{aligned}
\sin^2(\theta) &= \frac{2}{3} \sqrt{4\pi} Y_{00}(\Omega) - \frac{2}{3} \sqrt{\frac{4\pi}{5}} Y_{20}(\Omega) \\
\Rightarrow \langle l'm' | \sin^2(\theta) | lm \rangle &= 2 \frac{l^2 + l - 1 + m^2}{(2l+3)(2l-1)} \delta_{l'l} - \sqrt{\frac{((l_< + 2)^2 - m^2)((l_< + 1)^2 - m^2)}{(2l_< + 5)(2l_< + 3)^2(2l_< + 1)}} \delta_{l', l \pm 2}.
\end{aligned}$$

B.8.2 Radial matrix elements

$$\begin{aligned}
R_{nl}(r) &= \frac{2}{n^2} \sqrt{\frac{(n-l-1)!}{(n+l)!}} e^{-\frac{r}{n}} \left(\frac{2r}{n}\right)^l L_{n-l-1}^{2l+1}\left(\frac{2r}{n}\right), \\
L_{n-l-1}^{2l+1}\left(\frac{2r}{n}\right) &= \sum_{m=0}^{n-l-1} \binom{n+l}{n-l-1-m} \frac{(-2)^m}{m! n^m} r^m
\end{aligned}$$

$$\begin{aligned} \langle nl|r^j|n'l' \rangle &= 4 \frac{2^{l+l'}}{n^{l+2}n'^{l'+2}} \sqrt{\frac{(n-l-1)!(n-l-1)!}{(n+l)!(n'+l')!}} \\ &\quad \times \int_0^\infty dr (r^{j+2+l+l'} e^{-r \frac{n+n'}{nn'}} L_{n'-l'-1}^{2l'+1}(\frac{2r}{n'}) L_{n-l-1}^{2l+1}(\frac{2r}{n})) \end{aligned}$$

$$\begin{aligned} L_{n-l-1}^{2l+1}(\frac{2r}{n}) L_{n'-l'-1}^{2l'+1}(\frac{2r}{n'}) &= \sum_{m=0}^{n-l-1} \sum_{m'=0}^{n'-l'-1} \frac{(-2)^{m+m'}}{m!m'!n^m n'^{m'}} \binom{n+l}{n-l-1-m} \\ &\quad \times \binom{n'+l'}{n'-l'-1-m'} r^{m+m'} \end{aligned}$$

$$\int_0^\infty dr r^{j+m+m'+l+l'+2} e^{-r \frac{n+n'}{nn'}} = \frac{(j+m+m'+l+l'+2)!}{(\frac{n+n'}{nn'})^{j+3+l+l'+m+m'}}$$

$$\begin{aligned} \langle nl|r^j|n'l' \rangle &= 4 \frac{2^{l+l'}}{n^{l+2}n'^{l'+2}} \sqrt{\frac{(n-l-1)!(n-l-1)!}{(n+l)!(n'+l')!}} \\ &\quad \times \sum_{m=0}^{n-l-1} \sum_{m'=0}^{n'-l'-1} \frac{(-2)^{m+m'}}{m!m'!n^m n'^{m'}} \binom{n+l}{n-l-1-m} \\ &\quad \times \binom{n'+l'}{n'-l'-1-m'} \frac{(j+m+m'+l+l'+2)!}{(\frac{n+n'}{nn'})^{j+3+l+l'+m+m'}} \end{aligned}$$

B.9 Additional notes

B.9.1 Elimination of single derivative terms

In this paragraph we consider the N -dimensional ($N \in \mathbb{N}$) linear differential equation in second order

$$(\Delta - V(r) + \varepsilon)\psi(\mathbf{r}) = 0, \quad (\text{B.47})$$

with $r = \|\mathbf{r}\|$, $\mathbf{r} \in \mathbb{R}^N$. Due to the rotational symmetry we express the Laplace operator Δ in N -dimensional spherical coordinates

$$\Delta = \partial_r^2 + \frac{N-1}{r} \partial_r + \frac{1}{r^2} \Delta_{S^{N-1}}. \quad (\text{B.48})$$

Here $\Delta_{S^{N-1}}$ denotes the Laplace-Beltrami operator defined on the $N-2$ dimensional unit sphere. We choose the ansatz

$$\psi(\mathbf{r}) = \frac{R(r)}{r^k} Y_{lk}(\Theta) \quad (\text{B.49})$$

where Y_{lk} denote the eigenfunctions of the Laplace-Beltrami operator with

$$\Delta_{S^{N-1}} Y_{lk}(\Theta) = -l(l+N-2)Y_{lk}(\Theta), \quad l \in \mathbb{N}_0. \quad (\text{B.50})$$

We calculate the first and second derivatives of the wave function $\psi(\mathbf{r})$ with respect to the radial coordinate r

$$\partial_r \frac{R(r)}{r^k} = \frac{R'(r)}{r^k} - k \frac{R(r)}{r^{k+1}}, \quad \partial_r^2 \frac{R(r)}{r^k} = \frac{R''(r)}{r^k} - 2k \frac{R'(r)}{r^{k+1}} + k(k+1) \frac{R(r)}{r^{k+2}}. \quad (\text{B.51})$$

We insert this expression into Eq. (B.48) and get

$$\frac{R''(r)}{r^k} + (N-1-2k) \frac{R'(r)}{r^{k+1}} + (k^2 - l(l+N-2)) \frac{R(r)}{r^{k+2}}.$$

We see that by choosing $k = (N-1)/2$ we get rid of the term containing the first derivative. In this case the Schrödinger equation (B.47) becomes a one-dimensional problem

$$\left(\partial_r^2 - \underbrace{\left(\frac{(l-1+N/2)^2 - 1/4}{r^2} + V(r) \right)}_{V_{\text{eff}}(r)} + \varepsilon \right) R(r) = 0.$$

with an effective potential $V_{\text{eff}}(r)$. We get for the normalization of the wave function $\psi(\mathbf{r})$

$$\int d\mathbf{r} |\psi(\mathbf{r})|^2 = \int_0^\infty dr R^2(r) \int d\Omega Y(\Theta) = 1. \quad (\text{B.52})$$

By introducing

$$\delta_{N,\text{even/odd}} = \begin{cases} 1, & \text{if } N \text{ is even/odd} \\ 0, & \text{otherwise} \end{cases}$$

and using $N = 2n + \delta_{N,\text{odd}}$, $n \in \mathbb{N}$ we can rewrite the first term of $V_{\text{eff}}(r)$ in the following way

$$\frac{\left(j + \frac{\delta_{N,\text{odd}}}{2} \right)^2 - \frac{1}{4}}{r^2} \equiv \frac{l_N(l_N + 1)}{r^2}$$

with $l_N = j - \frac{\delta_{N,\text{even}}}{2}$, $j \in \mathbb{N}_0$. We see that the analysis of an arbitrary N -dimensional problem is equivalent to the $N = 2/3$ -dimensional problem, depending on if N is even/odd. The problems just differ in the specific value of k . Finally, we assume that $\lim_{r \rightarrow 0} r^2 V(r) < \infty$. In this case we get for the radial wave function $R(r)$ for $r \rightarrow 0$

$$- l_N = -\frac{1}{2}$$

$$R(r) = r^{\frac{1}{2}} (A + B \ln(x)) \quad (\text{B.53})$$

To fulfill the normalization condition (B.52) we only keep the first term, this means

$$R(r) = Ar^{\frac{1}{2}}.$$

$$- l_N \geq 0$$

$$R(r) = Ar^{l_N+1} + Br^{-l_N}. \quad (\text{B.54})$$

We obtain

$$R(r) = Ar^{l_N+1} \quad (\text{B.55})$$

due to the normalization condition (B.52).

In summary we get

$$R(r) \sim r^{l_N+1} \quad \forall l_N. \quad (\text{B.56})$$

B.9.2 The radial shifted harmonic oscillator in two and three dimensions

We consider a single particle in a cylindrical symmetric potential of a radial shifted harmonic oscillator in two and three dimensions, respectively. The Hamiltonian for this system is given by

$$H = \frac{\mathbf{p}^2}{2m} + \frac{m}{2}\omega^2(r - r_0)^2, \quad r_0 \geq 0. \quad (\text{B.57})$$

We introduce $x = \sqrt{m\omega}r$, $a = \sqrt{m\omega}r_0$, $\varepsilon = E/\omega$ and choose $\psi(\mathbf{r}) = (R(x)/x^{(N-1)/2})Y_{lm}(\Theta)$ as an ansatz for the wave function. This gives the following differential equation for $R(x)$:

$$\left(\partial_x^2 - \frac{l_N(l_N + 1)}{x^2} - (x - a)^2 + 2\varepsilon \right) R(x) = 0. \quad (\text{B.58})$$

We analyze the asymptotic behavior of $R(x)$.

$$x \rightarrow 0 : \quad \left(\partial_x - \frac{l_N(l_N + 1)}{x^2} \right) R(x) = 0, \quad \rightarrow R(x) \sim x^{l_N+1} \quad (\text{B.59})$$

$$x \rightarrow \infty : \quad (\partial_x - (x - a)^2) R(x) = 0, \quad \rightarrow R(x) \sim \exp\left(-\frac{1}{2}(x - a)^2\right) \quad (\text{B.60})$$

This leads to the ansatz

$$R(x) = x^{l_N+1} \exp\left(-\frac{1}{2}(x - a)^2\right) f(x) \quad (\text{B.61})$$

This leads to the following differential equation for $f(x)$:

$$\partial_x^2 f(x) + 2 \left(\frac{1 + l_N - (-ax) - x^2}{x} \right) \partial_x f(x) + \left(2\varepsilon - 2 - 2l_N + 1 - (-2a) \frac{1 + l_N}{x} \right) f(x) = 0. \quad (\text{B.62})$$

This equation is the canonical form of the biconfluent Heun differential equation [1, 1, 1₄] (BCH), the suitable solution is defined as

$$\text{HeunB}(\alpha, \beta, \gamma, \delta; x) = \sum_{k=0}^2 \frac{A_k(\alpha, \beta, \gamma, \delta)}{(1 + \alpha)_k k!} x^k \quad (\text{B.63})$$

with $(1 + \alpha)_k \equiv \Gamma(1 + \alpha + k)/\Gamma(1 + \alpha)$. In this case we have

$$\alpha = 2l_N + 1, \quad \beta = -2a, \quad \gamma = 2\varepsilon, \quad \delta = 0. \quad (\text{B.64})$$

The coefficients A_k are given by the following recurrence relation ($k \geq 0$):

$$A_{k+2} + 2aA_{k+1}(k + 2 + l_N) + 2A_k(\varepsilon - \frac{3}{2} - l_N - k)(k + 1)(k + 2(1 + l_N)) = 0 \quad (\text{B.65})$$

with $A_0 \in \mathbb{R}$, $A_1 = -2aA_0(1 + l_N)$. The factor A_0 are determined by the normalization condition. The BCH-equation possesses admits polynomial solutions of order n (i.e. $A_n \neq 0$) if the coefficients

following two coefficients vanish (i.e. $A_{n+2} = A_{n+1} = 0$). This means

$$\begin{aligned} -A_{n+2} &= 2aA_{n+1}(n+2+l_N) + 2A_n(\varepsilon - \frac{3}{2} - l_N - n)(n+1)(n+2(l_N+1)) = 0 \\ \wedge -A_{n+1} &= 2aA_n(n+1+l_N) + 2nA_{n-1}(\varepsilon - \frac{1}{2} - l_N - n)(n+1)(n+2l_N+1) = 0, \end{aligned}$$

which leads to

$$\begin{aligned} A_n(\varepsilon - 2(l_N+1) - n)(n+1)(n+2(l_N+1)) &= 0 \\ \wedge aA_n(n + \frac{3}{2} + l_N) + nA_{n-1}(\varepsilon - l_N - \frac{1}{2} - n)(n+2l_N+1) &= 0. \end{aligned}$$

Because $A_n \neq 0$ we obtain the following two conditions

$$\varepsilon n l_N = n + l_N + \frac{3}{2} \quad \wedge \quad aA_n(n + \frac{3}{2} + l_N) + nA_{n-1}(2 + 2l_N + 1) = 0. \quad (\text{B.66})$$

Constructing the coefficients A_n and A_{n-1} by Eq. (B.66) this relation gives a polynomial of order $n+1$ in the quantity a . This means that polynomial solutions are only provided in the case that the radial separation a fulfills Eq. (B.66). This fact simply reflects the fact that this problem belongs to a certain class of mathematical problem, so called *quasi-exactly solvable problems*. The corresponding differential equations are characterized by the fact that they cannot be transformed into a differential equation that has a polynomial solution [259–267].

B.9.3 Three-state model eigenvalues

$$\begin{aligned} &\det \left(\begin{bmatrix} \alpha_1 - \epsilon & g_1 & g_2 \\ g_1 & \alpha_2 - \epsilon & g_3 \\ g_2 & g_3 & \alpha_3 - \epsilon \end{bmatrix} \right) \\ &= \epsilon^3 - \epsilon^2(\alpha_1 + \alpha_2 + \alpha_3) + \epsilon(\alpha_1\alpha_2 + \alpha_1\alpha_3 + \alpha_2\alpha_3 - g_1^2 - g_2^2 - g_3^2) \\ &\quad + \alpha_1g_3^2 + \alpha_2g_1^2 + \alpha_3g_2^2 + 2g_1g_2g_3 - \alpha_1\alpha_2\alpha_3 \\ &\equiv \epsilon^3 - b\epsilon^2 + c\epsilon + d. \end{aligned}$$

We define $\Delta = 18bcd - 4b^3d + b^2c - 4c^3 - 27d^2$, $\Delta_1 = 2b^3 - 9bc + 27d$ and

$$C = \sqrt[3]{\Delta_1 + \sqrt{27\Delta}}, \quad u_1 = 1, \quad u_2 = \frac{-1 + i\sqrt{3}}{2}, \quad u_3 = \frac{-1 - i\sqrt{3}}{2}. \quad (\text{B.67})$$

The eigenvalues ϵ_k are given by

$$\epsilon_k = -\frac{1}{3}(b + 2\text{Re}(u_k C)), \quad k = 1, 2, 3. \quad (\text{B.68})$$

Bibliography

- [1] R. J. Tarrant, *Senecan Drama and Its Antecedents*, Harvard Studies in Classical Philology, 82 edition, 1978.
- [2] M. Kurz, M. Mayle, and P. Schmelcher, *Ultra-long-range giant dipole molecules in crossed electric and magnetic fields*, Europhys. Lett. **97**, 43001 (2012).
- [3] M. Kurz and P. Schmelcher, *Electrically dressed ultra-long-range polar Rydberg molecules*, Phys. Rev. A **88**, 022501 (2013).
- [4] A. T. Krupp, A. Gaj, J. B. Balewski, P. Ilzhöfer, S. Hofferberth, R. Löw, T. Pfau, M. Kurz, and P. Schmelcher, *Alignment of D-State Rydberg Molecules*, Phys. Rev. Lett. **112**, 143008 (2014).
- [5] M. Kurz and P. Schmelcher, *Ultralong-range Rydberg molecules in combined electric and magnetic fields*, J. Phys. B At. Mol. Opt. Phys. **47**, 165101 (2014).
- [6] C. J. Pethick and H. Smith, *Bose-Einstein Condensation in Dilute Gases*, Cambridge University Press, 2008.
- [7] M. H. Anderson, J. R. Ensher, M. R. Matthews, C. E. Wieman, and E. A. Cornell, *Observation of bose-einstein condensation in a dilute atomic vapor.*, Science **269**, 198 (1995).
- [8] S. N. Bose, *Plancks Gesetz und Lichtquantenhypothese*, Z. Phys. **26**, 178 (1924).
- [9] A. Einstein, *Quantentheorie des einatomigen idealen Gases*, Sitz. K. Preuss. Akad. Wiss. 1924 , 261 (1924).
- [10] A. Einstein, *Quantentheorie des einatomigen idealen Gases, 2. Abhandlung*, Sitz. K. Preuss. Akad. Wiss. 1925 , 3 (1925).
- [11] K. Davis, M. Mewes, M. Andrews, N. van Druten, D. Durfee, D. Kurn, and W. Ketterle, *Bose-Einstein Condensation in a Gas of Sodium Atoms*, Phys. Rev. Lett. **75**, 3969 (1995).
- [12] B. DeMarco and D. S. Jin, *Onset of Fermi Degeneracy in a Trapped Atomic Gas*, Science (80-.). **285**, 1703 (1999).
- [13] T. Bourdel, L. Khaykovich, J. Cubizolles, J. Zhang, F. Chevy, M. Teichmann, L. Tarruell, S. J. J. M. F. Kokkelmans, and C. Salomon, *Experimental study of the BEC-BCS crossover region in ^6Li* , Phys. Rev. Lett. **93**, 50401 (2004).
- [14] Z. Hadzibabic, P. Krüger, M. Cheneau, B. Battelier, and J. Dalibard, *Berezinskii-Kosterlitz-Thouless crossover in a trapped atomic gas*, Nature **441**, 1118 (2006).
- [15] M. R. Andrews, *Observation of Interference Between Two Bose Condensates*, Science (80-.). **275**, 637 (1997).
- [16] I. Bloch, T. Hänsch, and T. Esslinger, *Atom Laser with a cw Output Coupler*, Phys. Rev. Lett. **82**, 3008 (1999).
- [17] K. Noda, R. Peters, N. Kawakami, and T. Pruschke, *Many-body effects in a Bose-Fermi mixture*, Phys. Rev. A **85**, 043628 (2012).

- [18] S. Jochim, M. Bartenstein, A. Altmeyer, G. Hendl, S. Riedl, C. Chin, J. Hecker Denschlag, and R. Grimm, *Bose-Einstein condensation of molecules.*, Science **302**, 2101 (2003).
- [19] L. P. Pitaevskii, *Vortex Lines in an Imperfect Bose Gas*, Sov. Phys. JETP **13**, 451 (1961).
- [20] M. Lewenstein, A. Sanpera, and V. Ahufinger, *Ultracold Atoms in Optical Lattices: Simulating quantum many-body systems*, Oxford University Press, Oxford, 2012.
- [21] M. Greiner, O. Mandel, T. Esslinger, T. W. Hansch, and I. Bloch, *Quantum phase transition from a superfluid to a Mott insulator in a gas of ultracold atoms*, Nature **415**, 39 (2002).
- [22] E. Haller, R. Hart, M. J. Mark, J. G. Danzl, L. Reichsollner, M. Gustavsson, M. Dalmonte, G. Pupillo, and H.-C. Nagerl, *Pinning quantum phase transition for a Luttinger liquid of strongly interacting bosons*, Nature **466**, 597 (2010).
- [23] C. Chin, R. Grimm, P. Julienne, and E. Tiesinga, *Feshbach resonances in ultracold gases*, Rev. Mod. Phys. **82**, 1225 (2010).
- [24] B. Paredes, A. Widera, V. Murg, O. Mandel, S. Fölling, I. Cirac, G. V. Shlyapnikov, T. W. Hansch, and I. Bloch, *Tonks-Girardeau gas of ultracold atoms in an optical lattice*, Nature **429**, 277 (2004).
- [25] T. Lahaye, T. Koch, B. Frohlich, M. Fattori, J. Metz, A. Griesmaier, S. Giovanazzi, and T. Pfau, *Strong dipolar effects in a quantum ferrofluid*, Nature **448**, 672 (2007).
- [26] S. Wildermuth, S. Hofferberth, I. Lesanovsky, E. Haller, L. M. Andersson, S. Groth, I. Bar-Joseph, P. Krüger, and J. Schmiedmayer, *Bose-Einstein condensates Microscopic magnetic-field imaging*, Nature **435**, 440 (2005).
- [27] M. A. Nielsen and I. L. Chuang, *Quantum Computation and Quantum Information*, Cambridge University Press, Cambridge, U.K., 2000.
- [28] J. Doyle, B. Friedrich, R. V. Krems, and F. Masnou-Seeuws, *Editorial: Quo vadis, cold molecules?*, Eur. Phys. J. D **31**, 149 (2004).
- [29] B. Friedrich and J. M. Doyle, *Why are cold molecules so hot?*, Eur. J. Chem. Phys. Phys. Chem. **10**, 604 (2009).
- [30] M. Schnell and G. Meijer, *Cold molecules: preparation, applications, and challenges.*, Angew. Chem. Int. Ed. Engl. **48**, 6010 (2009).
- [31] D. S. Jin and J. Ye, *Introduction to ultracold molecules: new frontiers in quantum and chemical physics.*, Chem. Rev. **112**, 4801 (2012).
- [32] E. S. Shuman, J. F. Barry, and D. DeMille, *Laser cooling of a diatomic molecule*, Nature **467**, 820 (2010).
- [33] V. Zhelyazkova, A. Cournol, T. E. Wall, A. Matsushima, J. J. Hudson, E. A. Hinds, M. R. Tarbutt, and B. E. Sauer, *Laser cooling and slowing of CaF molecules*, Phys. Rev. A **89**, 053416 (2014).
- [34] M. Hummon, M. Yeo, B. Stuhl, A. Collopy, Y. Xia, and J. Ye, *2D Magneto-Optical Trapping of Diatomic Molecules*, Phys. Rev. Lett. **110**, 143001 (2013).
- [35] M. R. Tarbutt, B. E. Sauer, J. J. Hudson, and E. A. Hinds, *Design for a fountain of YbF molecules to measure the electron's electric dipole moment*, New J. Phys. **15**, 053034 (2013).

- [36] J. D. Weinstein, R. DeCarvalho, T. Guillet, B. Friedrich, and J. M. Doyle, *Magnetic trapping of calcium monohydride molecules at millikelvin temperatures*, Nature **395**, 148 (1998).
- [37] N. E. Bulleid, S. M. Skoff, R. J. Hendricks, B. E. Sauer, E. A. Hinds, and M. R. Tarbutt, *Characterization of a cryogenic beam source for atoms and molecules.*, Phys. Chem. Chem. Phys. **15**, 12299 (2013).
- [38] N. R. Hutzler, H.-I. Lu, and J. M. Doyle, *The buffer gas beam: an intense, cold, and slow source for atoms and molecules.*, Chem. Rev. **112**, 4803 (2012).
- [39] K. Jones, E. Tiesinga, P. Lett, and P. Julienne, *Ultracold photoassociation spectroscopy: Long-range molecules and atomic scattering*, Rev. Mod. Phys. **78**, 483 (2006).
- [40] J. Deiglmayr, A. Grochola, M. Repp, K. Mörtlbauer, C. Glück, J. Lange, O. Dulieu, R. Wester, and M. Weidemüller, *Formation of Ultracold Polar Molecules in the Rovibrational Ground State*, Phys. Rev. Lett. **101**, 133004 (2008).
- [41] K. Bergmann, H. Theuer, and B. Shore, *Coherent population transfer among quantum states of atoms and molecules*, Rev. Mod. Phys. **70**, 1003 (1998).
- [42] K. Aikawa, D. Akamatsu, M. Hayashi, K. Oasa, J. Kobayashi, P. Naidon, T. Kishimoto, M. Ueda, and S. Inouye, *Coherent Transfer of Photoassociated Molecules into the Rovibrational Ground State*, Phys. Rev. Lett. **105**, 203001 (2010).
- [43] C. Chin, R. Grimm, P. Julienne, and E. Tiesinga, *Feshbach resonances in ultracold gases*, Rev. Mod. Phys. **82**, 1225 (2010).
- [44] J. Deiglmayr, P. Pellegrini, A. Grochola, M. Repp, R. Côté, O. Dulieu, R. Wester, and M. Weidemüller, *Influence of a Feshbach resonance on the photoassociation of LiCs*, New J. Phys. **11**, 055034 (2009).
- [45] A. Fioretti, D. Comparat, A. Crubellier, O. Dulieu, F. Masnou-Seeuws, and P. Pillet, *Formation of Cold Cs₂ Molecules through Photoassociation*, Phys. Rev. Lett. **80**, 4402 (1998).
- [46] D. Wang, J. Qi, M. Stone, O. Nikolayeva, H. Wang, B. Hattaway, S. Gensemer, P. Gould, E. Eyler, and W. Stwalley, *Photoassociative Production and Trapping of Ultracold KRb Molecules*, Phys. Rev. Lett. **93**, 243005 (2004).
- [47] A. Kerman, J. Sage, S. Sainis, T. Bergeman, and D. DeMille, *Production and State-Selective Detection of Ultracold RbCs Molecules*, Phys. Rev. Lett. **92**, 153001 (2004).
- [48] J. Sage, S. Sainis, T. Bergeman, and D. DeMille, *Optical Production of Ultracold Polar Molecules*, Phys. Rev. Lett. **94**, 203001 (2005).
- [49] D. Kleppner, *Professor Feshbach and his resonance*, Phys. Today **57**, 12 (2004).
- [50] S. Inouye, J. Goldwin, M. L. Olsen, C. Ticknor, J. L. Bohn, and D. S. Jin, *Observation of heteronuclear feshbach resonances in a mixture of bosons and Fermions*, Phys. Rev. Lett. **93**, 183201 (2004).
- [51] S. Inouye, M. R. Andrews, J. Stenger, H.-J. Miesner, D. M. Stamper-Kurn, and W. Ketterle, *Observation of Feshbach resonances in a Bose-Einstein condensate*, Nature **392**, 151 (1998).
- [52] K. Pilch, A. D. Lange, A. Prantner, G. Kerner, F. Ferlaino, H.-C. Nägerl, and R. Grimm, *Observation of interspecies Feshbach resonances in an ultracold Rb-Cs mixture*, Phys. Rev. A (Atomic, Mol. Opt. Physics) **79**, 42718 (2009).

- [53] T. Köhler, K. Goral, and P. S. Julienne, *Production of cold molecules via magnetically tunable Feshbach resonances*, Rev. Mod. Phys. **78**, 1311 (2006).
- [54] F. H. Mies, E. Tiesinga, and P. S. Julienne, *Manipulation of Feshbach resonances in ultracold atomic collisions using time-dependent magnetic fields*, Phys. Rev. A **61**, 22721 (2000).
- [55] D. J. Papoular, S. Bize, A. Clairon, H. Marion, S. J. J. M. F. Kokkelmans, and G. V. Shlyapnikov, *Feshbach resonances in cesium at ultralow static magnetic fields*, Phys. Rev. A **86**, 040701 (2012).
- [56] K. Aikawa, D. Akamatsu, J. Kobayashi, M. Ueda, T. Kishimoto, and S. Inouye, *Toward the production of quantum degenerate bosonic polar molecules ^{41}K and ^{87}Rb* , New J. Phys. **11**, 055035 (2009).
- [57] W. Stwalley and H. Wang, *Photoassociation of Ultracold Atoms: A New Spectroscopic Technique.*, J. Mol. Spectrosc. **195**, 194 (1999).
- [58] H. Loh, K. C. Cossel, M. C. Grau, K.-K. Ni, E. R. Meyer, J. L. Bohn, J. Ye, and E. A. Cornell, *Precision spectroscopy of polarized molecules in an ion trap.*, Science **342**, 1220 (2013).
- [59] C. Chin, V. V. Flambaum, and M. G. Kozlov, *Ultracold molecules: new probes on the variation of fundamental constants*, New J. Phys. **11**, 055048 (2009).
- [60] M. G. Kozlov and L. N. Labzowsky, *Parity violation effects in diatomics*, J. Phys. B At. Mol. Opt. Phys. **28**, 1933 (1995).
- [61] J. Weiner and P. S. Julienne, *Experiments and theory in cold and ultracold collisions*, Rev. Mod. Phys. **71**, 1 (1999).
- [62] B. K. Stuhl, M. T. Hummon, and J. Ye, *Cold state-selected molecular collisions and reactions.*, Annu. Rev. Phys. Chem. **65**, 501 (2014).
- [63] A. Avdeenkov, D. Bortolotti, and J. Bohn, *Field-linked states of ultracold polar molecules*, Phys. Rev. A **69**, 012710 (2004).
- [64] R. González-Férez, M. Mayle, and P. Schmelcher, *Rovibrational dynamics of LiCs dimers in strong electric fields*, Chem. Phys. **329**, 203 (2006).
- [65] R. González-Férez, M. Weidemüller, and P. Schmelcher, *Photoassociation of cold heteronuclear dimers in static electric fields*, Phys. Rev. A **76**, 023402 (2007).
- [66] J. B. Balewski, A. T. Krupp, A. Gaj, D. Peter, H. P. Büchler, R. Löw, S. Hofferberth, and T. Pfau, *Coupling a single electron to a Bose-Einstein condensate.*, Nature **502**, 664 (2013).
- [67] S. V. Stepkin, A. A. Konovalenko, N. G. Kantharia, and N. Udaya Shankar, *Radio recombination lines from the largest bound atoms in space*, Mon. Not. R. Astron. Soc. **374**, 852 (2007).
- [68] V. Y. F. Leung, A. Tauschinsky, N. J. van Druten, and R. J. C. Spreeuw, *Microtrap arrays on magnetic film atom chips for quantum information science*, Quantum Inf. Process. **10**, 955 (2011).
- [69] H. Gorniaczyk, C. Tresp, J. Schmidt, H. Fedder, and S. Hofferberth, *Single-Photon Transistor Mediated by Interstate Rydberg Interactions*, Phys. Rev. Lett. **113**, 053601 (2014).
- [70] T. F. Gallagher, *Rydberg Atoms*, Cambridge University Press, Cambridge, U.K., 1994.

- [71] E. Urban, T. A. Johnson, T. Henage, L. Isenhower, D. D. Yavuz, T. G. Walker, and M. Saffman, *Observation of Rydberg blockade between two atoms*, Nat Phys **5**, 110 (2009).
- [72] D. Comparat and P. Pillet, *Dipole blockade in a cold Rydberg atomic sample*, J. Opt. Soc. Am. B **27**, A208 (2010).
- [73] J. S. Cabral, J. M. Kondo, L. F. Goncalves, V. A. Nascimento, L. G. Marcassa, D. Booth, J. Tallant, A. Schwettmann, K. R. Overstreet, J. Sedlacek, and J. P. Shaffer, *Effects of electric fields on ultracold Rydberg atom interactions*, J. Phys. B At. Mol. Opt. Phys. **44**, 184007 (2011).
- [74] H. Zhang, L. Wang, L. Zhang, C. Li, L. Xiao, J. Zhao, S. Jia, P. Cheinet, D. Comparat, and P. Pillet, *Stark-induced L-mixing interferences in ultracold cesium Rydberg atoms*, Phys. Rev. A **87**, 033405 (2013).
- [75] J. Chen, H. Zhang, L. Wang, S. Bao, L. Zhang, C. Li, J. Zhao, and S. Jia, *State transfer of nS ultracold Rydberg atoms in external electric fields*, Eur. Phys. J. D **68**, 265 (2014).
- [76] H. Friedrich and H. Wintgen, *The hydrogen atom in a uniform magnetic field - An example of chaos*, Phys. Rep. **183**, 37 (1989).
- [77] H. Friedrich and B. Eckhardt, editors, *Classical, Semiclassical and Quantum Dynamics in Atoms (Lecture Notes in Physics)*, Springer Heidelberg, Heidelberg, volume 485 edition, 1997.
- [78] H. Ruder, G. Wunner, H. Herold, and F. Geyer, *Atoms in Strong Magnetic Fields*, Springer Berlin / Heidelberg, 1994.
- [79] O. Dippel, P. Schmelcher, and L. S. Cederbaum, *Charged anisotropic harmonic oscillator and the hydrogen atom in crossed fields*, Phys. Rev. A **49**, 4415 (1994).
- [80] I. Lesanovsky, J. Schmiedmayer, and P. Schmelcher, *Electronic structure of atoms in magnetic quadrupole traps*, Phys. Rev. A **69**, 053405 (2004).
- [81] I. Lesanovsky, J. Schmiedmayer, and P. Schmelcher, *Rydberg atoms in a magnetic quadrupole field*, J. Phys. B At. Mol. Opt. Phys. **38**, S151 (2005).
- [82] M. Mayle, I. Lesanovsky, and P. Schmelcher, *Magnetic trapping of ultracold Rydberg atoms in low angular momentum states*, Phys. Rev. A **80**, 053410 (2009).
- [83] M. Mayle, I. Lesanovsky, and P. Schmelcher, *Dressing of ultracold atoms by their Rydberg states in a Ioffe-Pritchard trap*, J. Phys. B At. Mol. Opt. Phys. **43**, 155003 (2010).
- [84] R. Levi-Setti, *The Trilobite Book*, University of Chicago Press, Chicago, 2014.
- [85] C. H. Greene, A. S. Dickinson, and H. R. Sadeghpour, *Creation of Polar and Nonpolar Ultra-Long-Range Rydberg Molecules*, Phys. Rev. Lett. **85**, 2458 (2000).
- [86] E. L. Hamilton, C. H. Greene, and H. R. Sadeghpour, *Shape-resonance-induced long-range molecular Rydberg states*, J. Phys. B At. Mol. Opt. Phys. **35**, L199 (2002).
- [87] V. Bendkowsky, B. Butscher, J. Nipper, J. B. Balewski, J. P. Shaffer, R. Löw, T. Pfau, W. Li, J. Stanojevic, T. Pohl, and J. M. Rost, *Rydberg Trimers and Excited Dimers Bound by Internal Quantum Reflection*, Phys. Rev. Lett. **105**, 163201 (2010).
- [88] S. T. Rittenhouse, M. Mayle, P. Schmelcher, and H. R. Sadeghpour, *Ultralong-range polyatomic Rydberg molecules formed by a polar perturber*, J. Phys. B At. Mol. Opt. Phys. **44**, 184005 (2011).

- [89] C. Greene, E. Hamilton, H. Crowell, C. Vadla, and K. Niemax, *Experimental Verification of Minima in Excited Long-Range Rydberg States of Rb₂*, Phys. Rev. Lett. **97**, 233002 (2006).
- [90] V. Bendkowsky, B. Butscher, J. Nipper, J. P. Shaffer, R. Low, and T. Pfau, *Observation of ultralong-range Rydberg molecules*, Nature **458**, 1005 (2009).
- [91] B. A. Butscher, V. Bendkowsky, J. Nipper, J. B. Balewski, L. Kukota, R. Löw, T. Pfau, W. Li, T. Pohl, and J. M. Rost, *Lifetimes of ultralong-range Rydberg molecules in vibrational ground and excited states*, J. Phys. B At. Mol. Opt. Phys. **44**, 184004 (2011).
- [92] J. Tallant, S. T. Rittenhouse, D. Booth, H. R. Sadeghpour, and J. P. Shaffer, *Observation of Blueshifted Ultralong-Range Cs₂ Rydberg Molecules*, Phys. Rev. Lett. **109**, 173202 (2012).
- [93] M. A. Bellos, R. Carollo, J. Banerjee, E. E. Eyler, P. L. Gould, and W. C. Stwalley, *Excitation of Weakly Bound Molecules to Trilobitelike Rydberg States*, Phys. Rev. Lett. **111**, 053001 (2013).
- [94] D. A. Anderson, S. A. Miller, and G. Raithel, *Photoassociation of Long-Range nD Rydberg Molecules*, Phys. Rev. Lett. **112**, 163201 (2014).
- [95] W. Li, T. Pohl, J. M. Rost, S. T. Rittenhouse, H. R. Sadeghpour, J. Nipper, B. Butscher, J. B. Balewski, V. Bendkowsky, R. Löw, and T. Pfau, *A Homonuclear Molecule with a Permanent Electric Dipole Moment*, Science (80-.). **334**, 1110 (2011).
- [96] A. Gaj, A. T. Krupp, J. B. Balewski, R. Löw, S. Hofferberth, and T. Pfau, *From molecular spectra to a density shift in dense Rydberg gases.*, Nat. Commun. **5**, 4546 (2014).
- [97] I. Liu, J. Stanojevic, and J. Rost, *Ultra-Long-Range Rydberg Trimers with a Repulsive Two-Body Interaction*, Phys. Rev. Lett. **102**, 173001 (2009).
- [98] J. B. Balewski, A. T. Krupp, A. Gaj, D. Peter, H. P. Büchler, R. Löw, S. Hofferberth, and T. Pfau, *Coupling a single electron to a Bose-Einstein condensate.*, Nature **502**, 664 (2013).
- [99] I. Lesanovsky, P. Schmelcher, and H. R. Sadeghpour, *Ultra-long-range Rydberg molecules exposed to a magnetic field*, J. Phys. B At. Mol. Opt. Phys. **39**, L69 (2006).
- [100] J. Fraunhofer, *Bestimmung des Brechungs- und Farbenzerstreuungs-Vermögens verschiedener Glasarten, in Bezug auf die Vervollkommnung achromatischer Fernrohre*, Denkschriften der Königl. Akad. der Wissenschaften zu München **5**, 193 (1814).
- [101] N. Bohr, *On the Constitution of Atoms and Molecules*, Phil. Mag. Ser. 6, **26**, 1 (1913).
- [102] H. E. White, *Introduction to Atomic Spectra*, McGraw-Hill Book Company, Inc., New York and London, 1934.
- [103] G. J. Stoney, *On the cause of the interrupted spectra of gases*, Philos. Mag. Ser. 4 **41**, 291 (1871).
- [104] A. Schuster, *On Harmonic Ratios in the Spectra of Gases*, Proc. R. Soc. London **31**, 337 (1880).
- [105] J. J. Balmer, *Notiz über die Spectrallinien des Wasserstoffs*, Ann. der Phys. und Chemie **25**, 80 (1885).
- [106] J. R. Rydberg, *On the structure of the line spectra of the chemical elements*, Philos. Mag. Ser. 5 **29**, 331 (1890).

- [107] J. Dewar and G. D. Liveing, *On the spectra of sodium and potassium*, Proc. R. Soc. London, **29**, 398 (1879).
- [108] H. Friedrich, *Theoretical Atomic Physics*, Springer-Verlag, Berlin, Germany, 2nd edition, 1998.
- [109] A. R. P. Rau, *The quantum defect: Early history and recent developments*, Am. J. Phys. **65**, 221 (1997).
- [110] P. J. Mohr, B. N. Taylor, and D. B. Newell, *CODATA recommended values of the fundamental physical constants: 2006*, Rev. Mod. Phys. **80**, 633 (2008).
- [111] F. Paschen, *Zur Kenntnis ultraroter Linienspektren. I. (Normalwellenlängen bis 27000 Å.-E.)*, Ann. Phys. **332**, 537 (1908).
- [112] T. LYMAN, *An Extension of the Spectrum in the Extreme Ultra-Violet*, Nature **93**, 241 (1914).
- [113] F. S. Brackett, *Visible and Infra-Red Radiation of Hydrogen*, Astrophys. J. **56**, 154 (1922).
- [114] A. H. PFUND, *THE EMISSION OF NITROGEN AND HYDROGEN IN THE INFRARED*, J. Opt. Soc. Am. **9**, 193 (1924).
- [115] C. J. Humphreys, *The Sixth Series in the Spectrum of Atomic Hydrogen*, J. Res. Natl. Bur. Stand. (1934). **50**, 2380 (1953).
- [116] R. B. King, *Inorganic Chemistry of Main Group Elements*, John Wiley and Sons, Inc., London, 1994.
- [117] A. Sommerfeld, *Zur Quantentheorie der Spektrallinien*, Ann. Phys. **356**, 1 (1916).
- [118] J. J. Sakurai, *Modern Quantum Mechanics*, Addison Wesley Pub Co Inc (Juni 1967), 1967.
- [119] W. Li, I. Mourachko, M. W. Noel, and T. F. Gallagher, *Millimeter-wave spectroscopy of cold Rb Rydberg atoms in a magneto-optical trap: Quantum defects of the ns, np, and nd series*, Phys. Rev. A **67**, 52502 (2003).
- [120] C.-J. Lorenzen and K. Niemax, *Quantum Defects of the $n^2P_{1/2,3/2}$ Levels in ^{39}KI and ^{85}RbI* , Phys. Scr. **27**, 300 (1983).
- [121] A. Borovik, O. Zatsarinny, and K. Bartschat, *Resonance effects in electron and photon impact excitation of the p^6 subvalence subshell in alkali atoms*, J. Phys. B At. Mol. Opt. Phys. **42**, 044010 (2009).
- [122] A. Borovik, V. Ilyashevych, O. Zatsarinny, and K. Bartschat, *Resonance excitation of the $(4p^55s^2)^2P_{3/2,1/2}$ autoionizing states in Rb atoms by electron impact*, J. Phys. Conf. Ser. **388**, 042009 (2012).
- [123] A. Borovik, V. Roman, O. Zatsarinny, and K. Bartschat, *Electron impact excitation of the lowest doublet and quartet core-excited autoionizing states in Rb atoms*, J. Phys. B At. Mol. Opt. Phys. **46**, 015203 (2013).
- [124] M. Marinescu, H. R. Sadeghpour, and A. Dalgarno, *Dispersion coefficients for alkali-metal dimers*, Phys. Rev. A **49**, 982 (1994).
- [125] M. Marinescu, H. Sadeghpour, and A. Dalgarno, *Dispersion coefficients for alkali-metal dimers*, Phys. Rev. A **49**, 982 (1994).

- [126] H. A. Bethe and E. E. Salpeter, *Quantum Mechanics of One- and Two-Electron Systems*, Springer, Berlin, 1957.
- [127] K. Harvey and B. Stoicheff, *Fine Structure of the n^2D Series in Rubidium near the Ionization Limit*, Phys. Rev. Lett. **38**, 537 (1977).
- [128] F. Gounand, P. Fournier, J. Cuvellier, and J. Berlande, *Determination of natural radiative lifetimes for highly excited P states in rubidium*, Phys. Lett. A **59**, 23 (1976).
- [129] M. Hugon, F. Gounand, and P. R. Fournier, *Radiative lifetimes of highly excited F states in rubidium*, J. Phys. B At. Mol. Phys. **11**, L605 (1978).
- [130] F. Gounand, M. Hugon, P. R. Fournier, and J. Berlande, *Superradiant cascading effects in rubidium Rydberg levels*, J. Phys. B At. Mol. Phys. **12**, 547 (1979).
- [131] F. Gounand, M. Hugon, and P. Fournier, *Radiative lifetimes of highly excited states in rubidium*, J. Phys. **41**, 119 (1980).
- [132] A. Oliveira, M. Mancini, V. Bagnato, and L. Marcassa, *Measurement of Rydberg-state lifetimes using cold trapped atoms*, Phys. Rev. A **65**, 031401 (2002).
- [133] V. Nascimento, L. Caliri, A. de Oliveira, V. Bagnato, and L. Marcassa, *Measurement of the lifetimes of S and D states below $n=31$ using cold Rydberg gas*, Phys. Rev. A **74**, 054501 (2006).
- [134] L. Caliri and L. Marcassa, *Reply to "Comment on Measurement of the lifetimes of S and D states below $n=31$ using cold Rydberg gas"*, Phys. Rev. A **75**, 066503 (2007).
- [135] F. Gounand, *Calculation of radial matrix elements and radiative lifetimes for highly excited states of alkali atoms using the Coulomb approximation*, J. Phys. Fr. **40**, 457 (1979).
- [136] X. He, B. Li, A. Chen, and C. Zhang, *Model-potential calculation of lifetimes of Rydberg states of alkali atoms*, J. Phys. B At. Mol. Opt. Phys. **23**, 661 (1990).
- [137] C. E. Theodosiou, *Lifetimes of alkali-metal⁻atom Rydberg states*, Phys. Rev. A **30**, 2881 (1984).
- [138] T. Gallagher and W. Cooke, *Interactions of Blackbody Radiation with Atoms*, Phys. Rev. Lett. **42**, 835 (1979).
- [139] I. I. Beterov, D. B. Tretyakov, I. I. Ryabtsev, V. M. Entin, A. Ekers, and N. N. Bezuglov, *Ionization of Rydberg atoms by blackbody radiation*, New J. Phys. **11**, 013052 (32pp) (2009).
- [140] A. Krupp, *D-state Rydberg electrons interacting with ultracold atoms*, PhD thesis, University of Stuttgart, 2014.
- [141] J. B. Balewski, *A single electron in a Bose-Einstein condensate*, PhD thesis, University of Stuttgart, 2014.
- [142] E. Amaldi and E. Serge, *Effect of Pressure of High Terms of Alkaline Spectra*, Nature **133**, 141 (1934).
- [143] E. Amaldi and E. Serge, *Effetto della pressione sui termini elevati degli alcalini*, Nuovo Cim. **11**, 145 (1934).
- [144] C. Füchtbauer, P. Schulz, and A. F. Brandt, *Verschiebung von hohen Serienlinien des Natriums und Kaliums durch Fremdgase, Berechnung der Wirkungsquerschnitte von Edelgasen gegen sehr langsame Elektronen*, Zeitschrift für Phys. **90**, 403 (1934).

- [145] E. Fermi, *Sopra lo spostamento per pressione delle righe elevate delle serie spettrali*, Nuovo Cim. **11**, 157 (1934).
- [146] L. Presnyakov, *Broadening of Highly Excited Atomic Levels in an Atmosphere of Alkali-Metal Atoms*, Phys. Rev. A **2**, 1720 (1970).
- [147] V. A. Alekseev and I. I. Sobel'man, *A spectroscopic method for the investigation of elastic scattering of slow electrons*, Sov. Phys. JETP, **22**, 882 (1966).
- [148] G. Chew, *The Inelastic Scattering of High Energy Neutrons by Deuterons According to the Impulse Approximation*, Phys. Rev. **80**, 196 (1950).
- [149] J. E. G. Farina, *On the impulse approximation*, J. Phys. A. Math. Gen. **11**, 1915 (1978).
- [150] L. D. Landau and E. M. Lifschitz, *Course of Theoretical Physics, Volume III: Quantum Mechanics (Non-Relativistic Theory)*, Pergamon Press, Oxford, 3rd edition, 1977.
- [151] R. G. Newton, *Scattering theory of Waves and Particles*, Dover Publications, Inc., Mineola, New York, 2002.
- [152] T.-Y. Wu and T. Ohmura, *Quantum Theory of Scattering*, Dover Publications, Inc., Mineola, New York, 2011.
- [153] E. Fermi, *Sul moto dei neutroni nelle sostanze idrogenate*, Ric. Sci. **7**, 13 (1936).
- [154] J. von Stecher and C. Greene, *Renormalized mean-field theory for a two-component Fermi gas with s-wave interactions*, Phys. Rev. A **75**, 022716 (2007).
- [155] C. Bahrim and U. Thumm, *Low-lying 3P and 3S^e states of Rb-, Cs-, and Fr-*, Phys. Rev. A **61**, 22722 (2000).
- [156] A. Omont, *On the theory of collisions of atoms in Rydberg states with neutral particles*, Le J. Phys. **38**, 1343 (1977).
- [157] H. Späth, *Spline-Algorithmen zur Konstruktion glatter Kurven und Flächen*, Oldenbourg Verlag, München, 1973.
- [158] J. Schmidt, *Staircase algorithm and construction of convex spline interpolants up to the continuity C3*, Comput. Math. with Appl. **31**, 67 (1996).
- [159] T. M. Miller, *CRC Handbook of Chemistry and Physics*, CRC Press, Boca Raton, 81st edition, 2000.
- [160] C. J. Pethik and H. Smith, *Bose-Einstein Condensation in Dilute Gases*, Cambridge University Press, Cambridge, U.K., 2002.
- [161] C. Kittel, *Introduction to Solid State Physics*, John Wiley and Sons, New York, NY, 8th edition, 2005.
- [162] N. W. Ashcroft and N. D. Mermin, *Solid state physics*, Holt Rinehart and Winston, Austin, TX, 2002.
- [163] W. H. Miller, *Beyond transition-state theory: a rigorous quantum theory of chemical reaction rates*, Acc. Chem. Res. **26**, 174 (1993).
- [164] A. Fernandez-Ramos, J. A. Miller, S. J. Klippenstein, and D. G. Truhlar, *Modeling the kinetics of bimolecular reactions.*, Chem. Rev. **106**, 4518 (2006).

- [165] S. Cavalli, V. Aquilanti, K. C. Mundim, and D. De Fazio, *Theoretical reaction kinetics astride the transition between moderate and deep tunneling regimes: the F + HD case.*, J. Phys. Chem. A **118**, 6632 (2014).
- [166] E. Schrödinger, *What is life?*, Cambridge University Press, Cambridge, 1944.
- [167] K. R. Dronamraju, *Erwin Schrödinger and the origins of molecular biology.*, Genetics **153**, 1071 (1999).
- [168] P. A. M. Dirac, *Quantum Mechanics of Many-Electron Systems*, Proc. R. Soc. London. Ser. A **123**, 714 (1929).
- [169] M. Thomas, M. Brehm, R. Fligg, P. Vöhringer, and B. Kirchner, *Computing vibrational spectra from ab initio molecular dynamics.*, Phys. Chem. Chem. Phys. **15**, 6608 (2013).
- [170] D. Marx and J. Hutter, *Ab Initio Molecular Dynamics: Basic Theory and Advance Methods*, Cambridge University Press, Cambridge, 2009.
- [171] A. D. McLACHLAN and M. A. BALL, *Time Dependent Hartree Fock Theory for Molecules*, Rev. Mod. Phys. **36**, 844 (1964).
- [172] R. O. Jones, *The density functional formalism, its applications and prospects*, Rev. Mod. Phys. **61**, 689 (1989).
- [173] H.-D. Meyer, U. Manthe, and L. Cederbaum, *The multi-configurational time-dependent Hartree approach*, Chem. Phys. Lett. **165**, 73 (1990).
- [174] M. Beck, *The multiconfiguration time-dependent Hartree (MCTDH) method: a highly efficient algorithm for propagating wavepackets*, Phys. Rep. **324**, 1 (2000).
- [175] H. D. Meyer, F. Gatti, and G. A. Worth, editors, *Multidimensional Quantum Dynamics*, WILEY-VCH Verlag, Weinheim, 2009.
- [176] K. Sadri, D. Lauvergnat, F. Gatti, and H.-D. Meyer, *Rovibrational spectroscopy using a kinetic energy operator in Eckart frame and the multi-configuration time-dependent Hartree (MCTDH) approach.*, J. Chem. Phys. **141**, 114101 (2014).
- [177] D. P. Landau and Binder K., *A Guide to Monte-Carlo Simulations in Statistical Physics*, Cambridge University Press, Cambridge, 2009.
- [178] G. Kabbe, C. Wehmeyer, and D. Sebastiani, *A Coupled Molecular Dynamics/Kinetic Monte Carlo Approach for Protonation Dynamics in Extended Systems*, J. Chem. Theory Comput. **10**, 4221 (2014).
- [179] R. G. Parr and W. Yang, *Density-Functional Theory of Atoms and Molecules*, Oxford University Press, Oxford, 1989.
- [180] E. Runge and E. K. U. Gross, *Density-Functional Theory for Time-Dependent Systems*, Phys. Rev. Lett. **52**, 997 (1984).
- [181] M. E. Casida, *Time-dependent density-functional theory for molecules and molecular solids*, J. Mol. Struct. THEOCHEM **914**, 3 (2009).
- [182] E. I. Sánchez-Flores, R. Chávez-Calvillo, T. A. Keith, G. Cuevas, T. Rocha-Rinza, and F. Cortés-Guzmán, *Properties of atoms in electronically excited molecules within the formalism of TDDFT*, J. Comput. Chem. **35**, 820 (2014).

- [183] O. Sinanoglu, *Many-Electron Theory of Atoms and Molecules. I. Shells, Electron Pairs vs Many-Electron Correlations*, J. Chem. Phys. **36**, 706 (1962).
- [184] H. Monkhorst, *Chemical physics without the Born-Oppenheimer approximation: The molecular coupled-cluster method*, Phys. Rev. A **36**, 1544 (1987).
- [185] H. J. Monkhorst, *Calculation of properties with the coupled-cluster method*, Int. J. Quantum Chem. **12**, 421 (2009).
- [186] M. Born and R. Oppenheimer, *Zur Quantentheorie der Molekeln*, Ann. Phys. **389**, 457 (1927).
- [187] W. Domcke, D. Yarkony, and H. Köppel, *Conical Intersections*, World Scientific Publishing Co. Pte. Ltd., Singapore, 2004.
- [188] J. I. Steinfeld, *Molecules and Radiation: An Introduction to Modern Molecular Spectroscopy*, volume 9, Dover Publications, 2012.
- [189] N. C. Handy, Y. Yamaguchi, and H. F. Schaefer, *The diagonal correction to the Born-Oppenheimer approximation: Its effect on the singlet-triplet splitting of CH₂ and other molecular effects*, J. Chem. Phys. **84**, 4481 (1986).
- [190] E. F. Valeev and C. D. Sherrill, *The diagonal Born-Oppenheimer correction beyond the Hartree-Fock approximation*, J. Chem. Phys. **118**, 3921 (2003).
- [191] A. Tajti, P. G. Szalay, and J. Gauss, *Perturbative treatment of the electron-correlation contribution to the diagonal Born-Oppenheimer correction.*, J. Chem. Phys. **127**, 014102 (2007).
- [192] M. Baer, *BEYOND BORN-OPPENHEIMER Conical Intersections and Electronic Nonadiabatic Coupling Terms*, John Wiley and Sons, Inc., Hoboken, New Jersey, 2006.
- [193] W. Greub, *Linear Algebra*, volume 23 of *Graduate Texts in Mathematics*, Springer New York, New York, NY, 1975.
- [194] V. M. Borodin and A. K. Kazansky, *The adiabatic mechanism of the collisional broadening of Rydberg states via a loosely bound resonance state of ambient gas atoms*, J. Phys. B At. Mol. Opt. Phys. **25**, 971 (1992).
- [195] A. Omont, *On the theory of collisions of atoms in rydberg states with neutral particles*, J. Phys. Fr. **38**, 1343 (1977).
- [196] J. Tallant, D. Booth, and J. P. Shaffer, *Photoionization rates of Cs Rydberg atoms in a 1064-nm far-off-resonance trap*, Phys. Rev. A **82**, 63406 (2010).
- [197] R. Löw, *A versatile setup for experiments with rubidium Bose-Einstein condensates: From optical lattices to Rydberg matter*, PhD thesis, University of Stuttgart, 2006.
- [198] V. Bendkowsky, *ULTRALONG-RANGE RYDBERG MOLECULES: INVESTIGATION OF A NOVEL BINDING*, PhD thesis, University of Stuttgart, 2010.
- [199] J. Nipper, *Interacting Rydberg atoms: Coherent control at Förster resonances and polar homonuclear molecules*, PhD thesis, University of Stuttgart, 2012.
- [200] W. Phillips and H. Metcalf, *Laser Deceleration of an Atomic Beam*, Phys. Rev. Lett. **48**, 596 (1982).
- [201] B. Ohayon and G. Ron, *New approaches in designing a Zeeman Slower*, J. Instrum. **8**, P02016 (2013).

- [202] J. Nipper, J. P. Shaffer, R. Lo, T. Pfau, and V. Bendkowsky, *Observation of ultralong-range Rydberg molecules*, Nature **458**, 1 (2009).
- [203] L. Holmegaard, J. L. Hansen, L. Kalhøj, S. Louise Kragh, H. Stapelfeldt, F. Filsinger, J. Küpper, G. Meijer, D. Dimitrovski, M. Abu-samha, C. P. J. Martiny, and L. Bojer Madsen, *Photoelectron angular distributions from strong-field ionization of oriented molecules*, Nat. Phys. **6**, 428 (2010).
- [204] C. Z. Bisgaard, O. J. Clarkin, G. Wu, A. M. D. Lee, O. Gessner, C. C. Hayden, and A. Stolow, *Time-resolved molecular frame dynamics of fixed-in-space CS₂ molecules*, Science **323**, 1464 (2009).
- [205] J. L. Hansen, L. Holmegaard, L. Kalhøj, S. L. Kragh, H. Stapelfeldt, F. Filsinger, G. Meijer, J. Küpper, D. Dimitrovski, M. Abu-samha, C. P. J. Martiny, and L. B. Madsen, *Ionization of one- and three-dimensionally-oriented asymmetric-top molecules by intense circularly polarized femtosecond laser pulses*, Phys. Rev. A **83**, 023406 (2011).
- [206] A. Landers, T. Weber, I. Ali, A. Cassimi, M. Hattass, O. Jagutzki, A. Nauert, T. Osipov, A. Staudte, M. Prior, H. Schmidt-Böcking, C. Cocke, and R. Dörner, *Photoelectron Diffraction Mapping: Molecules Illuminated from Within*, Phys. Rev. Lett. **87**, 013002 (2001).
- [207] M. L. Lipciuc, A. J. van den Brom, L. Dinu, and M. H. M. Janssen, *Slice imaging of photodissociation of spatially oriented molecules*, Rev. Sci. Instrum. **76**, 123103 (2005).
- [208] N. H. Nahler, R. Baumfalk, U. Buck, Z. Bihary, R. B. Gerber, and B. Friedrich, *Photodissociation of oriented HXeI molecules generated from HIXe clusters*, J. Chem. Phys. **119**, 224 (2003).
- [209] A. J. van den Brom, T. P. Rakitzis, and M. H. M. Janssen, *Photodissociation of laboratory oriented molecules: Revealing molecular frame properties of nonaxial recoil*, J. Chem. Phys. **121**, 11645 (2004).
- [210] M. Wu, R. J. Bemish, and R. E. Miller, *Photodissociation of molecules oriented by dc electric fields: Determining photofragment angular distributions*, J. Chem. Phys. **101**, 9447 (1994).
- [211] R. N. Zare, *Laser Control of Chemical Reactions*, Science (80-.). **279**, 1875 (1998).
- [212] V. Aquilanti, M. Bartolomei, F. Pirani, D. Cappelletti, F. Vecchiocattivi, Y. Shimizu, and T. Kasai, *Orienting and aligning molecules for stereochemistry and photodynamics*, Phys. Chem. Chem. Phys. **7**, 291 (2005).
- [213] P. R. Brooks, *Reactive Scattering of K Atoms from Oriented CH₃I Molecules*, J. Chem. Phys. **45**, 3449 (1966).
- [214] S. Stolte, *Reactive Scattering Studies on Oriented Molecules*, Berichte der Bunsengesellschaft für Phys. Chemie **86**, 413 (1982).
- [215] F. Filsinger, G. Meijer, H. Stapelfeldt, H. N. Chapman, and J. Küpper, *State- and conformer-selected beams of aligned and oriented molecules for ultrafast diffraction studies*, Phys. Chem. Chem. Phys. **13**, 2076 (2011).
- [216] J. C. H. Spence and R. B. Doak, *Single Molecule Diffraction*, Phys. Rev. Lett. **92**, 198102 (2004).
- [217] M. H. G. de Miranda, A. Chotia, B. Neyenhuis, D. Wang, G. Quéméner, S. Ospelkaus, J. L. Bohn, J. Ye, and D. S. Jin, *Controlling the quantum stereodynamics of ultracold bimolecular reactions*, Nat. Phys. **7**, 502 (2011).

- [218] B. Friedrich and D. R. Herschbach, *Spatial orientation of molecules in strong electric fields and evidence for pendular states*, Nature **353**, 412 (1991).
- [219] B. Friedrich and D. R. Herschbach, *On the possibility of orienting rotationally cooled polar molecules in an electric field*, Zeitschrift für Phys. D Atoms, Mol. Clust. **18**, 153 (1991).
- [220] T. D. Hain, R. M. Moision, and T. J. Curtiss, *Hexapole state-selection and orientation of asymmetric top molecules: CH₂F₂*, J. Chem. Phys. **111**, 6797 (1999).
- [221] P. R. Brooks, *Reactions of oriented molecules.*, Science **193**, 11 (1976).
- [222] D. H. Parker and R. B. Bernstein, *Oriented Molecule Beams Via the Electrostatic Hexapole: Preparation, Characterization, and Reactive Scattering*, Annu. Rev. Phys. Chem. **40**, 561 (1989).
- [223] H. Stapelfeldt, *Colloquium: Aligning molecules with strong laser pulses*, Rev. Mod. Phys. **75**, 543 (2003).
- [224] L. Cai and B. Friedrich, *Recurring Molecular Alignment Induced by Pulsed Nonresonant Laser Fields*, Collect. Czechoslov. Chem. Commun. **66**, 991 (2001).
- [225] L. Cai, J. Marango, and B. Friedrich, *Time-Dependent Alignment and Orientation of Molecules in Combined Electrostatic and Pulsed Nonresonant Laser Fields*, Phys. Rev. Lett. **86**, 775 (2001).
- [226] B. Friedrich and D. Herschbach, *Alignment and trapping of molecules in intense laser fields*, Phys. Rev. Lett. **74**, 4623 (1995).
- [227] B. Friedrich and D. Herschbach, *Alignment enhanced spectra of molecules in intense nonresonant laser fields*, Chem. Phys. Lett. **262**, 41 (1996).
- [228] B. Friedrich, *Manipulating Molecules via Combined Static and Laser Fields*, J. Phys. Chem. A **103**, 10280 (1999).
- [229] B. Friedrich and D. Herschbach, *Enhanced orientation of polar molecules by combined electrostatic and nonresonant induced dipole forces*, J. Chem. Phys. **111**, 6157 (1999).
- [230] B. Schmidt and B. Friedrich, *Topology of surfaces for molecular Stark energy, alignment, and orientation generated by combined permanent and induced electric dipole interactions.*, J. Chem. Phys. **140**, 064317 (2014).
- [231] A. Boca and B. Friedrich, *Fine structure, alignment, and orientation of ³²S¹⁶O and ¹⁶O¹⁸O molecules in congruent electric and magnetic fields*, J. Chem. Phys. **112**, 3609 (2000).
- [232] H. Tanji, S. Minemoto, and H. Sakai, *Three-dimensional molecular orientation with combined electrostatic and elliptically polarized laser fields*, Phys. Rev. A **72**, 063401 (2005).
- [233] R. Baumfalk, N. H. Nahler, and U. Buck, *Photodissociation of oriented HXeI molecules in the gas phase*, J. Chem. Phys. **114**, 4755 (2001).
- [234] H. Sakai, S. Minemoto, H. Nanjo, H. Tanji, and T. Suzuki, *Controlling the Orientation of Polar Molecules with Combined Electrostatic and Pulsed, Nonresonant Laser Fields*, Phys. Rev. Lett. **90**, 083001 (2003).
- [235] H. J. Loesch and A. Remscheid, *Brute force in molecular reaction dynamics: A novel technique for measuring steric effects*, J. Chem. Phys. **93**, 4779 (1990).

- [236] A. Slenczka, B. Friedrich, and D. Herschbach, *Pendular alignment of paramagnetic molecules in uniform magnetic fields*, Phys. Rev. Lett. **72**, 1806 (1994).
- [237] U. Kappes and P. Schmelcher, *Adiabatic potential-energy surfaces of the H_2^+ ion in a strong magnetic field*, Phys. Rev. A **53**, 3869 (1996).
- [238] T. Detmer, P. Schmelcher, and L. Cederbaum, *Hydrogen molecule in a magnetic field: The lowest states of the Π manifold and the global ground state of the parallel configuration*, Phys. Rev. A **57**, 1767 (1998).
- [239] K. K. Lange, E. I. Tellgren, M. R. Hoffmann, and T. Helgaker, *A paramagnetic bonding mechanism for diatomics in strong magnetic fields.*, Science **337**, 327 (2012).
- [240] P. Schmelcher and L. Cederbaum, *Crossings of potential-energy surfaces in a magnetic field*, Phys. Rev. A **41**, 4936 (1990).
- [241] M. Mayle, S. T. Rittenhouse, P. Schmelcher, and H. R. Sadeghpour, *Electric field control in ultralong-range triatomic polar Rydberg molecules*, Phys. Rev. A **85**, 052511 (2012).
- [242] R. Feynman, *Forces in Molecules*, Phys. Rev. **56**, 340 (1939).
- [243] D. Carfi, *The pointwise Hellmann-Feynman theorem*, AAPP — Phys. Math. Nat. Sci. **88** (2010).
- [244] D. Baye, N. Clerbaux, and M. Vincke, *Delocalized states of atomic hydrogen in crossed electric and magnetic fields*, Phys. Lett. A **166**, 135 (1992).
- [245] I. Dzyaloshinskii, *Effects of the finite proton mass in a hydrogen atom in crossed magnetic and electric fields: a state with a giant electric dipole moment*, Phys. Lett. A **165**, 69 (1992).
- [246] P. Schmelcher and L. Cederbaum, *Two-body effects of the hydrogen atom in crossed electric and magnetic fields*, Chem. Phys. Lett. **208**, 548 (1993).
- [247] M. Fauth, H. Walther, and E. Werner, *Rydberg atoms in crossed external magnetic and electric fields: Experimental observation of an outer potential minimum*, Zeitschrift für Phys. D Atoms, Mol. Clust. **7**, 293 (1987).
- [248] G. Raithel, M. Fauth, and H. Walther, *Atoms in strong crossed electric and magnetic fields: Evidence for states with large electric-dipole moments*, Phys. Rev. A **47**, 419 (1993).
- [249] J. Avron, I. Herbst, and B. Simon, *Separation of center of mass in homogeneous magnetic fields*, Ann. Phys. (N. Y). **114**, 431 (1978).
- [250] B. Johnson, J. Hirschfelder, and K.-H. Yang, *Interaction of atoms, molecules, and ions with constant electric and magnetic fields*, Rev. Mod. Phys. **55**, 109 (1983).
- [251] J. Shertzer, J. Ackermann, and P. Schmelcher, *Positronium in crossed electric and magnetic fields: The existence of a long-lived ground state*, Phys. Rev. A **58**, 1129 (1998).
- [252] P. Schmelcher, *Giant dipole states of multielectron atoms in crossed electric and magnetic fields*, Phys. Rev. A **64**, 063412 (2001).
- [253] S. Zöllner, H.-D. Meyer, and P. Schmelcher, *Multi-electron giant dipole resonances of atoms in crossed electric and magnetic fields*, EPL (Europhysics Lett. **71**, 373 (2005).
- [254] P. Schmelcher and L. S. Cederbaum, *Two-body effects of the hydrogen atom in crossed electric and magnetic fields*, Chem. Phys. Lett. **208**, 548 (1993).

- [255] N. Samboy, J. Stanojevic, and R. Côté, *Formation and properties of Rydberg macrodimers*, Phys. Rev. A **83**, 50501 (2011).
- [256] Ronveaux A., editor, *Heuns Differential Equations*, Oxford University Press, New York, 1995.
- [257] B. Leaute and G. Marcilhacy, *On the Schrodinger equations of rotating harmonic, three-dimensional and doubly anharmonic oscillators and a class of confinement potentials in connection with the biconfluent Heun differential equation*, J. Phys. A. Math. Gen. **19**, 3527 (1986).
- [258] P. Machnikowski, *Exactly Solvable Problems in Quantum Mechanics*, PhD thesis, Technical University of Wroclaw, 1995.
- [259] A. Usheridze, *Quasi-Exactly Solvable Models in Quantum Mechanics*, Institute of Physics Publishing Bristol and Philadelphia, 1993.
- [260] V. Singh, *Continued fraction theory of the rotating harmonic oscillator*, J. Math. Phys. **23**, 1323 (1982).
- [261] S. Bose and N. Varma, *Exact solution of the Schrödinger equation for the central nonpolynomial potential $V(r)=r^2 + \lambda r^2/(1 + gr^2)$ in two and three dimensions*, Phys. Lett. A **141**, 141 (1989).
- [262] Y.-Z. Zhang, *Exact polynomial solutions of second order differential equations and their applications*, J. Phys. A Math. Theor. **45**, 065206 (2012).
- [263] M. Nieto and V. Gutschick, *Rotating harmonic oscillator: Its general solution and the lack of ground-state energy equipartition*, Phys. Rev. A **28**, 471 (1983).
- [264] A. V. Turbiner, *Quasi-exactly-solvable problems and $sl(2)$ algebra*, Commun. Math. Phys. **118**, 467 (1988).
- [265] L. J. El-Jaick and B. D. B. Figueiredo, *A limit of the confluent Heun equation and the Schroedinger equation for an inverted potential and for an electric dipole*, J. Math. Phys. **50**, 123511 (2009).
- [266] A. Ralko and T. T. Truong, *Heun functions and the energy spectrum of a charged particle on a sphere under a magnetic field and Coulomb force*, J. Phys. A. Math. Gen. **35**, 9573 (2002).
- [267] M. Hortacsu, *Heun Functions and their uses in Physics*, in *Proc. 13th Reg. Conf. Math. Phys.*, edited by U. Cami and I. Semiz, pages 23–39, Antalya, Turkey, World Scientific (2013).
- [268] V. Averbukh, N. Moiseyev, P. Schmelcher, and L. Cederbaum, *Transition from Rydberg to giant-dipole-moment states of hydrogen atoms in crossed fields: A suggestion for an experiment*, Phys. Rev. A **59**, 3695 (1999).
- [269] A. Khuskivadze, M. Chibisov, and I. Fabrikant, *Adiabatic energy levels and electric dipole moments of Rydberg states of Rb_2 and Cs_2 dimers*, Phys. Rev. A **66**, 042709 (2002).
- [270] E. Hairer, S. Norsett, and G. Wanner, *Solving ordinary differential equations I: Nonstiff problems*, Springer-Verlag, Berlin, 1993.

Acknowledgments

I would like to thank everybody who has contributed to this thesis both directly and indirectly.

- I am deeply thankful to my supervisor Prof. **Peter Schmelcher** for giving me the opportunity to perform my PhD studies in his group. I thank him for his invaluable help and the successful collaboration.
- I thank Dr. **Michael Mayle** for teaching me Rydberg physics at the beginning of my PhD studies. Even later he was always accessible and all his suggestions were very helpful.
- Thanks a lot to all group members for the nice and inspiring atmosphere! Special thanks to my office mates **Christian Morfonios** and **Panagotis Giannakeas** for supporting me during the past five years. *Σας ευχαριστώ!*
- Many thanks to all members of the other groups in the ZOQ and ILP. Special thanks to Prof. **Ludwig Mathey** and his people for sharing their seminars and several lunch and coffee breaks.
- Special thanks to **Bodo Krause** and the other PHYSNET administrators for their technical support.
- I thank both the students and organizers of the **ITN COHERENCE Network** for the inspiring conferences in Heidelberg, Pisa, Dresden and Granada.
- Many thanks to all people who have given me the opportunity to discuss my work with them. Special thanks to Prof. **Rosario González-Férez**, Prof. **Hossein Sadeghpour**, Prof. **Seth Rittenhouse**, Prof. **Chris Greene**, Prof. **Igor Lesanovsky** and many more.
- I thank Prof. **Tilman Pfau**, Dr. **Alexander Krupp** and all members of the 5th Institute of Physics of the University of Stuttgart for the very fruitful collaboration.
- Many thanks to my coaches and all members of the **Kyokushinkai Karate Club Hamburg**. OSU!
- I am indebted to my friends who have supported me during my PhD. Special thanks to **Sven Jansen**, **Kilian Thevissen** and **Tim Schröders**.
- Many, many thanks to my family. In particular, I would like to thank my parents **Karl-Heinz** and **Maria Kurz** and my sister **Alexandra Kurz**. Their moral support over the years has to be considered as priceless! Thank you!

Danksagung

An dieser Stelle möchte ich mich bei Allen bedanken, die direkt oder indirekt zum Entstehen dieser Arbeit beigetragen haben:

- Als erstes möchte ich mich bei meinem Doktorvater Prof. Dr. **Peter Schmelcher** dafür bedanken, dass er mir die Möglichkeit gegeben hat in seiner Arbeitsgruppe zu promovieren. Selbstverständlich bedanke ich mich für die sehr gute Betreuung und die erfolgreiche Zusammenarbeit.
- Besonderer Dank gilt Dr. **Michael Mayle**, der mich in das interessante Feld der Rydbergphysik eingeführt hat. Seine gewissenhafte Betreuung zu Beginn meiner Promotion war eine echte Hilfe. Auch später war er stets erreichbar und mit hilfreichen Ratschlägen zu Stelle.
- An dieser Stelle möchte ich allen Mitgliedern der Arbeitsgruppe Schmelcher danken, mit denen ich in den vergangenen Jahren zusammenarbeiten bzw. einfach nur kennenlernen durfte. Besonderen Dank gilt meinen langjährigen Büronachbarn **Christian Morfonios** und **Panagiotis Giannakeas**. *Σας ευχαριστώ!*
- Natürlich geht mein Dank auch an allen Mitarbeiter der anderen Gruppen im ZOQ und ILP. Besonders hervorheben möchte ich hier Prof. Dr. **Ludwig Mathey** und seine Gruppe, mit denen ich so manches Seminar, Mittagessen und selbstverständlich die ein oder andere Kaffeepause teilen durfte.
- Danke auch an die PHYSNET Administratoren für die technische Unterstützung in den vergangenen Jahren. Hier gilt mein besonderer Dank **Bodo Krause**. Ohne seinen Einsatz wäre ich so manches mal völlig aufgeschmissen gewesen.
- Viele Grüße und herzlichen Dank an alle Mitglieder und Organisatoren des **ITN COHERENCE Network** für die wunderbaren Konferenzen in Heidelberg, Pisa, Dresden und Granada.
- Danke an all diejenigen, mit denen ich mich in den letzten Jahren über meine Arbeit austauschen konnte und die somit dazu beigetragen haben, die Qualität dieser zu verbessern. Hierzu zählen Prof. **Rosario González-Férez**, Prof. **Hossein Sadeghpour**, Prof. **Seth Rittenhouse**, Prof. **Chris Greene**, Prof. **Igor Lesanovsky** und viele andere.
- Ich bedanke mich bei Prof. **Tilman Pfau**, Dr. **Alexander Krupp** und allen Mitarbeitern des 5. Physikalischen Instituts der Universität Stuttgart für die erfolgreiche Zusammenarbeit.
- Ebenfalls bedanken möchte ich mich bei den Trainern und Mitgliedern des **Kyokushinkai Karate Hamburg e. V.**. Das Training hat mir sehr oft geholfen neue Kraft zu tanken. Definitiv werde ich es in den kommenden Jahren fortsetzen. OSU!
- Nicht vergessen darf ich all meine Freunde, die in den vergangenen Jahren trotz der Entfernung und der doch recht seltenen Besuche Kontakt zu mir gehalten haben und stets erreichbar waren. Zu nennen sind hier insbesondere **Sven Jansen**, **Kilian Thevissen** und **Tim Schröders**.
- Ganz besonders muss ich meiner Familie, insbesondere meinen Eltern **Karl-Heinz** und **Maria Kurz** sowie meiner Schwester **Alexandra Kurz**, danken. Ihre finanzielle, aber vor allem moralische Hilfe war in den vergangenen Jahren von unschätzbarem Wert. Danke!

Declaration of authorship

I hereby certify that this thesis has been composed by me and is based on my own work, unless stated otherwise. No other person's work has been used without due acknowledgement in this thesis. All references and verbatim extracts have been quoted, and all sources of information, including graphs and data sets, have been specifically acknowledged.

Markus Kurz
Hamburg, 12/16/2014

Erklärung zur Urheberschaft

Hiermit erkläre ich, dass ich die vorliegende Dissertation selbständig verfasst und keine anderen als die angegebenen Hilfsmittel benutzt habe. Die Stellen der Dissertation, die anderen Quellen im Wortlaut oder dem Sinn nach entnommen wurden, sind durch Angaben der Herkunft kenntlich gemacht. Dies gilt auch für Zeichnungen, Skizzen, bildliche Darstellungen sowie für Quellen aus dem Internet.

Markus Kurz
Hamburg, 16.12.2014